Non-cytotoxic and Antibacterial Zinc/Graphene Nanocomposites: Synthesis and Performance Characteristics

THESIS

Submitted in partial fulfilment of the requirements for the degree of

DOCTOR OF PHILOSOPHY

By

AYUSH OWHAL

ID No. 2018PHXF0405P

Under the supervision of

Prof. Sachin U. Belgamwar

&

Co-supervision of

Prof. Jitendra S. Rathore

BIRLA INSTITUTE OF TECHNOLOGY AND SCIENCE, PILANI, PILANI CAMPUS

PILANI−333031, RAJASTHAN, INDIA

January 2024

BIRLA INSTITUTE OF TECHNOLOGY AND SCIENCE, PILANI

<u>CERTIFICATE</u>

This is to certify that the thesis entitled, "*Non-cytotoxic and Antibacterial Zinc/Graphene Nanocomposites: Synthesis and Performance Characteristics*" and submitted by Mr. **Ayush Owhal** ID No. **2018PHXF0405P** for award of **Doctor of Philosophy** of the institute embodies original work done by him under our supervision.

_____

Supervisor
Prof. Sachin U. Belgamwar
Associate Professor,
BITS-Pilani, Pilani Campus
Date:

_____

Co-Supervisor
Prof. Jitendra S. Rathore
Associate Professor,
BITS-Pilani, Pilani Campus
Date:

Abstract

Non-cytotoxic and Antibacterial Zinc/Graphene Nanocomposites: Synthesis and Performance Characteristics

by **AYUSH OWHAL**

Non-cytotoxic and antibacterial nanocomposites are a class of advanced materials that have gained significant attention in recent years due to their unique properties and potential applications in various fields, including biomedical, environmental, and industrial applications. These materials are typically composed of matrix materials, such as metallic, ceramic, and polymeric. Compared to polymeric- and ceramic-based nanocomposites, metal matrix nanocomposites (MMNCs) offer several advantages, such as high strength and durability.

Zinc (Zn)-based nanocomposites are known for their non-cytotoxicity, biodegradability, and antibacterial properties. Incorporating advanced nanofiller reinforcement, such as graphene nanoplatelets (GNPs), can further enhance their antibacterial, electrochemical, and tribo-mechanical properties. Many studies reported higher concentrations of GNPs as cytotoxic for the human body. However, attachments of biocompatible groups through functionalization (f-) can enable the safe application of GNPs.

There are various methods for the fabrication of MMNCs, such as vapour deposition, ball-milling, melt mixing, electroless deposition, and electro-co-deposition. Among all, electro-co-deposition is an economical, facile and industrially scalable method that can uniformly distribute the reinforcement without damaging the nanostructures of reinforcements.

In this study, two categories of Zn-based nanocomposites have been fabricated: (i) powder/pellet type and (ii) coating type. For powder fabrication, pristine GNPs were functionalized (f-) with polyethelene glycol to reduce their toxicity and f-GNP reinforced in Zn matrix using the modified electro-co-deposition (M-ECD) followed by powered metallurgy to obtain solid pellets of nanocomposite. For coating fabrication, pristine GNPs and Zn ions from ECD bath were co-deposited on steel substrate. Both powder/pellet and coating samples were characterized and tested for microstructure, morphology, tribo-mechanical, anti-corrosion, and anti-bacterial properties.

Powder of Zn/f-GNP nanocomposites were tested systemically for in-vitro cytotoxicity. The nanocomposite pellets of 100 mg/L of f-GNPs concentration in ECD bath has demonstrated a uniform slow degradation rate of 26×10^{-3} mm year^{-1}. The microhardness, compressive yield strength (CYS) and ultimate compressive strength (UCS) of Zn/f-GNP (100 mg/L) nanocomposite were 108.5 HV, 284.9 MPa, and 292.6 MPa, respectively, which were significantly higher than pure Zn pellets.

In coatings, the anti-bacterial activities of the Zn coatings enhanced with reinforcing GNPs against Staphylococcus aureus (S. aureus) and Escherichia coli (E. coli) bacteria. The microhardness, friction coefficient, wear loss, and polarization resistance values were remarkably improved up

to 151 HV, 0.48, 12.09 mg, and 2.3 kΩ.cm^2 for Zn/GNP (100 mg/L) nanocomposite coating, respectively.

In addition, Zn-Cu/GNP nanocomposite powder/pellets and γ-Zn Ni/GNP nanocomposite coatings were also fabricated. The performance characteristics were investigated and compared with pure alloys. Results suggested that these alloying and addition of GNPs have effectively enhanced the tribo-mechanical, and anti-corrosion performances of nanocomposites.

The proposed nanocomposites have the potential to be used in various applications, including biodegradable medical implants and antibacterial coatings to prevent healthcare-acquired infections (HCAI), food packaging, wound dressings, and water treatment.

$\cdots$

Acknowledgements

Contents

List of Figures

List of Tables

Abbreviations

MMNC	Metal Matrix Nanocomposite
MMC	Metal Matrix Composite
ECD	Electro-Co-Deposition
M-ECD	Modified Electro-Co-Deposition
GFM	Graphene Family Material
GNP	Graphene Nano-Platelet
ƒ-GNP	Functionalized Graphene Nano-Platelet
CNT	Carbon Nano-Tube
PEG	Poly-Ethylene Glycol
EDC	1-Ethyl-3-(3-Dimethylaminopropyl) Carbodiimide
SBF	Simulated Body Fluide
DAPI	4 ,6-Diamidino-2-PhenylIndole
FESEM	Field Emission Scanning Electron Microscopy
XRD	X-Ray Diffraction
JCPDS	Joint Committee on Powder Diffraction Standards
NMR	Nuclear Magnetic Resonance
EDS	Energy Dispersive Spectroscopy
SAED	Selected Area Electron Diffraction
FT-IR	Fourier-Transform-InfraRed spectroscopy
CR	Corrosion Rate
ECDC	European CDentre for Disease prevention and Control
HCAIs	Health-Care Associated Infections
EPS	Extracellular Polymeric Substances
ROS	Reactive Oxygen Species

Dedicated to my loving parents with a special feeling of gratitude.

Chapter 1

Introduction

Zinc (Zn) is post-transition metal with silvery-greyish appearance. It is the twenty-fourth most abundant element in the Earth's crust. Zn-based compounds, alloys and nanocomposites have several applications such as anti-corrosion, biodegradable implant, anti-bacterial, energy storage, photocatalysis, waste-water treatment, etc [1], [2]. Zn-based coatings for steel substrates are well known for sacrificial protection against corrosion and anti-bacterial protection. Apart from this, titanium-, gold-, silver-, chromium-, nickel-, and copper-based coatings have been widely tested for surface protection from corrosion and bacterial growth [3], [4]. But Zn-based coatings are gaining more research interest among all due to their low-cost, easy availability, high anti-corrosion and anti-bacterial properties which makes them suitable for low-cost coating applications in public facilities and infrastructures. Figure 1.1 presents the Engineering applications of Zn-based alloys and nanocomposites as coatings and structural materials.

Recent studies have shown that Zn-based structural implant materials may biodegrade with time and resorb by the human body [6]. Biodegradable implant materials can support the fractured tissues or bones during the healing of body fractures or injuries. After that, the implant material will degrade and absorb the body as the new tissues or bone structures reform. Zn shows a moderate degradation rate in humans, which is neither too fast as magnesium nor too slow as iron with promising biocompatibility [7]. This makes it one of the best metal elements for a biodegradable implant that can sustain up to its clinical role. Also, the degraded Zn compounds participate in several essential bio-enzymatic reactions, which help to decompose in the body. Parakasam et al. [8] reported the prospects of Zn as a structural material for biodegradable applications. They have compared the biocompatibility, corrosion behavior and mechanical properties of Zn. However, fabricating high-strength and ductile Zn nanocomposite while retaining its homogenized properties is always one of the main challenges in metallurgical engineering. To enhance the mechanical and corrosion properties of Zn-based alloys and nanocomposites, many researchers have focused on the addition of reinforcement particles in the Zn matrix [9]. Zhao et al. [10] have studied the anti-bacterial activity of coatings containing Zn and observed it through in vitro bacterial experiments. They reported that the coatings could inhibit the growth of
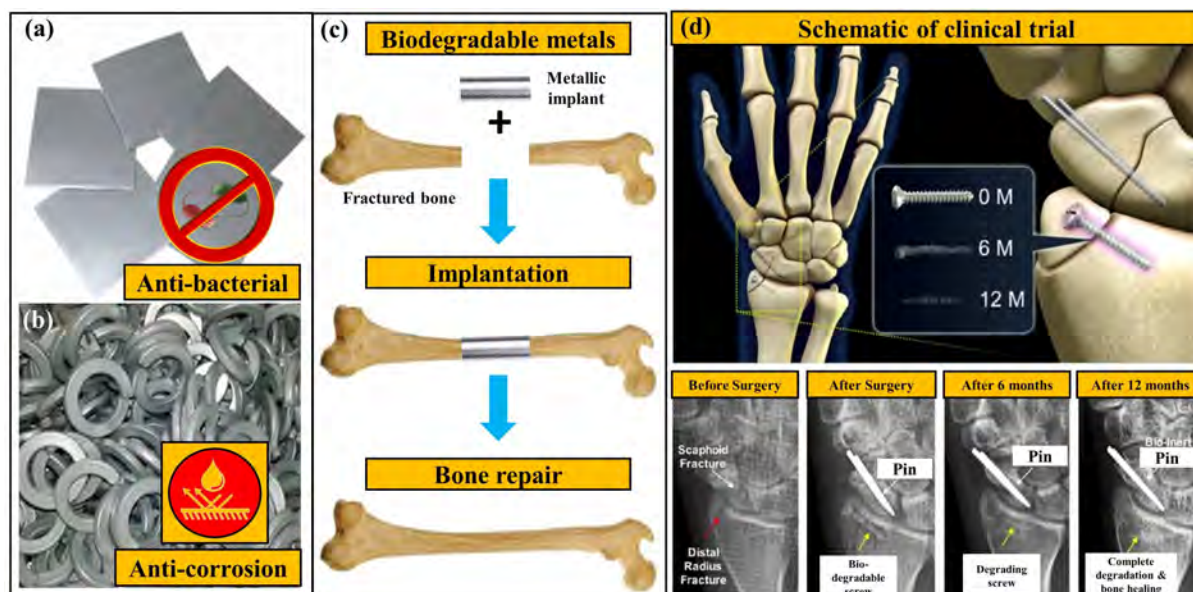
FIGURE 1.1: Engineering applications of Zn-based alloy and nanocomposites as coatings and structural material: (a) anti-bacterial coating for hospitals and public infrastructures, (b) anti-corrosion coating for fasteners and marine applications, (c) biodegradable implant material for structural support for bone healing and (d) schematic of orthopedic clinical trial for repairing of bone fracture through biodegradable implant, here, insert shows the before and after surgery X-ray images during 12 months of biodegradation of metallic implant and bone healing [5].

Staphylococcus aureus bacteria and had good anti-bacterial activity. Zn nanocomposite coatings are promising to increase the lifetime of engineering components in harsh conditions. This chapter describes a brief introduction to nanocomposites and the problem statement investigated in this thesis.

1.1 Composite

Composite materials are materials made from two or more different constituent materials, with properties that are significantly different from the properties of constituent materials. In far back as 1200 B.C., Egyptians and Hebrews have fabricated synthetic composite by the addition of straw as reinforcement in bricks to enhance their mechanical properties. Fiberglass is the first modern composite material and is extensively used in car bodies, building panels, sports equipment and boat hulls. Drivers for improved composite materials are weight reduction, cost reduction as well as improved performance by enhancing resistance to fatigue, corrosion, and mechanical damage. To meet the requirement of a particular application, the composite material can be fabricated by selecting an appropriate reinforcing element and matrix material. Composite materials include reinforced polymer matrix, ceramic matrix, and metal matrix. Composite materials have been commonly used for bridges, buildings and structural material for storage tanks and bathtubs. Also, composite materials have been used for industrial applications due to their high strength, less expensive, or lightweight than traditional materials.

1.2 Nanomaterials

Nanotechnology and nanoscience fields have attracted considerable research interest due to their wide range of applications and numerous benefits in several engineering sectors. Particularly, nanomaterials are considered as future of engineering materials. Nanomaterials have gained prominence in technological advancement due to their exceptional tunable properties and enhanced performance over their bulk counterparts. These nanomaterials are revolutionizing various industrial applications due to their outstanding, and unique characteristics. The engineering applications of nanomaterials are diversified in various sectors, such as biomedical, food processing, biotechnology, environmental remediation, anti-bacterial coating, construction, renewable energy, electronics, and energy storage. In short, nanomaterials are expected to bring a breakthrough development field of leading cutting-edge nanotechnology. Nanoparticles are defined as particulate matter with at least one dimension less than 100 nm [11]. When the scale of the material is within the range of 1-100 nm, the properties of the material may change so abruptly that the material may have some outstanding properties. Nanomaterials differ in properties from their macro counterpart. Many natural nanoparticles are present in the volcano dust, soil, seawater spills, humid matter, colloidal clay, soil, and atmosphere on the earth [12], [13]. Nanomaterials synthesized by nanotechnology have superior flexibility, strength, and surface-to-volume ratio. Atoms present on the surface of nanoparticles are quite active compared to other atoms. The powder form of nanoparticles can be used as a catalyst or solid fuel in the rocket [14]. Nanoparticles are being widely used in electronics, optics, medicine, chemistry, agriculture, food industries, and automobile industries [15].

GNPs, CNT, and C_{60} fullerene are 2-, 1- and 0-dimensional nanomaterials, and their properties are not similar to macroscopic carbon materials. The unexpected properties of nanocarbon have a novel scientific field that can drastically change our lifestyle. Among the various types of nanoparticles, GNPs have been paid special attention [16].

1.3 Nanocomposites

In nanocomposite material, the matrix serves different functions such as transferring load between the reinforcement, binding the reinforcement, providing the nanocomposite component with its net shape and protecting the reinforcement from mechanical and environmental damage. The basic dimensional shape of nanofillers in binding matrix can be (i) nanoparticles; (ii) nanotubes or nanofibers or whiskers; and (iii) nanolayers [17] (see Figure 1.2) and the materials for nanofillers can be: (i) inorganic along with advance allotropes of carbon and boron-nitride (graphene nanoplatelets (GNPs), fullerene, carbon nanotube (CNT) and boron-nitride nanotubes) (ii) organic and (iii) hybrid [18].
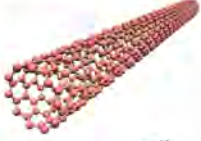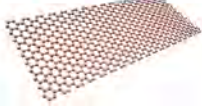
Dimensional shapes of nanofillers	Type	Examples

FIGURE 1.2: Dimensional shapes of nanofiller reinforcement.

1.3.1 Classification of nanocomposites

A nanocomposite material consists of two basic parts: Matrix and reinforcement (see Figure 1.3). Figure 1.3a explains the intercalated and exfoliated nanocomposite types. The nanocomposite materials can also be classified by their matrix type (e.g. organic and inorganic nanocomposites). Generally, the categorization of the nanocomposite materials is based on the name of matrix such as ceramic matrix nanocomposites (CMNCs), polymer matrix nanocomposites (PMNCs), and metal matrix nanocomposites (MMNCs) (see Figure 1.3b).

1.3.1.1 Ceramic matrix nanocomposites

Ceramic matrix nanocomposites (CMNCs) are nanocomposite materials and key materials for advanced energy systems. They generally consist of ceramic fibers or whiskers reinforced in a ceramic matrix, developing a ceramic fiber-reinforced material. CMNCs have been developed to overcome the brittleness problem of unreinforced ceramic materials. SiC/SiC, Al_2O_3/Al_2O_3, and C/SiC are the most used CMNCs in several industrial applications. Applications for CMNCs are being considered for the recirculating fan, Gas- fired radiant, burner tubes, canned motor, filtration, and heat exchanger [19].

1.3.1.2 Polymer matrix nanocomposites

Polymer matrix nanocomposites (PMNCs) are nanocomposite materials comprised of a specific type of fiber, bound together by the polymer matrix to accomplish desired properties. The fiber of PMNCs consists of aramid, glass fiber, and graphite. PMNCs are easy to fabricate compared to metal-matrix, ceramic-matrix, and carbon-matrix. PMNCs have many advantages such as good abrasion and corrosion resistance, lightweight, high strength, and high stiffness along the direction of reinforcement. Nowadays, PMNCs are widely used in automobiles, aircraft, marine structures, and other moving structures [20].
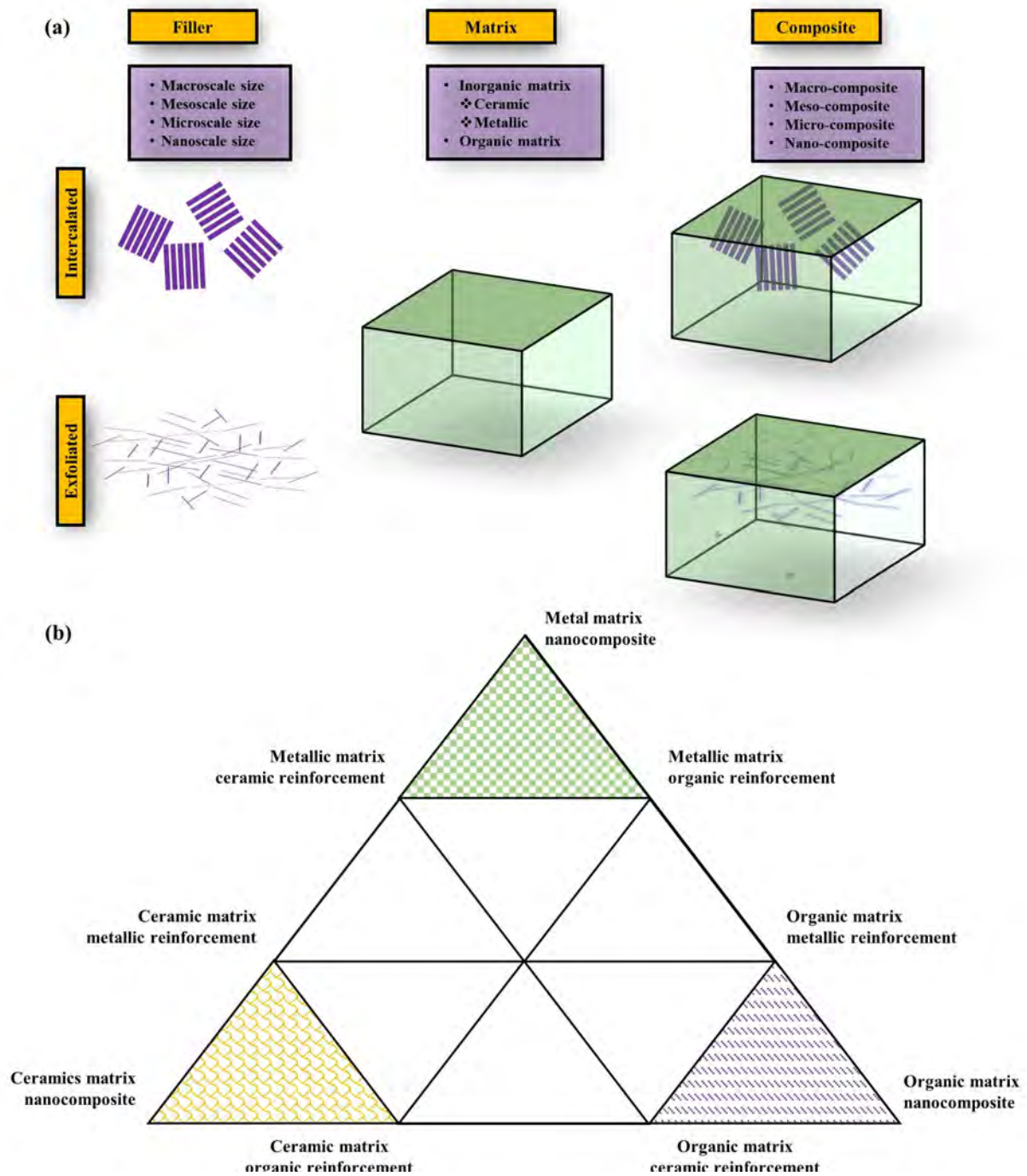
FIGURE 1.3: Classification of nanocomposites: (a) intercalated and exfoliated nanocomposite types comprised of different types of reinforcement and matrices. (b) metallic, ceramic and organic nanocomposites.

1.3.1.3 Metal matrix nanocomposites

Metal matrix nanocomposites (MMNCs) are nanocomposite materials synthesized by incorporating various reinforcing phases in the metal matrix. MMNCs are the potential contestants for operation in complex service conditions such as marine, nuclear power plants, automobile, chemical and infrastructure. In MMNCs, the main matrix materials can be Ni-, Cu-, Al-, Mg-, and Ti-based [21]. The main reinforcements used are alumina, carbide, and silicon. MMNCs with lightweight and high strength have been developed for satellites, aircraft, missiles, jet engines, and high-speed machinery. Presently, metal matrix is used in diesel engine piston developed by Toyota, which shows high wear resistance and high-temperature strength [22]. Metal matrices are most commonly used in several engineering applications. Presently, particulate-reinforced MMNCs have attracted considerable attention from researchers worldwide due to their low cost, ease of synthesis, and near-isometric enhancement in the overall properties. Also, the incorporation of nanoparticles in the metal matrix has shown significant enhancement in the mechanical, tribological, electrical, tribological, optical, and corrosion properties of the resulting nanocomposite [23]. In the next section, a brief introduction to some reinforcing nanomaterials and the significance of the nanosize effect are discussed.
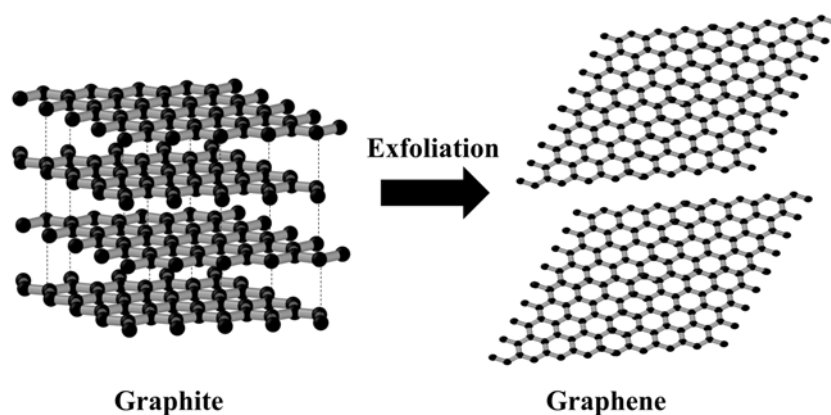
FIGURE 1.4: Graphite exfoliation into the single two-dimensional hexagonal graphene sheets of carbon atoms [16].

1.4 GNP-based nanocomposites

GNP is a one-atom-thick planar sheet of sp_2 hybridized carbon atoms arranged in a crystal lattice and yet stronger than diamond . In 2004, GNP was first isolated from graphite by the mechanical exfoliation method (Figure 1.4) [24]. To date, various methods to produce GNPs have been developed, such as exfoliation and cleavage, chemical vapor deposition, thermal decompositions, electrochemical methods, and pulsed-laser scribing [25]. GNPs have achieved a large theoretical

specific surface area, excellent electrical conductivity, and high mechanical strength [26]. Its remarkable electronic, mechanical, optical, electrochemical, and thermal properties compared with other carbon materials, makes it a promising material in electrical, chemical and automobile industrial applications [27]. GNPs have superior properties such as high fracture strength (125 GPa) [24], super charge-carrier mobility (200,000 $cm^2V^{-1}s^{-1}$), high Young's modulus (1 TPa), and extreme thermal conductivity (5,000 $Wm^{-1}K^{-1}$). GNPs have been widely used in electronic industries due to their superior carrier mobility (up to 350,000 $cm^2V^{-1}s^{-1}$) and high optical transparency (97.7%) [28].

The advantage of GNPs over CNT used in nanocomposites includes high-pressure processing result in damage to CNT structure; short CNT serve as a good reinforcing element however, not suitable for wear applications, CNT forms only point-to-point contact; however, GNPs have strong interfacial bonding; fracture strengthening is more in GNPs nanocomposites because of its planar geometry and high aspect ratio [29]. These extraordinary properties make GNPs an ideal reinforcing material for the nanocomposites, for possible enhancement in mechanical, tribological, anti-bacterial and corrosion properties of the resulting nanocomposite. To have the advantage of their extraordinary properties at the bulk level, scientists are exploring the possibility of preparing nanocomposites, termed GNPs-reinforced nanocomposites, which are detailed in the next section.

1.4.1   GNP-based MMNCs

Metal matrix nanocomposites have shown increased strength compared to conventional materials [30], [31]. Recently, several authors have fabricated GNP-reinforced MMNCs for metals like Al [32]–[34], Cu [21], [35], Zn [36], Mg [37], Ni [38] and Ti [39]. Different research groups have developed different processing routes for GNPs-reinforced metal matrix nanocomposites like powder metallurgy, casting, electroless deposition, melting and solidification, thermal spray, laser deposition, electrochemical deposition, sol-gel, and other novel routes [17]. Electrodeposition and powder metallurgy methods are extensively used for the synthesis of GNP-reinforced nanocomposites owing to several advantages over the other conventional processes [40]. There are two approaches for the synthesis of GNPs metal matrix nanocomposites that have been developed to enhance the mechanical, tribological, and corrosion properties. In the first approach, GNP-reinforced nanocomposites are formed through uniform dispersion of GNPs. However, in the second approach, GNPs-reinforced nanocomposites are developed by forming layered structures by alternate deposition of GNPs and metal matrix [41]. GNPs are very light in weight and cannot be dissolved in water, and it can be dispersed uniformly in a plating solution using a surfactant [42]. The strong GNPs coupling to the metal matrix particles caused highly increase in thermal conductivity [43]. Recently GNPs gained extensive interest in the electrochemistry field and have many applications in various sectors like antibacterial coatings [44], biosensors [45], bioimplants

[46], supercapacitors [47], transparent electrodes [48], sensors [49], nanoscale electronic devices [50], and field emission devices [51] and filler materials [52].

Owing to the excellent properties of GNP, it is believed that it could significantly improve the performance of nanocomposites. Also, GNPs are ideal to be an efficient reinforcing element to achieve high-quality nanocomposite materials.

1.5   Need for low cost and scalable synthesis Zn/GNPs nanocomposites

Zn-based MMNCs are a type of material made by combining a Zn matrix with reinforcing particles. The addition of these reinforcing particles can improve the mechanical properties of the material, such as its strength, stiffness, and toughness [53]. The Zn-based MMNCs are having many possibilities in the coating, structural, tribological, anti-corrosion and anti-bacterial and non-cytotoxic applications [54].

However, like any material, Zn-based MMNCs may also have limitations. Zn-based MMNCs are weak in tribo-mechanical strength [55]. A small amount of reinforcement of advanced carbon allotrope nanofiller, such as GNPs, CNT, and fullerene, can significantly enhance the tribo-mechanical performance of Zn matrix [56]. Here, 2D exfoliated layers of GNPs are effective nanofiller that can also enhance the anti-corrosion and anti-bacterial performances of Zn matrix due to outstanding properties of GNPs as discussed in section [48]. In the context of corrosion resistance, the high conductivity of GNPs reinforcement may help to dissipate the charge build-up that occurs during corrosion, reducing the rate of corrosion. Additionally, the strong bonding between the graphene layers and the Zn matrix may help to protect the Zn from corrosion [57]. This combination may further enhance the future implication of Zn-based MMNCs nanocomposite, as presented in Figure 1.5. Zn/GNP nanocomposites may be used in a various of applications, including as anti-bacterial coatings, bioimplant devices, and biodegradable orthopedic implants. The combination of Zn and GNPs in these materials can provide both antibacterial and anti-corrosive properties, making them well-suited for use in medical and biomedical applications. The Zn in the nanocomposite can help to kill bacteria and prevent their growth, while the GNPs can improve the durability and corrosion resistance of the material. These properties may make Zn/GNP nanocomposites a valuable tool for preventing the spread of bacterial infections and for use in medical implants and devices. It is important to note, however, that more research is needed to fully understand the potential applications and limitations of these materials.

1.5.1   Antibacterial coating applications

Zn/GNPs nanocomposites have shown potential for use as antibacterial coatings in hospital and public infrastructure settings. Zn in the nanocomposite can help to kill bacteria and prevent their growth, while the GNP can improve the durability and corrosion resistance of the coating [58],
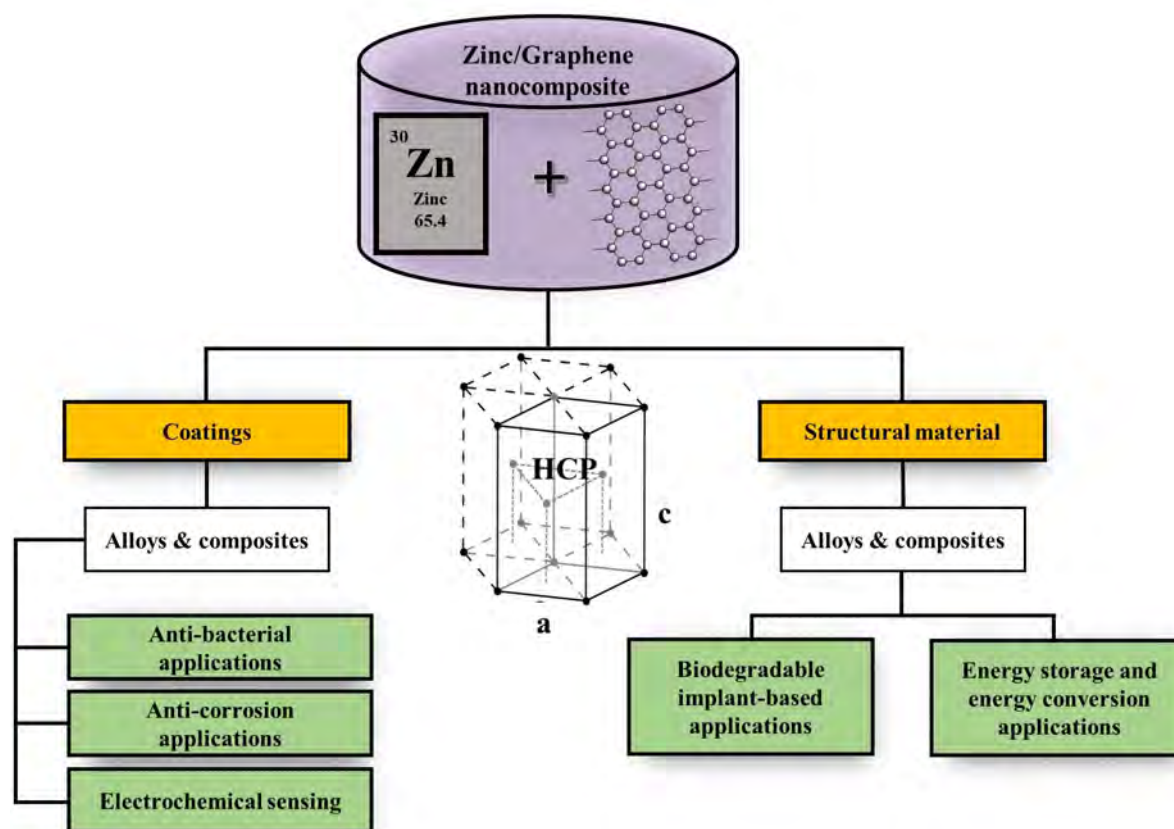
FIGURE 1.5: Future applications of Zn/GNPs nanocomposites.

[59]. GNPs have a high surface area, providing more sites for the attachment of zinc particles. This increased surface area can enhance the contact between the antibacterial agents and the bacterial cells, improving the overall antibacterial efficacy of the coating. These properties may make Zn/GNP nanocomposites a valuable tool for preventing the spread of bacterial infections in hospitals and other public spaces. It is important to note, however, that more research is needed to fully understand the potential applications and limitations of these materials.

1.5.2 Biodegradable implant applications

1.5.2.1 Biodegradable orthopedic implants

Zn is a biodegradable material that can be used in orthopedic implants. One of the potential advantages of using Zn metal in orthopedic implants is that their degradation rate can be tuned, allowing for more control over the lifespan of the implant. This can be beneficial in cases where the implant needs to be removed or replaced after a certain amount of time [60].

Additionally, Zn plays a protective role in enzyme synthesis, DNA replication, transcription, and expression, and the promotion of osseointegration and osteoinduction as an indispensable nutrient element in the human body [61]. This can help the implant to be more securely integrated into the patient's bone, reducing the risk of complications. Thus, Zn-based implants have been

shown to have a positive effect on bone strength, which can be beneficial for patients undergoing orthopedic surgery [62].

The natural degradation of Zn metal within the body over time has garnered significant interest in medical research, particularly in the context of degradable Zn matrices used in orthopedic implants. This approach is valued for its non-toxic nature, eliminating the need for post-surgery treatment or removal procedures after the completion of their intended clinical role [63]. Traditional orthopedic implants often require the patient to undergo additional surgeries or treatments after the initial implantation to ensure that the implant is properly integrated into the bone. Zn/GNPs, on the other hand, may not require this additional treatment, which can save the patient time and discomfort. The use of Zn/GNPs in orthopedic implants has been shown to result in less pain for the patient. This can be attributed to the fact that Zn/GNPs degrade slowly and gradually, reducing the amount of inflammation and discomfort that the patient experiences. This can help the patient to recover more quickly and comfortably from the surgery.

1.5.2.2 Biodegradable electronic devices

Zn/GNPs nanocomposites can also be a potential material for biodegradable electronic devices. These devices can be tuned to degrade at a specific rate, making them ideal for use as implants in the human body. Unlike traditional implants, Zn-based devices may not require post-surgery treatment and can be safely absorbed by the body over time. This can lead to less pain and discomfort for the patient.

Some possible applications for Zn-based implants include pulse rate sensors, electrocardiogram (ECG) monitors, and batteries [64]. These devices could potentially be used to monitor a patient's health and provide important information to doctors. Potential competitors for Zn/GNP and why Zn/GNP may be preferable compared to other alternatives:

Competitors for Zn/GNP in biodegradable electronics:

Magnesium (Mg) alloys: Magnesium alloys have been considered for biodegradable electronics due to their biocompatibility and relatively fast degradation rates. However, controlling the degradation rate and addressing issues such as hydrogen gas evolution during degradation are challenges associated with magnesium-based systems.

Silicon (Si) Nanomaterials: Silicon is a widely used material in electronics, and nanoscale silicon structures have been investigated for biodegradable devices. However, silicon degradation products can be less environmentally friendly, and achieving controlled degradation remains a challenge.

Polylactic acid (PLA) and polycaprolactone (PCL): Biodegradable polymers like PLA and PCL are used in some electronic components. However, achieving electrical conductivity comparable to traditional materials is a challenge, and these polymers may not be suitable for all electronic applications.

Advantages of Zn/GNP for Biodegradable Electronics:

Electrical Conductivity: GNPs provide excellent electrical conductivity, making them suitable for electronic applications. The combination of zinc and graphene in Zn/GNP nanocomposites allows for the retention of electrical properties while providing additional benefits.

Biocompatibility: Zinc is known for its biocompatibility, and the combination with graphene can enhance the overall biocompatibility of the nanocomposite. This is crucial for applications in medical devices or other scenarios where interaction with living tissues is involved.

Mechanical Strength and Flexibility: Graphene adds mechanical strength and flexibility to the nanocomposite, which is important for creating flexible and robust electronic devices. This can be particularly advantageous for applications like flexible electronics and wearable devices.

Biodegradability: Both zinc and graphene are materials that can biodegrade over time, especially in certain environmental conditions. This is a key advantage for reducing the environmental impact of electronic waste.

Synthesis Methods: The synthesis of Zn/GNP nanocomposites can be achieved using various scalable and cost-effective methods, making them more practical for large-scale manufacturing compared to some alternatives.

Versatility: Zn/GNP nanocomposites can be tailored for specific applications by adjusting the ratio of zinc to graphene and optimizing the fabrication process. This versatility allows for customization based on the requirements of different electronic devices.

However, it is important to note that the use of Zn/GNP-based implants is still in the research and development phase, and it is not yet clear if or when these devices will be available for clinical use.

1.6 Challenges in fabrication of Zn/GNP nanocomposites

In general, however, Zn-based MMNCs are comprised of a large portion of low-cost Zn matrix with a small amount of expensive nanofillers. The cost of fabricating Zn/GNP nanocomposites is a major factor that needs to be considered. The fabrication cost of these types of nanocomposites is still higher than the conventional engineering materials i.e. steel or aluminum [65]–[67]. The available nanocomposite fabrication methods like vapour deposition techniques (e.g. physical and chemical vapour deposition) and thermal spray are inappropriate for future use due to either lack of feasibility or their high cost.

Another main challenge in the fabrication of Zn/GNPs nanocomposite is agglomeration and structural damages due to Van der Waals attraction during mechanical mixing through conventional methods. This impacts the uniform dispersion and strength of GNPs nanofillers across the metal matrix, which further increases the cost of fabrication. Therefore, a novel approach to the fabrication of nanocomposites is needed, which should be more promising and economical compared to the previous.

1.7   Motivation

In recent years, biodegradable metallic implants have gained significant attention as an alternative to traditional permanent implants due to their biocompatibility and reduced risk of long-term adverse effects. These materials can be made from a variety of metals, including Mg, Zn and Fe, and they can be used in a range of applications, including packaging, medical devices, and agricultural equipment. Among them, non-cytotoxic Zn has been shown to possess a unique combination of moderate degradation properties ranging between fast degrading and low strength Mg and slow degrading and high strength Fe that make them ideal and less likely to cause any harm to the surrounding bones, tissues and cells.

Researchers are showing their interest in Zn-based biodegradable materials and shown to have non-cytotoxic properties. The non-cytotoxic properties make them safe for use in the human body. They have been shown to have excellent biocompatibility, meaning that they do not cause any adverse reactions or inflammation in the body. In addition to being non-cytotoxic, Zn-based biodegradable materials also possess antibacterial properties. This is critical for preventing infection and ensuring the success of the bioimplant procedure. The presence of antibacterial properties also helps to reduce the risk of complications and secondary infections, which is a major issue in bioimplants. Unlike traditional implant materials such as titanium, Zn can be naturally absorbed by the body over time. This reduces the risk of long-term complications and ensures that the implant does not have a lasting impact on the body. Another advantage of Zn-based biodegradable materials is that they are more easily recyclable than traditional plastics. Unlike plastic, which must be sorted and processed before it can be recycled, Zn can simply be melted down at low temperatures ($< 450°C$) and used to create new products. This not only makes them more environmentally friendly, but it also reduces the energy required to produce new products, thus reducing the carbon footprint of manufacturing.

However, there are some drawbacks to Zn-based biodegradable materials. One drawback is that they are generally more expensive to produce than traditional plastics. Additionally, such biodegradable materials are not as strong as traditional plastics, meaning that they may not be suitable for use in certain applications where high strength is required.

Reinforcing graphene in the biodegradable Zn matrix can be a promising approach to improve tribo-mechanical, anti-corrosion, and anti-bacterial properties for different applications. The high mechanical strength and flexibility of the composite will help to support the weight of the body and resist the stresses that occur during daily activities. Additionally, the high electrical conductivity of graphene has the potential to enhance the electrical stimulation of bone growth, which can be an important factor in the recovery process. The success of Zn/GNP nanocomposites with uniform biodegradation, as well as improving their tribo-mechnical properties, relies on having a uniform dispersion of graphene within the metal matrix while preserving its 2D structure. Although efforts can be made to achieve this, the challenge of achieving uniform dispersion without damaging the structure of graphene remains a crucial issue in the synthesis of composites.

Functionalizing graphene with biocompatible polymers and oxygen-containing groups can be the approach that can be used to reduce the cytotoxicity of graphene, which brings less risk environment for living cells.

Overall the Zn/GNP nanocomposite offers a range of benefits that improve outcomes and reduce the risk of complications in bioapplications and continue to push the boundaries of medical science to improve human lives.

The use of Zn/GNP nanocomposite coating can be a promising solution in the fight against bacterial infections and corrosion in a range of industries, including healthcare, food packaging, public infrastructure, and marine. In recent years, the spread of Healthcare Associated Infections (HCAI) has become a growing concern, particularly in hospitals where patients are already vulnerable to various health problems. Zn/GNP nanocomposite coating in a hospital environment can help prevent the spread of bacteria, reducing the risk of HCAI.

Food packaging is another important area where Zn/GNP nanocomposite coating can play a significant role. The coating can extend the shelf life of food products by preventing the growth of bacteria and keeping the packaging materials free from corrosion. This not only benefits consumers but also reduces food waste, saving resources and reducing the carbon footprint. Infrastructure, such as public toilets, transport services and handles in open places, play a crucial role in promoting hygiene and preventing the spread of contagious diseases. To enhance their durability and combat the transmission of germs, the use of Zn/GNP nanocomposite coatings can be a solution. These coatings may offer both antibacterial and anticorrosion properties, which means the use of Zn/GNP nanocomposite coating can prevent corrosion, reducing maintenance costs and extending the lifespan of assets.

In conclusion, the use of non-cytotoxic and antibacterial Zn/GNP nanocomposites could be a multi-functional solution that has a significant impact on various industries. Here, reinforcing a biodegradable matrix with a non-cytotoxic form of functionalized GNP holds great potential for the development of improved biodegradable implants. Zn/GNP nanocomposite coatings provide effective protection against bacterial infections and corrosion, which is essential in maintaining the health, safety, and longevity of our critical assets. The advancement in Zn/GNP nanocomposites seems a promising research work towards a more sustainable future!

Chapter 2

Literature Review

Chapter 1 showed that Zn-based nanocomposites are beneficial in low-cost coating and structural implant applications to overcome the existing challenges. This chapter summarizes the latest progress in the fabrication of Zn-based nanocomposites and provides an insight into the recent literature in the area of nanofillers for metal matrix nanocomposites that can enhance their Tribo-mechanical, corrosion resistance, anti-bacterial and non-cytotoxic properties. The gaps in research and the scope of future research are discussed in detail at the end of the chapter.

2.1 Introduction

The progress made in modern materials science and metallurgical technology has paved the way for handling challenging working conditions. The material surface is the most vulnerable site for different forms of attacks, including mechanical, tribological, electrochemical, chemical, and bacterial. As these attacks proceed, the degradation of material surfaces is initiated and leads to damage to material surfaces. The damages mainly due to the corrosion and wear attack at the material surface are not recoverable. Therefore, the protection of the material surface is very important. The degradation of material surfaces can be decreased by applying a surface coating or changing the entire material of the part that will reduce the effect of given working conditions and the surrounding environment and extend the service life of product. However, the application of a protective coating is more feasible and economical than changing the entire material of the part. Thus, surface modification technologies have found a wide range of applications in several engineering studies to protect the material surface from corrosion and wear. The selection of the suitable coating technique depends upon many factors including, application, economics, feasibility, etc. Total global coating market forecasts project the market to grow from USD 44.5 billion in 2020 to USD 83.6 billion by 2030, at a CAGR (compound annual growth rate) of $>6\%$ between 2020 and 2030 [68]–[70]. In Asia Pacific, China is the world's largest producer and consumer of coatings. Based on applications there are many categories such as anti-corrosion, thermal, electrical, anti-wetting, anti-bacterial, etc. Among all, three major areas of coatings (i) anti-corrosion, (ii) anti-bacterial, and (iii) hydrophobic coatings are important in economic

aspects. These categories of coating market forecasts project the market to grow from USD 28.5 billion in 2020 to USD 55.2 billion by 2030, at a CAGR of >10.2% between 2020 and 2030, refer Figure 2.1.
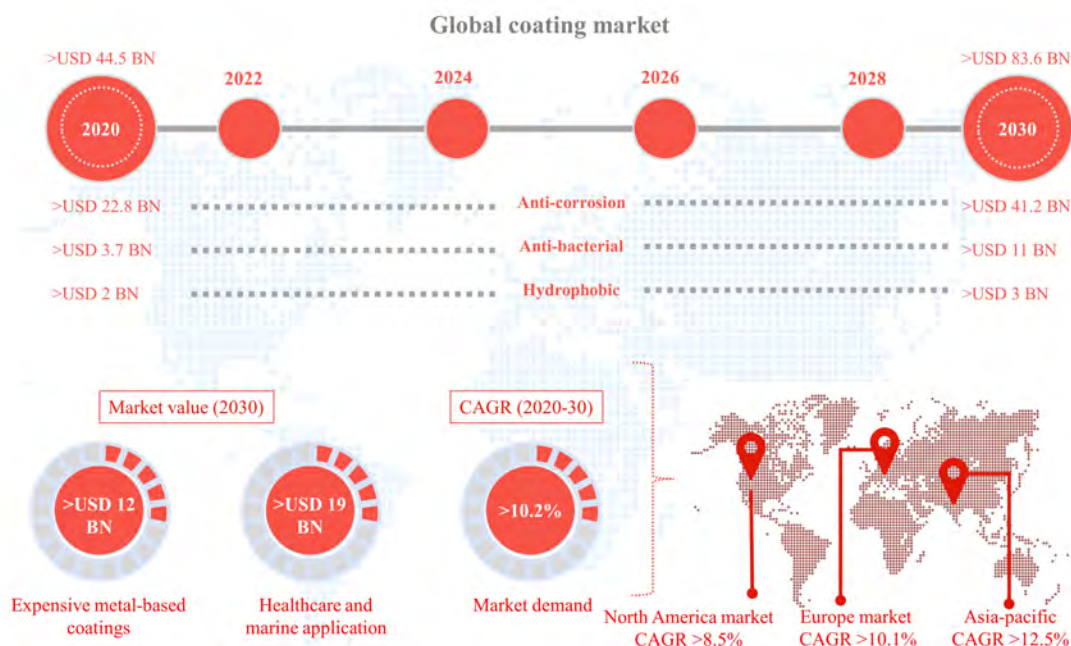
FIGURE 2.1: Global coating market for year 2020–30 and estimation of growth in demand in terms of CAGR (compound annual growth rate) (visited on 24th December 2022).

2.2   Anti-corrosion coating

Anti-corrosion coating slows down or prevents the electrochemical reactions that adversely decorate metals' structural integrity and change their corrosion-induced appearance. Figure 2.2 shows corrosion activity on the partial zinc-coated bolts using salt-spray tests, which show the effectiveness of a thin sacrificial layer of Zn to prevent corrosion [71]. This anti-corrosion coating property makes them applicable across diverse end-user industries such as marine, oil and gas, industrial, construction, energy (power plants, solar, wind turbines), automotive, and others. In addition, the report includes a detailed description of the different technologies used to produce anti-corrosion coating. Solvent-borne, waterborne, powder anti-corrosion coating, and high-energy cure coating are widely used technologies.

Figure 2.3 shows the global anti-corrosion coating market, by sector and material. By sector, marine applications are forecasted to be the most trending field of application of anti-corrosion coatings. By material, polymeric coatings are forecasted to be on top followed by zinc-based coatings. Here, zinc-based coatings are most prominent coatings among all metallic coatings due to easy availability, low-cost and high sacrificial performance to protect the substrate.
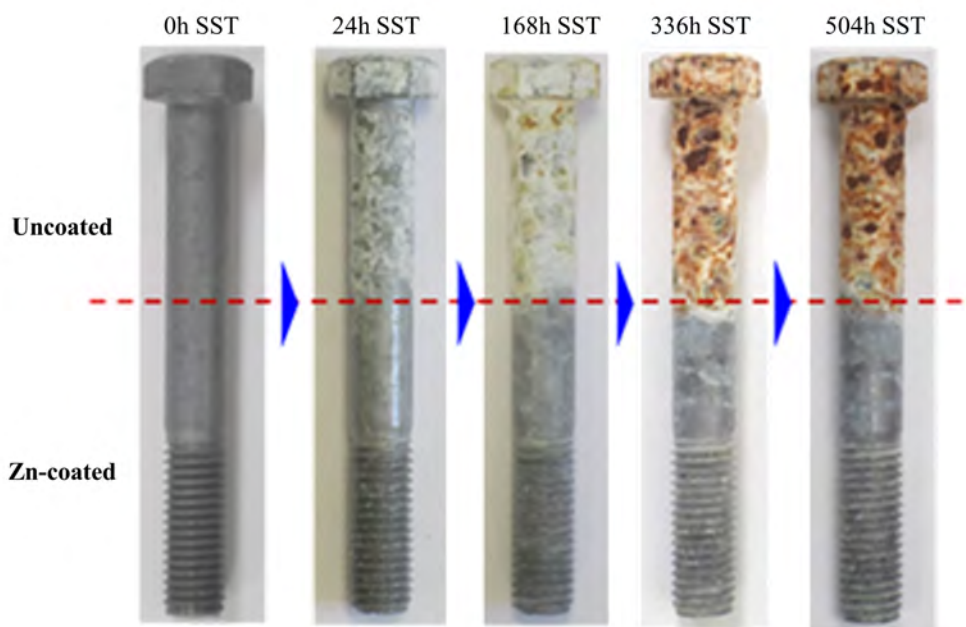
FIGURE 2.2: Corrosion activity on partial zinc coated bolts using salt-spray tests.
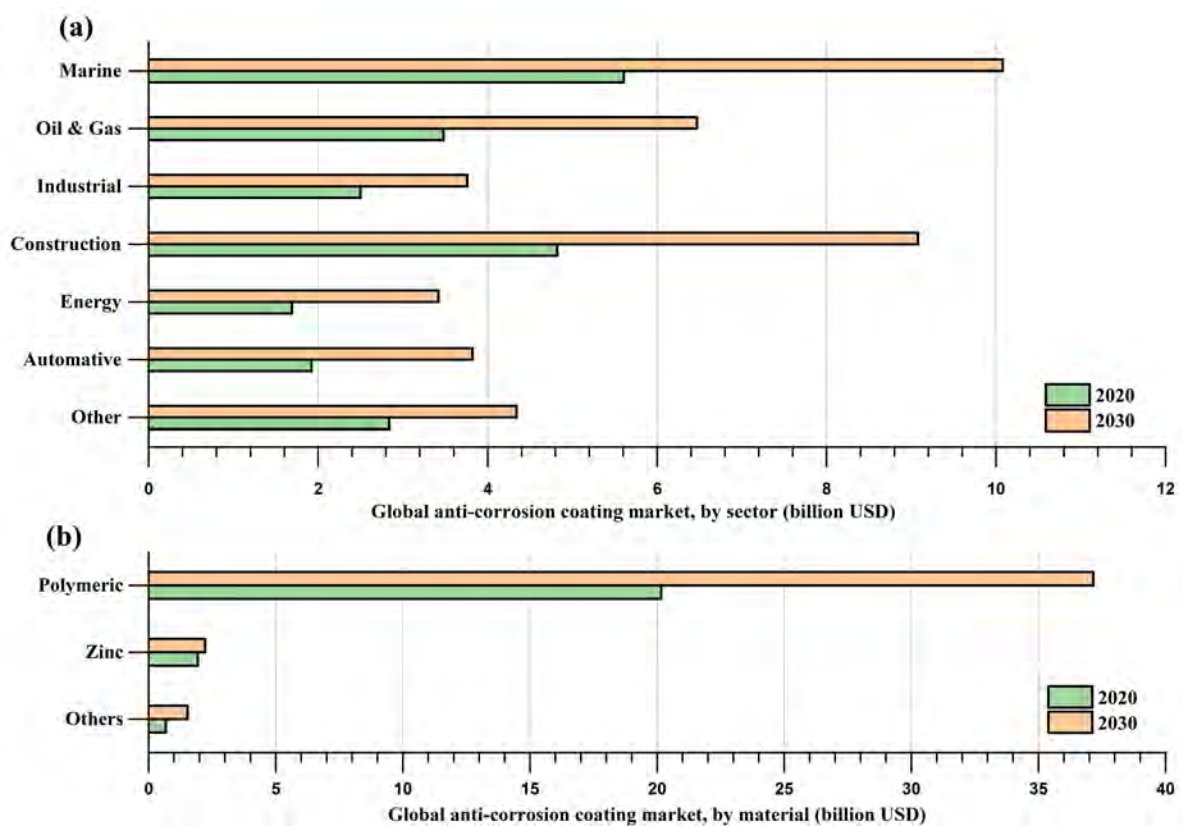
FIGURE 2.3: Global anti-corrosion coating market, by (a) sector and (b) material.

2.3   Anti-bacterial coating

The advance anti-bacterial coatings contain anti-bacterial agents inhibiting microbial contaminations. They have wide application usage in the construction, food, and healthcare industry. They are applied to doors, glass panels, walls, HVAC, tents, and counters.

2.3.1   Social significance of anti-bacterial coatings

2.3.1.1   Importance in biomedical devices and infrastructures

The bacterial spread on metallic surfaces are affecting human life either directly or indirectly. It has been reported that more than 64% of infections in hospitals are due to bacterial settlement on the surfaces (see Figure 2.4)[72]. Therefore, considerable commercial investment and academic research energies are focused on finding approaches to reduce the microbial numbers on the potential surfaces that are frequently coming in the human body's direct contact. The anti-bacterial material coating on such surfaces is widely believed approach to stop the community transmission of harming bacteria and viruses.
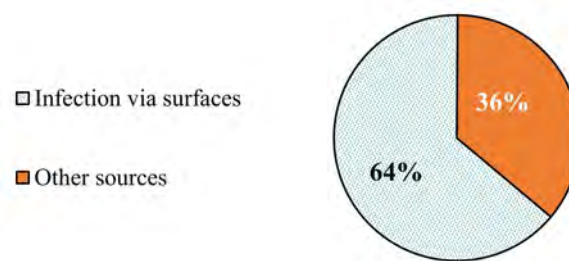
FIGURE 2.4: Main source of communicable diseases in hospital facilities [72].

In bio-engineering applications, the anti-bacterial material coatings can restrict bacteria's growth on biomedical implants inserted in the human body [73], [74]. Generally, frequent replacements of implants are required to avoid infection due to bacterial colonization on the surface of implants which would lead to excessive discomfort among patients. Therefore, to prevent bacterial infection, medical implants can be overlaid with an anti-bacterial material coating which is biocompatible and non-cytotoxic in nature [75], [76].

Healthcare-associated infections (HCAIs) are one of the major challenges in health services [77]–[79]. European Centre for Disease Prevention and Control (ECDC) reported more than 81 thousand HCAIs affected patients per day in European hospital facilities in 2011-12 [80]. Here, the main bacteria responsible for HCAIs in hospital facilities are *Staphylococcus aureus* (*S. aureus*) and *Escherichia coli* (*E. coli*). The colonization of such bacteria, fungi, and other microorganisms are responsible for forming biofilms on the surfaces by secreting strong extracellular polymeric substances (EPS) [81]. The biofilms adhere to the surfaces and help in bacteria colonization, which is often hard to sanitize with disinfectants and surfactants [82]. The mechanism of bacterial

colonization is subjected to environmental stimuli and a series of genetic changes in bacteria cells. However, five sequential stages for bacterial colonization have been identified for the growth and spread of bacteria, namely, (i) temporary/ reversible and permanent/ irreversible attachment, (ii) microcolony development, (iii) three-dimensional biofilm development, (iv) growth, and (v) spread [81], [83]. Researchers have shown that an anti-bacterial coating on the surfaces can be an effective and efficient solution to prevent HCAIs [84].

Furthermore, an increasing outbreak of diseases such as COVID-19 and SARS is likely to encourage use owing to stringent regulations for coating material selection to reduce the risk of touch contamination. Antibacterial coatings could be a safe and non-toxic solution, which is compatible with hospitals, schools, nurseries, and public settings. Thus, the market share for anti-bacterial coatings among other coatings is likely to stimulate.

2.3.1.2 Impact on marine industry

In marine applications, biofouling on marine installations and watercraft has several challenges shared with all other billion-dollar maritime industries developing technologies and working in the marine environment worldwide, leading to substantial economic losses and reduced operational lifespan of components, if poorly addressed [85]. In addition, biofouling increases hydrodynamic drag and extra weight on the surface of watercraft which reduces the speed and manoeuvrability and increases additional fuel consumption up to 40%. Thus, biofouling not only increases the shipment cost but also increases the release of harmful emissions to the environment such as the emission of SO_x, NO_x, CO_x and C_x-H_x compounds [86]. Also, biofouling causes microbiologically influenced corrosion (MIC) and distortion of marine installations and watercraft surfaces, which are typically irreparable at the point of application [87]. Here again, a low-cost bacteria-repelling coating with high tribomechanical and anti-corrosion performance can be a solution to the problem of biofouling on marine installations and watercraft surfaces [3], [4], [88], [89]. Figure 2.5 shows the global anti-bacterial coating market, by sector and coating material. Here, healthcare, public infrastructure, and food packaging applications are forecasted to be the most trending fields of anti-bacterial coatings. By material, polymeric coatings are forecasted to be on top followed by zinc-based coatings. Here, Zn-based coatings are the most prominent coatings among all metallic coatings due to easy availability, low-cost and high sacrificial performance to protect the substrate. The increasing prevalence of corrosion and bacterial growth and the rising demand for high-quality anti-corrosion and antimicrobial coatings to reduce surface transmission will boost the market demand. Anti-corrosion, anti-bacterial, and sustainable coatings combined market size exceeded USD 26 billion, globally in 2020 and is estimated to grow at over 10% CAGR between 2020 and 2030. This market is projected to reach USD 52.6 billion by 2027 [70].
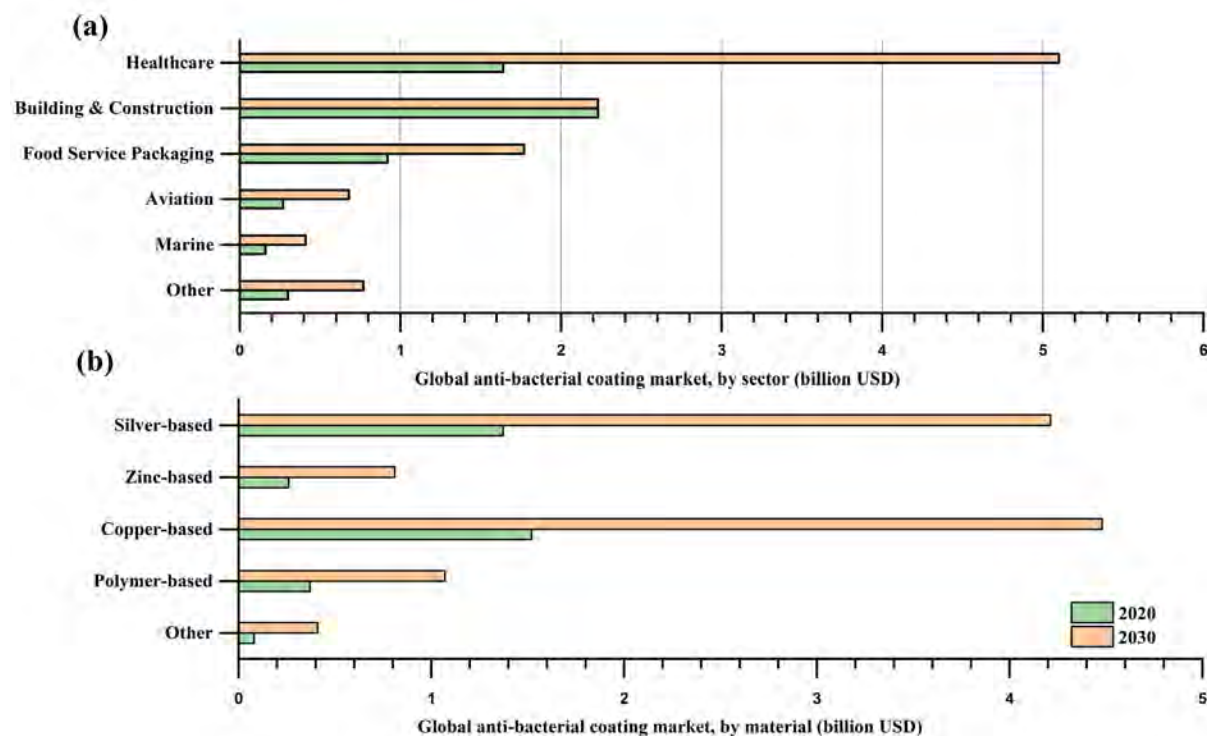
FIGURE 2.5: Global anti-bacterial coating market, by (a) sector and (b) material.

2.4 Anti-bacterial MMNC coating

In recent times, the use of anti-bacterial nanocomposite coatings is emerging rapidly for various engineering applications. Here, metal matrix nanocomposites (MMNCs) are acquiring a significant role in the upcoming field of anti-bacterial material applications owing to their high tribo-mechanical and anti-corrosion properties. The bio-responsive mechanism of MMNC coatings to perform anti-bacterial activities can protect surfaces in biological environments. The nanofillers in the metal matrix play a key role during anti-bacterial activities to kill the microbials. The composition of nanofillers can be inorganic, organic and hybrid, including advanced nano tropes (i.e., allotropes of carbon and BNNT), which can be reinforced in the metal matrix.

The anti-bacterial MMNC coating on the surface can prevent bacterial colonization by either effectively repelling or killing the microbes. This review focuses on the possible low-cost anti-bacterial MMNC coatings that can make the base substrate less vulnerable to microbial colonization.

2.4.1 Bio-responsive mechanism of anti-bacterial MMNC coatings

The anti-bacterial coating endures structural changes caused by enzymatic reactions in biological fluids or environments. Bio-responsiveness can be achieved by using biodegradable layers loaded with anti-bacterial nanofillers. The controlled degradation rate of the binding metal matrix allows the kinetics of anti-biotic release [90]. It is reported that the mechanisms of bactericidal action of

metallic nanofillers are: (1) interaction of metallic nanofillers with the bacterial cell-membranes; (2) the generation of reactive-oxygen-species (ROS), which may lead to adverse enzymatic activity, lipid-peroxidation, inhibition of growth and death of the cell; and most importantly (3) release of toxic metallic ions, Kittler et al. [91]. The bio-responsive mechanisms for anti-bacterial activity on MMNC coating surface are shown in Figure 2.6. Here, two types of mechanisms are possible based on the characteristics of the nanofiller and metal matrix. In the first type, the uniform composition of the nanofillers and metal matrix are anti-bacterial (see Figure 2.6a, and both nanofiller and metal degrade are taking a part in the anti-bacterial activity. Figure 2.6b show the anti-bacterial activity inside a microbial. The anti-bacterial releases from the MMNC coating are permeable in the microbial cell membrane and perform the process of protein denaturation which damages the DNA of microbial (see Figure 2.6b). In the second type, the metal matrix is only to perform controlled degradation to release anti-bacterial nanofillers, and then only nanofillers are responsible for killing bacteria (see Figure 2.6c).
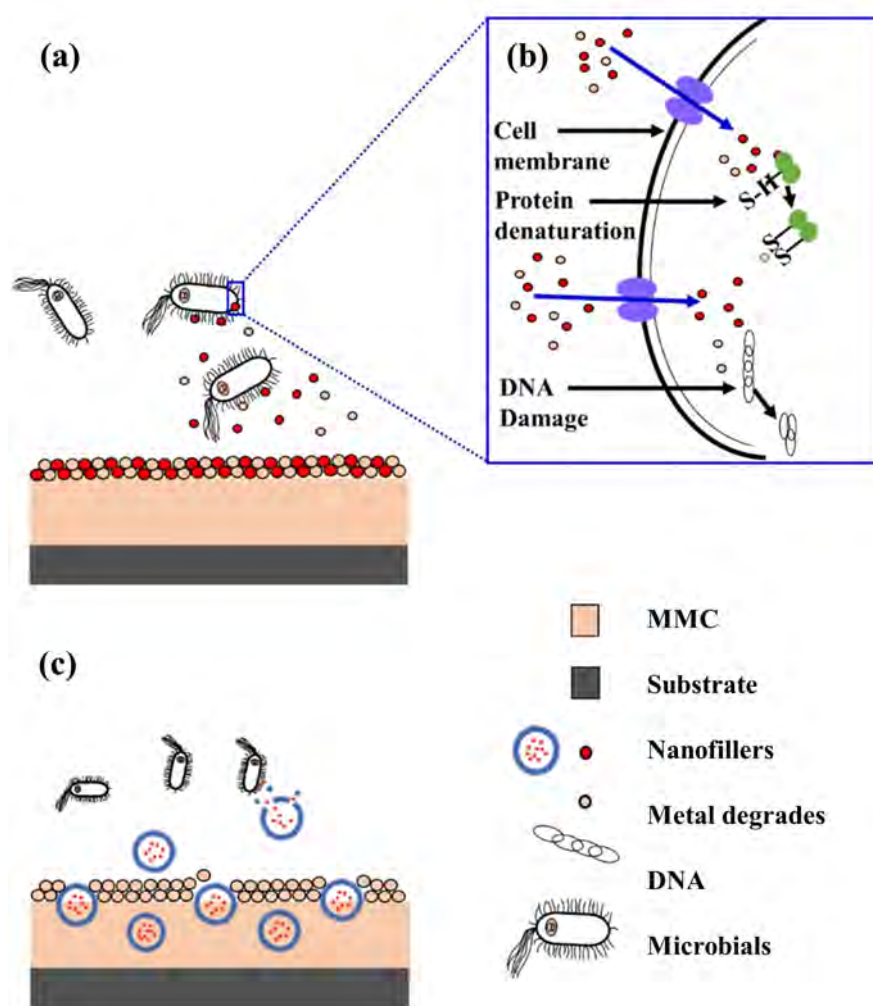
FIGURE 2.6: Schematic representation for protection mechanism of anti-bacterial MMNC [90].

2.4.2 Bio-repealing mechanism of anti-bacterial MMNC coatings

It is reported that smooth-coating surfaces are really attacked by microorganisms than rough-coating surfaces, where more surface area and more adhering force are available for microorganisms to be adhered to the surface [92]. Here hydrophilic surfaces have been reported to be less prompt for initial bacterial adhesion than hydrophobic surfaces [93]–[95]. However, the chemical properties of coatings can also repeal the initial attachment of free-swimming bacteria from the biological environment. The reports have shown that most microorganisms have an active outer surface that contains hydrophobic coverings and can be involved in bacterial attacks on the hydrophobic surface [96], [97].

2.4.3 Type of dispersion of nanofiller in MMNC coating

There are three dispersion types of nanofillers that can be possible in MMNC coatings, which are shown in Figure 2.7 [98], [99]. In the first type, the anti-bacterial MMNC coatings contain well-distributed nanofillers (see Figure 2.7a). The mechanical and electrochemical stabilities of this type of coating are expected to be the highest among all; thus their potential use is expected in many engineering applications. In the second type, the nanofillers are only attached to the anti-bacterial MMNC coating surface and thus result in poor mechanical properties of coatings (see Figure 2.7b). In the third type, the anti-bacterial MMNC coatings have agglomerated nanofillers which show inferior tribo-mechanical, anti-bacterial and anti-corrosion properties compared to the other two types (see Figure 2.7c). Among all, the first MMNC with well-incorporated nanofillers fits better for stable mechanical and electrochemical performances. However, the deposition of such coatings is a challenging and expensive task [100].

2.4.4 Various available compositions of nanofillers with their dimensional shapes and binding matrix for anti-bacterial application

A summary of various compositions of nanofillers with their dimensional shapes and binding matrix for anti-bacterial application are tabulated in Table 2.1. The nanofillers are studied for different possible binding matrices such as metallic, polymeric, and ceramic to check their applicability against bacterial colonization. Here, the nanofillers are characterized by advanced carbon-based (GNPs, CNTs, and fullerene), inorganic, organic and hybrid forms. Here, GNP (one of the advanced allotropes of carbon) is known as one of the best low-cost nanofiller owing high surface area, high anti-bacterial performance, mechanical strength and high resistance to corrosion [11].

Among the polymeric, ceramic and metallic matrices, the metallic matrix is suggested as the best and most reliable choice for bio-implant, marine, food processing and packaging, agriculture and other engineering applications owing to its durable and long-lasting tribo- mechanical strength. Metallic binding matrices are used in a variety of applications, including aerospace, automotive, and construction. Their strength and durability can make them an attractive choice for advanced
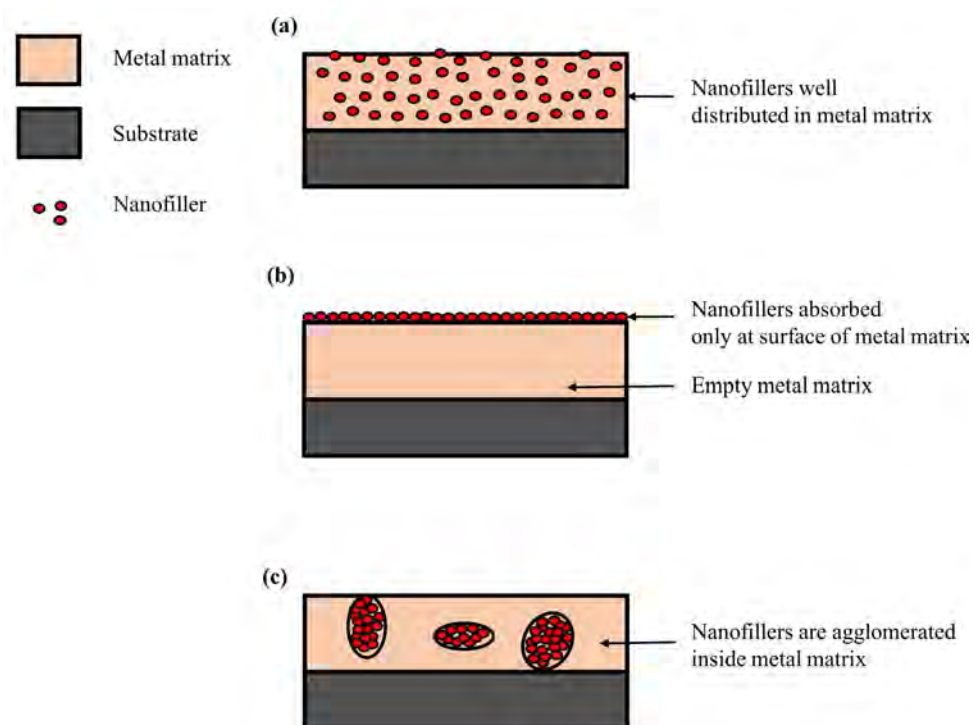
FIGURE 2.7: Type of dispersion of nanofillers in MMNC coatings [98]

bio-implant materials, marine, and sophisticated electronic device applications that require materials that can withstand harsh environments. In food processing and packaging applications, metallic binding matrices may be chosen for their corrosion resistance and ability to maintain their structural integrity under high temperatures.

However, it is important to note that the choice of a binding matrix for a particular application will depend on a variety of factors, including the specific properties required for the application, the cost of the materials, and the availability of the materials. In some cases, a polymeric or ceramic binding matrix may be a better choice due to its lower cost, ease of processing, or other specific properties. It is also worth considering that metallic binding matrices may have certain drawbacks, such as their weight or their potential to interfere with certain biological processes in bio-implants [101]. The metals such as Gold (Au), Silver (Ag), Titanium (Ti), and copper (Cu) nanoparticles are widely used for anti-bacterial applications, but they are quite expensive to use in bulk for public infrastructure. Whereas, in low-cost metal matrix, Zn and its alloys are considered one of the best owing to easy availability, lightweight and low melting point [102]. Also, Zn matrix with GNPs reinforcement and protective oxide precipitates on the surface shows high anti-bacterial properties and remarkable tribo-mechanical anti-corrosive performances [55].

TABLE 2.1: Anti-bacterial nanofillers used in various applications

Type of Nanofiller	Details of nanofillers				Reference
	Elements/ compounds	Dimensional shape	Binding matrix	Outcome	
Advance nanofillers / Carbon-based	Graphene	Nanolayer	Gold(Au)	Used for bactericidal activity and non-toxicity to mammalian cells. It has applications in anti-bacterial protection of medical devices.	[103]
	Graphene	Nanolayer	Ag-TiO$_2$	Silver-Graphene-TiO$_2$ nanocomposites used as anti-bacterial and anti- biofilm coating for controlling the spread of Campylobacter jejuni.	[104]
	Graphene	Nanolayer	Silicon oxide (SiO$_2$)	Used for bactericidal activity and non-toxicity to mammalian cells.It has applications in anti-bacterial protection of medical devices.	[105]
	Graphene	Nanolayer	ZnO	Used for bamboo coating to improve mould-resistant properties and anti-bacterial activity.	[96]
	Graphene	Nanolayer	ZnO-Ag	The anti-microbial agents selectively kill bacteria without harming surrounding cells.	[106]

TABLE 2.1: (continued)

| Type of Nanofiller | Details of nanofillers | | Binding matrix | Outcome | Reference |
	Elements/ compounds	Dimensional shape			
	CNTs	Nanorods	Ni	The oxygen-containing carbonaceous bonds on the surface of the CNTs causes anti-bacterial activity. The bacterial cell membrane rupture through the direct contact mechanism.	[107]
	CNTs	Nanorods	Cu	Gram negative Providencia bacteria is more suseptible to Cu/CNTs as compared to gram positive Bacillus Subtilis bacteria.	[108]
	BNNTs	Nanorods	Poly (propylene fumarate)	The nanocomposites exhibited anti-bacterial activity against *S. aureus* and *E. coli* bacteria, the biocide effect being more substantial with increasing nanotube loading.	[109]
	Carbides — Niobium carbide	Particles	Polyvinyl alcohol- poly-acrylic acid	Used against *E. coli* bacteria in food packaging	[110]
	Silicon carbide/ Zinc oxide	Particles	Zn	Used for photocatalytic degradation of organic pollution and bacteria in the application of liquid filtration system.	[39]
Inorganic	Nitrides — Boron nitride	Nanoflakes	polypropylene	Used for a bactericidal activity for the protection of bioimplants and medical devices.	[44]

TABLE 2.1: (continued)

| Type of Nanofiller | Details of nanofillers | | Binding matrix | Outcome | Reference |
	Elements/ compounds	Dimensional shape			
	Titanium nitride	Particles	-	Enhancement in the anti-bacterial inhibition efficiency by ∼40% of Ti64 alloy surface	[111]
Oxides	Tungsten oxide	Particles	Methyl methacrylate	Used against *E. coli*, Staphylococcus aureus and bacteriophage T4 (DNA virus)	[112]
	Copper oxide (CuO)	Particles	Polypropylene	The results show that CuO particles are more effective in anti-microbial activities, whereas for Cu particles, the prior formation of an oxide layer is required.	[35]
	TiO_2	Nanorods	Ag	The sharp-end nanorods break the bacterial cell membrane, causing the bacterial cell to dry out and die with more than 50% efficiency.	[113]
Metals	Ag	Particles	Ti-6Al-4V	Used for a bactericidal activity for biomedical implants against bacterial adhesion with anti-bacterial rates up to 91% against *S. aureus* and 97% against *E. coli*.	[9]

TABLE 2.1: (continued)

| Type of Nanofiller | Details of nanofillers | | Binding matrix | Outcome | Reference |
	Elements/ compounds	Dimensional shape			
	Ag	Particles	Zn	Zn/Ag are said to be self-hygienic composite coatings that can be employed for various potential applications, e.g., shopping carts, handrails on buses, railings, etc., to avoid contamination of metal surfaces by people's hands.	[114]
	Ag-TiO$_2$	Particles	Dental polymers	A potent bactericidal effect was achieved against S. mutans.	[115]
	Cu	Particles	Cellulose	Anti-bacterial activity has been observed for the nanocomposite samples against Gram-positive (S. aureus) and Gram-negative (K. pneumoniae) bacteria.	[116]
	Cu	Particles	Polypropylene	The results show that CuO particles are more effective in anti-microbial activities, whereas for Cu particles, the prior formation of an oxide layer is required.	[35]
	Cu	Particles	Low-density polyethylene (LDPE)	The results show that the introduction of a porous structure Cu/LDPE composite gives a remarkable improvement in the cupric ion release that can improve the lifespan.	[26]

TABLE 2.1: (continued)

| Type of Nanofiller | Details of nanofillers | | Binding matrix | Outcome | Reference |
	Elements/ compounds	Dimensional shape			
Organic	Anti-biotic	Vancomycin	Particles	SiO$_2$ sol-gel	Controlled anti-bacterial release of van-comycin form sol-gel against *S. aureus*. Used in bioimplants only.	[117]
Hybrid	Hydroxyapatite (HA)	Nanoparticles	Cobalt	The bioactivity of HA with the mechanical properties of metal matrix improves the lifespan of the implant.	[118]
	HA	Particles	Silver	Biofilm coverage rates on the coating surface after 14 days was minimum up to 6.6%.	[119]
	SiC (silicon carbide)/Ag	Nanorods and nanopar-ticles	Cellulose	Used to generate oxidative stress in the cell followed by mechanical damage to the membrane of bacteria.	[120]
	GNPs/Fe/N/TiO$_2$	Nanolayers	-	Cotton fabrics treated with graphene dec-orated with iron co-doped TiO$_2$ NPs are harmless for human skin cells and could be used to develop self-cleaning anti-microbial textiles.	[121]

TABLE 2.1: (continued)

| Type of Nanofiller | Details of nanofillers | | Binding matrix | Outcome | Reference |
	Elements/ compounds	Dimensional shape			
	Ag/CNTs	Nanorods	Ni	The Ni-removed Ag/CNTs bactericidal activity in the dark (inactivation of 93±4% in 60 min), as compared to the partial bactericidal activity of the Ni-removed CNTs and the Ag–Ni/CNTs (inactivation of 42±17% and 3 ±24% in 60 min).	[107]

2.5 Recent research and developments in metal matrix nanocomposites

The coating technologies have been developed with several metallic and non-metallic binding matrices to develop multipurpose coating materials [104], [110]. The metallic coatings are known for easy availability, low cost and high tribo-mechanical performances. The metal matrix coatings with incorporated nanofillers, known as metal matrix nanocomposite (MMNC) coatings, can have enhanced anti-bacterial, tribo- corrosion, and mechanical properties. In recent times Ag, Cu, Ti, Zn, Co, and Ni-based coatings have been extensively studied to protect surfaces from bacterial attack [122], [123]. Here, most of the metal-based coatings are very expensive, and estimates show that hat the market value for expensive metal-based antimicrobial coating can grow up to USD 1.75 billion by the year 2030 [69]. An increasing number of Scopus publications on Zn-based coatings are showing the interest of researchers, especially, for anti-corrosion and anti-bacterial coatings (see Figure 2.8). The major research fields of applications of Zn-based coatings are medicine, biomedical science, material science, engineering, and chemistry.
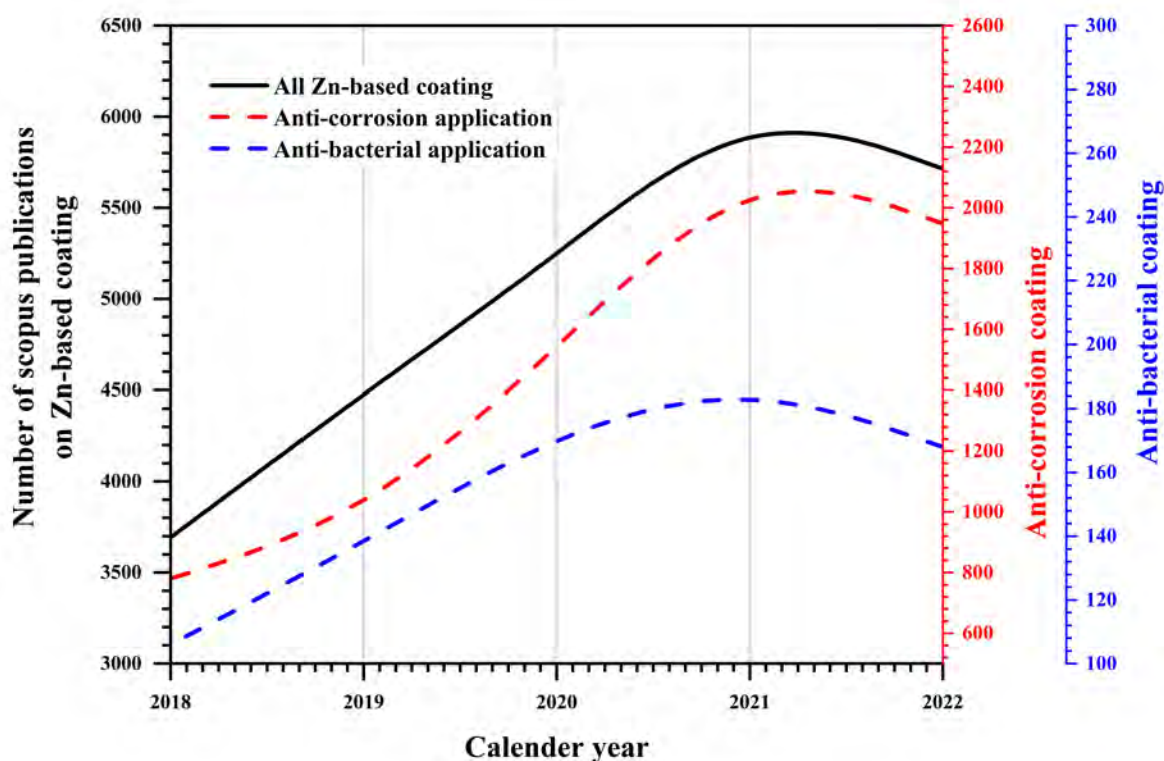
FIGURE 2.8: Publications on Zn-based coatings. Data extracted from archives of SCOPUS on date: 24th December 2022.

Figure 2.9 illustrates the application areas of Zn-based coatings and their respective research contributions: (a) overall Zn-based coatings, (b) anti-corrosion applications, and (c) anti-bacterial application. Data extracted from archives of SCOPUS on date: 24th December 2022. Zn-based

coating electrodeposited on steel is considered one of the most effective and economical methods for providing efficient and reliable protection from corrosion and bacterial growth [122], [124], [125]. However, the mechanical and tribological performance of Zn-based coating is still a major challenge.
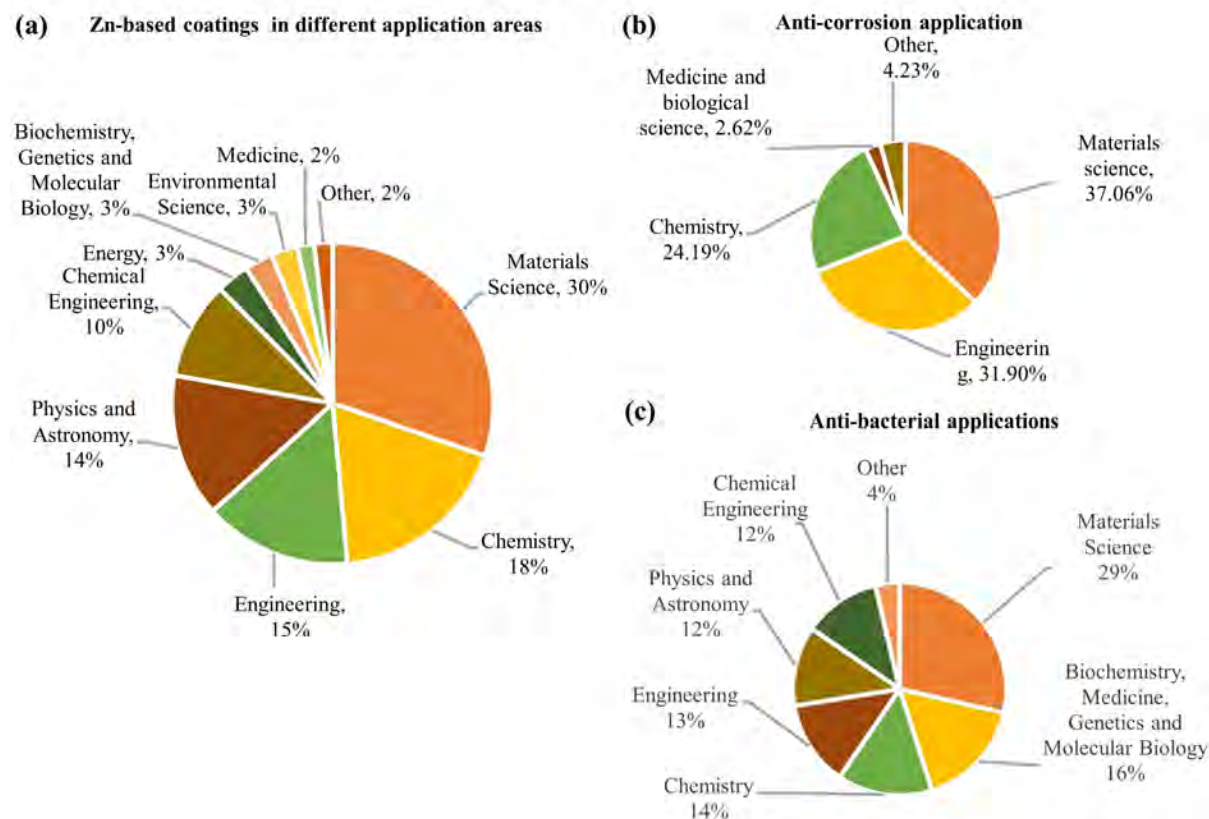
FIGURE 2.9: The application areas of Zn-based coatings and their respective research contribution. Data extracted from archives of SCOPUS on date: 24th December 2022.

2.6 Method to synthesis the MMNC coating

Coatings have been considered one of the best surface modification and enhancement techniques, where a thin preventive coating layer can significantly reduce the cost of components and maintenance. Many coating methods are available in wide varieties and ranges of applications, giving different outcomes in terms of cost-effectiveness, type of materials and their properties, and performances. The available coatings methods can enhance the different types of surface properties such as anti-bacterial, anti-corrosion, wear, microhardness, surface texture, thermal and electrical conductivity, etc. However, there are some limitations of coating methods such as distortion, cracks, delamination, the inclusion of contaminations into the substrate and sometimes variation in physical properties. The available methods that can be used to prepare MMNCs' coatings are physical vapor deposition (PVD) [111], chemical vapor deposition (CVD), thermal-spraying [126],

[127] (different available thermal spray methods are as follow: (i) cold-spraying [128], [129], (ii) plasma-spraying [130]–[132], (iii) high-velocity oxy-fuel (HVOF) spray [133]–[135], (iv) plasma transferred wire arc spray [136], (v) radio frequency inductively coupled spray [137], [138], (vi) detonation gun spray [139], [140], (vii) direct current blown arc spray [141], self-propagating high-temperature method (SHS) [142], high energy milling assisted heat treatment method [143], laser cladding [144], direct vapor deposition (DVD), chemicalposition [145], electro-less-deposition [146], and Electro-co-deposition [55], [147]–[150](see Table 2.2).

TABLE 2.2: Co-deposition methods to prepare MMNC coatings

Co-deposition Methods	Working principal	Process parameters	Coatings microstructure	Advantages	Disadvantages	Reference
Electro-co-deposition	In an electrolytic bath-cell, the Metal ions reduced on cathode (substrate).	Bath Composition, bath temperature and current density	3D- crystalline structures	• Cost-effective. • Extremely fine coatings can be obtained. • Industrially scalable. • Near all types of nanofillers can easily be incorporated into the coating.	• The base matrix should be metallic. • Nanofiller could be added up to certain extent.	[151]–[153]

TABLE 2.2: (continued)

Co-deposition Methods	Working principal	Process parameters	Coatings microstructure	Advantages	Disadvantages	Reference
Sol-gel	Precursors or reagents are dilute with a polar-solvents to form a suspension (sol) that gelates (gel) on the substrate to form coating.	Concentration and type of nanofillers, precursors, and solvents, gel annealing temperature and aging time, dipping and spinning rates	Geometrically ordered porous or dense structures can be obtained	• High surface areas of the coating can be obtained • Process runs close to room temperature. • Precise composition of coating can be obtained. • Applicable to both organic and non-inorganic coatings.	• Precursors are limited to certain types of metal oxides. • Lengthy process. • Precursors may be hazardous.	[154]–[156]

TABLE 2.2: (continued)

Co-deposition Methods	Working principal	Process parameters	Coatings microstructure	Advantages	Disadvantages	Reference
Vapor deposition: physical, chemical, and atomic-layer	The constituents of coating are evaporated or vaporized under high vacuum and then condensed on the surfaces.	Nucleation of compounds, shape and structure of the surface, and rate of evaporation.	Anisotropic perpendicular arrangement of close-packed structures	• Well-distributed-dense coatings can be obtained. • Applicable to both organic and non-inorganic coatings.	• Highly clean surfaces are required prior to the deposition. • Vaporized constituents are flammable and hazardous. • Close chamber process with high vacuum pressure.	[113], [157], [158]

TABLE 2.2: (continued)

Co-deposition Methods	Working principal	Process para-ments	Coatings mi-crostructure	Advantages	Disadvantages	Reference
Thermal spray-ing: flame, HVOF, and plasma	The pre heated (upto melting) fine-powdered particles of coating mate-rial are sprayed on the surfaces.	Degree of melting of fine-powder particles, fluid viscosity, and wettability of the surface.	Anisotropic lamellar ar-rangement of flat and lenticular particles.	• Very fine microstruc-tures. • The process can con-trol phase structure to a certain extent. • Precisely controlled coating thickness.	• Presence of oxides and voids. • Not for flammable coatings.	[25], [159]–[161]

TABLE 2.2: (continued)

Co-deposition Methods	Working principal	Process parameters	Coatings microstructure	Advantages	Disadvantages	Reference
Dip-coating, brush-coating, normal spray-coating and hand rolling	Liquid blend of some solute-solvents (resins, volatile-carrier, and additives) are simply painted on the surfaces.	Composition of the liquid mixture, viscosity, and molar-weight of the constituents.	Amorphous/crystalline/crosslinked/branched structures.	• Various organic and inorganic surfaces can be coated. • Comparatively facile method. • The fast coating is possible. • Several organic and organic nanofiller can be reinforced in the matrix of the coating.	• It is limited to organic matrix coatings. • Generally, solvents are flammable. • Poor tribo-mechanical properties. • Not long-lasting.	[162], [163]
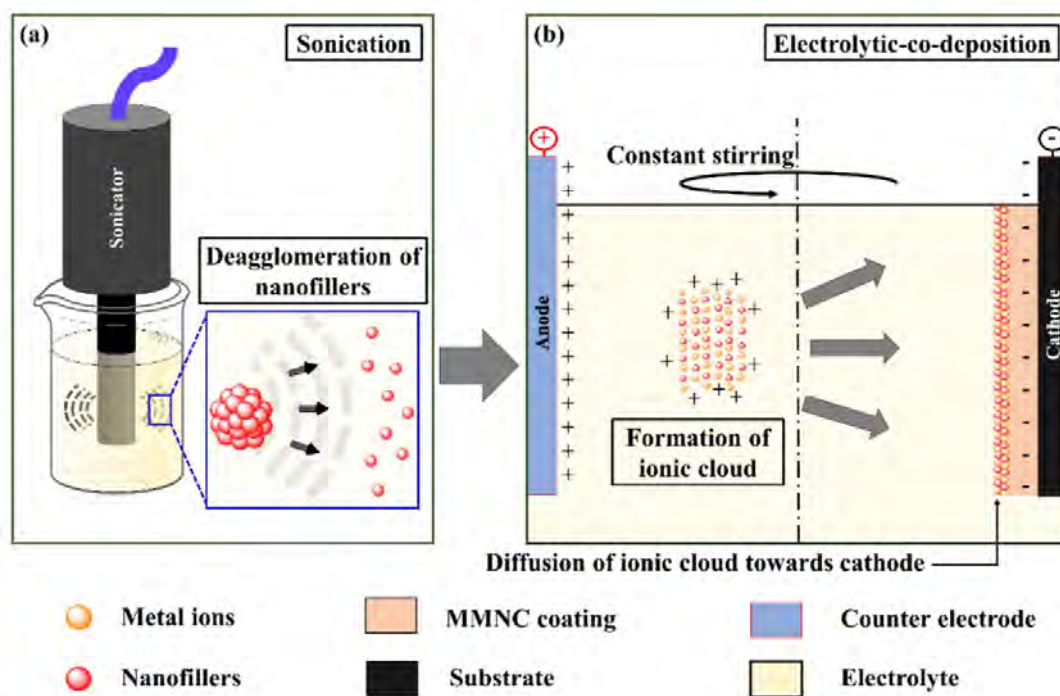
FIGURE 2.10: Electro-co-deposition method [151].

Schematics from Figure 2.10 and Figure 2.11 illustrate the available coating methods such as Electro-co-deposition, sol-gel, thermal spray, and spraying, brushing and hand rolling. In Electro-co-deposition method, the nanofiller in the electrolyte can be deagglomerated by sonication (as shown in Figure 2.10a). Subsequently, the substrates are placed at cathode in well-sonicated electrolyte with a consumable/ non-consumable anode to perform Electro-co-deposition, as illustrated in Figure 2.10 [164]–[167].

In sol–gel dipping method (see Figure 2.11a) the substrate is dipped into the solution for a time to form the coating which settles under gravity, and the process ends with polymeric reactions. In sol-gel spin-coating method (see Figure 2.11a), the acting force is a centrifugal force for the coating, which spreads the solution from the centre to the corners. In the thermal spraying method (see Figure 2.11b), the spray gun is used to spray the coating material through an energized flowing medium and raises the material mixture's temperature to the melting point, which spreads on the surfaces to solidify. In simple spray, brush, and roller deposition methods (see Figure 2.11c), the solution blend or mixture is spread over the substrate, simply by mechanical means. Among all, the Electro-co-deposition is a low-cost and prominent synthesis method to prepare MMNC coating using simple chemical salts and reagents in an electrolyte bath [168]. The salts of Zn, Cu, Mg, Ni, Ag, Au, etc. metals are easily available and can be used in electrolyte preparation to synthesis MMNCs with even distribution of nanofillers (as illustrated in Figure 2.10). The deposition rate of an ionic cloud of nanofiller and metal ions, composition, microstructure, surface morphology, tribo-mechanical and electrochemical
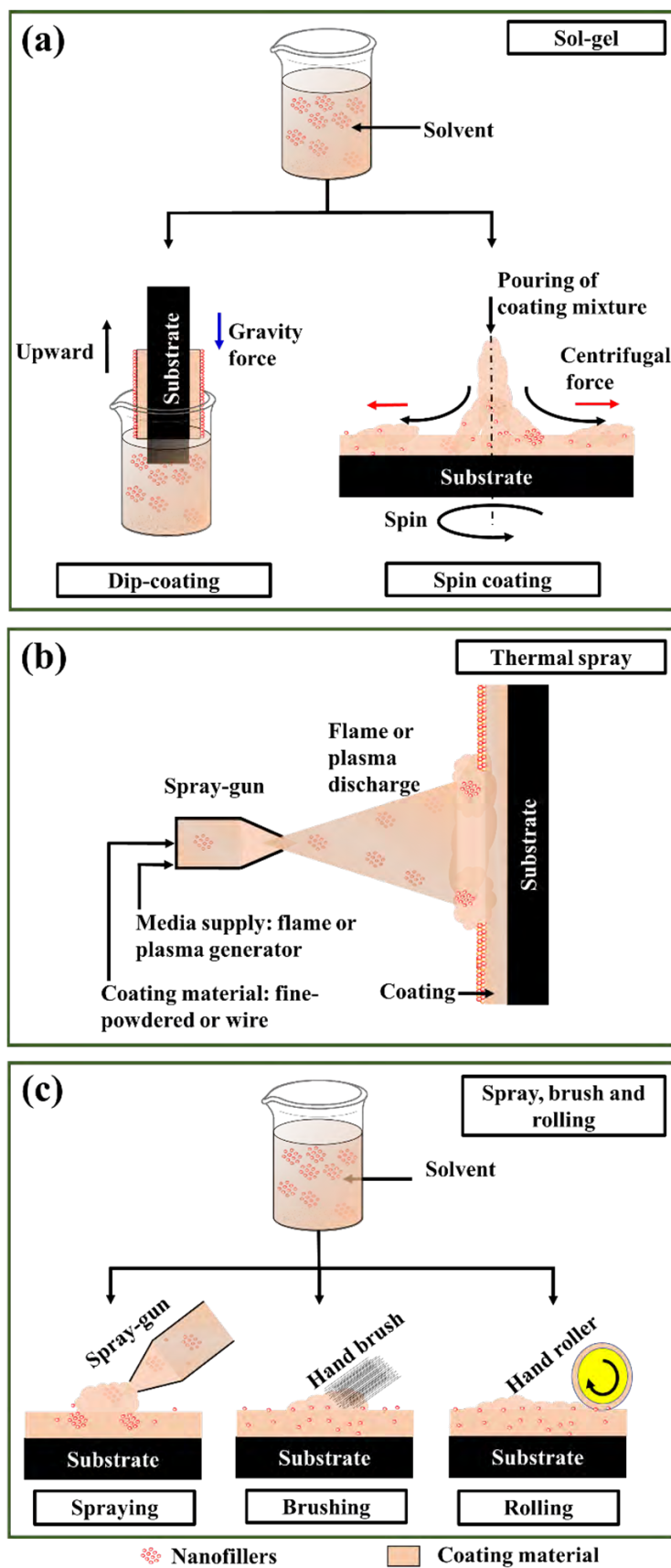
FIGURE 2.11: (a) sol-gel [154] (b) thermal spray [162] (d) spray, brush and hand-roll [168].

properties of MMNC coating directly depends on the parameters of Electro-co-deposition like current density on the substrate, pH and composition of electrolyte bath, etc. [169]–[172]. Based on the above discussions about the problem of bacterial colonization, bactericidal mechanisms, various nanofillers with binding metal matrix and available methods of synthesis. Whereas, the low-cost Zn and its alloys can be considered for a binding matrix of anti-bacterial MMNC coatings [17], [102], [173]. Zn and its alloys can be easily and uniformly decorated by graphene nanofillers using the Electro-co-deposition method [55], [147]–[149]. This coating can be characterised by several advanced destructive and non-destructive techniques including X-ray diffractometry (XRD), X-ray photoelectron spectroscopy (XPS), infrared spectroscopy, optical profilometry, scanning electron microscopy (SEM), atomic force microscopy (AFM), etc. [174], [175].

2.7 Biomaterials

Biomaterials are natural or synthetic materials that are employed in biotechnology to artificially improve the working of tissues, bones, and organs under injuries. Implantable materials can reduce adverse immune responses while preserving their clinical role because the body restricts any foreign material from augmenting its natural bioactivities. The property of a material that makes it compatible with the human body is called biocompatibility. Biomaterials can be classified based on their degree of biocompatibility as being bioactive, tolerant, bioinert, and biodegradable performances.

A bioactive material in the bone tissue environment can create an environment compatible with osteogenesis by making chemical bonds with the bone tissue [10]. Bioactive materials can be divided into two classes: osteoconductive and osteoinductive materials [1]. Osteoconductive materials allow bone growth along the surface of the bioactive material. The ceramics hydroxyapatite and tricalcium phosphate are examples of such osteoconductive materials [176]. Osteoinductive materials can stimulate the growth of new bone. Some osteoinductive materials are also referred to as osteoproductive materials in that bone growth can be stimulated away from the implant site [177]. Bioactive glasses are examples of such osteoproductive materials [178]. When a bioactive material is implanted into the human body, it stimulates a biological response from the body, which leads to a series of biophysical and biochemical reactions between the implant and tissue that eventually lead to mechanically strong chemical bonding [10].

Biotolerant materials are accepted by the host but separated from the host tissue by the formation of fibrous tissue (scar tissue). This fibrous tissue layer is induced by the release of ions, corrosion products, and chemical compounds from the implant [179]. Almost all synthetic polymers and most metals fall into this category.

Bioinert materials are stable in the human body and do not react with body fluids or tissues. Generally, bioinert materials are encapsulated by fibrous tissues to isolate them from the surrounding bone, similar to biotolerant materials. However, under certain conditions, bioinert materials can have a direct structural, and functional connection with the adjacent bone tissue

without being separated from the host tissue [180]. Titanium and its alloys are non-biodegradable examples of such bioinert materials.

Biodegradable materials are materials that dissolve in contact with body fluids. The dissolution products are usually secreted via the kidneys, without causing serious effects on the environment. Biodegradable materials are used for medical goods such as surgical sutures, tissues in growth materials, and controlled drug release [181], [182]. The most common biodegradable materials are polymers such as polyglycolic and polylactic acids, and their co-polymers [183]. Examples of biodegradable ceramics are calcium phosphates [184], and magnesium is an example of biodegradable metal [185]. In 2005, researchers Zartner et al. implanted a biodegradable 3 mm magnesium stent in a 6-week-old preterm baby, born at week 26 of gestation [186]. Figure 2.12 illustrates the different biomaterial classifications [187]. An example of a biotolerant material is illustrated in Figure 2.12a, where a fibrous layer surrounds the screw. Figure 2.12b shows a bioinert material, where there is direct contact between the bone tissue and the implant screw. A bioactive material is shown in Figure 2.12c, where the material has caused a chemical reaction between the implant screw and the bone tissue. Figure 2.12d illustrates a biodegradable material, where the material has degraded, and the degradation products were released into the bone tissue.

(a) Biotolerant   **(b)** Bioinert   **(c)** Bioactive   **(d)** Biodegradable
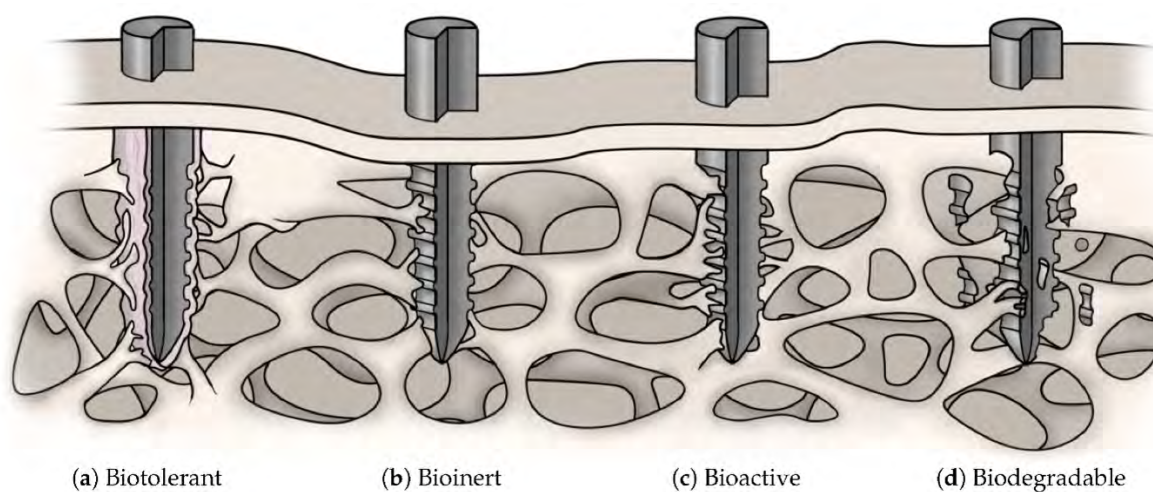
FIGURE 2.12: Schematic representation of biomaterial classifications explained using the case of bone implants [187].

These biomaterials interact with biological systems for medical objectives, including the treatment of cardiovascular, dental, orthopedic, and neurological diseases. The global biomaterials market size was valued at USD 64.8 billion in 2020 and is projected to reach USD 212.4 billion by 2030, registering a CAGR of 12.7% from 2021 to 2030.

The global biomaterials market size was valued at USD 39 million in 2020 and is projected to reach USD 144 billion by 2030, registering a CAGR of 12.7% from 2021 to 2030. Biomaterials are synthetic or natural materials that are artificially generated and employed in medical technology

to improve the function of damaged tissues, bones, and organs. These biomaterials interact with biological systems for medical objectives, including the treatment of cardiovascular, dental, orthopedic, and neurological diseases. Growth in the geriatric population, rise in prevalence rates of cardiovascular and orthopedic disorders, advancement in medical technology, and increase in awareness regarding implantable devices drive the growth of the biomaterials market. In addition, the rise in funding by the government to increase research and development activities in the field of biomaterials and increase awareness about the advantages of biomaterials products further drive the growth of market. However, the high cost of biomaterial implants and compatibility issues are expected to restrain the growth of the market.
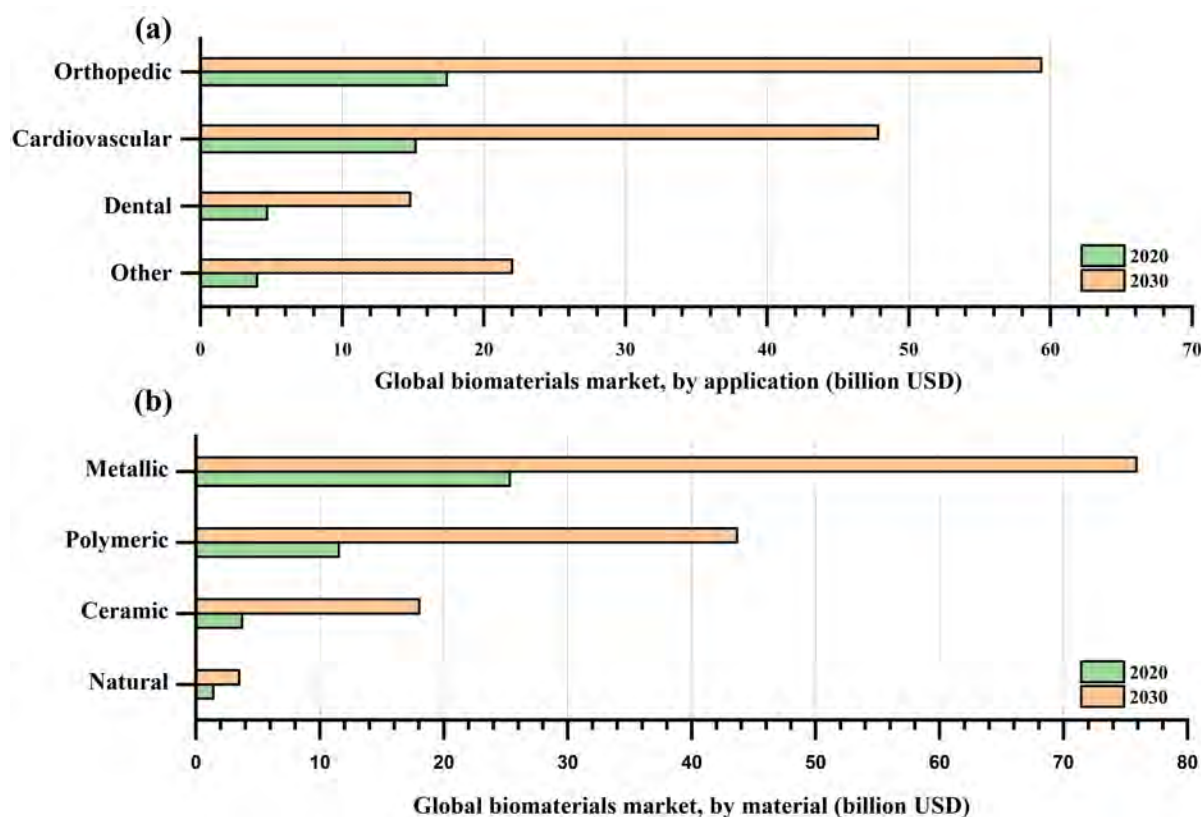
FIGURE 2.13: Global biomaterials market, by application and material [188].

Figure 2.13 shows the global biomaterials market, by application and material. Orthopedic, cardiovascular, and dental applications are forecasted to be most trending field of biomaterials. By material, metallic biodegradable and non-degradable biomaterials are forecasted to be on top due to superior mechanical performance compare to polymeric and ceramic biomaterials.

2.8 Metal-based biomaterials

Metal-based implants provide excellent internal support and fixation for orthopedic injuries compared to polymer- or ceramic-based implants owing to their superior mechanical performance

[189], [190]. Ti alloys, Co-Cr alloys, and stainless steel have been extensively employed as implant material [191]. However, these are non-biodegradable and high-strength implant materials ($\sim$110 GPa for Ti alloys, $\sim$200 GPa for stainless steel, $\sim$240 GPa for Co–Cr alloys), thus mismatch with the elastic moduli of natural bone ($\sim$30 GPa) resulting stress-shielding of the bones at implant location that causing bone resorption, and subsequent implant loosening [192]. Therefore, such implant materials need to remove after the orthopedic injury has healed. The metal matrix nanocomposite coatings, can have enhanced anti-bacterial, tribo-mechanical, and anti-corrosion properties without much compromising the non-cytotoxic behavior of material.

2.8.1 Fabrication methods for MMNC-based material

Over the years, the application of structural MMNCs in different industries has gained researchers' interest. The optimization challenge of mechanical, thermal, electrical and corrosion properties has developed many fabrication methods for the MMNCs [193], [194]. The selection of a suitable method depends on the desired type of nanofillers (particles, fibres, nanorods and nanosheets), distribution type (uniform and non-uniform), quantity and ratio of reinforcement in the metal matrix. MMNC fabrication methods can be classified based on the processing temperature of the metal matrix during the reinforcement of nanofillers, as shown in Figure 2.14 . The three-processing temperature-based methods are (i) liquid-state, (ii) two-phase (solid-liquid) processes, and (iii) solid-state [195].

2.8.1.1 Liquid-state fabrication of MMNCs

Liquid-state methods include the dispersion nanofillers into a molten metal matrix, then solidification to form MMNCs. In this process, the nanofillers must be selected according to the metal matrix. To select the right nanofiller, various factors, including the melting point, strength, density, thermal expansion coefficient, the shape and size of nanofillers, thermal stability, and preparation or procuring cost, must be carefully considered in addition to the compatibility of the nanofillers with the matrix. The nanofillers and molten metal matrix is needed to be adequately bonded to achieve the required mechanical properties. Therefore, the nanofillers should get properly wet with the molten metal matrix. However, ceramics are the best nanofillers for liquid-state fabrication processes of MMNCs. The liquid-state fabrication can be achieved through modifications in available methods, such as stir, infiltration, and squeeze casting.

(a) *Stir casting method*

Stir casting is established as one of the simplest and low-cost commercial MMNC fabrication methods. The experimental setup for stir casting is shown in Figure 2.15a. This method was first identified in 1968 by mechanical mixing aluminum oxide particles with molten aluminum matrix [196]. However, it can be used to fabricate different MMNCs as well. A mechanical stirrer is required in stir casting for the dispersion of nanofillers within the molten matrix.
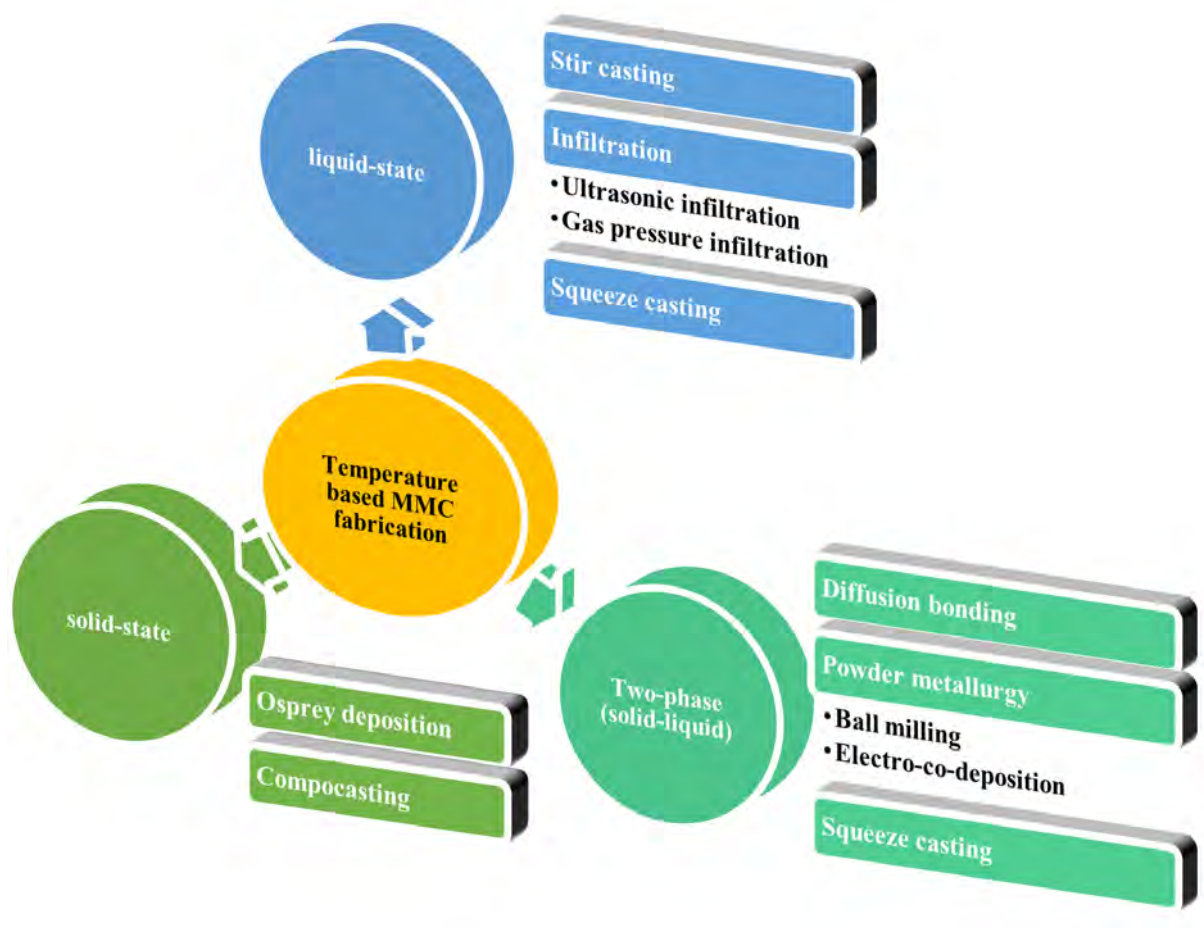
FIGURE 2.14: Procession temperature-based MMNC fabrication methods for structural material.

Achieving a uniform dispersion of nanofillers depends on the material properties and process parameters, such as the wettability between nanofillers and molten metal matrix, relative density, mixing strength, and solidification rate. Furthermore, the desired dispersion of the nanofillers in the molten metal matrix also depends on the type of mechanical stirrer (ultrasonic, electromagnetic or centrifugal stirrer) and geometry, the stirrer placement during mixing, process temperature, and the features and specifications of the reinforced nanofillers.

(b) *Infiltration method*

Infiltration is another liquid-state process for the fabrication of MMNCs. Here, the nanofillers are uniformly dispersed to soak the metal matrix and fill the empty spaces between the nanofillers. Different methods can be used for infiltration. Forced infiltration and spontaneous infiltration are two categories of infiltration methods with and without external pressure, respectively. The forced infiltration can be achieved by external pressure through ultrasonic, centrifugal, electromagnetic, mechanical, or gaseous. The common forced infiltration methods are ultrasonic and gas pressure-based infiltration.
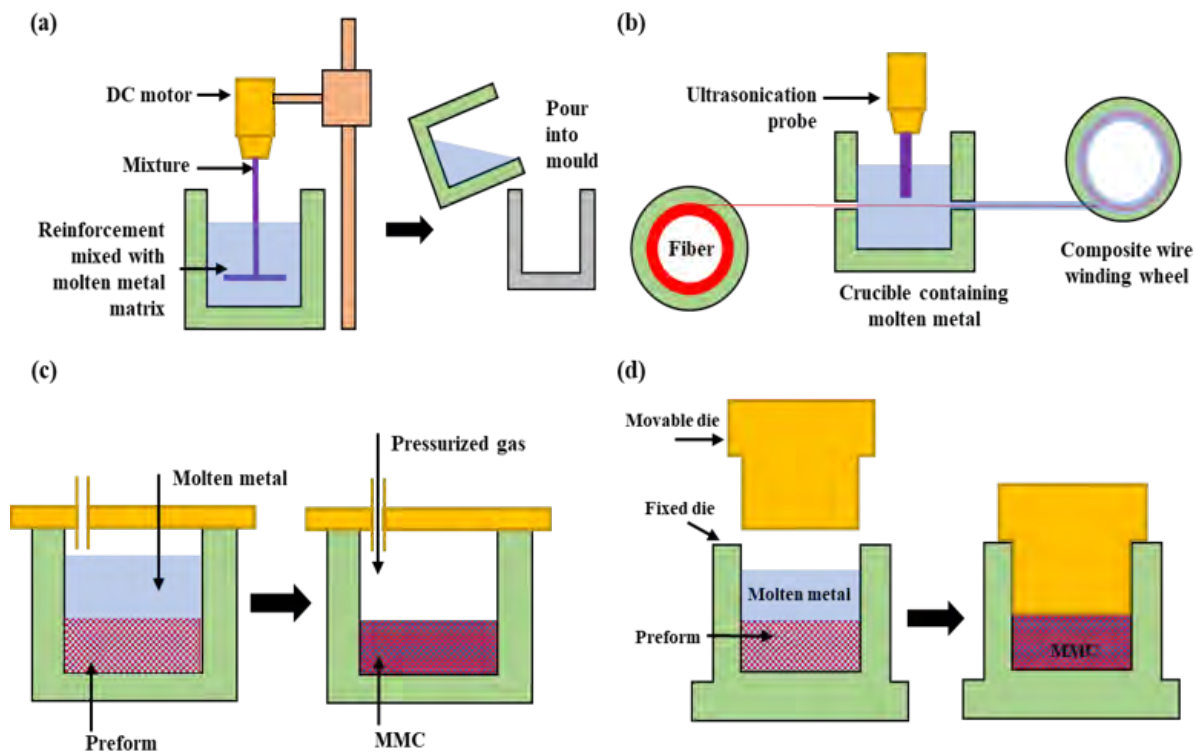
FIGURE 2.15: (a) Stir casting method, (b) Ultrasonic infiltration method, (c) Gas pressure infiltration method, and (d) Squeeze casting method.

(i) Ultrasonic infiltration method

Ultrasonic infiltration is the simplest method to fabricate MMNCs with continuous carbon fiber reinforcement in a metal matrix [197]. Figure 2.15b schematically illustrates the ultrasonic infiltration process for the fabrication of MMNCs. This process includes the immersion of nanofillers in the molten metal matrix followed by an ultrasonication process to the crucible, which transfers ultrasonic vibrations to the melt.

(ii) Gas pressure infiltration method

Gas pressure infiltration method is shown in Figure 2.15c. In this process, molten metal matrix infiltrated into the nanofillers the pressure applied by an inert gas with excellent geometrical accuracy. But the damage of nanofiller structures, matrix contraction, coarse grain, a requirement of preforms, and undesirable interaction reactions are some limitations.

(c) *Squeeze casting method*

The concept of squeeze casting dates was suggested by Chernov in 1878 [198]. In this process, the infiltration process is carried out by applying force on molten metal using a movable die, as shown in Figure 2.15d. This is to allow the melt to infiltrate into the dispersed

nanofillers. These infiltration methods also allow the reinforcement of ceramic nanofillers such as aluminium oxide, silicon carbide, and silicon oxide. A high-quality composite using this process is associated with several parameters including type of nanofillers, preheating temperature of the melt, tools, melting quality, external cooling, pressure, and time duration. The parts fabricated by this process have properties such as high thermal conductivity, weldability, and dimensional accuracy with smooth surface texture. The composite prepared by this technique can be applied to advance automotive parts applications.

2.8.1.2 Two-phase (solid-liquid) processes

Two-phase methods include both solid and liquid phases of the metal matrix during fabrication of MMNCs [199]. This mean, the nanofillers are reinforced in the metal matrix in a transition region of the phase diagram where both solid and liquid phases of metal can coexist, simultaneously. Osprey deposition and compocasting are available processes that fall in the same category.

(a) *Sprey Deposition method*

Osprey deposition process is an economical method for the fabrication of high-quality MMNCs. This process reinforces nanofillers in flowing molten matrix followed atomization by inert gas jet to obtain the final mix accumulated on a bed of reinforced matrix[200]. This process is a combination of consolidation and mixture processes in powder metallurgy.

(b) *Compocasting method*

Compocasting method is considered as an improved version of the stir-casting method [19]. In this method, the nanofillers are reinforced in the matrix at a semi-solid processing temperature. The steps of compocasting method are given as follows:

- The semi-solid phase of the matrix stirred to crush the dendrites.
- The nanofillers are added to the matrix.
- The squeeze casting transforms the material into a thixotropic phase to form MMNC.

2.8.1.3 Solid-State fabrication of MMNCs

The solid-state fabrication of MMNCs involves developing solid-state bonding between the metal matrix and the nanofillers at elevated temperatures and low pressure. These processes include diffusion bonding and powder metallurgy.

(a) *Diffusion bonding method*

Diffusion bonding is a simple solid-state process for the fabrication of MMNCs. This process includes reinforcement of nanofillers in foils and sheets of a metal matrix to fabricate MMNCs. The elevated temperature at the interface of the metal matrix and nanofillers allows the diffusion bond between them. The advantage of this process is its

compatibility with a wide range of MMNCs with precise orientation and volume fraction of nanofillers in the metal matrix.

(b) *Powder metallurgy*

Powder metallurgy is one of the robust and low-cost approaches for the fabrication of MMNCs. This process includes three basic steps. (i) preparation of a homogeneous mixture of metal matrix and reinforcement; (ii) Compaction of the mixture until achieving a density of approximately 75%; (iii). Sintering or heat treatment. This process allows almost all types of nanofillers such as ceramic nanoparticles (aluminum oxide, silicon oxide, silicon oxide, titanium oxide, etc.) and carbon allotropes (GNPs, CNTs and carbon dots). There are two different approaches are available for preparing the powder mixture of MMNC are as following:

(A) Ball milling

In the ball milling process, the fine metal powder is procured from the manufacturer and mixed with nanofillers using ball mill for several hours to obtain a homogeneous mixture of MMNC [201], as shown in Figure 2.16a.

(B) Modified electro co-deposition

Modified electro co-deposition is a facile approach to fabricating MMNCs [202]. The experimental setup for MMNC composite fabrication is illustrated in Figure 2.16a. In this process, an electrolyte bath is prepared with diluted metal salt and uniformly dispersed nanofillers. Five electrodes setup including one cathode and four anodes can be used for co-deposition of the ionic cloud of metal ions and nanofillers to form MMNC deposits on cathode tip, which collects on the bottom of the bath. The process completes after washing and drying the nanocomposite powder. The electro co-deposition method is superior to the ball milling method due to the preparation of powder mixture of metal matrix and nanofillers without harsh mixing. It avoids matrix micro welds and structural damage to nanofillers like graphene, CNTs and boron nitride nanotube and sheets. An option of in-situ synthesis of nanofiller is also available with electro co-deposition, which makes it a more facile and fast method for the fabrication of MMNCs.

2.9 Biodegradable metal matrix

Recently, Mg- [203], Zn- [2], and Fe-based [204] alloys have attracted much attention owing to their biodegradability, nontoxicity, low density, and mechanical strength in which elastic moduli of ∼45 GPa for Mg and ∼90 GPa for Zn, which match those of bones better than other metals do. Mg, Zn, and Fe. However, Mg-based alloys and nanocomposite materials are still susceptible to fast biodegradation (within 1–4 months), and are accompanied by hydrogen gas
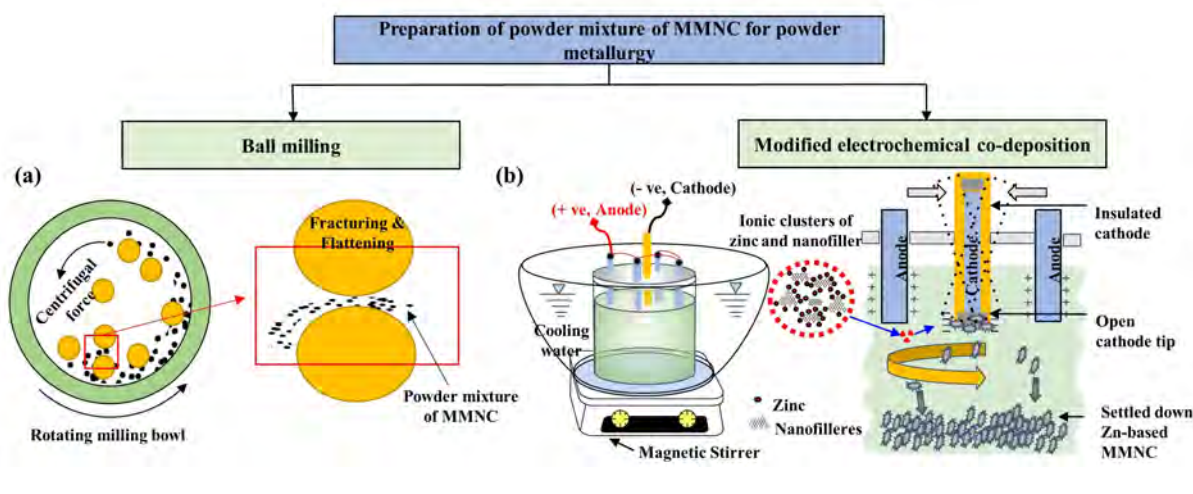
FIGURE 2.16: Preparation of powder mixture of MMNC for powder metallurgy: (a) ball milling and (b) modified electro co-deposition metallurgy.

evolution, which could lead to abrupt failure of the loadbearing implants before the completion of their clinical role [205]. Fe materials typically degrade too slowly (over 2–3 years), and the degradation products are retained in tissues for a long time. Meanwhile, researchers have been tested Zn-based alloys and nanocomposites for biodegradable implant applications [2], [192], [206]. Zn materials have degradation rates between those of Mg and Fe, and their degradation products are fully bioresorbable without harmful hydrogen gas evolution [192], [206]. Zn-based compounds are essential in the human body and extensively participate in many non-toxic biological functions, supporting the immune system, DNA, and protein adhesion, and enzymatic reactions that can promote bone mineralization [207]. Zn does not produce hydrogen cavitation caused by fast degradation and avoids abrupt failure [208]. Bowen et al. [209] have explored the bio-absorbable performance of pure Zn in biological conditions. They positioned pure Zn wire samples into the rat blood vessels and observed the best biodegradation rate of 20×10^{-3} mm/ year for the first 3 months of implantation. Subsequently, the wire implants degraded speedily in biological conditions, so that no implant residuals endure in the body. In another study, Bowen et al. [210], have installed Mg, Fe and Zn implants into the rat abdominal aorta. With this approach, they found the intermediate degradation rate of Zn implant is slower than that of Mg implant and faster than Fe implant, which is perfect for biodegradable applications. Therefore, Zn is a better choice for biodegradable metallic materials than Mg and Fe, with a better in vivo biodegradation rate and biocompatibility for tissue regeneration and therapy. Zn-based degradable biomaterials have recently emerged thanks to their intrinsic physiological relevance, biocompatibility, biodegradability, and pro-regeneration properties. Zn-based biomaterials mainly include: metallic zinc alloys, zinc ceramic nanomaterials, and zinc metal–organic frameworks. Metallic zinc implants degrade at a desirable rate, matching the healing pace of local tissues, and stimulating remodeling and formation of new tissues. Zn-based metallic implant for biodegradable applications (Figure 2.17: cardiovascular stents (Figure 2.17a, surface interaction of Zn-based

implant with damaged tissue (Figure 2.17b and orthopedic implants including fixative plate, screw, and scaffolds to support the new bone formation (Figure 2.17c [211]. Zn-based ceramic nanomaterials are also beneficial for tissue engineering and therapy thanks to their nanostructures and antibacterial properties. Researchers have shown their interest in Zn-based materials owing to their low-cost, availability, biocompatibility, and biodegradability, which can be observed by recent trend of number of publications in the last five years, as shown in Figure 2.18. Yang et al. [9] have prepared nanocomposite of pure Zn matrix and hydroxyapatite (HA) reinforcements using spark plasma sintering. They have reported improved non-cytotoxicity and effective antibacterial properties of Zn-5HA nanocomposite compared to pure Zn. The biodegradation of pure Zn and Zn-5HA composite was 1.7 and 3.2% by volume after 2 months, respectively. Zn-5HA composite was more effective in promoting local bone formation at injury than pure Zn. However, both pure Zn and Zn-HA composites are weak in mechanical strength at a normal body temperature of 37°C. The required compressive strength ($\sim$ 200 MPa) for the support and fixation of bone injuries can only be achieved by alloying or reinforcing the higher-strength materials into the Zn matrix [212].

However, there is a possibility of enhancement in mechanical, tribological and corrosion properties of Zn-based. Based upon the detailed literature review on MMNCs, particularly on low-cost Zn-based MMNCs and their applications in coatings and biodegradable structural materials, research gaps have been determined and presented in the next section.

2.10 Gaps in existing research and investigations

In chapter 1 and 2, we have reviewed the emerging Zn-based nanocomposites for anti-corrosion, anti-bacterial coating and biodegradable structural material. From the literature review, a few significant gaps still exist in studies on the synthesis and performance characteristics of Zn-based nanocomposites. The following issues are figured out and addressed in this thesis and detailed below:

1. To create metal matrix nanocomposites, various reinforcing agents can be used, including organic (e.g. hydroxyapatite) and inorganic (e.g. Ag, Au, ZnO, TiO$_2$, and Al$_2$O$_3$) materials. While these low-cost organic, ceramic and metallic nanofillers possess poor tribomechanical, anti-corrosion and antibacterial properties, there is a need to identify a more effective reinforcing element to produce Zn matrix nanocomposite for non-cytotoxic and antibacterial applications.

   Proposed solution − Recently, graphene nanoplatelets have been identified as a superior reinforcing element for composite coatings due to their exceptional mechanical, antibacterial, chemical, and physical properties. However, there has been limited research on graphene nanoplatelets reinforced composite. This study proposes using graphene nanoplatelets as
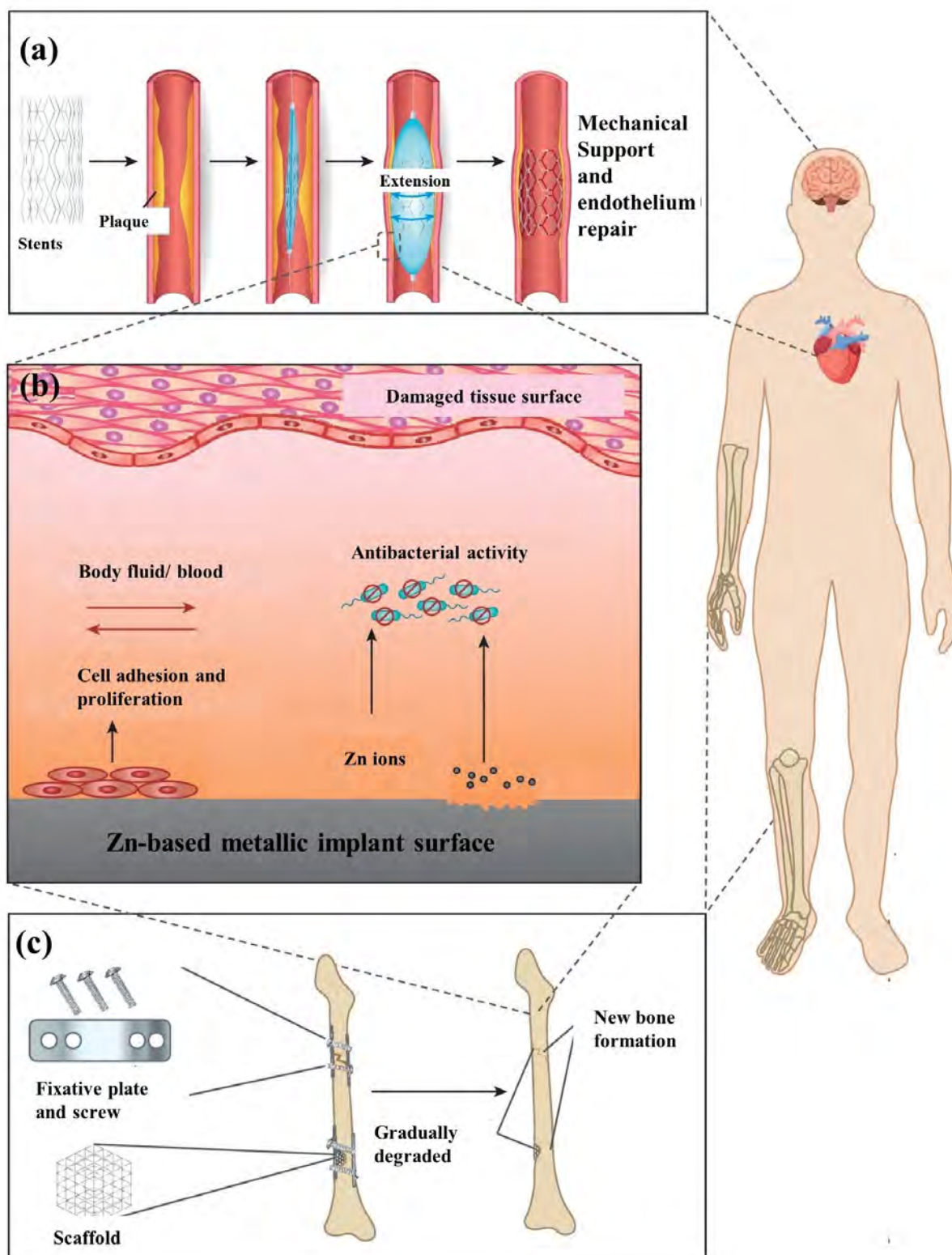
FIGURE 2.17: Zn-based metallic implant for biodegradable applications: (a) cardiovascular stents, (b) surface interaction of Zn-based implant with damaged tissue and (c) orthopedic implants including fixative plate, screw, and scaffolds to support the new bone formation [211].
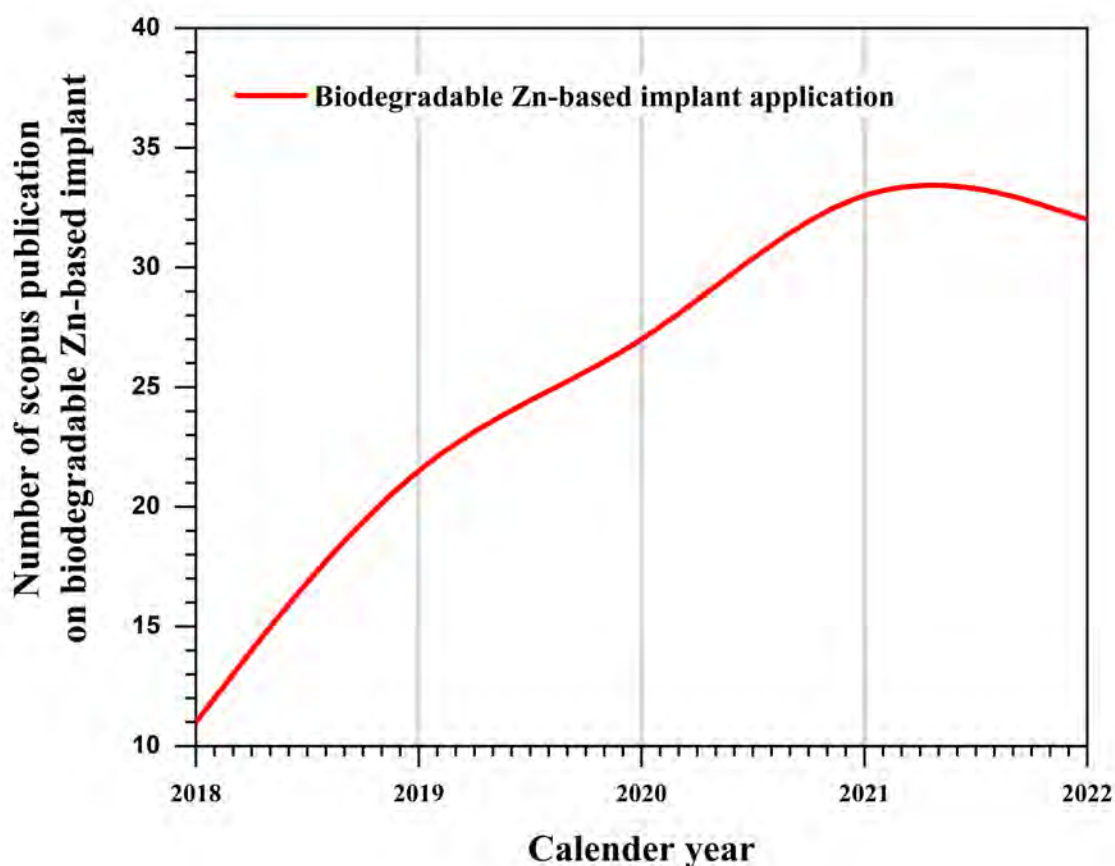
FIGURE 2.18: Publications on biodegradable Zn-based implants. Data extracted from archives of SCOPUS on date: 24th December 2022.

a reinforcement in the synthesis of Zn matrix composite coatings, which has not been explored in the literature.

2. The success of graphene-based composites with uniform biodegradation, as well as improving their tribo-mechnical properties, relies on having a uniform dispersion of graphene within the metal matrix while preserving its structure. Although efforts have been made to achieve this, the challenge of achieving uniform dispersion without damaging the structure of graphene remains a crucial issue in the synthesis of composites. Hence, it is imperative to find a solution to overcome these challenges.

   Proposed solution – The high surface area to volume ratio of graphene layers makes them prone to clustering, making it difficult to achieve a homogeneous and uniform dispersion. There have been many attempts in the literature to spread out these particles within a metal matrix using electro-co-deposition process. The aim of this research is to find a way to prevent the clumping of graphene nanoplatelets during the electro-co-deposition while preserving their structure, to enhance the mechanical, tribological, and corrosion properties by ensuring a uniform distribution of the nanoplatelets within the metal matrix.

3. Graphene has been shown to have antibacterial properties, but it also has a cytotoxic effect, meaning it can be harmful to living cells. Therefore, To make graphene biodegradable and safe for use in biological systems, a method must identify to modify its surface chemistry and reduce its toxicity.

   Proposed solution − Functionalizing graphene with biocompatible polymers and oxygen-containing groups are all approaches that can be used to reduce the cytotoxicity of graphene. Functionalizing with biocompatible polymers involves attaching biocompatible polymers and functional groups such as -COOH, or -OH to the graphene, which can reduce its cytotoxicity and reactivity by blocking the direct contact between the graphene and the living cells.

4. There has been a lot of research on Zn-based coatings using the electrodeposition method. The electrodeposition method is cost-effective and widely employed for producing thin films of metals and metal alloys. However, its main drawback is that it restricts the thickness of the composite to merely a few microns. No studies have been conducted to identify an economical and scalable method for producing large amounts of GNP-reinforced Zn-based nanocomposites.

   Proposed solution − In this study, a noval and facile approach is proposed for fabrication of GNP-strengthened Zn matrix. The proposed method helps to achieve a uniform distribution of GNPs within the Zn matrix without altering its structure. This method combines electro-co-deposition and powder metallurgy to produce the desired outcomes. This novel method enables the large-scale fabrication of a powder-form GNP-reinforced Zn-based MMNC.

2.11   Problem statement

Zn-based nanocomposites have many possibilities in coating and biodegradable structural applications owing to low cost, low melting point, anti-corrosion, antibacterial and non-cytotoxic properties. However, Zn MMNCs are weak in tribo-mechanical strength. A small amount of reinforcement of advanced nanofillers such as GNPs can significantly enhance the mechanical performance of MMNCs. Recently, GNPs (a 2D carbon allotrope with 0.142 nm C-C bond length) have been identified as one of the best suitable reinforcing elements in the field of MMNCs due to their outstanding mechanical, chemical, and physical properties and high specific area. However, GNP-based MMNC for non-cytotoxic, anti-bacterial and biodegradable has not been explored in the literature. The surface modification techniques can also be explored for surface modification to develop the non-cytotoxicity form of GNP reinforcements. For GNP-based nanocomposites, the enhancement in the properties depends upon the uniform dispersion of GNPs in the metal matrix and their structures. There have been many attempts to increase the uniformity of graphene dispersion without compromising its structure. Nevertheless, achieving uniform dispersion of

graphene in a metal matrix without compromising its structure is still a major challenge in the field of nanocomposite synthesis. Therefore, a method to overcome the above challenges needs to be investigated.

2.12 Objectives

Based on the existing knowledge and gaps in research, the following four objectives are designed:

1. Study various MMNCs fabrication techniques to suggest the best fitting approach to uniformly disperse the GNP reinforcement in the Zn matrix.

2. Development of large-scale powder metallurgy assisted technique for fabrication of Zn-MMNCs and synthesis of Zn/GNP nanocomposite coatings.

3. Study the technique to reduce the cytotoxicity of GNP reinforcement before adding to Zn matrix.

4. In-vitro study for the non-cytotoxic and anti-bacterial composition of biodegradable Zn/GNP nanocomposite.

5. Study the effect on tribo-mechanical and anti-corrosion properties of Zn/GNP nanocomposites by varying weight proportion of GNPs.

6. Optimization of process parameters for microhardness and corrosion protection efficiency of Zn/GNP nanocomposite.

2.13 Organization of the Thesis

Zn has been widely employed in several industries such as mechanical, chemical, electrical & electronics, marine, food-packaging and biomedical due to their remarkable physical, anti-bacterial and electrochemical properties. Currently, most efforts are focused on using Zn-based MMNC in biodegradable implants and antibacterial coating applications to improve their surface properties, such as microhardness, anti-corrosion, and wear resistance through the incorporation of several reinforcing elements. A significant amount of research on Zn-based nanocomposite coatings using the electro-co-deposition method has been carried out. Also, a more efficient method needs to be developed for facile, low cost and large-scale production of Zn-based MMNC. Zn-based nanocomposites prepared using GNPs as a reinforcing element through the electro-co-deposition method suggest a simple and economical way to improve the overall performance characteristics.

In chapter 3, the synthesis of Zn/GNP nanocomposite has been discussed in two different forms. 1. Electro-co-deposition of Zn/GNP nanocomposite coating on the metallic substrate. 2. Synthesis of Zn/GNP nanocomposites in the powder form by using a conventional electro-co-deposition

method which is simple, economical and suitable for large-scale production of Zn/GNP nanocomposite powder.

In chapter 4, the functionalization technique of GNPs to reduce their cytotoxicity and a detailed study of modified electro-co-deposition technique for non-cytotoxic, anti-bacterial and biodegradable Zn/f-GNP nanocomposite with material characterization and tribo-mechnical testing.

In chapter 5, the details of the surface morphology, elemental composition, and microstructure characterization followed by mechanical, tribological and corrosion properties of Zn/GNP nanocomposite coatings.

In chapter 6, the effect of ECD parameters and GNPs concentration on mechanical and corrosion protection efficiency of Zn/f-GNP nanocomposite and Zn/GNP nanocomposite coatings.

In chapter 7, the details of Zn alloy-based nanocomposite, including Zn-Cu/GNP nanocomposite with conventional powder-making electro-co-deposition method followed by powder metallurgy and electro-co-deposited anti-bacterial Zn-Ni/GNP nanocomposite coating.

In chapter 8, the overall conclusions and future scope of the present study have been discussed.

Chapter 3

Experimental Details

Chapter 2 was concerned primarily with the various types of fabrication methods of Zn -based MMC and provides an insight into the fabrication of GNP-reinforced Zn MMCs through electro co-deposition assisted powder metallurgy methods. As well as the need and the scope for future research are discussed in detail. In this chapter, the discussion is devoted to the development of synthesis methods. Two synthesis methods are developed for the Zn/GNP nanocomposite coatings using the electro co-deposition method and for the Zn/GNP nanocomposite powder using a modified electro co-deposition method. Subsequently, the method is followed by the powder metallurgy method to fabricate solid pellet samples. The detailed instrumentation and methodology sections are discussed in this chapter.

3.1 Electro co-deposition of Zn/GNPcoatings

The flowchart followed for the fabrication, characterization and testing of the Zn/GNP nanocomposite coating is represented in Figure 3.1.

3.1.1 Materials

3.1.1.1 Chemicals

Analytical-grade chemicals and de-ionized (DI) water were used to prepare the bath solution. Reagents with a purity of 99% were supplied by Merck Specialties Pvt. Ltd. and SRL Chemical Pvt. Ltd. All electrolyte solutions were formed using DI water. A volume of 250 ml of sulphate bath was composed of zinc sulfate pentahydrate ($ZnSO_4.7H_2O$) as the zinc source, sodium sulphate (Na_2SO_4), boric acid (H_3BO_4) and Ethylenediaminetetraacetic acid (EDTA) as a complex agent for coating and powder synthesis, respectively. Sulfuric acid (H_2SO_4) was used to adjust the pH value of the electrolyte solution for coating.

FIGURE 3.1: Flow of processes during fabrications of Zn/GNP nanocomposite coating followed by characterization, and testing

3.1.1.2 Particulates

GNPs were used as a reinforcing element without any further purification in the electrolyte bath for the synthesis of Zn/GNP nanocomposites coatings. The GNPs (thickness 5-15 nm with surface area 500 m^2/g, purity 99.9%) used in the coatings were reduced graphene oxide procured from Alfa Aesar.

3.1.1.3 Experimental requirements

A D.C. power supply (TESTRONIX 92 D, with voltage ranges from 0 V to 30 V and current control ranges from 0 A to 10 A) was employed to achieve co-deposition of Zn atoms and GNP nanofillers to form Zn/GNP nanocomposite coating. A pure Zn (99.9%) coating titanium rod of 3 mm diameter is connected to anode end. A magnetic stirrer for constant stirring the electrolyte bath. A vacuum filtration is required to remove insoluble impurities from the electrolyte solution. A probe sonicator for de-agglomeration of GNP nanofillers in the electrolyte bath. A polishing machine to prepare the substrate for electro co-deposition.

3.1.2 Experimental setup and process parameters

Experimental setup is comprised of electrolyte bath, magnetic stirrer, D. C. power supply, anode and cathode (substrate), as illustrated in Figure 3.2. The major controlled process parameters

for the experimentation are consternation of Zn salt in electrolyte bath (0.1 M to 0.5 M) [213], GNP content in electrolyte bath, pH of electrolyte bath (3 to 5) [122], temperature (25 °C to 35 °C), steering speed (100 rpm to 300 rpm) [214], current density (2 A/dm^2 to 8 A/dm^2) [38], and plating time (20 min to 60 min) (see Table 3.1).
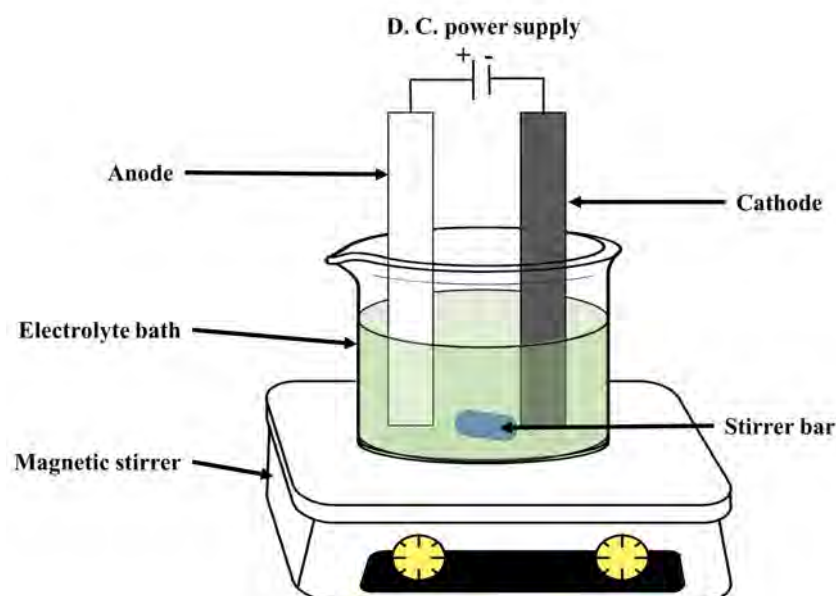
FIGURE 3.2: Experimental setup for coating

3.1.3 Preparation of substrate

Substrate plays a significant role in the electrodeposition of metal composite coatings. Substrate material should have good electrical conductivity and mechanical strength. At present, the substrate should be stable in the electrolyte bath. The substrate surface should be smooth and scratch-free. In the present work, we have used stainless steel as a substrate material. Normally, the stainless-steel substrate surface is covered with dirt, grease, oil, and oxide layers. The pre-treatment of the stainless-steel substrate involved steps, as shown in Figure 3.3.

Initially, the stainless-steel substrate was mechanically polished with different grades (150#, 600#, 1000# and 2500#) of silicon carbide papers to get a bright and smooth surface. Then, degrease in acetone to remove oil, dirt, grease, etc. After this, the substrate was washed with running water. Subsequently, the substrate was activated by dipping in a 5.0 M H_2SO_4 solution for about 3 minutes. Activation of substrate slightly increases the roughness of substrate to obtain good adhesion for the coatings onto the substrate. Again, the substrate was washed using running water and finally rinsed with DI water before the deposition process.
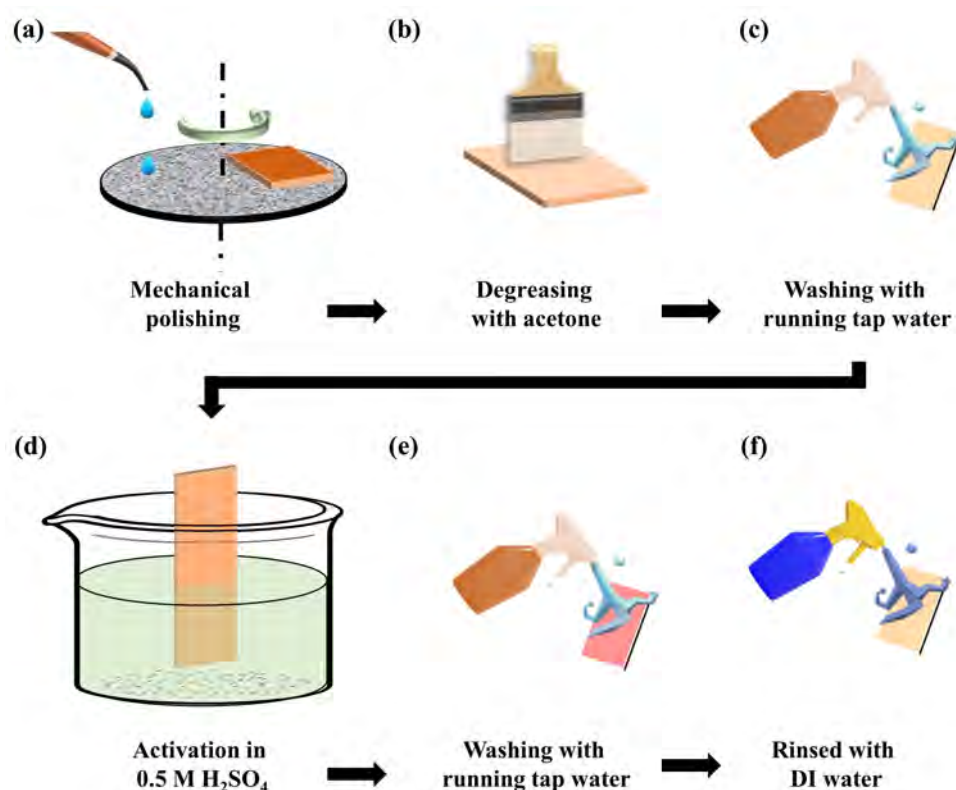
FIGURE 3.3: Pretreatment steps for preparation of stainless-steel substrate before electro co-deposition:(a) mechanical polishing, (b) degreasing with acetone, (c) washing with running water, (d) activation in 0.5 M H_2SO_4, (e) washing with running tap water, (f) rinsed with DI water.

3.1.4 Preparation of electrolyte bath

All chemical constituents ($ZnSO_4.7H_2O$, Na_2SO_4, and H_3BO_4) of electrolyte bath were mixed with DI water in a glass beaker using magnetic stirrer at 400 rpm for 60 min, as illustrated in Figure 3.4a. Vacuum filtration was used to remove insoluble impurities from the electrolyte solution. Subsequently, in order to achieve uniform dispersion of nanoparticles in the electrolyte bath, ultrasonication treatment was provided to the electrolyte solution to break down the agglomeration of nanoparticles, as illustrated in Fig. 3.4b.

3.1.4.1 Electro co-deposition of Zn/GNP nanocomposites coatings on stainless-steel substrate

The electro-co-deposition setup to prepare composite coatings is illustrated in Figure 3.5a. A pure Zn (99.9%) rod of 3 mm diameter was placed as an anode and a stainless-steel plate of dimensions 20 $\times$ 20 $\times$ 1.5 mm was placed as cathode. The prepared electrolyte solution was filled in a borosilicate glass beaker of 500 ml. The anode and cathode electrodes were immersed vertically into the electrolyte solution. A D.C. power supply was employed as a constant current source. The electrolyte solution was prepared using DI water by the addition of a known amount
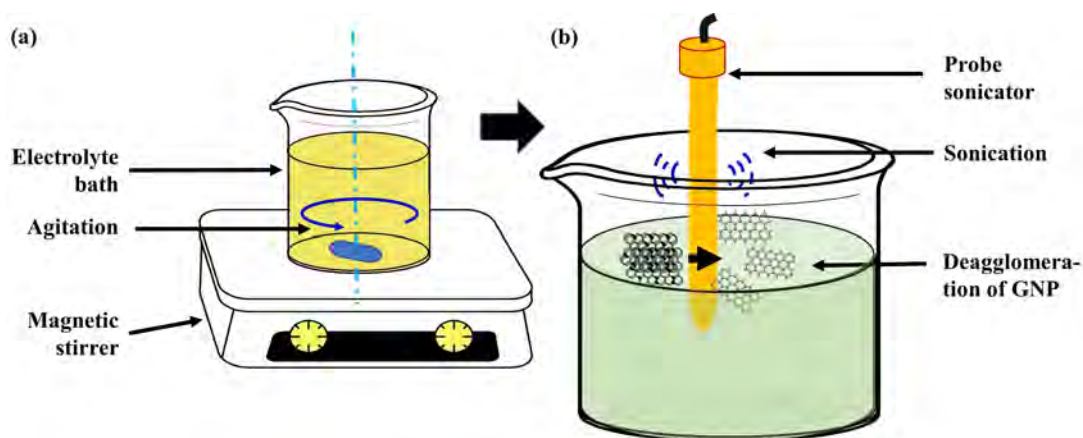
FIGURE 3.4: Preparation of sulphate-based electrolyte bath for Zn/GNP nanocomposite coating. (a) mixing of chemical reagents in DI water and (b) Deagglomeration of GNP in electrolyte bath.

of metal salts, complexing agent, and nanoparticles. The concentration of metal salts and electrodeposition process parameters were optimized by evaluating the composition of the coating. The co-deposition of GNPs and Zn^{2+} on the substrate is illustrated in Figure 3.5b.

Electro-co-deposition of coatings was carried out under magnetic stirring to maintain the uniform concentration of metal ions in the electrolyte bath. Each experiment was performed using a new electrolyte solution to maintain the concentration of electrolytes. After the deposition process, prepared coating samples were rinsed with DI water and dried in an inert atmosphere.
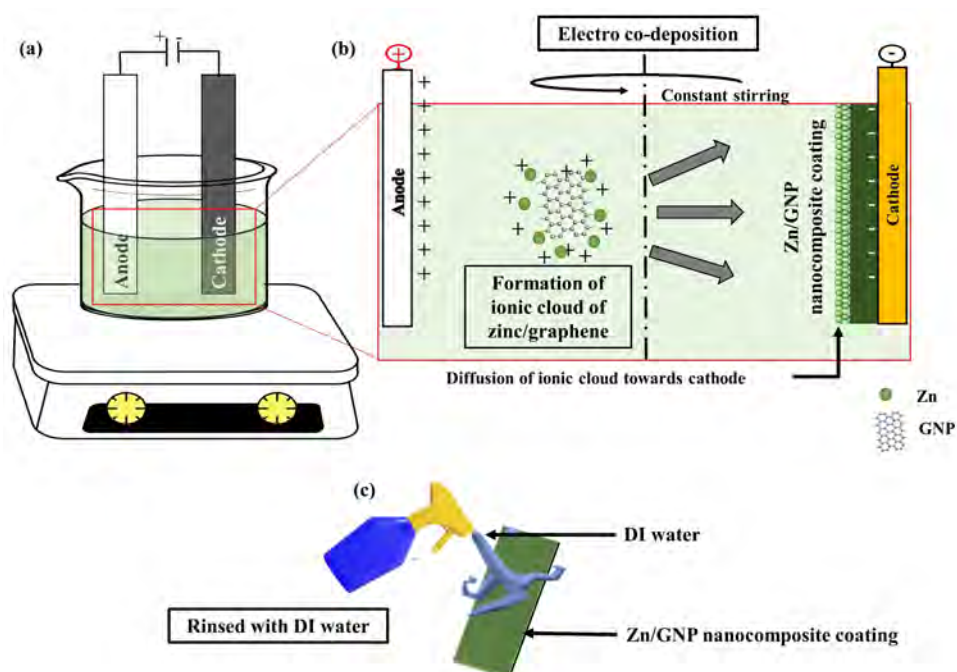
FIGURE 3.5: Schematic of fabrication of Zn/GNP nanocomposite coating. (a) electro co-deposition setup, (b) co-deposition mechanism, and (c) rinsed with DI water.

TABLE 3.1: Electrolyte bath composition and process parameters for Zn/GNP nanocomposite powder fabrication

Parameter	Values	Reference
Zinc sulfate pentahydrate (ZnSO$_4$.7H$_2$O)	(0.1 M to 0.5 M)	[213]
Sodium sulphate (Na$_2$SO$_4$)	0.5 M to 1 M	[215]
Boric acid (H$_3$BO$_4$)	0 M to 0.5 M	[215]
pH	3-5	[122]
DC current supply	2 A/dm^2 to 8 A/dm^2	[38]
Agitation	200 to 350 rpm	[214]
Run time	20 min. to 60 min.	[202]
GNPs' concentration	25, 50, 100 and 200 mg/L	This study
Temperature	25 °C to 35 °C	This study

3.1.5 Characterization and testing of Zn/GNP nanocomposites coatings

Zn and its composite coatings are widely used in automobile, marine, chemical and metallurgical applications.
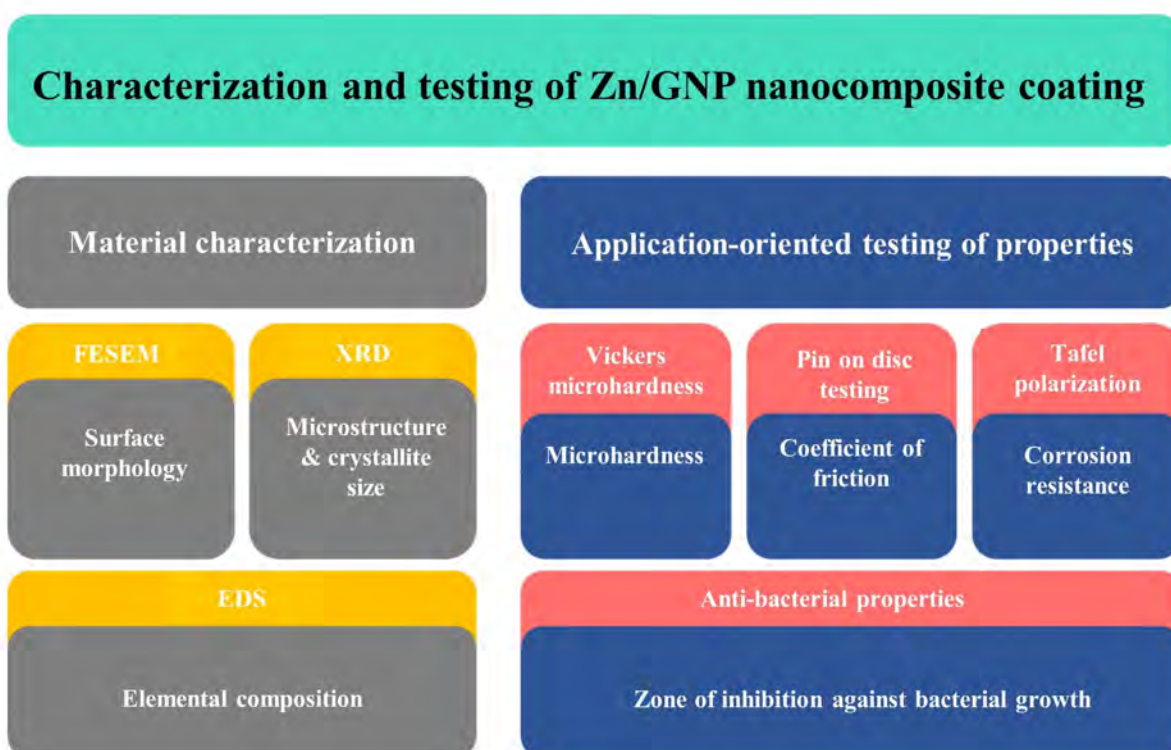
FIGURE 3.6: Characterization and testing of Zn/GNP nanocomposite coating.

FIGURE 3.7: Field emission scanning electron microscopy (FESEM) attached with energy dispersive spectroscopy (EDS, Oxford Instruments).

However, these coatings have been exposed to wear and corrosion during service life. Hence in these applications, hardness, wear resistance, and corrosion resistance properties of coatings are mostly considered because they directly affect the lifetime of engineering components. For this reason, the characterization of composite coatings has great importance in the field of materials science. Nowadays, several techniques are used to characterize and evaluate the performance of composite coatings, such as scanning electron microscopy (SEM), energy dispersive spectroscopy (EDS), X-ray diffraction spectroscopy (XRD), microhardness tester, tribometer, and potentiostat, etc. Different techniques employed to characterize and evaluate the performance of Zn/GNP nanocomposites coatings are shown in Figure 3.6.

3.1.5.1 Surface morphology and elemental composition

Scanning electron micrographs and elemental compositional analysis of prepared samples were performed using FEI-Apreo-S field emission scanning electron microscopy (FESEM) fitted with an energy dispersive spectroscopy (EDS). FESEM attached with EDS is shown in Figure 3.7.

FIGURE 3.8: X-ray diffractometer.

3.1.5.2 Microstructural analysis

X-ray diffractograms of prepared samples were taken using RIGAKU MiniFlex-II X-ray diffractometer (XRD) with Cu Kα radiation (see Figure 3.8). The rate of scanning for 2θ (40°– 80°) was 0.05°s^{-1}. The average crystallite size of the prepared samples was measured using the Scherrer equation (Equation 3.1) as follows [216],

$$D = \frac{K\lambda}{\beta \cos\theta} \tag{3.1}$$

where D is the grain size, K is the Scherrer constant ($= 0.9$), λ is the wavelength of the X-ray used in the experiment, β is the full width at half maximum (FWHM) of the X-ray diffraction peak, and θ is the Bragg angle.

3.1.5.3 Microhardness testing

A Vickers hardness tester (Mitutoyo, HM-200) was used to measure the microhardness of prepared samples (Figure 3.9). The applied load was 20 g for 20 s. Equipped with the optical system ideal for automatic measurement of the dimensions of indentation images.

Make: **Mitutoyo**, Japan
Model: HM-200 (**Automatic**)
Year: 2020
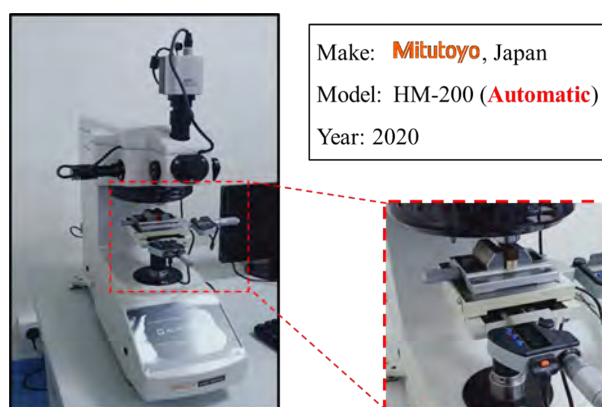
FIGURE 3.9: Vickers microhardness tester.

3.1.5.4 Tribological testing

The tribological performance was analyzed by a pin-on-disc wear machine (DUCOM, TR-20LE) under dry sliding conditions (Figure 3.10). The pin was a high carbon chromium-bearing steel (GCr15) with a diameter of 6 mm. The friction coefficient was recorded under a constant load of 500 g for 600 s.

3.1.5.5 Corrosion testing

To estimate the corrosion performance of prepared samples in 3.5 wt.% of NaCl aqueous solution at room temperature, CHI604E potentiostat/galvanostat instrument (Figure 3.11) based on the usual three electrodes cell configuration was used.

FIGURE 3.10: Tribometer.

FIGURE 3.11: Electrochemical workstation for Tafel polarization studies.

3.2 Electro co-deposition method for Zn/GNP powder

In this method, we have combined good features of electro co-deposition method and convectional powder metallurgy method to develop a modified electro-co-deposition method for the simple, economic and bulk production of Zn/GNP nanocomposites. Currently, many different methods are adopted to prepare GNP-reinforced metal composites like powder metallurgy and electrodeposition [148], [152], [217], [218]. Powder metallurgy is efficient and versatile in fabricating metal composites, and it has great potential for enhancing the properties of the composites [219], [220]. On the other hand, the main disadvantage of this method is that during the high-energy ball milling, the graphene structure will be damaged, and it may deteriorate the properties of the resulting composite [32]. The common coating methods include sputtering, electrodeposition, flame spraying, and chemical vapor deposition. However, the electrodeposition method is widely used for synthesising pure, alloy, and composite coatings due to several advantages such as simplicity of operation, cost-effectiveness, scalability, and high production rate [173]. Also, the properties of prepared composites can be controlled by optimizing the process parameters such as current density, pH, temperature, amount of reinforcement, and bath composition [16]. To achieve the co-deposition of two metals, the standard reduction potentials of these metals must be similar. The standard reduction potentials for nickel and copper are -0.25 V and + 0.34 V, respectively. For the co-deposition of Zn, the standard reduction potential difference can be decreased by adding a suitable complexing agent [215]. In our work, the electro-co-deposition

is carried out from a sulfate electrolyte with the addition of sodium citrate as a complexing agent. The addition of EDTA can act as a buffering agent, hence eliminating the need for additional additives [173], [215]. In the present work, Zn/GNP nanocomposites were prepared using a modified electrochemical-co-deposition method followed by the conventional powder metallurgy method. In a modified electro-co-deposition method, Zn/GNP powder samples are synthesized by simultaneous deposition of GNPs and Zn atoms on the tip of the insulated cathode to ensure the uniform distribution of GNPs in the Zn matrix. Using an electro-co-deposition method eliminates the ball-milling step in the powder metallurgy method, and thus prevents the structural damage of GNPs. The effects of different concentrations of GNPs in the electrolyte bath on the microstructural, mechanical and tribological properties of Zn/GNP nanocomposites were systematically studied.

3.2.1 Experimental setup

In an electro-co-deposition method, co-deposition of Zn ions and GNPs was carried out on the tip of an insulated cathode electrode. The actual experimental setup for a conventional electro-co-deposition of nanocomposite powder is shown in Figure 3.12. The experimental setup consisted of four platinum (Pt) coated electrodes (length 10 cm and diameter 3 mm) that were used as an anode, and one insulated Pt-based electrode (excluding the tip surface) was used as a cathode. Pt is a highly conductive and corrosion-resistant metal, making it a popular choice for use as an electrode material in electro-co-deposition processes. Some of the main advantages of using Pt electrodes for electro-co-deposition include:

- High conductivity: It has a very high electrical conductivity, which allows it to transfer electrical current and facilitate the electrodeposition process efficiently.

- Corrosion resistance: It's highly resistant to corrosion, meaning it can be used in a wide range of environments without degrading or losing its effectiveness over time.

- Chemical stability: Pt is highly chemically stable, making it resistant to reactions with other chemicals that may be present in the electrodeposition process.

- Durability: Pt is a very durable material, meaning that electrodes made from it will typically last longer and require less maintenance than other materials.

. Four Pt-coated titanium anodes (length 10 mm and diameter 10 mm) were fixed circumferentially in the Perspex sheet. All four cathode electrodes are connected in series. All experiments were carried out in a 500 ml borosilicate container. A magnetic stirrer with a hot plate (0- 1500 rpm, 0-200°C) was used to agitate and maintain the temperature of the electrolyte solution. A manual jerk was provided to the central cathode electrode to separate the co-deposited nanocomposite powder from the tip of cathode. D.C. Power supply (TESTRONIX 92 D, 0-30 V and 0-10 Amp) was employed to achieve co-deposition of Zn ions and GNPs to form Zn/GNP powder.
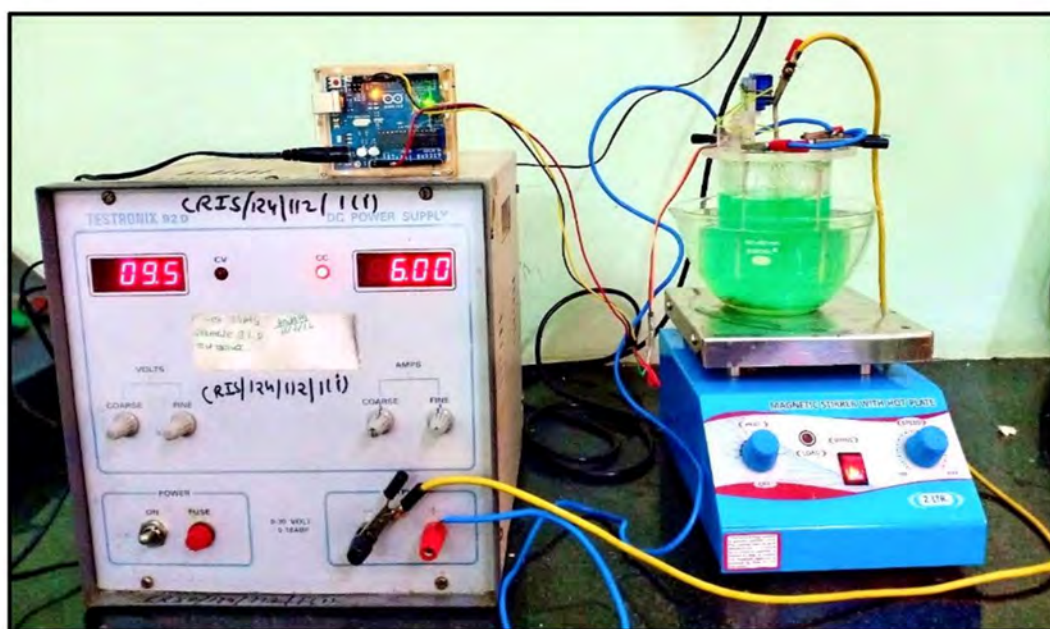
FIGURE 3.12: Conventional experimental setup for electro co-deposition of nanocomposite powder.

3.2.2 Materials

3.2.2.1 Chemicals

Reagents of all analytical grades with a purity of 99% were supplied by Merck Specialties Pvt. Ltd. All electrolyte solutions were formed using deionized (DI) water. A volume of 450 ml of sulphate bath was composed of zinc sulfate pentahydrate ($ZnSO_4.7H_2O$) as the zinc source, and sodium sulfate (Na_2SO_4) as a complex agent. De-ionized (DI) water of pH 6.9–7 was used to dissolve the reagents and cleansing purposes.

3.2.2.2 Particulates

Gray-black powder form of GNPs (99.9% pure) was used as a reinforcing element without further purification in the electrolyte bath to synthesize Zn/GNPs nanocomposite powder samples. The GNPs (thickness 5-15 nm and surface area 500 m^2/g) used in the coatings were reduced graphene oxide procured from Alfa Aesar. PEG 6000, 1-Ethyl-3-(3-dimethylaminopropyl) carbodiimide (EDC) and other chemical reagents of purity of 99.5% (supplied by Merck Specialties Pvt. Ltd.) were used for fuctionallization of GNPs.

3.2.2.3 Electrodes

Platinum (Pt)coated Titanium (Ti) electrodes with 10 μm coating thickness, 3 mm diameter and 100 mm length were obtained from Titanium tantalum Product limited Chennai, India.

3.2.3 Experimental procedure

The electrolyte bath consisted of $ZnSO_4.7H_2O$ (0.1 to 0.3M) and EDTA (0.15 M) (complexing agent) [215]. The GNPs (25, 50, and 200 mg/L) were added to the electrolyte bath under continuous magnetic stirring at 300 rpm for 20 minutes and followed by sonication using direct probe sonication at 20 kHz, 500 W for one hour. The magnetic stirring and direct probe sonication were provided to dissolve the reagents and unbound the agglomerated GNPs in the electrolyte bath, respectively.

All electrodes are partially dipped in the electrolyte bath and powered by a DC power supply, as illustrated in Figure 3.13a. Here, the tip of the insulated cathode was exposed to the electrolyte bath. The agglomerated clouds of positively charged Zn^{2+} metal ions and the unbound GNPs were co-deposited at the exposed cathode tip to form Zn/GNP nanocomposite. The slurry of Zn/GNP nanocomposite was settled down to the bottom of the bath due to self-weight, as illustrated in Figure 3.13b. Continuous stirring and cooling were provided to maintain uniformity across the bath. The process was continued for nearly 3 hours and ended when the electrolyte solution became colorless.
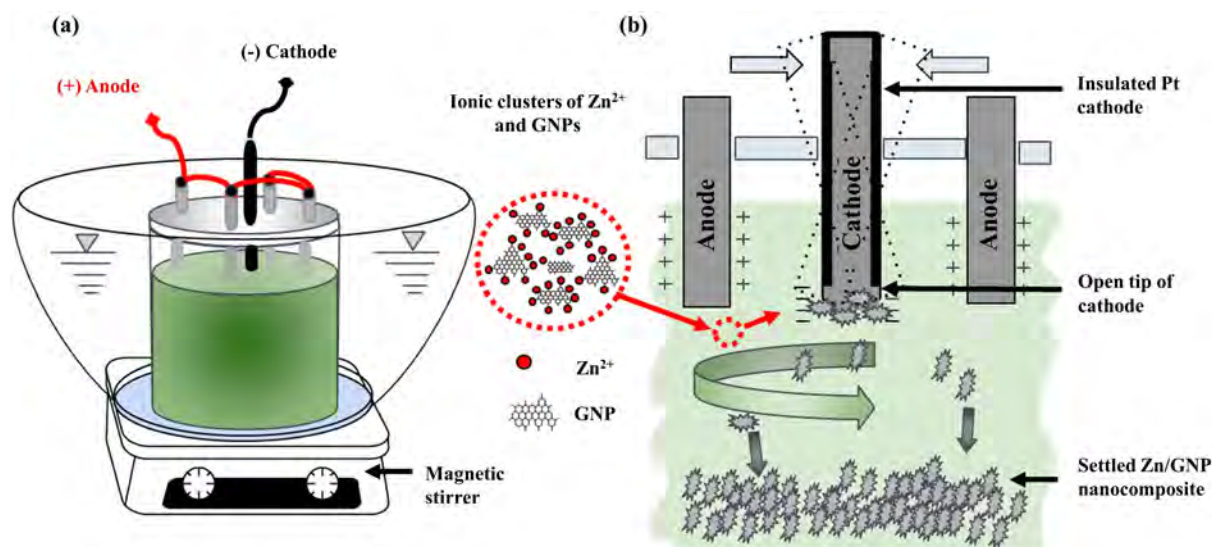
FIGURE 3.13: Schematic representation of synthesis of Zn/GNP nanocomposite using conventional ECD method followed by powder metallurgy: (a) ECD-based experimentation setup with continuous bath sonication, insert view shows the conjugation of GNP nanofillers with Zn ions and (b) co-deposition as Zn/GNP nanocomposite at cathode tip.

Thereafter, the slurry of Zn/GNP nanocomposite was rinsed with DI water and dried at 70 °C temperature under vacuum (at 3.99 kPa) using a rotary evaporator. The dried powder

nanocomposite samples were stored in an inert atmosphere to avoid oxidation. The dried powder samples were uniaxially compacted in cylindrical shapes (diameter 25 mm and thickness 3 mm) at 400 MPa and sintered using an electric furnace at 338 °C temperature (0.80 Tm, melting temperature of Zn matrix) for 60 minutes in an inert atmosphere then followed by furnace cooling, as illustrated in thermal procedure in Figure 3.14. The pure Zn samples were prepared without adding GNPs in the electrolyte bath.

FIGURE 3.14: Sequence of the thermal procedure applied to sinter Zn/GNP nanocomposite pellets.

TABLE 3.2: Electrolyte bath composition and process parameters for Zn/GNP nanocomposite powder fabrication

Parameter	Values	Reference
$ZnSO_4.7H_2O$	0.1 M to 0.5 M	This study
EDTA	0.15 M	[215]
pH	10 (maintained by aqueous NaOH)	[165]
DC current supply	2 A to 6 A	[152]
Agitation	400 rpm	[221]
Run time	3 hours.	[202]
GNPs' concentration	25, 50, 100 and 200 mg/L	This study
Temperature	35 °C	This study

3.2.4 Characterization of Zn/GNP nanocomposites

3.2.4.1 Morphological and microstructural study

In order to study the surface morphology, internal microstructure, elemental composition, and crystallite size of the Zn/GNP powder sample SEM, TEM, EDS, and XRD analysis techniques were used. Also, to determine the microhardness, coefficient of friction, tensile properties

and corrosion resistance of sintered Zn/GNP nanocomposites microhardness tester, tribometer, universal testing machine and potentiostat were used.

The surface morphology and internal microstructure of prepared powder samples were examined using field emission scanning electron microscopy (FESEM, FEI-Apreo-S) and high-resolution transmission electron microscopy (HRTEM, Tecnai G220 FEI, S-Twin operating at 200 kV). FESEM equipped with electron dispersive spectroscopy (EDS) was employed to examine the composition and distribution of elements in the prepared powder samples.

X-ray diffractometer (XRD, RIGAKU MiniFlex-II) was employed to analyze the phase constituents of powder samples using Cu K radiation $\lambda = 1.5418$ Å. The 2 ranged from 40 to 80° at a scan rate of $0.05°\text{s}^{-1}$. The Scherrer equation was used to estimate the average crystallite size of the prepared powder samples.

3.2.4.2 Tribo-mechanical tests

Vickers microhardness of nanocomposites was determined using a semi-automatic microhardness tester (Mitutoyo HM-200, Japan), with an applied load of 20 g with load holding time of 15 s. Five micro-size indentations were made for each sample during the microhardness measurement. Uniaxial compression tests were performed in accordance with ASTM E9-89a (2000) standards at room temperature using a universal material test machine (BISS UNO 100, India) (Capacity = 100 kN) [222]. The compression testing samples were prepared with cylindrical dimensions of diameter 6 ± 0.02 mm and height 12 ± 0.02 mm. Five specimens were taken for each prepared sample group. Tribological characterization of nanocomposite samples was performed on a pin-on-disk (DUCOM Tribometer) experimental setup at room temperature. Samples size of a diameter 25.4 ± 0.02 mm and a height 4 ± 0.2 mm were used. The counter body was a pin of 6 mm diameter made of GCr15 steel with a hardness of 60-67 HRC. The specific load was 5 N, and the linear slipping velocity was 0.25 m s^{-1} at a radius of 8 mm, and the test continued for 10 min. The total sliding distance covered for each test was about 100 m. All tribological tests were conducted under dry conditions at room temperature (about 27 °C) and humidity 35%.

3.2.4.3 Degradation test

(a) *Immerssion test*

The degradation behavior of prepared Zn/GNP nanocomposite examined by immersion and electrochemical tests. The sintered pellet specimens of diameter 12.7 mm and thickness 3 mm were cleaned and washed in ethanol and DI water respectively before testing. During the immersion test, the samples were immersed in conventional simulated body fluid (SBF) at 37 ± 0.5 °C for 56 days according to ASTM G31-72 [223]. The ratio exposed surface area of sample to volume of SBF media was maintained to 1 cm^2: 20 mL. The samples were rinsed by aqueous CrO$_3$ solution (200 g/L) before weight loss measurement to remove the

corrosion products from the surface. The corrosion rate (CR_{WL}, mm/ year) was calculated using relation (Equation 3.2) [224], [225],

$$CR_{WL} = 8.74 \times 10^4 \frac{W}{A \cdot t \cdot \rho}.$$ (3.2)

Where 'W' weight loss (g) of the samples during the immersion time 't' (hour(s)), 'A' is exposed surface area of the samples (cm^2), and 'ρ' is density of prepared samples (g/cm^3). Three sample groups were measured for each test. The corroded samples were characterized using FESEM, XRD and EDS analysis to understand the corrosion morphology, microstructures, and elemental composition, respectively [226].

(b) *Electrochemical test*

Electrochemical tests were used to analyze the corrosion behavior of the prepared Zn/GNP nanocomposite samples via potentiodynamic polarization curves recorded using potentiostat workstation (CH Instruments - 604E Potentiostat/ Galvanostat, USA). A three-electrode electrochemical cell setup was adopted with a standard Ag/AgCl reference electrode. The samples were polished with 4000 greet SiC paper and cleaned with ethanol and DI water. Experimentations were performed at 37 °C temperature in SBF, pH = 7.4. The samples were exposed to SBF solution with a surface area of 1 cm^2. The range and scan rate were 1.5 V to -1.2 V and 0.5 mV s^{-1}, respectively. The electrochemical corrosion rate (CR_{EC}, mm/year) was calculated using [224],

$$CR_{EC} = 3.27 \times 10^{-3} \frac{I_{corr} \cdot W_{eq}}{\rho}.$$ (3.3)

Where 'I_{corr}' is corrosion current density (gm/cm^2), 'W_{eq}' is the equivalent weight of pure Zn, 'ρ' is the density of prepared samples (g/cm^3). Three measurements were taken for each sample group.

3.2.4.4 Cell cytotoxicity

(a) *Cell preparation and culture:*

Human keratinocyte (HaCaT) cells were cultured at 37 °C, 5% CO2 in Dulbecco's modified minimal essential medium (DMEM; HiMedia, India) supplemented with 10% fetal bovine serum (FBS; RM1112, HiMedia, India) and 1% penicillin-streptomycin mixture (10378-016, Gibco, USA). Cells (50% confluency in DMEM with 10% FBS) were rinsed with phosphate-buffered saline (PBS) and substituted with a treatment containing media.

(b) *Cell viability and proliferation assay:*

Assessment of cell viability was performed by MTT assay [33]. The assay measures the viability of living HaCaT cells via the cleavage of MTT (3-[4,5-dimethylthiazol-2-yl]-2,5-diphenyltetrazoliumbromide) to purple formazan crystals by the cell's mitochondrial dehydrogenases. Approximately 6000 cells per well were seeded in 96 well plate in 10% FBS containing DMEM media. Cells were grown till 60-70% confluency and then treated with different concentrations of pure Zn and Zn/GNP nanocomposites (ranges 20 μg/ml to 100 μg/ml), which were initially suspended in PBS (stock concentration 5 mg/ml) and subsequently kept at 37 °C, 5% CO_2 for 72 hours. Thereafter, MTT (20 μL; stock concentration of 5 mg/mL) was added. Cells were then again incubated for 4 hours; post which formazan crystals were solubilized in DMSO, and absorbance was measured at a wavelength of 570 nm with a differential filter of 630 nm using a Multiskan Sky spectrophotometer (Thermo Fisher Scientific, USA). The percentage of viable cells was calculated using the formula [227]:

$$Cell\ viability = \left(\frac{Mean\ absorbance\ value\ of\ drug - treated\ cells}{Mean\ absorbance\ of\ control} \right) \times 100. \quad (3.4)$$

4,6-Diamidino-2-phenylindole (DAPI blue) staining was used to evaluate HaCaT cell attachment [33]. For microscopic imaging [224], cells were plated on coverslips. After incubation with nanocomposite samples for 72 hours (about 3 days), the coverslips were washed with PBS and fixed with 2 % paraformaldehyde at room temperature for 15 min. After that blocking was done for 2 hours with 1% BSA. The coverslips were incubated with DAPI for 10 min and further mounted with 70 % glycerol. Images were taken through ZEISS Axio Scope.A1 microscope (Zeiss, Germany).

3.2.4.5 Antibacterial test

Antibacterial tests of sintered pellets of Zn/GNP nanocomposite were performed within in-vitro environment of *Staphylococcus aureus* (*S. aureus*, MTCC No. 96) and *Escherichia coli* (*E. coli*, MTCC No. 1652). Before antibacterial tests, the pellet samples were rinsed well using ethanol and DI water and dried at 120 ºC in hot air oven. The bacterial strain was grown in Luria Broth medium. The zone of inhibition (ZOI) was measured by the modified agar-disc diffusion method as per National Committee for Clinical Laboratory Standards, 1993. The plates were incubated overnight in 5% CO_2 bacterial culture environment at 37 °C, and the ZOIs were measured on a millimetric scale. The pure Zn pellet was a control, and three tests were performed for each prepared nanocomposite sample group.

3.2.4.6 Statistical analysis

Statistical analysis was performed using GraphPad Prism 9. The graphical representations of data show the means $\pm$ standard deviations. One-way analysis of variance (ANOVA) followed by

Tukey's post-hoc-test was performed when different results were compared. A P-value <0.05 was acknowledged as a statistically substantial variation between means [228].

3.3   Conclusion

The conclusions based on the work carried out at this point are as follows:
For nanocomposite coating fabrication

- In the present chapter, we have discussed the electro-co-deposition method to synthesize Zn/GNP nanocomposite coatings. The electrodeposition of Zn/GNP nanocomposite coatings was carried out at (a) various current densities and (b) various concentrations of GNP in the electrolyte bath. In addition, the ultrasonication treatment was given to the electrolyte before the deposition process to achieve uniform dispersion of GNPs in the electrolyte bath.

For nanocomposite powder fabrication

- Before the process of fabrication of Zn/GNP nanocomposite powder, the GNPs were functionalized with PEG to attach non-toxic functional groups. The attached functional group modifies the active sites on the surface of exfoliated GNPs, that make them more compatible with biological tissue.

- The bulk production of Zn/GNP nanocomposite powder was carried out using a modified electro-co-deposition method. Then conventional powder metallurgy method was used to fabricate Zn/GNP nanocomposites. Before the deposition process, prolonged ultrasonication was employed to break the agglomeration of GNPs and achieve GNPs' uniform dispersion in the electrolyte bath.

- In the modified electro-co-deposition method, co-deposition of GNPs and zinc metal ions occurs at the cathode electrode's tip surface. The Zn/GNP nanocomposite powder was obtained after drying the co-deposits. This method provides facile, economic and bulk production of Zn/GNP nanocomposite powder with a uniform dispersion of GNPs into the Zn matrix.

- The convectional powder metallurgy method was employed to prepare Zn/GNP nanocomposites obtained from a modified electro-co-deposition method. A modified electro-co-deposition method eliminates the ball milling step in the powder metallurgy method, which helps prevent GNPs from structural damage during processing.

In the next chapter, a detailed characterization of (a) Zn/GNP nanocomposite coatings synthesized by electro-co-deposition method and (b) Zn/GNP nanocomposites powder synthesized by a modified electro-co-deposition method are discussed in detail. The characterization of Zn/GNP nanocomposite coatings includes SEM. EDS and XRD analysis. The characterization of Zn/GNP

nanocomposite powder includes SEM, EDS, XRD and TEM analysis. The powder samples were compacted and sintered to test the in-vitro degradation and tribo-mechanical performances of resulting solid-state nanocomposite pellets. The in-vitro cytotoxic and antibacterial behavior of Zn/GNP nanocomposites samples were tested and discussed in detail.

Chapter 4

Non-cytotoxic Zn/f-GNP Nanocomposite Powder and Pellets

4.1 Overview

Zn alloys and composites have recently been recognized as potential biodegradable materials for bone implants and vascular stents. Although new class of Zn-based materials have superior mechanical integrity than polymeric materials during biodegradation, the reinforcement of biocompatible form of graphene nanoplatelets (GNPs) in Zn matrix can be utilized to further enhance their effectiveness for loadbearing implants. In this work, pristine GNPs were functionalized with polyethelene glycol to reduce their toxicity [229] and reinforced in Zn matrix using the modified electro-co-deposition (M-ECD) method. The influence of various concentrations of functionalized GNPs (f-GNPs) in ECD bath on microstructure, interface bonding of functional groups, morphology, and elemental composition, corrosion resistance, and tribo-mechanical behavior of Zn/f-GNP nanocomposite have been studied. The Zn/f-GNP nanocomposites were also tested systemically for biological responses by in-vitro cytotoxicity and antibacterial studies. The nanocomposite sample of 100 mg/L of f-GNPs concentration in ECD bath has demonstrated a uniform slow in-vitro degradation rate of $26 \pm 0.8 \times 10^{-3}$ mm/year. The primary degradation products included zinc oxide [ZnO], zinc hydroxide [Zn(OH)$_2$], and simonkolleite [Zn$_5$(OH)$_8$Cl$_2$H$_2$O] observed from x-ray diffraction of corroded nanocomposites. The microhardness, compressive yield strength and ultimate compressive strength of Zn/f-GNP (100 mg/L) nanocomposite were 108.5 HV, 284.9 MPa, and 292.6 MPa, respectively, which were significantly higher than pure Zn. In addition, the good in-vitro human keratinocyte cell viability and effective antibacterial activity of Zn/f-GNP nanocomposite render it a very attractive biodegradable implant material for future implication in orthopedic fixation (screw, pins, sutures, and plates) and stents (coronary and cardiovascular stents) applications.

4.2 Introduction

Biodegradable implants have the ability to be absorbed in the body after the completion of their clinical role to avoid post-implant surgeries and make the treatment less painful and economical for the patients [230]. Metal-based implants provide excellent internal support and fixation for orthopedic injuries compared to polymer- or ceramic-based implants owing to their superior mechanical performance [189], [190]. Ti alloys, Co-Cr alloys, and stainless steel have been extensively employed as implant materials [191]. However, these are non-biodegradable and high-strength implant materials ($\sim$110 GPa for Ti alloys, $\sim$200 GPa for stainless steel, $\sim$240 GPa for Co–Cr alloys), thus mismatch with the elastic moduli of natural bone ($\sim$30 GPa) resulting stress-shielding of the bones at implant location that causing bone resorption and subsequent implant loosening [192]. Therefore, such implant materials need to remove after the orthopedic injury has healed.

Recently, Mg [203]- and Zn [2]-based alloys have attracted much attention owing to their biodegradability, nontoxicity, low density, and mechanical strength with elastic moduli of $\sim$45 GPa for Mg and $\sim$90 GPa for Zn, which match those of bones better than other metals do. However, Mg-based alloys and composites are still susceptible to fast biodegradation, which could lead to abrupt failure of the loadbearing implants before the completion of their clinical role [205]. Meanwhile, researchers have been tested Zn-based alloys and composites for biodegradable implant applications [192], [231]. The reported outcomes for in-vitro and in-vivo tests are very motivating because of their moderate corrosion rates ranges between Mg and Fe [206]. Zn-based compounds are essential in the human body and extensively participate in many non-toxic biological functions, supporting the immune system, DNA, and protein adhesion, and enzymatic reactions that can promote the bone mineralization [207]. Zn does not produce hydrogen cavitation caused by fast degradation and avoids abrupt failure [232]. Bowen et al. [209] have explored the bio-absorbable performance of pure Zn in biological conditions. They positioned pure Zn wire samples into the rat blood vessels and observed the best biodegradation rate of 20×10^{-3} mm/ year for the first 3 months of implantation. Subsequently, the wire implants degraded speedily in biological conditions, so that no implant residuals endure in the body. In another study, Bowen et al. [210], have installed Mg, Fe and Zn implants into the rat abdominal aorta. With this approach, they found the intermediate degradation rate of Zn implant is slower than that of Mg implant and faster than Fe implant, which is perfect for biodegradable applications. Yang et al. [212] have prepared nanocomposite of pure Zn matrix and hydroxyapatite (HA) reinforcements using spark plasma sintering. They have reported improved non-cytotoxicity and effective antibacterial properties of Zn-5HA nanocomposite compared to pure Zn. The biodegradation of pure Zn and Zn-5HA composite was 1.7 and 3.2% by volume after 2 months, respectively. Zn-5HA composite was effective in promoting local bone formation at injury than pure Zn. However, both pure Zn and Zn-HA composites are weak in mechanical strength at a normal body temperature of 37°C. The required compressive strength ($\sim$ 200 MPa) for the support and fixation of bone injuries can

only be achieved by alloying or reinforcing the higher strength materials into the Zn matrix[233]. The advancement in nanocomposites showed that a small amount of reinforcement of carbon allotropes can significantly enhance the mechanical, wear and biodegradation performance of metal matrices [43], [234], [235].

Especially, graphene nanoplatelets (GNPs, a 2D carbon honeycomb lattice with 0.142 nm C–C bond lengths) have emerged as one of the effective nanofiller reinforcements for the metal matrices due to its high strength to weight ratio, high specific surface area, thermal properties, and non-magnetic nature [236]–[238]. It was reported that GNP reinforced nanocomposites can perform antibacterial activities against both gram positives and negative bacteria [44]. In addition, it has been found that the single-layer GNP comprised of sp^2-C in metal matrix nanocomposite acted as an impermeable nanosheet providing a nanoscale barrier to resist the corrosion attacks on metal matrix [239]. Chen et al. [240] synthesized GNP reinforced magnesium matrix composites by thixotropic molding. They reported the GNP content of 0.6 wt% can achieve the microhardness and yield tensile strength of 92.3 HV and 245 MPa, respectively. Rashad et al. [241] reported the effect of GNP reinforcement on the mechanical properties of aluminum (Al) matrix composite, where the yield tensile strength increased by 11.8% (up to 190 MPa) compared with pure aluminum. In a study, Dai et al. [242] have synthesized GNP reinforced Zn matrix composites using ball milling assisted spark plasma sintering method. They have reported that the ultimate tensile strength and microhardness is increased by 126% and 20.3%, respectively, than those of pure zinc. The load transfer and dislocation strengthening ability associated with GNP improved the strengthening mechanisms of the Zn matrix.

For biodegradable implant applications, the main two aspects are potential cytotoxicity and possible non-biodegradability [243]. The recent studies on GNP-containing nanocomposites have shown that the cytotoxicity of GNPs can be determined based on their size, concentration, and formed structure in the nanocomposite [244], [245]. However, the functionalization of GNP with biocompatible groups can decrease cytotoxicity and lower the risk of penetration into the cell membrane [246]. On the other hand, the functionalization of GNP allows the partial breakage of $sp^2 \breve{} sp^2$ bonds into $sp^3 \breve{} sp^3$ bonds for inserting some pendent groups like; hydroxy, epoxy, and carboxylic acid [247]. These attachments facilitate uniform biocompatible contact of GNP with enzymes in the biological environment, thus promoting the biodegradation of reinforced GNPs in nanocomposites [247], [248]. Polyethylene glycol (PEG) exhibits a low toxicity and higher solubility in aqueous solutions and easily forms bioconjugates on GNPs' surfaces with attached hydroxyl, carbonyl, carboxyl, and epoxide functional groups [249]. The presence of those reactive functional groups imparts excellent aqueous solubility and enzymatic reactions for biodegradation [250]. In addition, the functionalization of GNP allows real-time detection techniques such as nuclear magnetic resonance (NMR), computed tomography (CT) [251], and ultrasound [252] to detect the structural integrity, and mineralization of the implant. Thereby helpful for in-depth investigation of the bone repair.

The problem of agglomeration of GNP at higher concentration is typically inevitable during the fabrication of metal matrix nanocomposites through available methods. In a related study, Munir et al. [253] have reported that the higher concentration of GNP (>1 wt.%) into the Zn matrix using conventional ball milling method can cause agglomerations of GNP and thus formation of hydrophilic surfaces (contact angle < 90°), which generates micro-galvanic corrosion in harsh environmental condition. However, the mechanical ball milling method has been considered as an inefficient method to achieve uniform dispersion of GNP in Zn matrices, as it damages the nanostructure of GNPs and reduces the effect of reinforcement. In the previous works [55], [173], we have suggested an electrolytic co-deposition (ECD) method for fabrication of Zn-based nanocomposites without damaging the structure of GNPs, wherein, ex-situ step was used to de-agglomerated GNPs. But, during the co-deposition process, the existence of high - stacking and van der Waals attraction forces between GNP layers can facilitate agglomeration and restacking of nanoplatelets in ECD bath. Therefore, this method needed a design improvement was required in the available setup to avoid agglomeration of GNPs in ECD bath during long co-deposition runs.

In this work, functionalized GNPs (f-GNPs) were prepared to reinforce into the Zn matrix using modified experimental setup for ECD method. This modified ECD (M-ECD) method was comprised of continuous ultrasonic assistance given to ECD bath for in-situ de-agglomeration process of f-GNPs. As the co-deposition started, the Zn/f-GNP ionic clouds were diffused at cathode tip to prepare Zn/f-GNP nanocomposite powder. The prepared powder samples with different concentrations of f-GNP in ECD bath were characterized for composition, microstructure, interface bonding of functional groups and surface morphology. Further, the powder samples were compacted and sintered to test the corrosion and tribo-mechanical performances of resulting solid-state nanocomposite pellets. The current research contribution addressed the suitability of Zn/f-GNP nanocomposite for potential tunable biodegradable implant applications based on its in-vitro biodegradation, tribo-mechanical, non-cytotoxic and antibacterial behavior.

4.3 Experimental procedure

4.3.1 Functionalization of GNPs

As-procured pristine GNP powder was mixed in DI water with continuous stirring and sonication for 30 mins. This step exfoliated the GNP powder and formed suspension of deagglomerated GNPs. For functionalization, 20 ml aqueous 1-Ethyl-3-(3-dimethylaminopropyl) carbodiimide (EDC) solution, 2.0 mg ml^{-1}, was mixed with 100 ml GNPs suspension, 2.0 mg ml^{-1}, and then pH adjusted to 8.0 using 5 mM NaOH$_{(aq)}$. Here, EDC act as carboxyl activating agent. In the next step, the suspension was added to 100 ml of aqueous PEG 6000, 1.0 mg ml^{-1}, and sonicated for 20 min followed by stirring for 24 hours to prepare the f-GNPs. The suspension was filtered and washed five times with DI water to remove the unreacted PEG and any water-soluble

impurities. In the final step, the filtered slurry of f-GNPs was centrifuged and dried in a rota evaporator. The f-GNPs were characterized for functional group attachments and structural changes and stored in inert conditions for further use in experimentation.

4.3.2 Synthesis of Zn/f-GNP nanocomposite

The ECD bath was comprised of 0.2 M $ZnSO_4.7H_2O$, 0.15 M Ethylenediaminetetraacetic acid (EDTA, complexing agent), 5 mM NaOH(aq) for maintaining pH 8 and different concentrations of as-prepared f-GNP (25, 50, 100 mg/L). The mixture was continuously stirred at 250 rpm, and bath sonication at 20 kHz, 500 W. These continuous stirring and bath sonication attachments have maintained homogeneity and de-agglomerated state of f-GNP in the bath during the process of co-deposition. The M-ECD process for fabrication of Zn/f-GNP nanocomposite powder is represented in Figure 4.1a and b.

ECD bath composition, electrode specification, and experimental parameters are shown in Table 4.1. During the experimentation, the anode was assigned to four fully exposed non-consumable electrodes and the cathode was assigned to one partially exposed electrode (at the tip). Here, the Zn/f-GNP ionic clouds from the ECD bath were co-deposited on cathode tip. The deposits were drop-down and settled at the bottom during the process. The nanocomposite slurry obtained from ECD bath was washed with DI water and filtered to remove soluble impurities. Then, desiccated to powder form using rota-evaporator at 70°C under a high vacuum of 10^{-6} kPa and stored in air-tight vails to avoid contamination. The nanocomposite powder samples were die-compacted at pressure of 80 MPa and sintered at 335 °C (0.8Tm, melting point of Zn) for 3 hours under inert environment followed by furnace cooling, see Figure 4.1c. The actual experimental setup is shown in Figure 4.2.

4.3.3 Characterization for as-prepared f-GNPs

The characterization of the samples was studied at different steps of synthesis using various advanced analytical tools [254]. The attached functional groups to f-GNP nanofillers were analyzed using Fourier transform infrared spectroscopy (FT-IR; Perkin Elmer, USA), where the powder form of test samples mixed with potassium bromide (KBr) and pressed in the form of pellets. Measurements were taken in transmission mode within the range of wavenumbers 4,000–500 cm^{-1}. X-ray diffraction (XRD; Rigaku MiniFlex-II, Japan) was done by using Cu K-alpha radiation of wavelength ($\lambda = 1.5418$ Å) within the diffraction angle range of $2\theta = 20°$ to 50° at scanning rate of 3° min^{-1} and step size of 0.1°. Raman spectroscopy was performed on LabRAM HR Evolution Instrument (HORIBA, France) in the range of wavenumbers 1000–2000 cm^{-1} using laser excitation wavelength of 532 nm. The morphology of f-GNP was analyzed by field emission scanning electron microscope (FESEM, Apreo LoVac, FEI, USA).
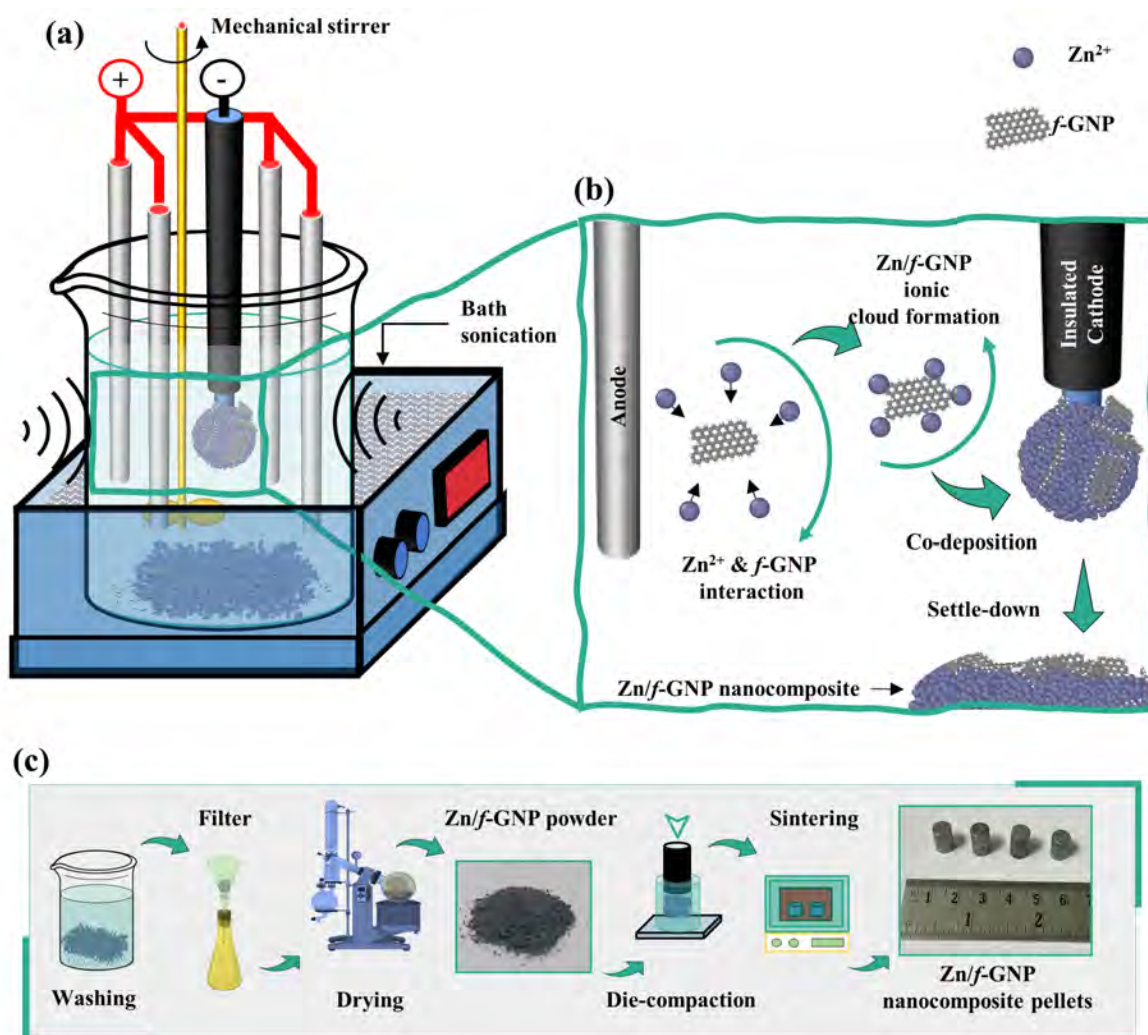
FIGURE 4.1: Schematic representation of synthesis of Zn/f-GNP nanocomposite using M-ECD method followed by powder metallurgy: (a) M-ECD-based experimentation setup with continuous bath sonication, (b) insight view of conjugation of functionalized f-GNP nanofillers with Zn ions and co-deposition as Zn/f-GNP nanocomposite at cathode tip, and (c) washing of collected Zn/f-GNP nanocomposite slurry using DI water, then filtered and vacuum dried using rato-evaporator to recover the dry powdered form of Zn/f-GNP nanocomposites, subsequently, die-compacted and sintered to make solid pellets.

4.4 Result and discussion

4.4.1 Characterization

As-prepared f-GNP nanofillers were characterized before being used as nanofillers in the Zn matrix. Here, the preparation and characterization are schematically shown in Figure 4.3a. From Figure 4.3b, the FT-IR spectra confirmed the successful synthesis of f-GNP nanofillers. The characteristic transmission bands of GNPs were located at $\sim$1750 cm^{-1} (C=O stretching at carboxy group), $\sim$1575 cm^{-1} (C=C stretching), $\sim$3425 cm^{-1} (C–OH stretching) and $\sim$1090 cm^{-1} (C–O of epoxy stretching), respectively [255]. After covalent bonding of PEG functional group,

TABLE 4.1: ECD bath composition, electrode specification and process parameters for Zn/f-GNP nanocomposite powder fabrication

ECD bath composition	
$ZnSO_4.7H_2O$	0.5 M
Ethylenediaminetetraacetic acid (complexing agent)	0.15 M
NaOH(aq)	5 mM
f-GNP concentrations	25, 50, 100 mg/L
Electrode specification	
Electrode material	Platinum (Pt) coated Titanium (Ti) electrode
Electrode diameter (for 4 anodes and 1 cathode tip)	3.5 mm
Radial distance from cathode to anodes	30 mm
Experimental parameters	
pH of ECD bath	8
Magnetic stirring	250 rpm
Bath sonication	20 kHz, 500 W
Bath temperature	35°C
DC current supply	4 A
Pre-process time (for sonication and stirring)	1 hour
Co-deposition time	3 hours
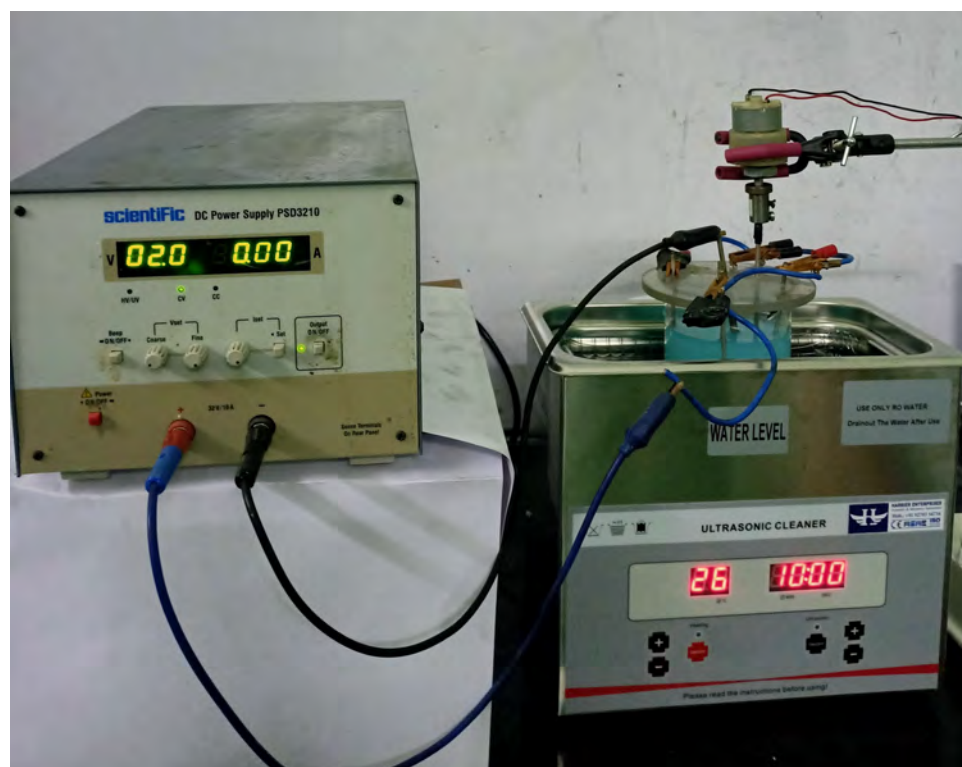
FIGURE 4.2: Experimetal setup for modified electro-co-deposition method.

the resulting f-GNP nanofillers exhibited obvious C–O ($\sim$1090 cm^{-1}) and C–H ($\sim$2910 cm^{-1}) stretching vibrations [256]. Also, the peak at $\sim$1635 cm^{-1} (C=C) indicated the – aromatic rings, which could provide loading sites for Zn ions attachments on f-GNPs during co-deposition process [257].
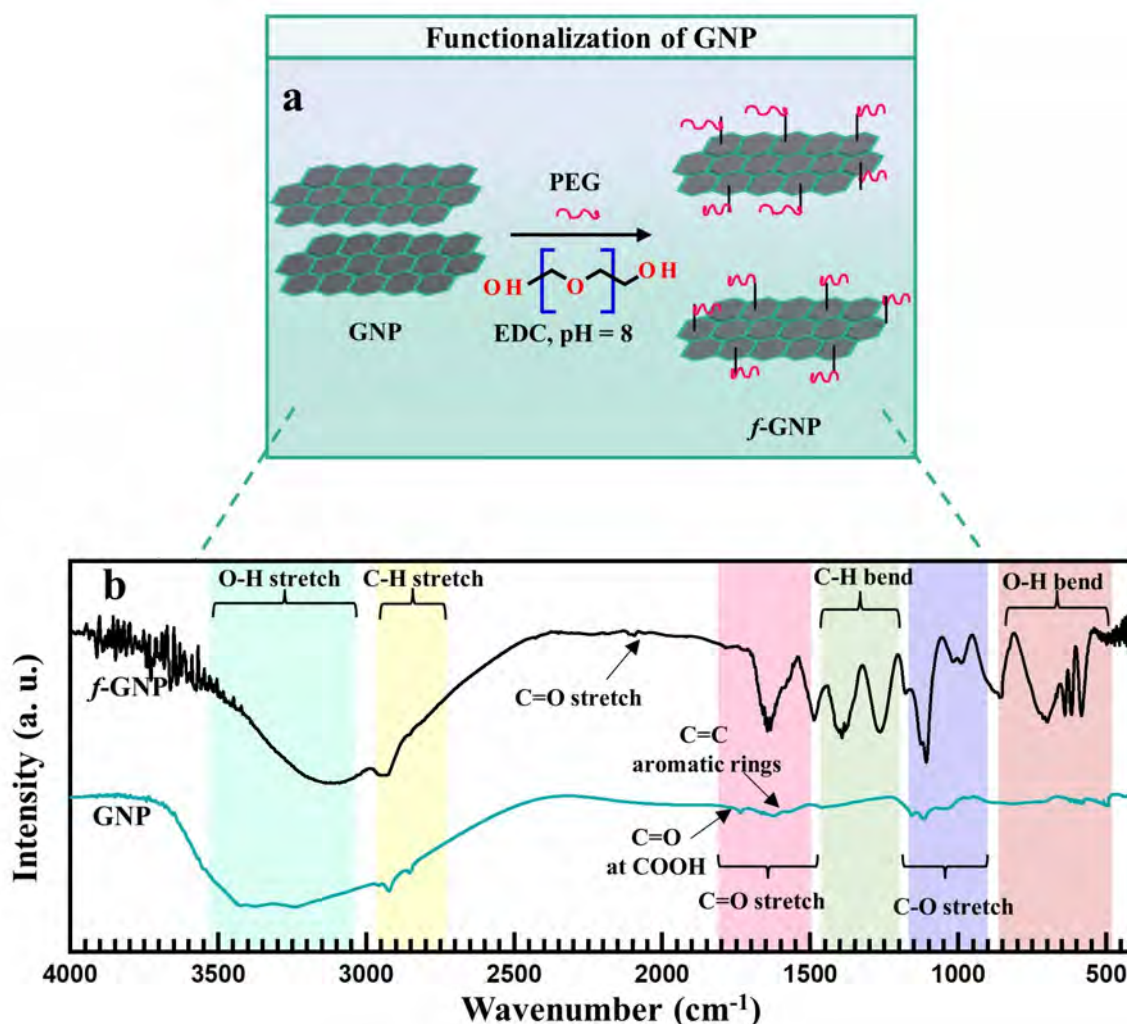
FIGURE 4.3: Preparation and characterization of f-GNP nanofillers: (a) Schematic representation functionalization of pristine GNP using sulphate bath treatment at pH = 4, (b) FT-IR spectra, where the characteristic transmission bands in FT-IR spectra at around 3445, 2923, 1590, 1024 cm^{-1} are attributed to O–H, C–H, C=C and O=S=O attachments, respectively.

In the XRD patterns for GNP powder, the crystal planes were evident at (0 0 2) and (1 0 0), which is typical for graphene [258], whereas XRD patterns for as-prepared f-GNP nanofillers also shown the crystallographic planes for PEG 6000 at (1 2 0), (1 1 1), and (2 0 0) [259], as depicted in Figure 4.4a. Raman spectroscopy was used to characterize pristine GNPs and f-GNP nanofillers (see Figure 4.4b). Typical features of GNPs in Raman spectra included the G band at 1585 cm^{-1} and the D band at 1328 cm^{-1}. The G band assigned to the E$_2g$ phonon of sp^2-hybridized carbon atoms, while the prominent D band related to the breathing mode of

k-point phonons of A1g symmetry that arise owing to local defects and disorder, an indication of disorder associated with vacancies, and amorphous carbon species, particularly at the edge of GNPs [257]. Intensity ratio, $I_{(D/G)}$ of D band to G band of GNPs and f-GNPs were about 1.18 and 1.12, respectively, as shown in Figure 4.4b. The $I_{(D/G)}$ value of GNPs was almost same after the functionalization, suggesting the defect density in the graphene crystals has not changed significantly. Figure 4.4c shows FESEM micrographs of f-GNPs where the de-agglomeration of nanosheets was confirmed. During co-deposition, these de-agglomerated f-GNP nanofillers can easily conjugate with Zn ions to form Zn/f-GNP ionic cloud, that co-deposited at cathode tip as Zn/f-GNP nanocomposite powder.
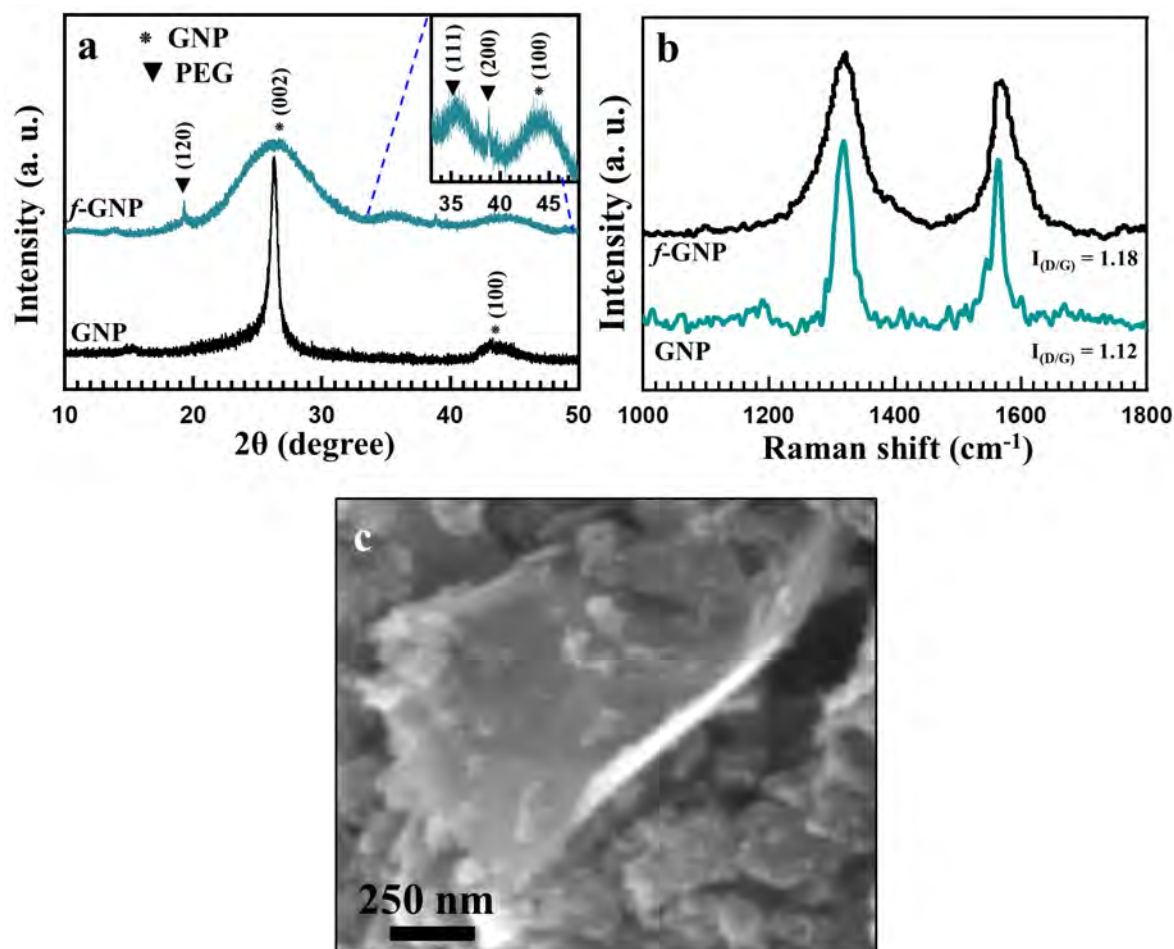
FIGURE 4.4: Preparation and characterization of f-GNP nanofillers: (a)XRD spectrum, where diffraction peaks at 2 = 26.48 and 43.63 could be attributed to (0 0 2) and (1 0 0) crystal planes of GNPs, respectively, (b) Raman spectra, insert shows the $I_{(D/G)}$ ratios for pristine GNP and f-GNP, and (c) FESEM image of as-prepared f-GNP power sample.

The vacuum-dried co-deposited Zn/f-GNP nanocomposite powder samples were characterized for microstructure, attached functional groups, crystal defects, crystallite size and surface morphology to confirm the desired and successful uniform growth of Zn matrix across f-GNP nanofillers during M-ECD process. TEM analysis of Zn/f-GNP nanocomposite powder sample prepared with 100

mg/L of concentration of f-GNP in the ECD bath is presented in Figure 4.5a-d. Figure 4.5(a) shows TEM image of the Zn/f-GNP cluster deposit. It can be seen that, the hexagonal growth of Zn deposits on the surface of f-GNP was achieved during M-ECD process. These Zn deposits were uniformly distributed and nanocrystalline across the Zn/f-GNP cluster and formed new nucleation sites for co-deposition.

Figure 4.5b shows the high-resolution TEM image of Zn matrix, where the estimated interplanar d-spacing of adjacent lattice fringes were 0.261 nm corresponds to (1 0 1) crystallographic plane of Zn [260]. The hexagonal Zn growth on the Zn/f-GNP cluster has average crystallite size of 25.6 nm, as represented in the size distribution chart in Figure 4.5c. Figure 4.5d shows the selected area electron diffraction (SAED) spectra of the Zn/f-GNP cluster deposit, that represents lattice diffractions at (0 0 2), (1 0 0), (1 0 1), (1 0 2), (1 0 3), (1 1 0), and (0 0 4) crystallographic planes of hexagonal close-packed (hcp) Zn matrix. Hence, the TEM analysis confirmed the nanocrystalline hcp growth of Zn matrix across f-GNP nanofillers during M-ECD process.

From FT-IR spectra shown in Figure 4.6a, the characteristic transmission peeks for Zn matrix attachment to f-GNP were established by bands at 479 cm^{-1} (assigned to Zn–O–C attachments). The characteristic transmission bands of f-GNP at 1156 cm^{-1} and 1681 cm^{-1} were assigned to C–O stretching vibrations and C=O stretching of -COOH groups, respectively, and the weak absorptions at 1397 cm^{-1} and 3092 cm^{-1} were due to C–H bending and stretching. The structural changes in f-GNPs after reinforcement in Zn matrix nanofillers was analyzed by using Raman spectra. Raman spectra of prepared nanocomposite powder samples are presented in Figure 4.6b. The characteristic G and D bands were recorded at around 1583 cm^{-1} and 1350 cm^{-1}, corresponding to the sp^2 bonded carbon atoms and defects/disorders in f-GNP nanofillers, respectively [261] (see Figure 4.4b). Whereas, no such bands were recorded for pure Zn powder due absence of f-GNP nanofillers. The D and G bands in the Raman spectrum of GNPs refer to the defect-induced and GNP's in-plane vibrational modes, respectively. The D band is caused by defects such as lattice distortions, edges, impurities, and other structural imperfections, while the G band is associated with the carbon-carbon bonding in the GNP 2D lattice. In highly intact GNPs, the D band is relatively weaker because the number of defects and structural imperfections decreases, and the G band is stronger because of the in-plane vibrational modes. This results in a lower D/G ratio, which is a commonly used parameter to quantify the quality and structural homogeneity of GNPs. The peak intensity $I_{(D/G)}$ ratio, decreased from 1.32 to 1.03 on increasing the f-GNP nanofillers concentration in the ECD bath from 25 mg/L to 200 mg/L, respectively, which could be associate with the increased defect density in non-sp^2 domains at higher concentration of f-GNP nanofillers. Compared with Zn/f-GNP (25 mg/L) nanocomposite, Zn/f-GNP (50 and 100 mg/L) nanocomposite bands was slightly shifted toward higher values. These shifts in the Raman peak were attributed to the increased chemical interaction between Zn ions and f-GNPs at higher concentration of f-GNP nanofillers in the ECD bath [262].

XRD diffraction measurements were performed to determine whether the addition of f-GNP
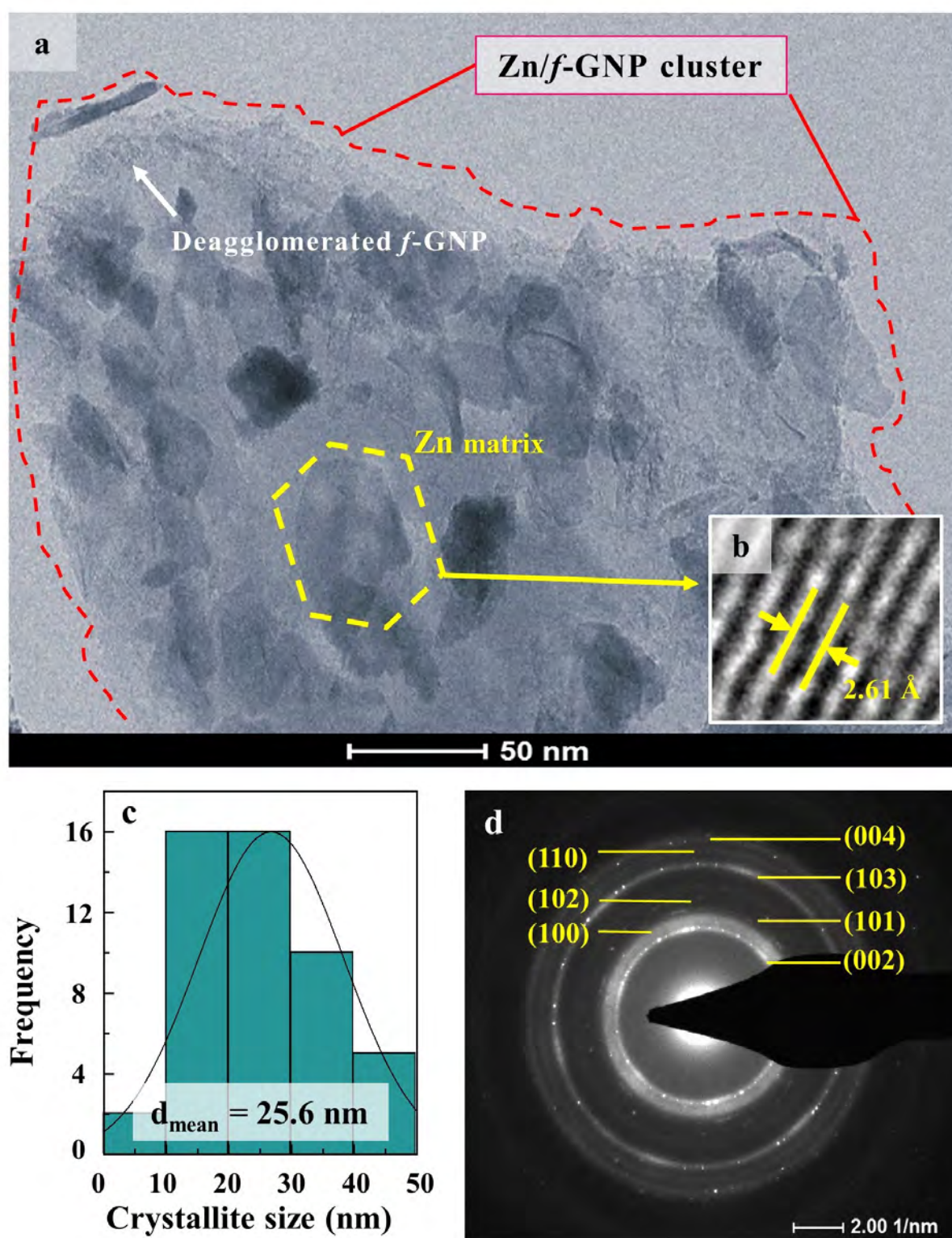
FIGURE 4.5: Characterization of prepared Zn/f-GNP nanocomposite powder: (a-d) TEM analysis of Zn/f-GNP nanocomposite powder sample prepared with 100 mg/L concentration of f-GNP nanofillers in the ECD bath: (a) Low-resolution TEM image showing the Zn/f-GNP cluster incorporating hexagonal zinc crystallographic growths, (b) insert showing a lattice fringe with d-spacing of 2.61 Å at Zn (0 0 2) crystal plane, (c) crystallite size distribution of hexagonal Zn matrix growth at different nucleation sites on Zn/f-GNP cluster, and (d) SAED spectra of Zn/f-GNP nanocomposite, where the diffraction patterns correspond to Zn matrix are visible at (0 0 2), (1 0 0), (1 0 1), (1 0 2), (1 0 3), (1 1 0), and (0 0 4) crystal planes.

TABLE 4.2: Crystallite size and carbon content of pure Zn and Zn/f-GNP nanocomposite samples.

Sample	Crystallite size (nm)	Carbon content (wt%)
Pure Zn	56.4 ± 4.1	-
Zn/f-GNP (25 mg/L)	43.6 ± 1.1	1.1 ± 0.2
Zn/f-GNP (50 mg/L)	35.2 ± 1.5	2.8 ± 0.5
Zn/f-GNP (100 mg/L)	28.6 ± 2.3	5.2 ± 1.5
Zn/f-GNP (200 mg/L)	24.7 ± 0.6	7.6 ± 2.2

nanofillers affects the hcp crystalline structure of Zn/f-GNP nanocomposite, as shown in Figure 4.6c. The XRD patterns revealed that the diffraction peaks of all prepared samples corresponded to (0 0 2), (1 0 0), (1 0 1), (1 0 2), (1 0 3), (1 1 0), and (0 0 4) crystal planes, which accordance with the hcp Zn matrix (JCPDS card no. 004-0831) [263] and also supports the observations obtained from TEM analysis (refer Figure 4.5d). It was clearly seen that the broadening of XRD peaks' occurred with decreased intensities on increasing the f-GNPs concentration, which signifies the refinement of the crystallite size and inducing microscale-stresses with lattice defects in the crystallography of deposits of Zn matrix.

The crystallite size, D (in nm) was determined using the Scherrer equation 3.1. The average crystallite size of deposits of prepared nanocomposite samples was decreased by 49.28% from 56.4 nm for pure Zn to 28.6 nm for Zn/f-GNP (100 mg/L) nanocomposite (see Table 4.2). The XRD study revealed that f-GNP content in the ECD bath influenced the crystallography and decreased the crystallite size of deposits of Zn/f-GNP nanocomposite.

The modifications in the surface micrograph of Zn/f-GNP nanocomposite due to increase in concentrations of f-GNP in the ECD bath are shown in Figure 4.7a–d. After addition of f-GNP in the ECD bath, the orderly oriented hexagonal crystallite growth of pure Zn deposits (Figure 4.7a) turned into underdeveloped crystals of Zn deposits for Zn/f-GNP (25 and 50 mg/L) nanocomposite sample (Figure 4.7b-c) and the changes in crystallography can be clearly observed at the edges of Zn growth. However, the deposits of Zn/f-GNP (100 mg/L) nanocomposite have no clear hexagonal crystallographic growth but increased nucleation site of decreased crystallite sizes with disordered orientations. These results revealed the relation between nucleation and crystallographic growth of Zn deposits in the presence of impermeable f-GNP in the ECD bath. EDS elemental distribution mapping and spectrum study of pure Zn and Zn/f-GNP nanocomposites samples are presented in Figure 4.7e–h. From Figure 4.7e–h, it can be observed that C content were well-dispersed across the elemental distribution maps of Zn/f-GNP nanocomposites, which confirmed the uniform reinforcement of f-GNP nanofillers into the Zn matrix. The increased f-GNP concentration in the ECD bath from 25 mg/L to 100 mg/L, increased the chances of incorporating f-GNP into the Zn matrix during the co-deposition process; thus, an increase in C content from 1.1% to 3.2% (see Table 4.2) was observed in the EDS mapping. This f-GNP content provides large number of active sites for new attachments and nucleation of Zn deposits during co-deposition and due to presence of more number reduces of nuclei the chances of crystal
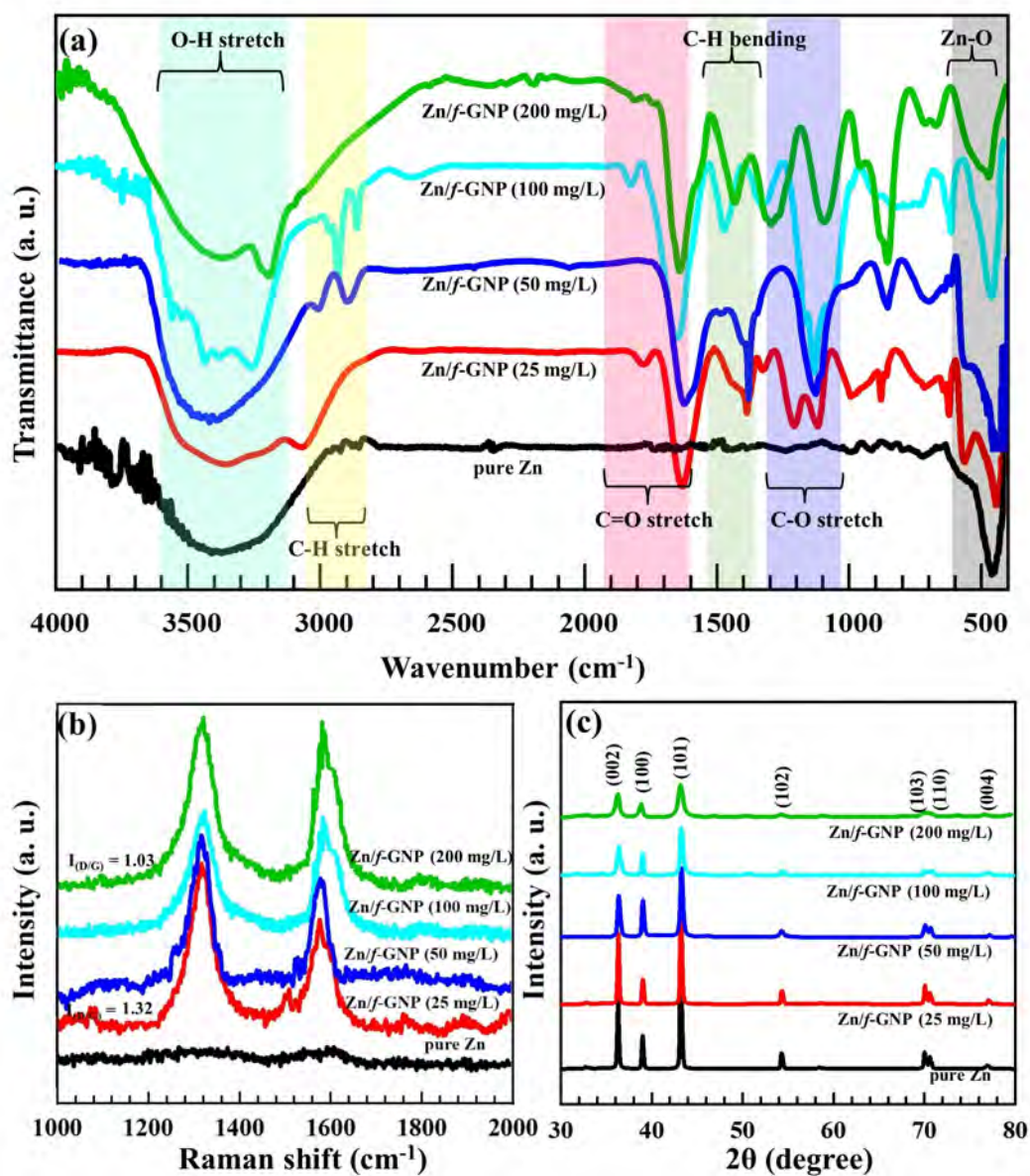
FIGURE 4.6: Characterization of prepared Zn/f-GNP nanocomposite powder (a) FT-IR spectra, (b) Raman spectra and (c) XRD spectrum of prepared pure Zn and Zn/f-GNP nanocomposite samples, here, the diffraction peaks in XRD spectrums matched well with hcp peaks of Zn Matrix in accordance with JCPDS Card No. 004-0831.
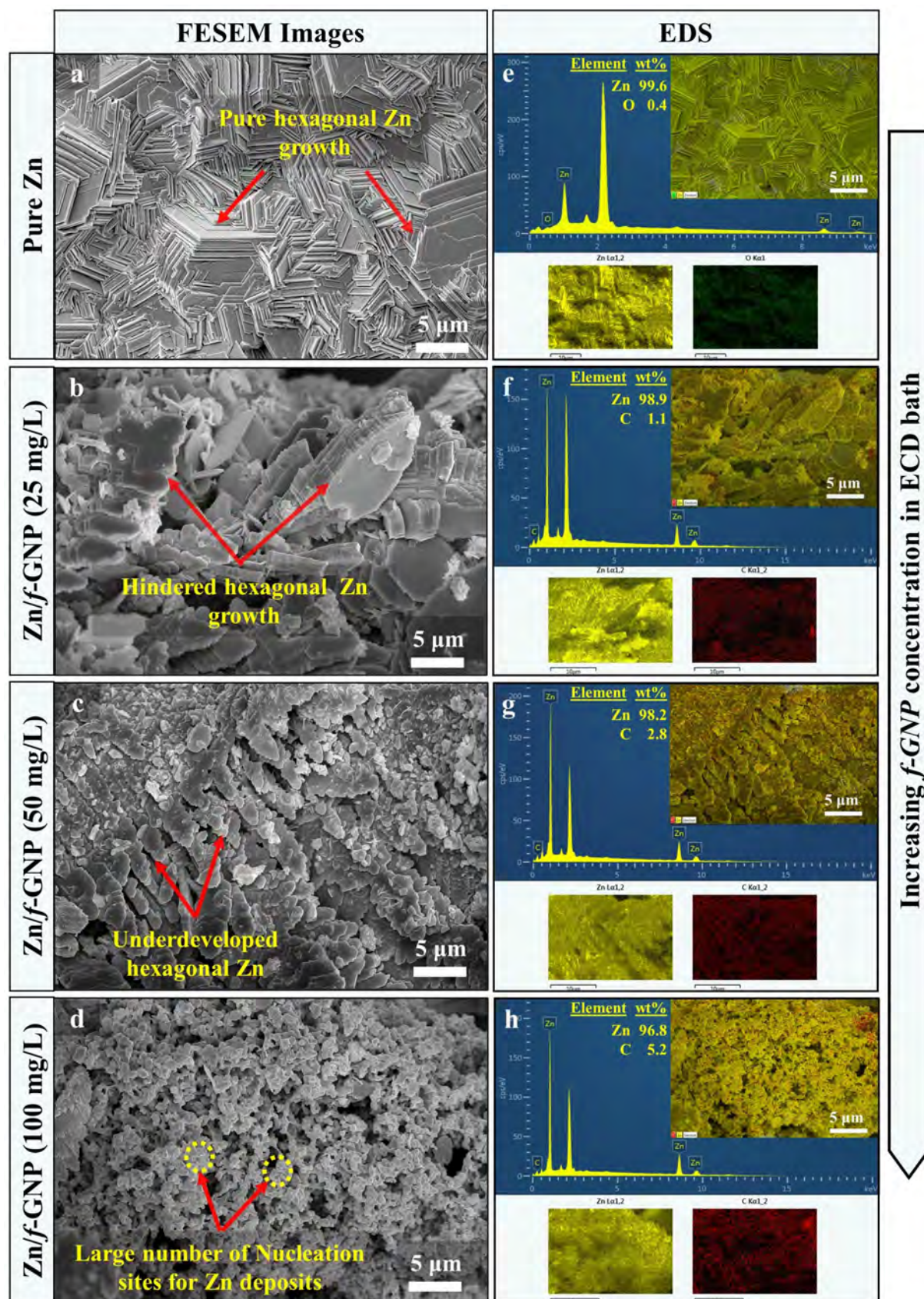
FIGURE 4.7: (a-d) FESEM images and (e-h) EDS analysis of pure Zn and Zn/f-GNP nanocomposites with increasing concentration of f-GNP in the ECD bath. Insert of EDS spectrum shows elemental compositions and distribution map for Zn (yellow), C (red) and O (green) content.

growth decreases and hence reduces the average crystallite sizes.

4.4.2 Degradation behavior

4.4.2.1 Immersion behavior

The immersion test in SBF solution was performed for 56 days at 37 ± 0.5 °C in order to examine degradation behavior and the results are represented in Figure 4.8a. As shown in the results, the sample group of pure Zn pellets exhibited a rapid rise in corrosion rate in immersion test (CR_{WL}) values, which were consistently higher than the nanocomposite sample groups with the value of $87.2 \pm 4.3 \times 10^{-3}$ mm/year after completion of 56 days. Whereas the Zn/f-GNP (100 mg/L) nanocomposite sample group showed average CR_{WL} values of $26 \pm 0.8 \times 10^{-3}$ mm/year, which was 70.18% lower than pure Zn. The samples prepared with 25 and 50 mg/L of f-GNP concentration in ECD bath have exhibited intermediate CR_{WL} of values $43.6 \pm 4.7 \times 10^{-3}$ mm/year and $29.1 \pm 2.8 \times 10^{-3}$ mm/year, respectively. The higher CR_{WL} values in pure Zn was attributed to the alkali corrosion reactions caused by the OH^- anions in the SBF solution and oxidized the Zn matrix to Zn^{2+} (Equation 4.1). The electrons at the anode participate in cathodic reaction with oxygen to produce hydroxide (Equation 4.2) and forming degradation products, such as hydroxide, (Equation 4.3). This rapid corrosion rate of pellets of pure Zn resulted from high hydroxide content may lead to an alkaline poisoning effect after implantation in human body [264].

Anodic reaction:

$$Zn \rightarrow Zn^{2+} + 2e^- \tag{4.1}$$

Cathodic reaction:

$$O_2 + H_2O + 4e^- \rightarrow 4OH^- \tag{4.2}$$

By product:

$$Zn^{2+} + 4OH^- \rightarrow Zn(OH)_2 \tag{4.3}$$

4.4.2.2 Electrochemical corrosion behavior

The electrochemical measurement method for potentiodynamic polarization curves was used to evaluate the degradation of the prepared nanocomposite samples in SBF, and the results are represented in Figure 4.9a. The corrosion current density (I_{corr}), corrosion potential (E_{corr}) and Tafel slopes (β_a, anodic and β_c, cathodic) were measured by the Tafel extrapolation method. The corrosion protection efficiency ($\eta_{corr}\%$) after reinforcing with f-GNP was calculated by using the values of the I_{corr}, as in the following equation:

$$\eta_{corr}(\%) = \frac{I_{corr(Zn)} - I_{corr}}{I_{corr(Zn)}} \times 100. \tag{4.4}$$
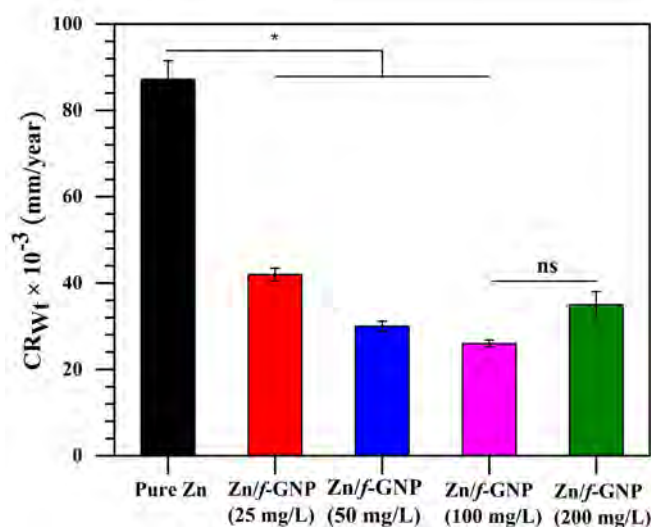
FIGURE 4.8: Corrosion rate pure Zn and Zn/f-GNP nanocomposite samples after immersion of 56 days in SBF solution. *P $<$ 0.05 by one-way ANOVA with Tukey's post hoc test.

TABLE 4.3: Obtained electrochemical parameters for prepared nanocomposites.

Sample	$I_{\mathbf{corr}}$ (μA cm^{-2})	β_a (mV decade^{-1})	β_c (mV decade^{-1})	η_{corr}%
pure Zn	4.215 ± 1.52	67.1 ± 5.1	172 ± 11.2	0
Zn/f-GNP (25 mg/L)	3.348 ± 0.84	76 ± 4.7	201.9 ± 15.4	20.5
Zn/f-GNP (50 mg/L)	2.323 ± 0.21	64.5 ± 3.3	125.8 ± 9.3	44.8
Zn/f-GNP (100 mg/L)	0.675 ± 0.05	32.7 ± 1.0	76.1 ± 4.1	83.9
Zn/f-GNP (200 mg/L)	0.591 ± 0.35	51.7 ± 4.6	88.9 ± 3.7	85.9

where $I_{corr(Zn)}$ is the corrosion current densities for the pure Zn. The calculated electrochemical parameters are shown in Table 4.3. Compared with pure Zn, the polarization curve of the Zn/f-GNP nanocomposites had obvious characteristics, as found in immersion test. The nanocomposite samples with 100 mg/L of f-GNP concentration in ECD bath exhibit the highest corrosion protection efficiency of 83.91% with decrease in electrochemical corrosion rate (CR$_{EC}$) values from 130.4×10^{-3} mm/year for pure Zn to 21×10^{-3} mm/year for Zn/f-GNP (100 mg/L) nanocomposite sample (refer Table 4.3 and Figure 4.9c). This may be attributed to the presence of impermeable f-GNP across Zn matrix towards corrosion protection [265]. Consequently, f-GNP de-accelerated the electrochemical interaction, thereby, the corrosion of Zn matrix in SBF solution.

The corrosion resistance performances during immersion and electrochemical tests of pure Zn were inadequate because of easy release of Zn^{2+} and OH$^-$ in the SBF solution. Whereas those were enhanced for Zn/f-GNP nanocomposites with protective f-GNP-ZnO barriers, as illustrated in Figure 4.10a. These corrosion barriers in prepared nanocomposites have reduced the local degradations by covering the micro-galvanic cells at pores and voids and contributed to controlled uniform degradation. To understand the mechanism of corrosion resistance, the corroded surfaces
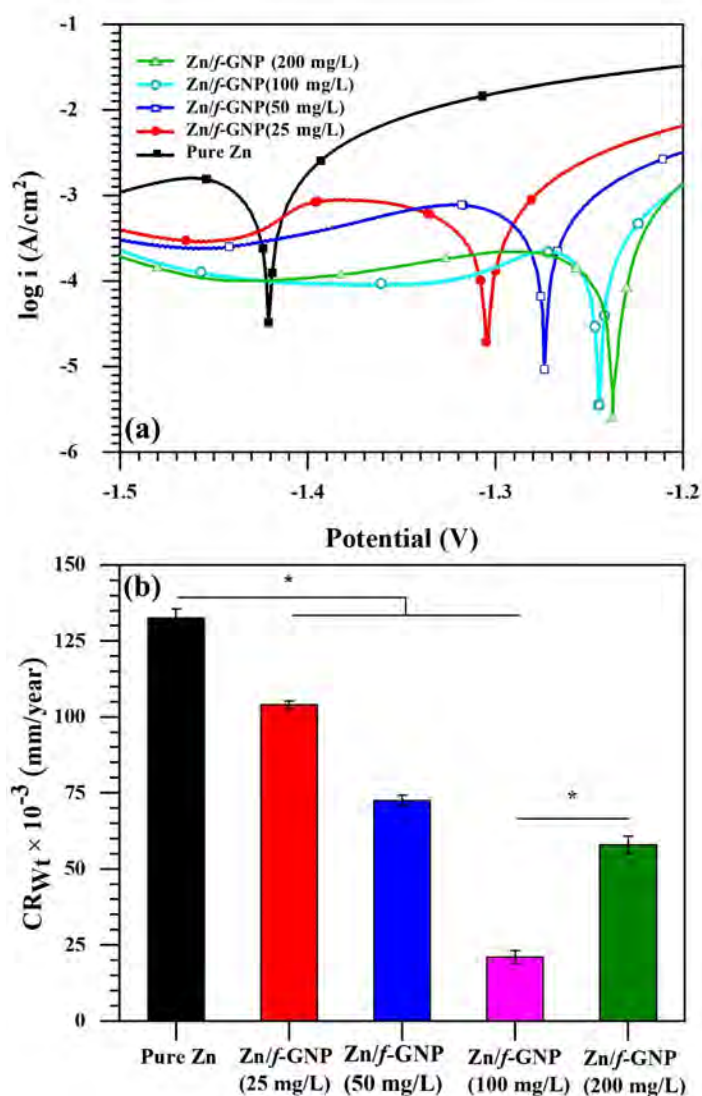
FIGURE 4.9: Electrochemical corrosion behaviour of pure Zn and Zn/f-GNP nanocomposite samples: (a) potentiodynamic polarisation curves and (b) electrochemical corrosion rate. *P < 0.05 by one-way ANOVA with Tukey's post hoc test.

of nanocomposites were further characterized using FESEM, XRD and EDS.

Figure 4.10b-e illustrates the FESEM images of the surface micrograph of corroded Zn/f-GNP nanocomposite sample groups after immersion in SBF solution for 56 days. For pure Zn sample, the large size pores and voids can clearly be observed on the surface (see Figure 4.10b). These pores and voids in pure Zn hindered the mechanical integrity of pellets, that causing weight loss while cleaning for weight measurement. Whereas nanocomposites of 25 and 50 mg/L of f-GNP concentration in the ECD bath, the surfaces depict decreased numbers of the pits and voids formation with reduced sizes, which confirmed enhancement the anti-corrosion performance and mechanical integrity of nanocomposites (see Figure 4.10c-d). For further increase in f-GNP concentration in ECD bath up to 100 mg/L, the nanocomposite shows very few, and small
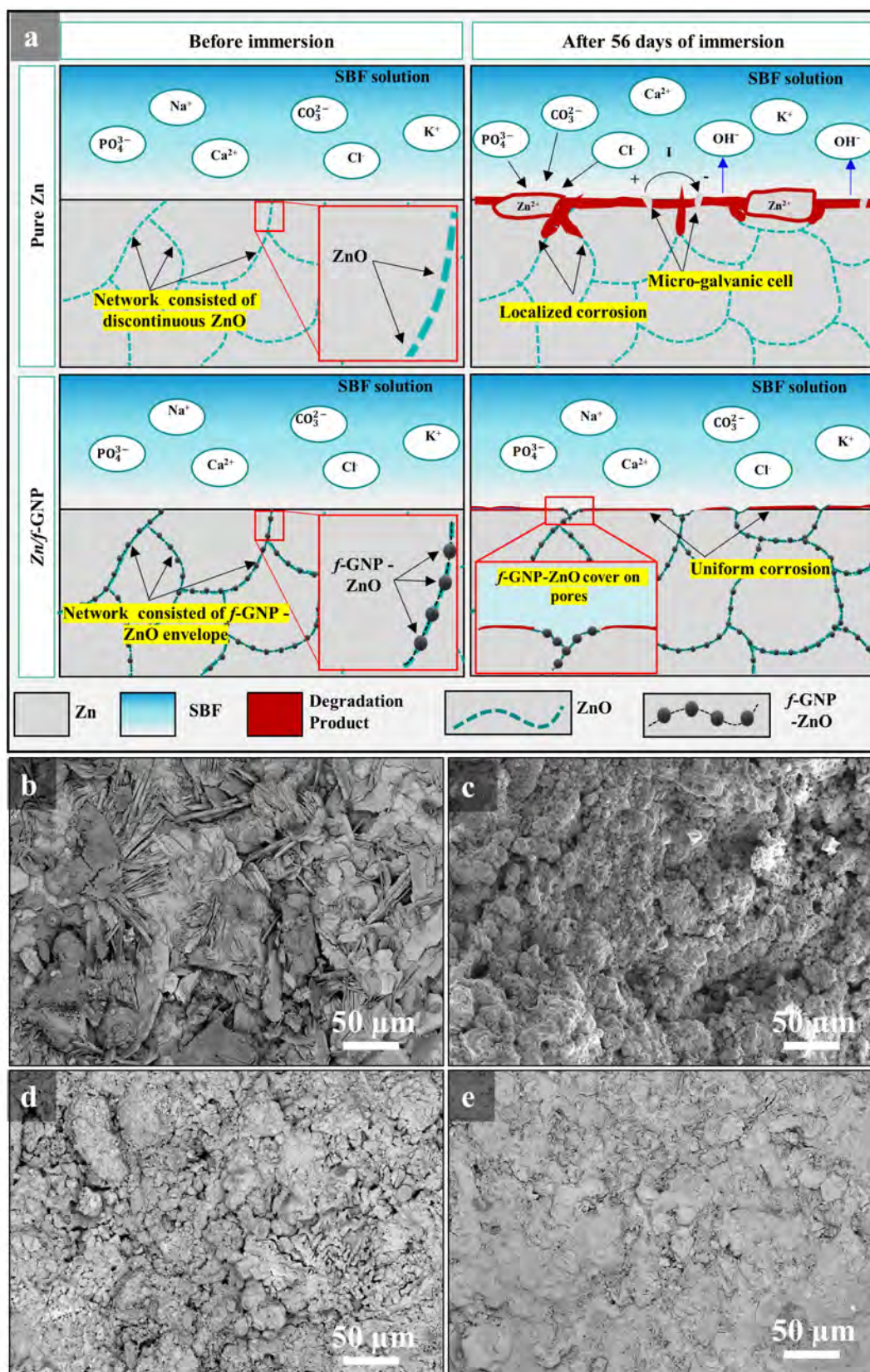
FIGURE 4.10: (a)Illustration of mechanism of corrosion on the surface of pure Zn and Zn/f-GNP nanocomposite for before and after 56 days of immersion in corrosive environment of SBF solution. (b-e) FESEM imaging for surface morphology of corroded surfaces of (c) pure Zn and Zn/f-GNP nanocomposites of (f) 25 mg/L, (d) 50 mg/L, and (e) 100 mg/L of f-GNP concentrations after immersion.

pits and voids (see Figure 4.10e). Figure 4.11 shows the XRD diffraction pattern of pure Zn and Zn/f-GNP nanocomposite samples after immersion in SBF solution for 56 days. Along with the XRD peaks corresponding to Zn, the peaks of ZnO, $Zn(OH)_2$, and $Zn_5(OH)_8Cl_2H_2O$ (simonkolleite) confirmed the formation of corrosion products on the surfaces of samples [266], [267].
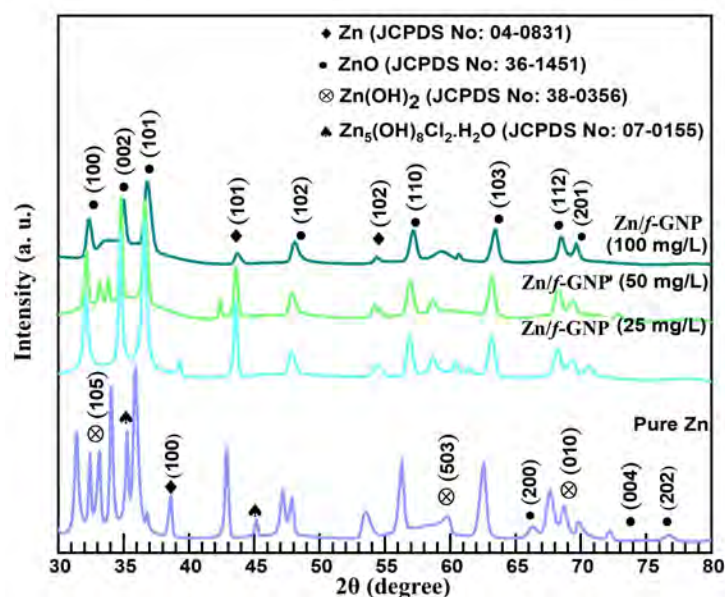
FIGURE 4.11: XRD pattern of pure Zn and Zn/f-GNP nanocomposite samples after immersion; here, the diffraction peaks in XRD spectrums matched well for Zn, ZnO, $Zn(OH)_2$, and $Zn_5(OH)_8Cl_2H_2O$ in accordance with JCPDS Card No. 004-0831, 36-145, 38-0356, and 07-0155, respectively.

From Figure 4.12, EDS analysis of corroded surface of Zn/f-GNP (100 mg/L) nanocomposite sample has confirmed the comparative large C and O content of f-GNP-ZnO barrier, which was impermeable for other corrosive contents of SBF solution. The f-GNP-ZnO barrier has protected the exposed surface from corrosion attacks and reduced the accumulation of corrosion products on the surfaces. Thus, XRD peak intensities for corrosion product were found shortened for nanocomposite samples on increasing the f-GNP content in nanocomposite samples (see Figure 4.11). Overall, this investigation revealed that, the protective barrier of Zn/f-GNP nanocomposites decreased the rate of corrosion, provided uniform and tunable degradation, and allowed the nanocomposite to retain its mechanical integrity for longer by avoiding large pits and voids on the surface.

4.4.3 Tribo-mechanical behavior

Pure Zn, in general, has weak tribo-mechanical characteristics and would fail to fulfil the requirements for bioimplant applications [16]. In this study, the effect of f-GNP reinforcement in a Zn matrix was explored for tribo-mechanical testing, as represented in Figure 4.13-4.15.
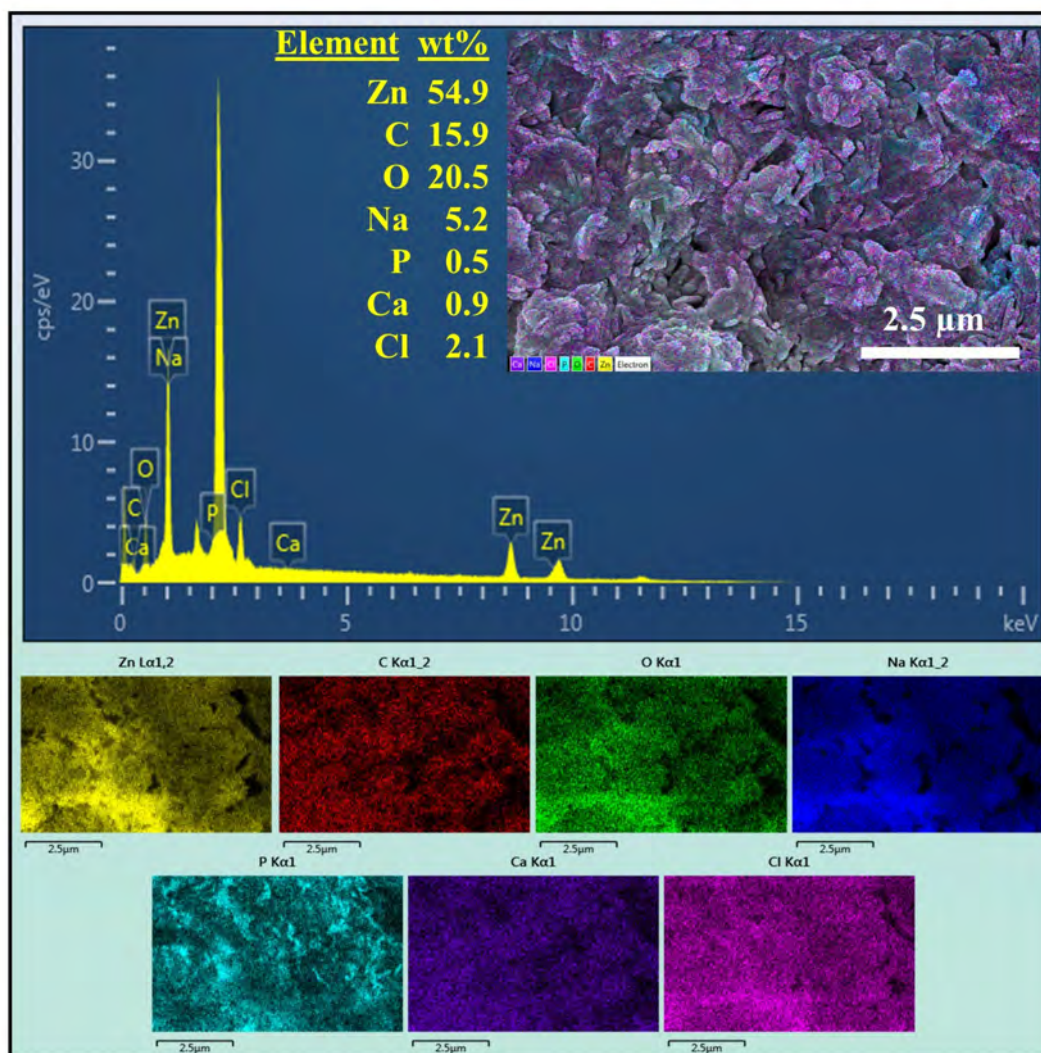
FIGURE 4.12: EDS analysis of Zn/f-GNP (100 mg/L) nanocomposite sample with after immersion of 56 days. Insert of EDS spectrum shows elemental compositions and distribution map for Zn (yellow), C (red), O (green), Na (blue), P (cyan), Ca (purple), and Cl (magenta) content. *$P < 0.05$ by one-way ANOVA with Tukey's post hoc test.

4.4.3.1 Mechanical behavior

Vickers microhardness was measured under constant load condition at room temperature. Figure 4.13a shows the measured microhardness for sintered pellet samples of pure Zn and Zn/f-GNP nanocomposites. With a measured average microhardness value of 57 ± 1.3 HV, it is obvious that pure Zn has a low resistance to plastic deformation, but after adding f-GNP, the microhardness was increased significantly by 88.97% to 108.5 ± 2.1 HV for Zn/f-GNP (100 mg/L) nanocomposite. The inclusion of f-GNP content in the Zn matrix reduced the crystallite size (see Table 4.2), that induced a grain-strengthening effect and obstructed the dislocation movement and interfaces in the nanocomposite [268]. The plane-like structure and superior shear strength of the f-GNP layers across the Zn/f-GNP nanocomposite clusters also acted as a resistive barrier

to dislocation movement at the nanocomposite interface, increasing the average microhardness even further [173]. Figure 4.13b shows compression test results for prepared specimens of sintered pure Zn and nanocomposite samples. Pure Zn samples exhibits lowest average compressive yield strength (CYS), ultimate compression strength (UCS) and compressive strain (ε_c) of 97.5 ± 10.8 MPa, 163.35 ± 13.6 MPa and 0.28, respectively. The CYS, UCS, and ε_c of Zn/f-GNP nanocomposites were improved significantly by adding reinforcement of f-GNP nanofillers to 182.3 ± 7.9 MPa, 214 ± 9.6 MPa and 0.21 (25 mg/L of f-GNP), 246.5 ± 7.3 MPa, 267.6 ± 13.9 MPa and 0.17 (50 mg/L of f-GNP), 284.9 ± 6.6 MPa, 292.6 ± 11.3 MPa and 0.10 (100 mg/L of f-GNP), respectively. Here, the interfacial bonding between evenly dispersed high strength f-GNP layers and Zn matrix increased the compressive strength of nanocomposites. But, at higher f-GNP concentrations in the ECD bath causing re-agglomeration of f-GNPs due to Van der Waal interactions that imparted lower aspect ratio f-GNP layers in Zn matrix and thus promoted the chance of crack propagation and imparting brittleness. Therefore, ε_c was decreased 59.2% on increasing the concentration of f-GNPs in the ECD bath from 25 mg/L to 100 mg/L. However, the obtained mechanical properties of prepared nanocomposites were in acceptable range, as reported in previous studies for the bio-implant applications [269].
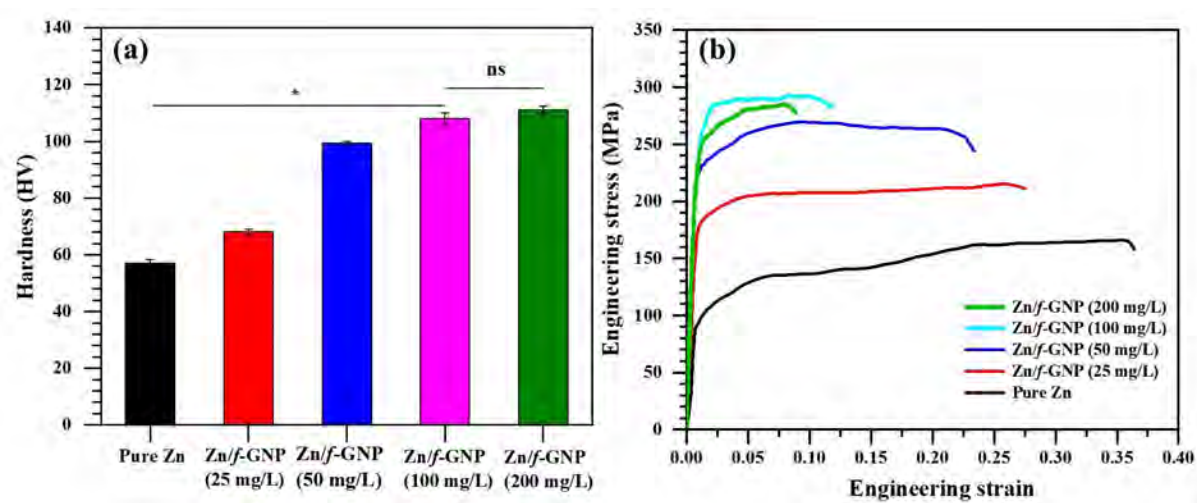
FIGURE 4.13: Mechanical behavior of prepared sintered pellet samples of pure Zn and Zn/f-GNP nanocomposites: (a) microhardness and (b) compression test. *P < 0.05 by one-way ANOVA with Tukey's post hoc test.

4.4.3.2 Tribological behavior

Tribological test results of sintered nanocomposite pellet samples are presented in Figure 4.14-4.15. During the pin on disc experiment, the parameters such as applied pin load, hardness, and diameter of pin and relative speed between pin and disk were set to constant values to record the exact values of friction coefficient and SWR of prepared nanocomposite samples. The obtained friction coefficient graphs for pin-on-disc experiments turned smoother and more stable after

addition of f-GNP content in Zn matrix as observed from Figure 4.14a. The average friction coefficient graph value of 0.74 for pure Zn samples was significantly decreased by 58.1% to 0.31 for Zn/f-GNP (100 mg/L) nanocomposite samples. These results suggest that the incorporated f-GNP nanofillers provide lubricating properties to Zn matrix by reducing direct contact with counter sliding surface. The specific wear rate (SWR) is given by,

$$SWR = \frac{\Delta m}{\rho LD}. \tag{4.5}$$

Where, Δ m is wear loss, ρ is density, L is load applied and D is distance covered. The obtained specific wear rate values are presented in Figure 4.14b, which reveals that the average SWR from the surface of Zn/f-GNP nanocomposite samples was remarkably decreased by 47.36% for loss for Zn/f-GNP (100 mg/L) nanocomposite sample compared to the pure. This improvement in wear performance was attributed to grain-strengthening effect due to decreased crystallite size and increased microhardness of the nanocomposite.
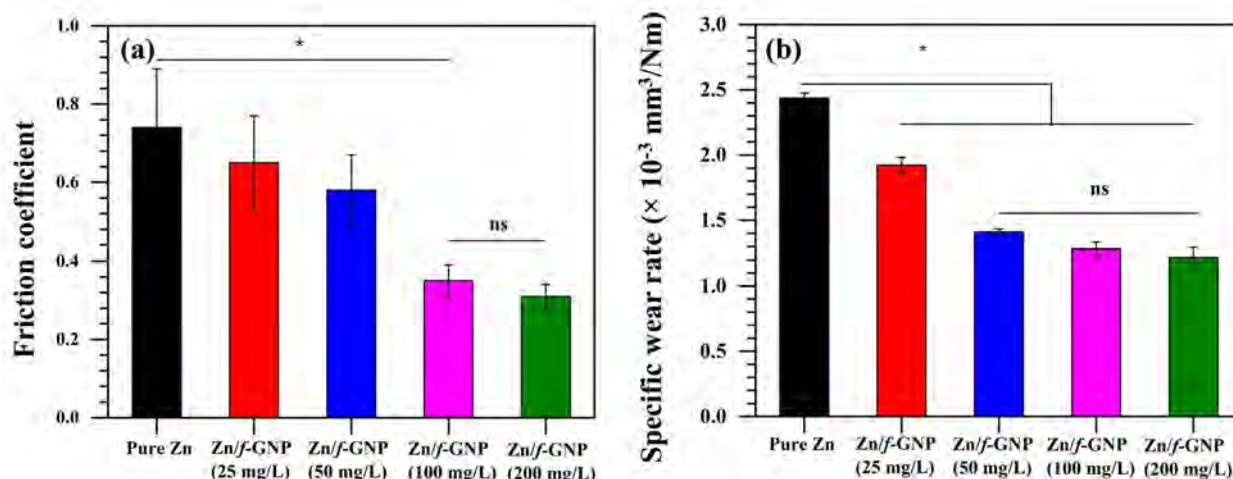
FIGURE 4.14: Tribological behavior of prepared sintered pellet samples of pure Zn and Zn/f-GNP nanocomposites: (a) friction coefficient and (b) Specific wear rate. *P $<$ 0.05 by one-way ANOVA with Tukey's post hoc test.

Figure 6(e-f) shows the FESEM micrographs of the surface of pure Zn and Zn/f-GNP (100 mg/L) nanocomposite samples for analyzing the marked wear tracks during the tribological tests. It was clearly observed that the surface morphology of pure Zn surface appeared rough and more broken as compared to Zn/f-GNP (100 mg/L) nanocomposite. Furthermore, the worn-out surface of pure Zn exhibits evident delamination patches and spots due to its poor surface hardness. As a result, the graph of pure Zn friction coefficients was increasing, with some unusual variations due to newly generated rough delamination areas on the surface (refer Figure 4.14a). The harder surfaces of Zn/f-GNP (100 mg/L) nanocomposite samples showed negligible delamination and their wear products were microscale size debris, as marked in Figure 4.15d, resulting in no abrupt wear losses. The formation of Zn/f-GNPs debris prevented the direct sliding contact between

two surfaces during the pin on disc experiments, as illustrated in Figure 4.15 a and thus, shifting the mechanism from sliding to rolling friction mode.
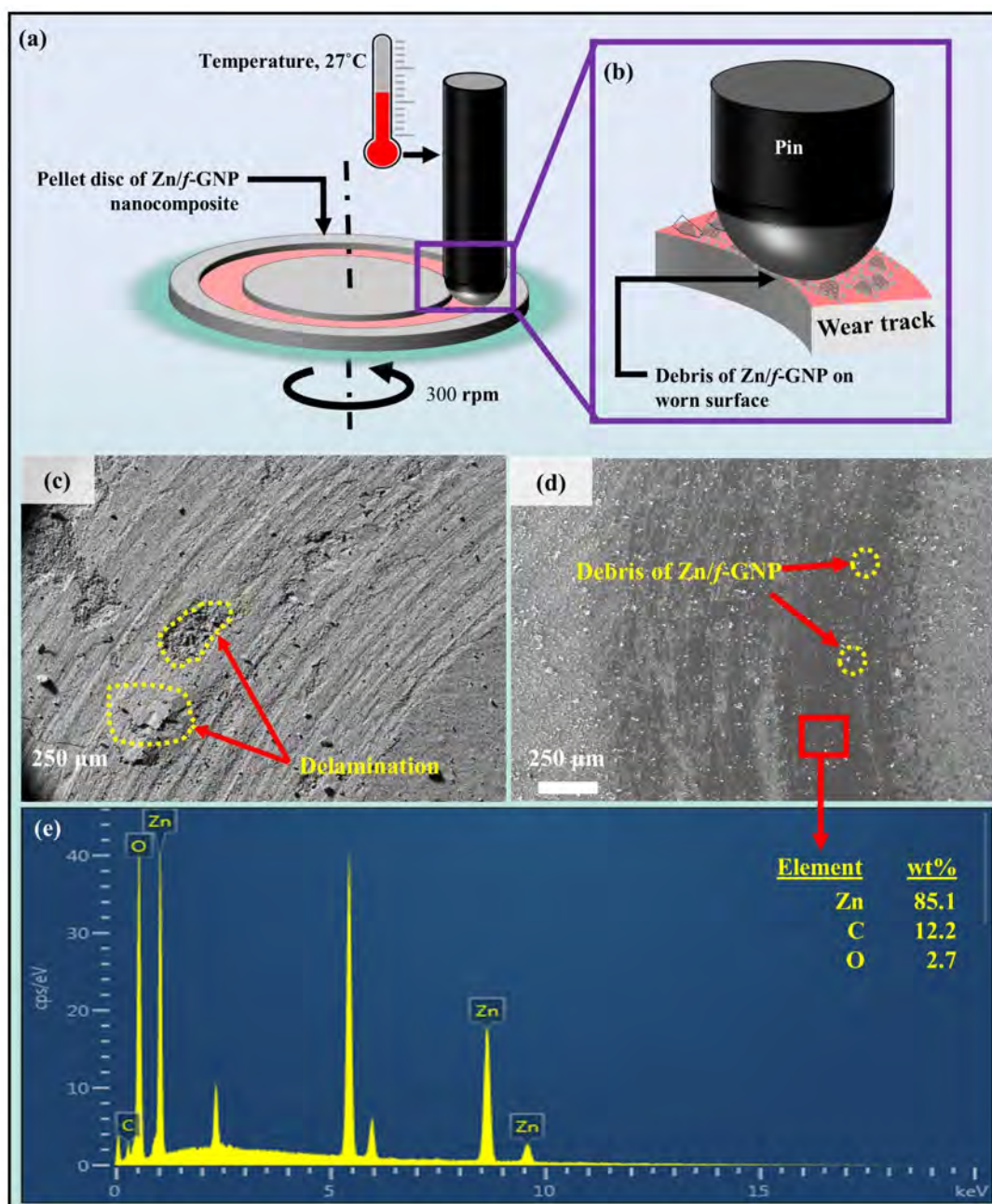
FIGURE 4.15: (a) Illustration of pin on disc setup for tribological tests; insert shows the debris on wear track of Zn/f-GNP nanocomposites, (b-c) FESEM images of marked wear tracks during the tribological tests on (b) pure Zn with and (c) Zn/f-GNP (100 mg/L) nanocomposite; here, delamination and debris formation are marked in yellow circles, and (e) EDS spectrum for elemental composition on wear track of Zn/f-GNP (100 mg/L) nanocomposites.

Moreover, the EDS spectrum for elemental composition of worn surface of Zn/f-GNP (100 mg/L) nanocomposite showed the presence of f-GNP nanofillers in squeezed out debris (see Figure 4.15e) and, thus provided solid graphitic lubrication to further reduce the friction coefficient. Hence,

the reinforcement of f-GNPs using M-ECD method was found a promising approach to enhance the tribo-mechanical performance of Zn/f-GNP nanocomposite.

4.4.4 Cytotoxicity behavior

The cytotoxicity of GNP-based nanocomposites depends on the complex bio–nano interfaces between nanocomposites and contacting biological environment due to its physicochemical characteristics like shape, size, composition, and exposure times. Therefore, to understand the possible cytotoxicity due to prepared nanocomposites, we tested for their cell viability responses. In this work, HaCaT cells were first treated with pristine GNPs and f-GNPs (20 μg ml^{-1}) for 72 hours of cell culture, and then the cell viability was measured via microplate spectrophotometer, as represented in Figure 4.16. It was found that f-GNP had significantly high viability compared to pristine GNPs, which confirmed that the PEG grafted GNPs were reducing the dead cell percentage during the cell culture compare to pristine GNPs. These results are consistent with results of available comparative studies on pristine GNPs and PEG grafted GNPs [229], [270], [271].
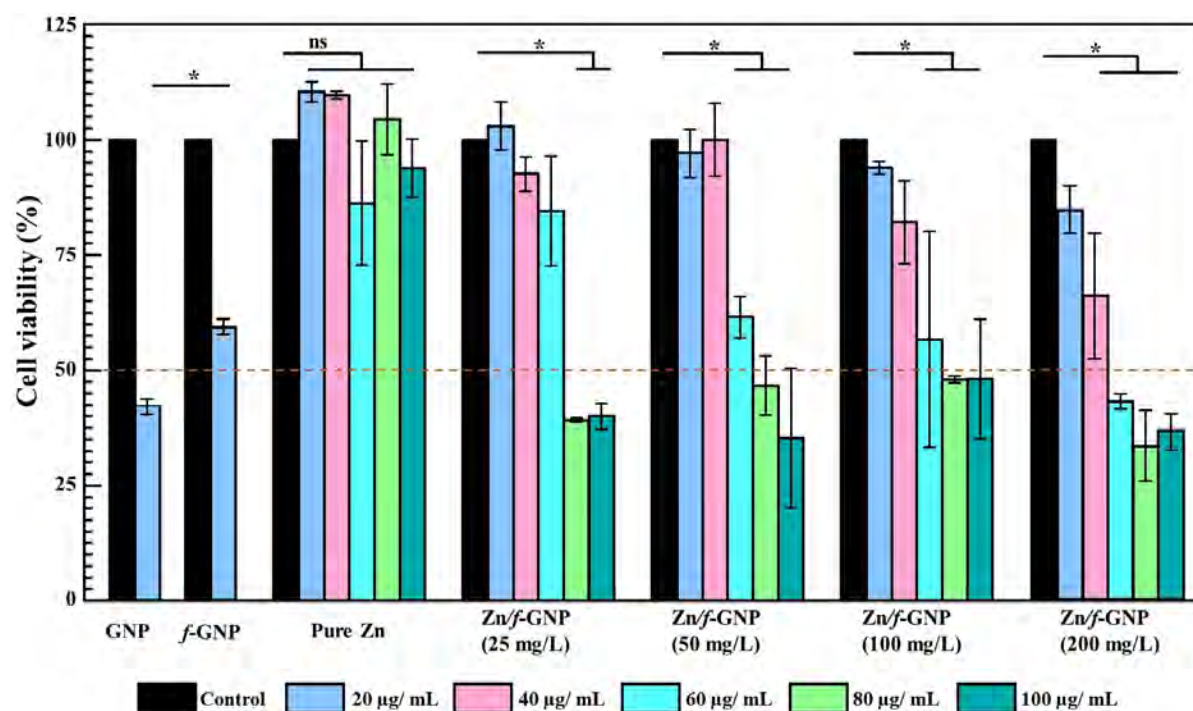
FIGURE 4.16: Cell viability assay of pristine GNP, f-GNP, pure Zn and Zn/f-GNP nanocomposites at different concentrations in cell media. *P $<$ 0.05 by one-way ANOVA with Tukey's post hoc test.

Evaluation of cytotoxic effect of f-GNP reinforced Zn matrix on HaCaT cells was clearly found to be concentration dependent, as represented in Figure 4.16. The cell viability of pure Zn was higher than that of f-GNP reinforced nanocomposite samples. It was found that the IC50 (concentration required to reduce viability by 50%) was up to 60 μg ml^{-1} of nanocomposite

TABLE 4.4: Antibacterial behavior of pure Zn and Zn/f-GNP nanocompsites.

Sample	ZOI (mm)	
	S. aureus (gram-positive)	*E. coli* (gram-negative)
pure Zn	17 ± 1	15 ± 0.5
Zn/f-GNP (25 mg/L)	18 ± 0.5	16 ± 2
Zn/f-GNP (50 mg/L)	19 ± 0.5	18.5 ± 1
Zn/f-GNP (100 mg/L)	23 ± 1.5	21 ± 1
Zn/f-GNP (200 mg/L)	24 ± 1	21 ± 2

concentration in cell media. Whereas, a decrease in cell viability was observed at higher Zn/f-GNP nanocomposite concentrations in cell media, which may be due to f-GNP-ZnO associated toxicities that eventually caused cell death [229]. To confirm the results of the cell growth at 60 μg ml^{-1} concentrations, we also performed a DAPI staining-based microscopic imaging.
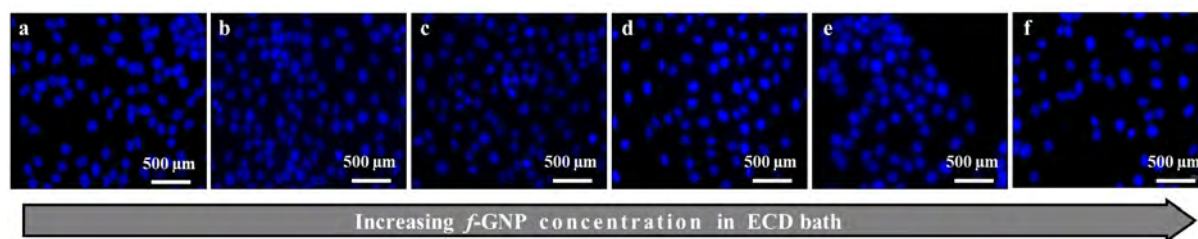
FIGURE 4.17: DAPI staining of HaCaT cells exposed for 72 hours to (a) control, (b) pure zinc, and (d-f) Zn/f-GNP nanocomposite prepared with f-GNP concentration of (c) 25 mg/L, (d) 50 mg/L, (e) 100 mg/L, and (f) 200 mg/L in the ECD bath.

Figure 4.17a–f shows DAPI staining of cell nuclei morphology on pure Zn and Zn/f-GNP nanocomposite samples after 72 hours of cell culture at concentration of 60 μg ml^{-1}. Nuclear changes such as fragmented nuclei, condensed or deformed nuclei which lead to apoptosis or necrosis across prepared nanocomposites, can be visualised by DAPI staining. Generally, exposed cells undergoing apoptosis demonstrate characteristic condensation of the attached cell nuclei [272]. However, it was clearly seen that HaCaT cells exposed to pure Zn and Zn/f-GNP nanocomposites samples exhibited nuclei morphology similar to the cells exposed to controlled environment, further validating the non-cytotoxic behavior of the prepared nanocomposites.

4.4.5 Antibacterial behavior

The test for antibacterial activity was performed by comparing the size of zone of inhibitions (ZOIs) developed across the prepared nanocomposite pellet samples against in-vitro environment of *S. aureus* (gram-positive) and *E. coli* (gram-negative). Measured ZOIs values are given in Table 4.4. It was observed that the prepared samples exhibited smaller ZOIs for gram-negative bacteria than that for gram-positive bacteria, which occurred due to additional outer protective membrane barriers in gram-negative bacteria [53,54].

Zn/f-GNP (100 mg/L) nanocomposites have shown a strong inhibition against both bacteria strains with average ZOI of 23 mm and 21 mm, which were 35.2% and 40% higher than that of 17 mm and 15 mm across pure Zn for gram-positive and gram-negative bacteria, respectively. These results also revealed that the antibacterial performance of nanocomposite samples was improved by increasing the f-GNP content in the Zn matrix. Here, the synergistic effects of ZnO and f-GNPs led to the superior antibacterial activity of the nanocomposites. The direct contact of ZnO-f-GNPs on the bacterial cell membranes may be the possible mechanism for the improvement in antibacterial activity [55,56], resulting in cell membrane disruption through cell permeability and thus induced bacterial death. These in-vitro studies served as a preliminary indication of the biocompatibility of prepared Zn/f-GNP nanocomposite samples.

TABLE 4.5: Comparison of necessarily required parameters between the prepared Zn/f-GNP nanocomposite materials and previously reported Zn-based biodegradable materials.

Composition	Method	Corrosion rate ($\times 10^{-3}$ mm/year)			Micro-hardness (HV)	CYS (MPa)	ϵ_c	Reference
		CR_{WL}	CR_{EC}	Medium				
natural bone	natural	-	-	-	-	130-180	0.01-0.02	[192]
pure zn	casting	75	140	Hank's sol.	34 ± 1.7	97	-	[225]
pure Zn	HE	80	145	SBF	40 ± 7	105	0.03-0.60	[273]
Zn–1%Mg	HR	90	150	Hank's sol.	79	280	-	[33]
Zn–5%Mg	SPS	-	427	Hank's sol.	80	186 ± 26.54	0.8	[274]
Zn–1%Ca	HR	89	150	Hank's sol.	65	275	0.75	[33]
Zn–1%Sr	HR	97	177	Hank's sol.	62	330	0.7	[33]
Zn–0.1%Fe	HE	20	-	SBF	40	98	-	[9]
Zn–(0.4–2)%Ag	HE	25-30	-	SBF	44-56	99-146	0.33-0.56	[9]
Zn–1%HA	BM + PM	-	327	Hank's sol.	46	62	0.8	[275]
Mg–3%Zn–(0.5–3)%Ag	BM + PM	375-700	180-680	SBF	59-76	175.2 ± 15.23	8.7-11.7	[276]
Zn–10HA	BM + PM	-	856	Hank's sol.	44	49	0.3	[275]
Zn–Cu/GNP	ECD + PM	2.5	25-11.5	SBF	110-151	224-341	0.27-39	This study
pure Zn	M-ECD + PM	97.2	130.1	SBF	57	97	0.29	This study
Zn/f-GNP	M-ECD + PM	18-48	104-21	SBF	68.8-108.5	182-284	0.08-0.20	This study

HE: hot extrusion, HR: hot rolling, SPS: spark plasma sintering, BM: ball milling, PM: powder matullurgy, M-ECD: modified ECD

4.5 Discussion

Biodegradability, tribo-mechanical properties and non-cytotoxicity are necessary criteria required for nanocomposites being considered as biodegradable implant materials. Based on biocompatibility, pure Zn matrix have received extensive investigations and been well-approved to clinical trials and use [16,67]. In this work, GNPs were functionalized with PEG to enhance their non-toxic behavior. Thereafter, the as-prepared -f-GNP were co-deposited with Zn ions to fabricate Zn/f -GNP nanocomposites followed by metallurgical characterization. The sintered pellets of nanocomposite were tested for parameters such as degradation, tribo-mechanical, cytotoxicity and antibacterial behaviors. Table 4.5 compares the necessarily required parameters between the prepared Zn/f-GNP nanocomposites materials and previously reported Zn-based biodegradable materials regarding the biodegradation and mechanical properties. The degradation of Zn matrix initiates a sequence of reactions within the physiological environment, resulting in the formation of gaseous, solid, and soluble compounds. Corrosion on metal surfaces results in hydrogen evolution, which is frequent in Zn and its alloys. Yang et al. [16] showed no sign of excessive gas production around in-vivo studies of pure Zn and its alloys using X-ray imaging, micro-computed tomography (Micro-CT), and histology. Other clinical studies have also found satisfactory results with low hydrogen generation during the degradation of Zn-based implants.

The cytotoxicological effect of prepared Zn/f-GNP nanocomposite was quantified using in-vitro biological assay tests that may help to assess their potential to replace existing metallic biodegradable implant material. In addition, the in-vitro cytotoxicity of f-GNP were also analyzed before reinforcing into Zn matrix to confirmed that the functionalization of pristine GNP through PEG helped to reduce their cytotoxicity against HaCaT cells, as shown in Figure 4.16 and 4.17. Generally, Zn-based compounds are essential elements for bone metabolism, but their advantages and consequences depend on daily intake or release in the human body and threshold values. Several studies reported that Zn^{2+} concentration effects the cell viability, proliferation, spreading and migration [274], [276]. Wherein, low Zn^{2+} concentrations of promoted the viability, proliferation, adhesion and migration of osteoblast cells, endothelial cells, and vascular smooth muscle cells, while high concentrations of Zn^{2+} had opposite effects [1]. From Figure 4.16, in-vitro cytotoxicity results of prepared Zn/f-GNP nanocomposites confirmed the cell viability of IC50 level. However, researchers have reported the in-vivo non-cytotoxicity conditions across biodegradable implants; such as, the formation of confluent protein layers on that avoids direct contact of cells with the implant surface and the blood flow that helps to reduce the local concentration of cytotoxic ions or degradation products [192], [277].

Meanwhile, in this study, the in-vitro biodegradation, non-cytotoxicity and antibacterial performances of prepared Zn/f-GNP nanocomposites were motivating and assuring biocompatibility and thus, we suggested their in-vivo trials for future implication in potential biodegradable implant applications.

4.6 Conclusion

In summary, we proposed a novel approach for synthesis of non-cytotoxic Zn-based nanocomposites by modified electro co-deposition approach followed by the typical powder metallurgy process. Herein, the uniform dispersion of PEG grafted GNPs in the ECD bath was insured by continuous ultra-sonication treatment (20 kHz frequency and 500 W power) during co-deposition. The influence of different concentrations of f-GNPs (0, 25, 50, 100 and 200 mg/L) in the ECD bath on the biodegradation and tribo-mechanical performances of the prepared nanocomposites were thoroughly investigated for their uniform and tunable behaviors. The following conclusions were drawn after analyzing the experimental results of material characterizations, in-vitro degradation, tribo-mechanical properties, cytotoxicity and antibacterial test studies:

- The successful covalent bonding of PEG functional group with GNPs was confirmed by FT-IR spectra of as-prepared f-GNPs, resulting C–O ($\sim$1090 cm^{-1}) and C–H ($\sim$2910 cm^{-1}) stretching vibrations. From Raman spectra, the intensity peak ratio ($I_{(D/G)}$) of f-GNPs was obtained lower than that of GNPs indicated the defects into the graphene crystals by the nucleophilic reaction between PEG functional groups and GNPs.

- The hexagonal growth of Zn deposits on the surface of f-GNP was well-achieved, as observed from TEM images of the Zn/f-GNP clusters, resulting new nucleation sites for co-deposition during M-ECD process. The characteristic transmission peeks in FT-IR spectra confirmed the bonding between Zn matrix and f-GNP via Zn–O–C attachments.

- The formation HCP microstructure of the Zn matrix with reducing crystallite size on increasing the concentration in the ECD bath was revealed by XRD patterns. This reduced crystallite size of Zn/f-GNP nanocomposite was due to large nucleation sites during co-deposition at higher f-GNP concentrations, which confirmed by FESEM images. The uniform dispersion of f-GNP across Zn matrix was confirmed by EDS color mapping.

- The uniformly distributed impermeable layers of f-GNPs provided even barrier protection from corrosive OH$^-$ and Cl$^-$ attacks and prevented the void and pits formation on the surface of nanocomposite to avoid micro-galvanic corrosion. Thus, the electrochemical corrosion was tunable from 130.4×10^{-3} mm/year (for pure Zn) to 21×10^{-3} mm/year (for 100 mg/L of f-GNP).

- Superior mechanical properties of f-GNP and grain strengthening effect enhanced the tribo-mechanical properties of Zn/f-GNP nanocomposites. The compressive yield strength of Zn/f-GNP nanocomposites was ranges from 182.3 ± 7.9 MPa (for 25 mg/L of f-GNP) to 284.9 MPa (for 100 mg/L of f-GNP), which was significantly higher than pure Zn and comparable to bone strength. The friction coefficient and SWR of Zn/ f-GNP (100 mg/L) nanocomposites reduced by 58.1% and 47.36%, respectively, on comparing with pure Zn.

The harder surfaces of Zn/f-GNP nanocomposite samples showed negligible delamination during tribological tests.

- It was found that PEG-grafted GNPs had significantly high HaCaT cell viability compared to pristine GNPs. The IC50 up to concentration of 60 μg ml^{-1} of nanocomposites in cell media, suggesting their non-cytotoxicity level, which further confirmed by DAPI staining for 72 hours of cells attachment. Also, the Zn/f-GNP nanocomposite pellets inhabited the growth of *S. aureus* and *E. coli* bacteria in terms of ZOI formation and performed better than the control pure Zn.

Based on the above conclusions, the proposed Zn/f-GNP nanocomposites were not only non-cytotoxic and anti-bacterial but also sustainable with respect to tunable degradation and tribo-mechanical performances. Findings of this study may have future implication of Zn/f-GNP nanocomposites for low-cost biodegradable orthopedic implant (sutures, screw, pins and plates) and stent (coronary and cardiovascular) applications.

Chapter 5

Antibacterial Zn/GNP Nanocomposite Coatings

5.1 Overview

Frequently touched surfaces in the hospital environment act as a reservoir for the bacteria responsible for healthcare-associated infections (HCAIs). In this study, GNP was incorporated in low-cost Zn coating using electrochemical co-deposition (ECD) to prevent HCAIs. The effects of different concentrations of GNP in the ECD bath (25, 50, 100 and 200 mg/L) for microstructural, tribo-mechanical, anti-corrosion, and anti-bacterial features of coatings are evaluated in detail. The microhardness, friction coefficient, specific wear rate, and polarization resistance values were remarkably improved from 77 HV, 0.7, 26.1 mg and 13.68 kΩ.cm^2 for pure Zn coating to 151 HV, 0.48, 12.09 mg, and 2.3 kΩ.cm^2 for Zn/GNP (100 mg/L) nanocomposite coating, respectively. The anti-bacterial activities of the coatings enhanced with the increase in GNP concertation in the ECD bath and Zn/GNP (100 mg/L) nanocomposite coating exhibited inhibition zone of 22 mm and 25 mm against *S. aureus* and *E. coli* bacteria.

5.2 Introduction

Healthcare-associated infections (HCAIs) are one of the major challenges in health services [77]–[79]. European centre for disease prevention and control (ECDC) reported more than 81 thousand HCAIs affected patients per day in European hospital facilities in 2011-12 [80]. Here, the main bacteria responsible for HCAIs in hospital facilities are *Staphylococcus aureus* (*S. aureus*) and *Escherichia coli* (*E. coli*). The colonization of such bacteria, fungi, and other microorganisms is responsible for forming biofilms on the surfaces by secreting strong extracellular polymeric substances (EPS) [81]. The biofilms adhere to the surfaces and help in bacteria colonization, which is often hard to sanitize with disinfectants and surfactants [82]. The mechanism of bacterial colonization subjected to environmental stimuli and a series of genetic changes in bacteria cells.

However, five sequential stages for bacterial colonization have been identified for the growth and spread of bacteria, namely, (i) temporary/ reversible and permanent/ irreversible attachment, (ii) microcolony development, (iii) three-dimensional biofilm development, (iv) growth, and (v) spread [81], [83]. Researchers have shown that an anti-bacterial coating on the surfaces can be an effective and efficient solution to prevent HCAIs [84], see Figure 5.1.
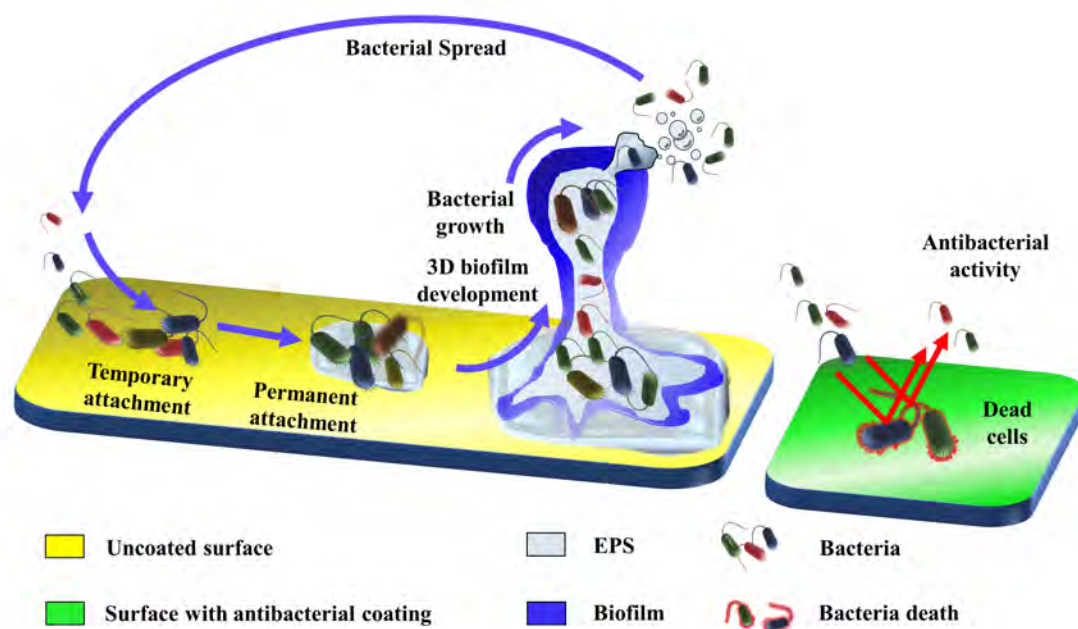
FIGURE 5.1: Illustration of comparison between ordinary surfaces undergoing bacterial colonization (left) with coated surface executing anti-bacterial activity (right).

Graphene family materials (GFMs) can exhibit a strong anti-bacterial activity with high tribo-mechanical advantages and adequate anti-corrosion properties at very low concentrations in the nanocomposite coating owing to the high surface-to-volume ratio [278], [279]. GFMs have been established as one of the advanced anti-bacterial nanofillers in organic and inorganic binders and proved their efficacy against various bacteria [280]. The literature shows that the GNPs block the respiratory chain of bacteria that prevents the growth and proliferation ability [281], as shown in Figure 5.1. GNP and associated conjugates attached to the cell membrane and puncher to produce holes (pores), thus generating oxidative stress in the form of reactive oxygen species (ROS) and damaging the critical cellular components such as proteins and nucleic acids [282], [283]. Thereby, GNP applications are very common in the field of medicine, dentistry, indwelling medical devices, enteral feeding tubes and wound drains for preventing HCAIs [44], [284], [285]. The GNP nanofillers are also high water, and oil-repellent nanomaterial [286]. Lin et al. [287] have reported the excellent frictional properties and high wear resistance of multilayer GNP-based coatings against scratches or other physical damages. Kirkland et al. [288] have reported that the GNP reinforcements are an effective corrosion barrier and can save substrate material from

external electrochemical attack. Sreevatsa et al. [289] have investigated the potential of GNP as an ionic barrier; here, a single atomic GNP improved the corrosion-resistant properties of the steel substrate. Due to the above reasons, the GNP-based coating technologies have been developed with several metallic and non-metallic binding matrices to develop multipurpose coating materials [147], [290].
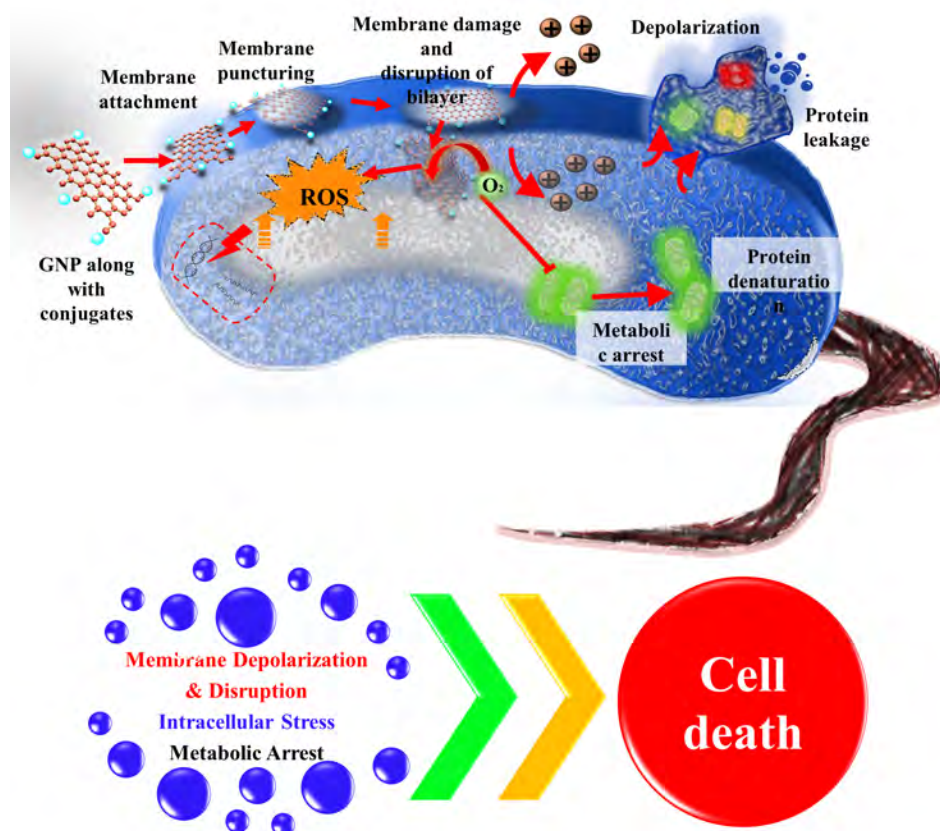
FIGURE 5.2: Anti-bacterial activity of GNP via membrane depolarization and disruption, intracellular stress and metabolic arrest [114], [284].

In recent times, Ti-, Co-, Cu-, Ag-, Zn-, and Ni-based coatings have been extensively studied to protect surfaces from bacterial attack [122], [123]. Among all, Zn-based coatings are one of the low-cost anti-bacterial coatings which can also form a protective layer comprised of oxides, carbonates or hydrated sulfates based upon the nature of the environment and can provide protection to the substrate [291]. In addition, Zn is one of the abundantly available metals on the earth's crust, which makes it suitable for the purpose of mass utilization in public infrastructure [55], [292]. But poor tribo-mechanical performance is a serious disadvantage of Zn coating [293]. The reinforcement of GNP nanofillers in Zn-based coating can enhance the tribo-mechanical performance of Zn-based coatings and fulfil the requirement of low-cost, tribo-mechanically fit, anti-corrosive and anti-bacterial coating [294], [295]. However, the evaluation of GNP-reinforced Zn nanocomposite coating for anti-bacterial properties is yet to be carried out.

Many methods, such as plasma and thermal spraying [126], [128], electroless coating [296], vapor deposition (physical and chemical) [297] and electrochemical-co-deposition (ECD) have been used to synthesis GNP nanofiller based nanocomposite coatings [147], [298]. Here, ECD is a facile, inexpensive, industrially scalable and sustainable method to fabricate nanocomposite coatings [299]. In this study, GNP-reinforced Zn nanocomposite coatings were prepared using the ECD method. The characterization and testing results were discussed in detail to understand the effect of different concentrations of GNP in the ECD bath on the tribo-mechanical, anti-corrosion and anti-bacterial properties of prepared nanocomposite coatings.

5.3 Experimental procedure

5.3.1 Coating deposition

The used ECD bath composition and operating parameters are listed in Table 5.1. The volume of the ECD bath was 400 ml. The different concentrations of GNP (25, 50, 100 and 200 mg/L) were added to the ECD bath under magnetic agitation (400 rpm) for 60 min and uniformly dispersed with the help of ultrasonication treatment (20 kHz, 500 W) for 30 min. The prepared ECD baths were adjusted to a pH of 3.5 ± 0.1.
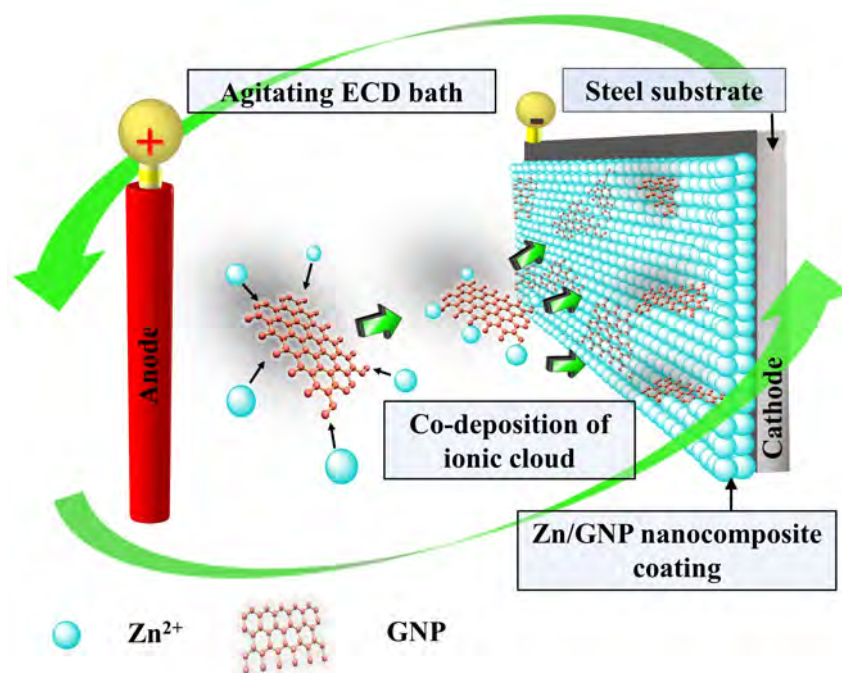
FIGURE 5.3: Co-deposition of Zn/GNP nanocomposite coatings from agitating ECD bath [300].

The schematic representation of ECD of Zn/GNP nanocomposite coatings is illustrated in Figure 5.3. In this process, the medical grade 316 stainless-steel plates of dimensions of 20 mm × 20 mm × 1.5 mm were used as a cathode and a pure Zn rod of 3 mm diameter were used as

an anode. The stainless-steel plates were polished with 600, 800, 1000 and 2500 grit abrasive papers and washed with distilled water and then acetone. A pure Zn coating was also prepared for comparison. The prepared coatings were washed using running water and dried for further characterization and testing.

TABLE 5.1: Electrolyte bath composition and process parameters for Zn/GNP nanocomposite coating fabrication

Parameter	Values
$ZnSO_4.7H_2O$	0.5 M
Na_2SO_4	1 M
H_3BO_4	0.3 M
pH	3.5
DC current supply	4 A/dm^2
Agitation	350 rpm
Run time	60 min.
GNPs' concentration	25, 50, 100 and 200 mg/L
Temperature	27°C

5.3.2 Coating characterization

X-ray diffraction technique was used to study the microstructure and average crystallite size of the coatings. The scans were obtained from 30° to 90° with a step size of 0.02° and a scan rate of 2°/min. The surface morphology of the coatings was observed using a field emission scanning electron microscope with an acceleration voltage of 20 kV. Energy dispersive spectroscopy was used to determine the elemental composition of nanocomposite coatings. Vickers hardness tester was used to measure the microhardness of prepared coatings. The applied load was 20 g for 20 s. The tribological performance was analyzed by a pin-on-disc wear machine under dry sliding conditions. The pin was a high carbon chromium-bearing steel (GCr15) with a diameter of 6 mm. The friction coefficient was recorded under a constant load of 500 g for 600 s. The offset radius was 5 mm and the rotating speed of the test specimen was 250 rpm. The coatings were weighed before and after the wear test using a digital balance to measure the wear loss with an accuracy of 0.1 mg. The corrosion performance of coatings was evaluated using a potentiostat (CHI604E) in 3.5 wt% NaCl solution without agitation at room temperature. In a three-electrode cell arrangement, reference and counter electrodes were Ag/AgCl and Pt, respectively, and the prepared coatings were the working electrodes. Before anti-bacterial test, the prepared nanocomposite coatings were washed under running ethanol and DI water, subsequently air-dried at 120º C to neutralize the effect of ECD bath composition. In-vitro anti-bacterial activity of prepared nanocomposite coatings was evaluated against gram-positive bacteria *S. aureus* (MTCC 96) and Gram-negative bacteria *E. coli* (MTCC 1652). The zone of inhibition (ZOI) was determined by the modified Agar disc diffusion method as defined by the national committee for clinical laboratory standards (1993). Each bacterial strain was grown in Luria Broth media (Himedia Laboratories, India).

100 µL of overnight grown bacterial culture (107 cfu/mL) was spread using a sterile spreader. The plates were incubated overnight at 37°C, and the ZOI around the discs were measured on a millimetre (mm) scale. Here, the pure Zn coating was used as a control.

5.4 Result and discussion

5.4.1 XRD analysis

Figure 5.4 displays the XRD patterns of pure Zn and Zn/GNP nanocomposite coatings prepared at different GNP concentrations in the ECD bath.
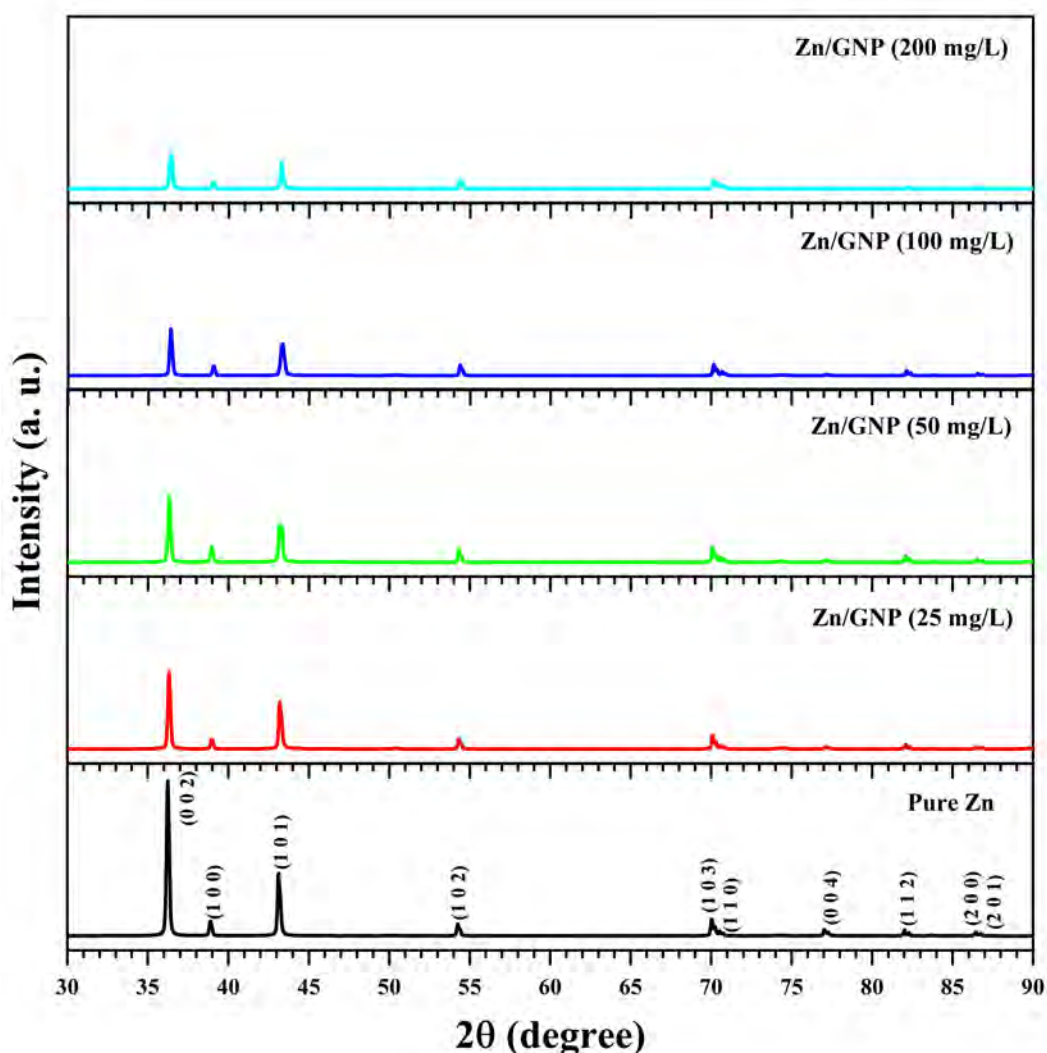
FIGURE 5.4: XRD patterns of pure Zn and Zn/GNP nanocomposite coatings matched well with JCPDS Cards No. 004-0831.

The XRD patterns of all prepared coatings were well-matched with the hexagonal Zn (JCPDS Cards No. 004-0831). The XRD data revealed that signals from the (002), (100), (101) and
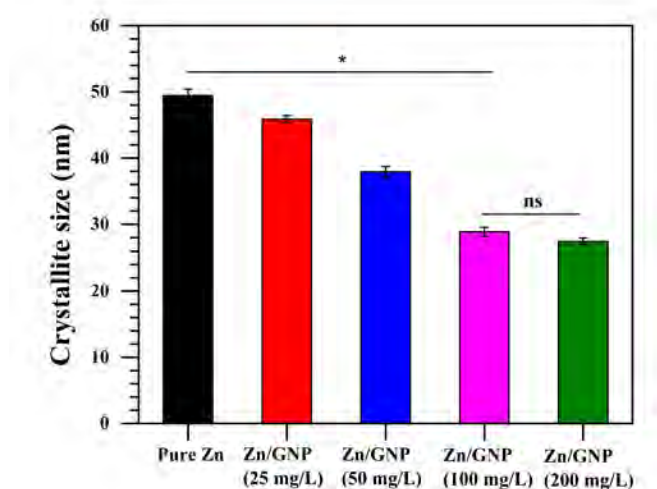
FIGURE 5.5: Calculated crystallite size of pure Zn and Zn/GNP nanocomposite coatings. *P $<$ 0.05 (significant) and otherwise not significant (ns) by one-way ANOVA with Tukey's post hoc test.

(103) Zn planes predominated in the XRD pattern. The metallic compactness in the deposits resulted in higher relative intensity peaks at strong (002) orientation for the Zn matrix. After, incorporation of GNP into the Zn matrix, peaks broadening has occurred. Also, the intensities of all peaks have reduced with the increase in GNP concentration in the ECD bath, which signifies that the addition of GNP was inducing micro-stresses and lattice defects thereby affecting the crystallographic orientation and crystallinity of Zn deposits. Moreover, the peak broadening was attributed to the refinement in the crystallite size of the coating.

The crystallite size of the prepared coatings was calculated using the Scherrer equation given in Chapter 3. Figure 5.5 shows the average crystallite size of pure Zn and Zn /GNP nanocomposite coatings. The average crystalline size of deposits was decreased by 41.66% from 49.44 nm for pure Zn to 28.84 nm for Zn/GNP (100 mg/L) nanocomposites coating, indicating a modification in competition between nucleation and crystal growth of deposits in the presence of impermeable GNP content in the ECD bath. During the deposition process, GNP provide preferential sites for crystal growth of hexagonal Zn and hence average crystallite size was decreased. The XRD analysis revealed that the addition of small amounts of GNP in the ECD bath modified the crystallite orientation, crystallinity and crystallite size of Zn/GNP nanocomposite coatings.

5.4.2 Morphological and elemental composition analysis

The effects of increasing concentrations of GNP in ECD bath on the surface morphology of Zn/GNP nanocomposite coatings are shown in Figure 5.6a-d. The pure Zn coating has large and orderly oriented hexagonal crystallite growth aligned parallel to the substrate surface (Figure 5.6a). After the addition of 25 mg/L of GNP in the ECD bath, the changes in crystallinity are clearly

observed by marking the edges of underdeveloped hexagonal crystallite growth (Figure 5.6b). The surface morphology of Zn/GNP (50 mg/L) nanocomposite coating has no clear hexagonal shapes but partially grown crystallites of decreased sizes and disordered orientations (see Figure 5.6c). However, the Zn/GNP nanocomposite coating prepared at 100 mg/L of GNP concentration in the ECD bath exhibited evident nucleation sites for new Zn deposits with smaller crystallite size (Figure 5.6d).

The EDS mapping analysis of Zn/GNP nanocomposite coatings is shown in Figure 5.6e-g. From Figure 5.6e-g, it can be observed that Zn, C and O elements are well-dispersed in the coating surface. Here, O content confirmed the presence of ZnO. The presence of C element in the coating surface confirmed the incorporation of GNP into the Zn matrix. The C content of Zn/GNP nanocomposite coatings increased from 1.23% to 5.17%, with the increase in GNP concentration in the ECD bath from 25 mg/L to 100 mg/L. The increased GNP content in the ECD bath also increased the chances of incorporating GNP into the Zn matrix during the co-deposition process; thus, an increase in carbon element was observed in the EDS mapping.

5.4.3 Tribo-mechanical performance

5.4.3.1 Microhardness

The microhardness values of pure Zn and Zn/GNP nanocomposite coatings are shown in Figure 5.7. The results show that the addition of GNP has a great impact on the microhardness of the coatings. The microhardness values of Zn/GNP nanocomposite coatings were higher than that of the pure Zn coating. The microhardness of Zn/GNP nanocomposite coating increased from 105 HV to 143 HV with the increase in GNP concentration from 25 mg/L to 50 mg/L in the ECD bath. The Zn/GNP nanocomposite coating prepared at 100 mg/L of GNP concentration in the ECD bath has 96.1% higher microhardness in comparison to 77 HV for pure Zn coating.

The increased microhardness of Zn/GNP nanocomposite coatings was mainly due to the strengthening effect with the decrease in crystallite size. In addition, the free dislocation path was reduced due to the plane-like geometry, and the superior strength of GNP resulted in effective load-bearing performance and thus improved the microhardness of coatings.

5.4.3.2 Tribological performance

The tribological performance of nanocomposite coatings generally depends on material properties, type of counterpart, forms of wear debris and contact conditions. Here, friction coefficient and specific wear rate are used as the parameters to investigate the tribological performance of nanocomposite coatings. The obtained results for the friction coefficient of pure Zn and Zn/GNP nanocomposite coatings are shown in Figure 5.8. From Figure 5.8, the average friction coefficient of Zn/GNP nanocomposite coatings was lower than that of the pure Zn coating. With the increase in GNP concentration in the ECD bath from 25 mg/L to 100 mg/L, the average friction coefficient of Zn/GNP nanocomposite coatings was decreased from 0.67 to 0.48.
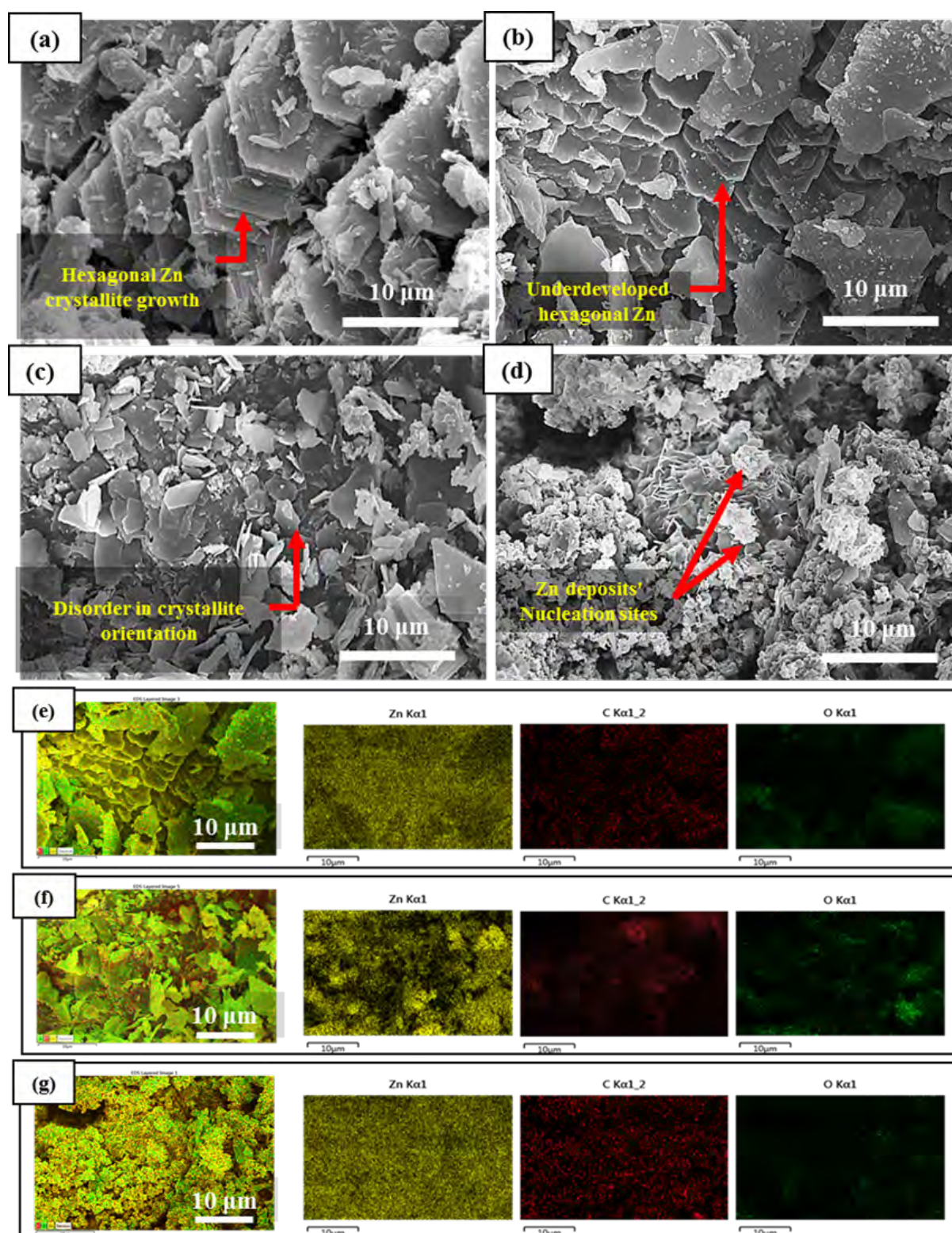
FIGURE 5.6: FESEM images of (a) pure Zn and (b-d) Zn/GNP nanocomposite coatings for GNP concentration of (b) 25 mg/L, (c) 50 mg/L and (d) 100 mg/L in the ECD bath; (e-f) EDS mapping of coatings for GNP concentration of (e) 25 mg/L, (f) 50 mg/L and (g) 100 mg/L in the ECD bath.
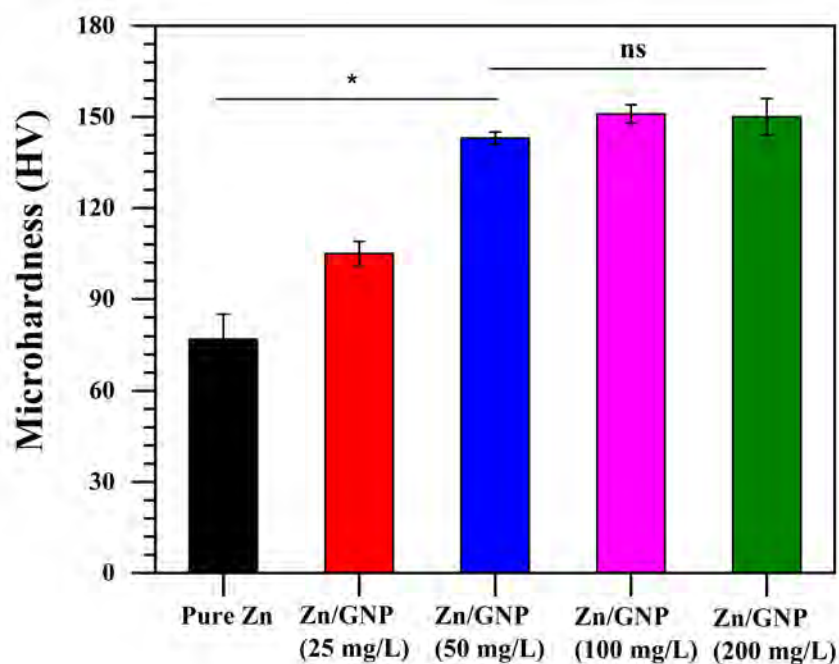
FIGURE 5.7: Microhardness of pure Zn and Zn/GNP nanocomposite coatings. *P < 0.05 (significant) and otherwise not significant (ns) by one-way ANOVA with Tukey's post hoc test.
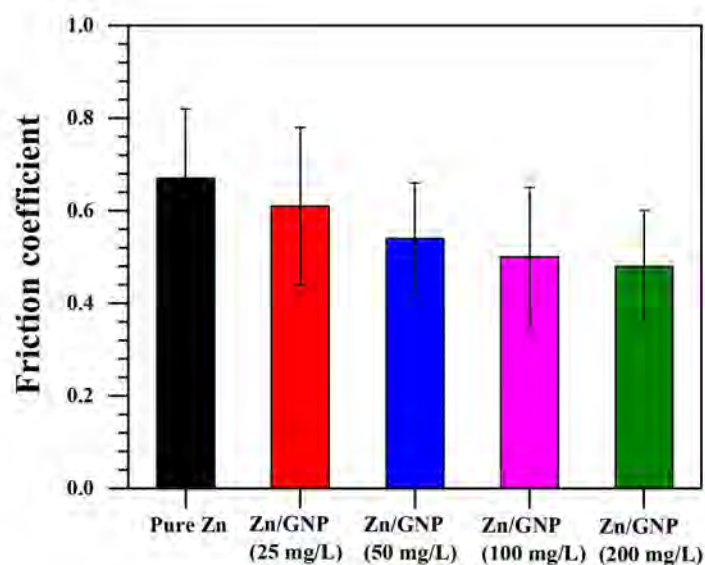
FIGURE 5.8: Friction coefficient of pure Zn and Zn/GNP nanocomposite coatings.

The enhancement in the friction coefficient was attributed to the incorporation of GNP into the Zn matrix [263]. During the sliding process, wear debris were produced between the mating surfaces. The wear debris produced by the Zn/GNP nanocomposite coatings contains GNP. The GNP nanofillers have excellent lubricating properties and low shear strength [147], [169]. Thus, the friction coefficient of Zn/GNP nanocomposite coatings decreased with the increase in the GNP concentration in the ECD bath.

Figure 5.9 presents the specific wear rate (SWR) measured from the difference of initial and final weight of prepared coatings. It can be seen from Fig. 4c that the Zn/GNP nanocomposite coating displayed a lower value of specific wear rate than that of pure Zn coating. It can be seen that with the increase in GNP concentration in the ECD bath, the specific wear rate of prepared nanocomposite coatings was decreased. Here, Zn/GNP (100 mg/L) nanocomposite coating has a minimum specific wear rate of 12.09 mg. GNP debris forms a protective layer on the wear track and works as a dry lubricant to reduce the wear of coating. In addition, the increased GNP content of Zn/GNP nanocomposite coating increased the microhardness of the coating, which reduced the specific wear rate and improved the durability of the coating.
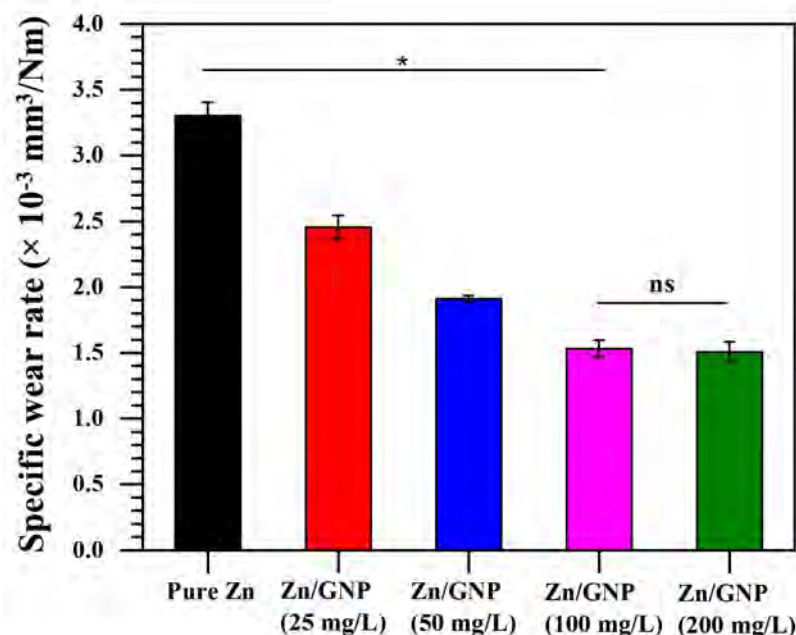
FIGURE 5.9: Specific wear rate of pure Zn and Zn/GNP nanocomposite coatings. *P < 0.05 (significant) and otherwise not significant (ns) by one-way ANOVA with Tukey's post hoc test.

5.4.4   Corrosion behavior

The electrochemical tests were conducted for the prepared coatings with the scanning corrosion potential ranging from -2 V to -0.5 V at a scan rate of $10\,\mathrm{mV\,s^{-1}}$. Fig. 6 shows the potentiodynamic polarization curves for prepared pure Zn and Zn/GNP nanocomposite coatings. The values

TABLE 5.2: Electrochemical corrosion parameters of pure Zn and Zn/GNP nanocomposite coatings

Sample	I_{corr} (μ A/cm^2)	β_a (mV/decad)	β_c (mV/decad)	R_p (kΩ.cm^2)
Pure Zn	10.228 ± 1.3	87.0 ± 12.9	137.0 ± 15.0	2.22 ± 0.5
Zn/GNP-25 mg/L	6.310 ± 0.5	62.2 ± 7.1	335.1 ± 24.1	3.60 ± 0.7
Zn/GNP-50 mg/L	2.553 ± 0.3	76.6 ± 6.8	169.8 ± 13.5	8.91 ± 0.9
Zn/GNP-100 mg/L	2.222 ± 0.1	89.6 ± 11.4	261.1 ± 18.4	13.0 ± 1.1
Zn/GNP-200 mg/L	2.051 ± 0.1	78.4 ± 9.0	278.2 ± 12.4	15.6 ± 1.4

of electrochemical parameters such as corrosion current density (I_{corr}), anodic Tafel slope (β_a) and the cathodic Tafel slope (β_c) were extracted from potentiodynamic polarization curves and summarized in Table I. The polarization resistance, R_p (kΩ.cm^2) values for prepared coatings were calculated using the Stern-Geary equation (Eq. 5.1) as follows [169], [263]:

$$R_P = \frac{\beta_a \cdot \beta_c}{2.303(\beta_a + \beta_c)} \left(\frac{1}{I_{corr}}\right).$$ (5.1)
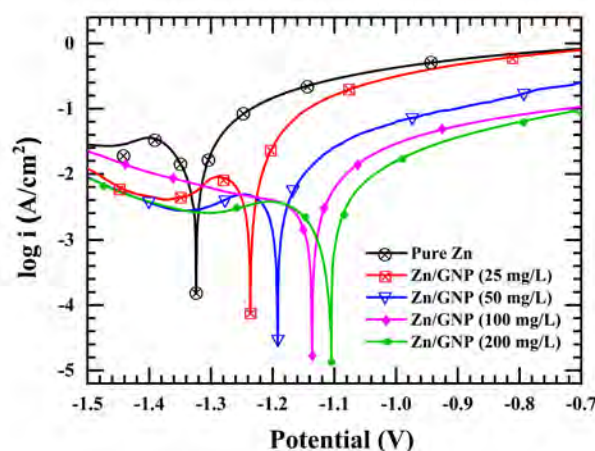
FIGURE 5.10: Potentiodynamic polarization curves for pure Zn and Zn/GNP nanocomposite coatings

With the increasing GNP concentration in the ECD bath, a positive shift was observed in the polarization curve with decreased Icorr value, which indicated the enhancement in the anti-corrosion properties. From Table I, the R_p value of pure Zn was 2.22 kΩ.cm^2, whereas, the R_p of Zn/GNP nanocomposite coatings prepared at 25 mg/L, 50 mg/L and 100 mg/L concentration of GNP in the ECD are about 3.68, 8.98 and 13.38 kΩ.cm^2, respectively. Here, the increased nucleation sites during the deposition of Zn/GNP nanocomposite coating developed the micro electrical-short-circuits across the grains, which increased the R_p values and improved the anti-corrosion performance. In addition, the presence of precipitated oxides of Zn that

TABLE 5.3: Anti-bacterial properties of Zn/GNP nanocomposite coating

S No.	Sample	S. aureus (Gram-positive) ZOI (mm)	E. coli (Gram-negative) ZOI (mm)
1	Pure Zn	14 ± 1	16
2	Zn/GNP (25 mg/L)	17 ± 1.5	20 ± 0.5
3	Zn/GNP (50 mg/L)	20 ± 1	23 ± 1.5
4	Zn/GNP (100 mg/L)	22 ± 1.5	25 ± 1.5
5	Zn/GNP (200 mg/L)	23 ± 0.5	25 ± 1

irreversibly passivate also improved the anti-corrosion performance. The direct role of well-dispersed GNP reinforcement in anticorrosion performance of Zn/GNP nanocomposite coatings can be summarized in two possible mechanisms:

(a) The outstanding impermeable barrier ability of GNP against the interaction between Zn and aggressive environment to obstruct the permeation of corrosive agents;

(b) The 2-D geometry and high aspect ratio of GN sheets not only lengthen the diffusion paths significantly but also help block/reduce micro-pores in Zn/GNP nanocomposite coatings

Moreover, the smaller crystallite sizes of Zn/GNP nanocomposite coatings implicit less possibilities of micro-voids, pores and cracks based local micro-galvanic cells and thus improved the anti-corrosion performance.

5.4.5 Anti-bacterial behavior

The anti-bacterial activity of pure Zn and Zn/GNP nanocomposite coatings was determined on Gram-positive (*S. aureus*) and Gram-negative (*E. coli*) bacteria using agar well diffusion. Table 5.3 shows the anti-bacterial effect of prepared nanocomposite coatings against the bacteria, which is the measured diameter of ZOI.

It was observed that Zn/GNP nanocomposite coatings showed promising anti-bacterial activities against both bacteria with ZOI that ranged from 17 mm to 22 mm for *S. aureus* and 20 mm to 25 mm for *E. coli*. Here, the increase in GNP concentration in ECD bath was inhibiting the bacterial growth around the nanocomposite coatings. Wherein, Zn/GNP (100 mg/L) nanocomposite coatings inhibited the growth of *S. aureus* and *E. coli* with the highest ZOI of 22 mm and 25 mm, respectively. Whereas, the pure Zn coatings as a control formed 14 mm and 16 mm of ZOI for *S. aureus* and *E. coli*, respectively. Thus, prepared Zn/GNP nanocomposite coatings showed better anti-bacterial properties than pure Zn.

5.5 Conclusion

In this study, low-cost, industrially scalable, and anti-bacterial Zn/GNP nanocomposite coatings were prepared using ECD method. The different GNP concentrations in the ECD bath were used

to understand the effects on tribo-mechanical, anti-corrosion, anti-bacterial behavior of prepared nanocomposite coating. The following conclusions were made from this study:

- Formation HCP microstructure of the Zn matrix with reducing crystallite size on increasing the GNP concentration in the ECD bath was observed in XRD patterns.

- Disordered morphology and formation of new nucleation sites in nanocomposite coating was observed in FESEM images on increasing the GNP concentration in the ECD bath.

- Distribution of anti-bacterial GNP across the Zn matrix in terms of carbon content was confirmed using EDS mapping. In addition, the presence of oxygen content confirmed the protective ZnO precipitates, which provides barrier protection to the coating from the external environment.

- Microhardness of 143 HV for Zn/GNP (100 mg/L) nanocomposite coating measured highest among all prepared coatings, which was 185.57% higher than 77 HV for pure Zn coating.

- The friction coefficient and specific wear rate of coatings reduced by 31.42% and 53.63%, respectively, on comparing pure Zn coating with Zn/GNP (100 mg/L) nanocomposite coating.

- The presence of impermeable GNP and protective ZnO precipitates on the Zn/GNP nanocomposite coatings provides an electrochemical barrier that reduces the corrosion current with the increase in GNP concentration in the ECD bath.

- The Zn/GNP nanocomposite coating performs better than the control pure Zn coating in anti-bacterial behavior against both Gram-positive (*S. aureus*) and Gram-negative (*E. coli*) bacteria when tested for agar well diffusion. Wherein, Zn/GNP (100 mg/L) nanocomposite coating samples inhibited the growth of *S. aureus* and *E. coli* with the highest ZOI of 22 mm and 25 mm, respectively.

Based on the above conclusions, the prepared nanocomposite coatings were not only anti-bacterial but also sustainable in terms of adequate tribo-mechanical and high anti-corrosion performances. Thus, Zn/GNP nanocomposite coatings may be useful in the future for low-cost and industrially scalable anti-bacterial coating applications. In continuation of the development of sustainable antibacterial coatings for future applications, high-strength alloying elements like Ni, Cu, Fe, etc can also be alloyed with pure Zn matrix of Zn/GNP nanocomposite coatings to further enhance their mechanical performances.

Chapter 6

Process Parameter Optimization

6.1 Overview

Zn/f-GNP nanocomposite coatings have been shown to have improved mechanical and corrosion properties compared to pure Zn. The addition of GNPs to Zn improves microhardness which is one of the important mechanical properties, due to the strong interfacial bonding between the GNPs and Zn matrix. Improved microhardness can provide insight into the material's strength and resistance to wear and tear. Additionally, the GNPs can act as a barrier to prevent corrosion, as it protects the underlying Zn from coming into contact with corrosive agents. However, the corrosion behaviour of Zn/f-GNP nanocomposite coatings prepared by the ECD or M-ECD methods can be affected by the quality of the interface between the Zn and f-GNPs at different concentrations of GNPs in an ECD bath, as well as the specific experimental environment in which the nanocomposite is fabricated. Further optimization research is needed to fully understand the mechanical and corrosion behaviour of these materials for different process parameters and compositions.

In this chapter, the effect of ECD parameters such as pH, current supplied, GNPs concentration and agitation to ECD bath on microhardness and corrosion protection of Zn/f-GNP nanocomposite prepared by the M-ECD method are briefly discussed. Similarly, the effect of ECD parameters such as pH, current, f-GNPs concentration and agitation to ECD bath on microhardness and corrosion protection of Zn/f-GNP nanocomposite coatings prepared by M-ECD method followed by powder metallurgy method are discussed. The set of experiments were performed based on the design developed by Taguchi method. Taguchi method is a statistical method used for the design of experiments (DOE) because it can help to identify the important factors that affect the performance of a process. This method can help to identify which factors have the most significant impact on the performance of the process and can be used with a relatively small number of experimental runs. Additionally, the Taguchi method can be used to optimize the performance of a process.

6.2 Effect of ECD parameters on microhardness and corrosion protection efficiency of Zn/f-GNP nanocomposite

6.2.1 Experimental design

In the current investigation, pH, current supplied, GNP concentration and agitation to the ECD bath have been selected as process variables. The fixed ECD parameter for the experimental study is listed in Table 6.1. The respective process variable range selected for this study is listed in Table 6.2. The experiments have been designed based on the Taguchi method, and the results have been analyzed for the microhardness value of nanocomposite coating. Based on the results of the above studies. Analysis of variances (ANOVA) studies is performed to recognize the significance of process parameters. In the present work, we have investigated as the maximum microhardness, and corrosion protection efficiency η_{corr} as performance index and have chosen a larger-the-better S/N ratio for microhardness and corrosion protection efficiency (refer Equation 6.1).

$$\frac{S}{N} = -10log\frac{1}{N}\sum\frac{1}{y_i^2}.$$ (6.1)

where, y_i is N observation of response variable.

In M-ECD method, major parameters, which influence the quality of prepared Zn/f-GNP nanocomposite coating are 1) pH, 2) current supplied, 3) GNP concentration in the electrolyte and 4) agitation during co-deposition. With the four parameters as variables and considering four levels of each variable, a fractional factorial design of 16 experiments is done with L16 orthogonal array. Table 6.2 presents the respective process variable with their corresponding levels with which the nanocomposite coatings have experimented, and optimization of microhardness and corrosion protection efficiency using Taguchi was performed using MINITAB software. The experiments have been conducted using Taguchi experimental design (L16 orthogonal array) and are shown in Table 6.3.

TABLE 6.1: Fixed ECD parameter for experimental study of nanocomposite fabrication

Fixed parameters	Quantity
Electrodeposition time	180 min
Zinc sulaphate	0.5 M
Ultrasonication frequency	20 kHz
Bath temperature	27 $\pm$ 2°C

6.2.2 Statistical analysis of experimental results

The statistical modelling for the microhardness and corrosion protection efficiency of Zn/f-GNP nanocomposite coatings synthesized by ECD method has been done. General first-order models are developed for estimating the microhardness and corrosion protection efficiency of the coatings.

TABLE 6.2: Input variables and their levels for experimental study of Zn/f-GNP nanocomposite fabrication.

Parameter No.	Description	Level 1	Level 2	Level 3	Level 4
A	pH	4	6	8	10
B	Current supplied (A)	1	2	3	4
C	f-GNP concentration (mg/L)	25	50	100	200
D	Agitation (rpm)	150	250	350	450

TABLE 6.3: The basic Taguchi L16 orthogonal array

Exp. No.	Parameters				Notation
	A	**B**	**C**	**D**	
1	1	1	1	1	$A_1B_1C_1D_1$
2	1	2	2	2	$A_1B_2C_2D_2$
3	1	3	3	3	$A_1B_3C_3D_3$
4	1	4	4	4	$A_1B_4C_4D_4$
5	2	1	2	3	$A_2B_1C_2D_3$
6	2	2	1	4	$A_2B_2C_1D_4$
7	2	3	4	1	$A_2B_3C_4D_1$
8	2	4	3	2	$A_2B_4C_3D_2$
9	3	1	3	4	$A_3B_1C_3D_4$
10	3	2	4	3	$A_3B_2C_4D_3$
11	3	3	1	2	$A_3B_3C_1D_2$
12	3	4	2	1	$A_3B_4C_2D_1$
13	4	1	4	2	$A_4B_1C_4D_2$
14	4	2	3	1	$A_4B_2C_3D_1$
15	4	3	2	4	$A_4B_3C_2D_4$
16	4	4	1	3	$A_4B_4C_1D_3$

TABLE 6.4: Experimental results for microhardness and corrosion protection efficiency

Exp. No.	Microhardness (HV)				$_{corr}(\%)$			
	Ist	**IInd**	**IIIrd**	**Average**	**Ist**	**IInd**	**IIIrd**	**Average**
1	48.6	51.3	49.2	49.7	10.4	11.5	10.9	10.9
2	69.8	66.6	70.0	68.8	29.1	29.1	26.9	28.4
3	99.8	110.1	83.5	97.8	65.6	65.4	61.3	64.1
4	105.7	108.9	106.7	107.1	85.0	80.7	87.0	84.2
5	59.0	58.0	57.9	58.3	20.5	23.9	17.6	20.7
6	68.3	72.1	69.3	69.9	12.1	10.9	10.7	11.2
7	100.6	100.1	98.1	99.6	83.1	82.2	79.5	81.6
8	99.5	101.3	103.4	101.4	81.6	81.3	85.9	82.9
9	69.7	71.1	71.9	70.9	26.4	33.5	29.2	29.7
10	73.8	72.3	71.4	72.5	79.4	79.2	77.9	78.8
11	90.7	88.2	90.8	89.9	17.5	17.5	17.4	17.5
12	85.2	87.5	81.1	84.6	47.1	42.6	45.9	45.2
13	80.7	84.1	80.6	81.8	69.9	65.8	72.7	69.5
14	82.9	81.2	82.5	82.2	41.5	42.5	43.0	42.3
15	79.4	81.4	77.7	79.5	42.0	41.6	42.1	41.9
16	77.0	80.0	79.1	78.7	19.9	20.5	18.1	19.5

The models are developed by regression analysis of the experimental data as listed in Table 6.4. The microhardness obtained for the coatings in all three sets of sixteen experiments has been subjected to statistical analysis. The analysis done for the microhardness is given in Table 6.5. The microhardness of coatings is analyzed by using variance analysis. The analysis is carried out by using the Taguchi method with significant values of process parameters. The data obtained by this analysis are shown in Table 6.5.

FIGURE 6.1: Main effect plot showing effect of process parameters on change in microhardness.

The model was obtained after performing regression analysis which is given as Equation 6.2:

$$\text{Microhardness} = 41.88 - 0.186 \text{ A} + 9.3 \text{ B} + 0.1537 \text{ C} - 0.0085 \text{ D} \tag{6.2}$$

where, microhardness in HV, A is the pH, B is the current density (A/dm^2), C is the amount of GNP concentration (mg/L) and D is the agitation (rpm).

The main effect plots of microhardness in terms of different process parameters are shown in Figure 6.1.

TABLE 6.5: Analysis of variance for microhardness

Source	DF	Adj SS	Adj MS	F-Value	P-Value	R^2
Regression	4	3444.81	861.20	29.31	0.000	91.42
pH	1	2.78	2.78	0.09	0.764	
Current density	1	1728.87	1728.87	58.85	0.000	
f-GNP	1	1698.63	1698.63	57.82	0.000	
Agitation	1	14.54	14.54	0.49	0.496	
Error	11	323.16	29.38			
Total	15	3767.97				

TABLE 6.6: Analysis of variance for corrosion protection efficiency

Source	DF	Adj SS	Adj MS	F-Value	P-Value	R^2
Regression	4	10036.1	2509.03	20.05	0.000	87.94
pH	1	42.6	42.63	0.34	0.571	
Current density	1	1439.9	1439.90	11.51	0.006	
f-GNP	1	8484.8	8484.77	67.81	0.000	
Agitation	1	68.8	68.82	0.55	0.474	
Error	11	1376.4	125.13			
Total	15	11412.5				

The analysis done for the corrosion protection efficiency is shown in Table 6.6. The corrosion protection efficiency has been investigated by variance analysis. The study is carried out by using the Taguchi method with significant values of process parameters. The data obtained by this analysis are shown in Table 6.6.

The model was obtained after performing regression analysis which is given as Equation 6.3:

$$\eta_{corr} = 4.0 + 0.73 \text{ A} + 8.48 \text{ B} + 0.343 \text{ C} + 0.0185 \text{ D} \tag{6.3}$$

where, η_{corr} represents corrosion protection efficiency in %, A is the pH, B is the current supplied in A, C is the amount of f-GNP concentration in mg/L and agitation in rpm.

The main effect plots of corrosion protection efficiency in terms of the process parameters are shown in Figure 6.2.

It can be seen from the main effect plot that for the considered range of process parameters used pH, current supplied and agitation to ECD bath have an insignificant effect on microhardness and corrosion protection efficiency. It can be observed from the main effect plots that GNP concentration in the ECD bath was found to be the most significant process parameter for microhardness and corrosion protection efficiency of Zn/f-GNP nanocomposite.

For the validation of the developed regression model, a few numbers of experiments have been carried out at random values of process parameters. The data for this set of experiments are shown in Table 6.7.

The optimized values of process parameters for the maximum value of the microhardness and corrosion protection efficiency are shown in Table 6.8.
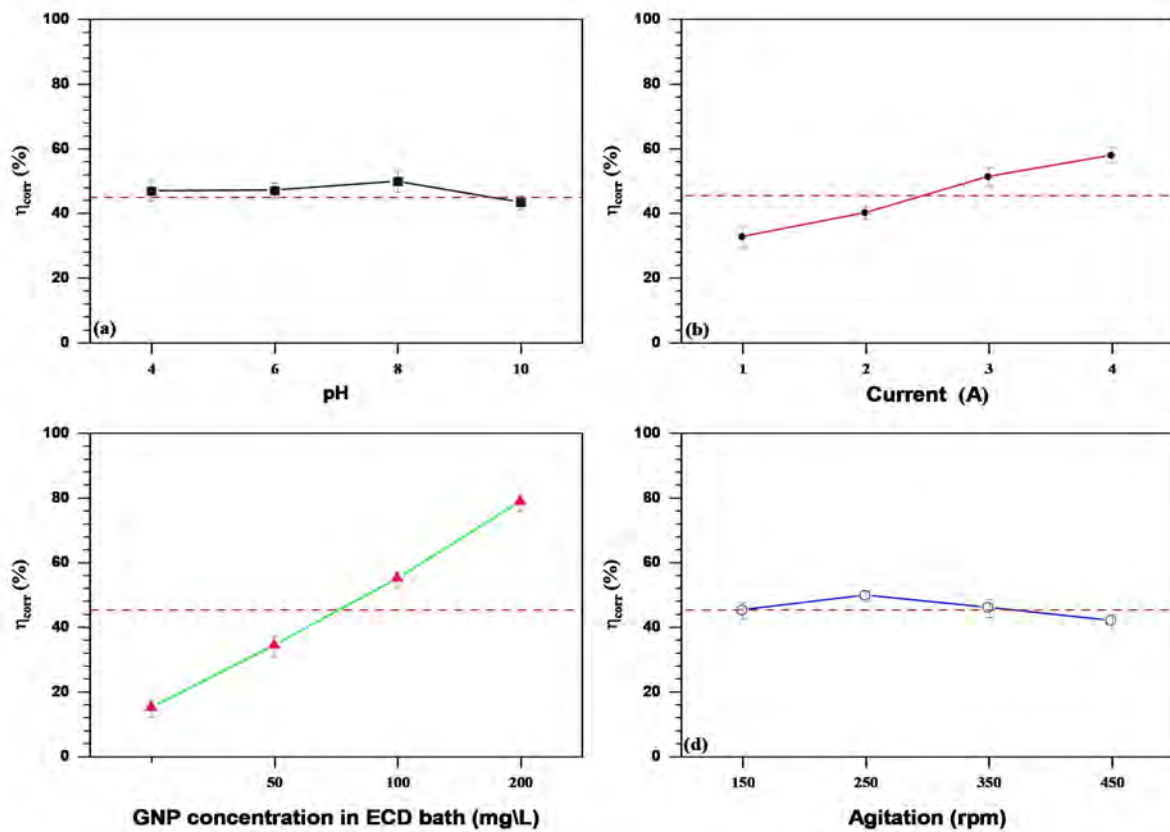
FIGURE 6.2: Main effect plot showing effect of process parameters on change in corrosion protection efficiency

TABLE 6.7: Experiments for the validation of the regression model developed by variance analysis.

Sr. No.	Process Parameters				Microhardness (HV)		$\eta_{\text{corr}}(\%)$	
	A	B	C	D	Regression predicted	Experimental	Regression predicted	Experimental
1	4	4	50	450	82.1	81.5 ± 2.1	66.3	67.2 ± 1.6
2	8	1	100	150	63.7	64.1 ± 2.2	55.4	54.5 ± 2.2
3	4	2	25	150	62.3	63.0 ± 1.8	35.2	45.7 ± 1.1

TABLE 6.8: The optimized values of process parameters for the maximum value of the microhardness and corrosion protection efficiency of Zn/f-GNP nanocomposite coatings.

Parameter No.	Description	Value
A	pH	4
B	Current supplied (A)	4
C	GNP concentration (mg/L)	200
D	Agitation	250

Zn/f-GNP nanocomposite are fabricated by M-ECD method and tested for microhardness and corrosion protection efficiency. The microhardness and corrosion protection efficiency of coatings are investigated by using a microhardness tester and potentiostat, respectively. All prepared coatings are tested under the identical conditions in the controlled environment. From the results, it is revealed that the microhardness and corrosion protection efficiency of the Zn/f-GNP nanocomposite increases with increase in the GNP concentration in the ECD bath. By Taguchi and regression analysis, it is found that the f-GNP concentration in the electrolyte is the most influencing parameter of the process for microhardness and corrosion protection efficiency of the Zn/f-GNP nanocomposite coatings. The addition of f-GNP decreases the crystallite size of the coating and hence requires more power for penetration, which results in a rise in microhardness [9]. More concentration of the zinc sulfate in the electrolyte results in an increase in the amount of Zn in the Zn/f-GNP nanocomposite coatings and improves the microhardness value. Also, f-GNPs act as an inert physical barrier to the initiation and growth of corrosion defects and hence improving the corrosion resistance [224].

6.3 Effect of ECD parameters on microhardness and corrosion protection efficiency of Zn/GNP nanocomposite coatings

We also studied the effect of ECD parameters such as pH, current, GNP concentration and agitation to ECD bath on the microhardness and corrosion protection efficiency of the Zn/GNP nanocomposite coating. Taguchi's statistical method has been employed to design the experiments. The available literature on Zn/GNP nanocomposite lacks any statistical investigation to conclude on parameter, which may significantly influence mechanical and corrosion properties of the Zn/GNP nanocomposite coating.

6.3.1 Experimental design

In the current investigation, pH, current, GNP concentration and agitation to ECD bath have been selected as process variables. The fixed ECD parameter for the experimental study is listed in Table 6.9. The respective process variable range selected for this study is listed in Table 6.10. The experiments have been designed based on the Taguchi method, and the results have been analyzed for microhardness and corrosion protection efficiency values of Zn/GNP nanocomposite coatings. Based on the results of the above studies. Analysis of variances (ANOVA) studies are performed to recognize the significances of process parameters. In the present work, we have investigated as the maximum hardness and high corrosion protection efficiency (Rp) as performance index and have chosen a larger-the-better S/N ratio for hardness and corrosion protection efficiency Equation 6.4.

$$\frac{S}{N} = -10log\frac{1}{N}\sum\frac{1}{y_2^i}.$$ (6.4)

where y_i is N_i observation of response variable.

In ECD method, major parameters, which influence the quality of formed Zn/GNP nanocomposite coating are 1) pH 2) current density 3) GNP concentration in the electrolyte and 4) agitation to ECD bath. With the four parameters as variables and considering four levels of each variable, a fractional factorial design of 16 experiments is done with L16 orthogonal array. Table 6.11 shows the respective process variable with their corresponding levels with which the nanocomposite coatings have experimented and optimization of microhardness and corrosion protection efficiency using Taguchi was performed using MINITAB software. The L16 orthogonal array having four parameters with four levels is selected to conduct experiments. The optimal level of the process parameters is obtained by using Taguchi optimization technique and a mathematical model is developed using regression analysis to predict the output from a selected range of process parameters. The experimental output values are used to find the best combination of optimal parameters. Here the objective is to maximize the microhardness and corrosion protection efficiency of Zn/GNP nanocomposite coatings. The higher the value of microhardness and corrosion protection efficiency better is the result. For the optimization of the process parameters using the Taguchi method, the objective is taken as larger is better.

TABLE 6.9: Fixed ECD parameter for experimental study of nanocomposite coating fabrication

Fixed parameters	Quantity
Electrodeposition time	60 min
Zinc sulfate	0.5 M
Ultrasonication time	60 min
Bath temperature	$27 \pm 2^{\circ}C$

6.3.2 Statistical analysis of experimental results

The statistical modelling for the microhardness and corrosion protection efficiency of Zn/GNP nanocomposite coatings prepared by ECD method has been studied and discussed. General first-order models are developed for estimating the microhardness and corrosion protection efficiency of the coatings. The models are developed by regression analysis of the experimental data as listed in Table 6.11. The microhardness obtained for the coatings in all three sets of sixteen experiments have been subjected to statistical analysis as given in Table 6.12. The analysis done for the microhardness is given in Table 6.13. The microhardness of coatings is analyzed by using

TABLE 6.10: Input variables and their levels for experimental study of nanocomposite coating fabrication.

Parameter No.	Description	Level 1	Level 2	Level 3	Level 4
A	pH	3	3.5	4	4.5
B	Current density (A/dm^2)	2	4	6	8
C	GNP concentration (mg/L)	25	50	100	200
D	Agination (rpm)	150	250	350	450

TABLE 6.11: The basic Taguchi L16 orthogonal array

Exp. No.	Parameters				Notation
	A	B	C	D	
1	1	1	1	1	$A_1B_1C_1D_1$
2	1	2	2	2	$A_1B_2C_2D_2$
3	1	3	3	3	$A_1B_3C_3D_3$
4	1	4	4	4	$A_1B_4C_4D_4$
5	2	1	2	3	$A_2B_1C_2D_3$
6	2	2	1	4	$A_2B_2C_1D_4$
7	2	3	4	1	$A_2B_3C_4D_1$
8	2	4	3	2	$A_2B_4C_3D_2$
9	3	1	3	4	$A_3B_1C_3D_4$
10	3	2	4	3	$A_3B_2C_4D_3$
11	3	3	1	2	$A_3B_3C_1D_2$
12	3	4	2	1	$A_3B_4C_2D_1$
13	4	1	4	2	$A_4B_1C_4D_2$
14	4	2	3	1	$A_4B_2C_3D_1$
15	4	3	2	4	$A_4B_3C_2D_4$
16	4	4	1	3	$A_4B_4C_1D_3$

TABLE 6.12: Experimental results for microhardness and corrosion protection efficiency

Exp. No.	Microhardness (HV)				$\eta_{corr}(\%)$			
	Ist	IInd	IIIrd	Average	Ist	IInd	IIIrd	Average
1	59.8	62.7	61.1	61.2	11.2	12.1	13.3	12.2
2	84.1	82.8	80	82.3	31.0	28.5	36.5	32
3	110.4	110.1	112.5	111	63.5	61.8	62.2	62.5
4	146.4	149.5	147.5	147.8	74.7	81.8	79.6	78.7
5	72.0	70.3	74	72.1	28.9	33.1	24.4	28.8
6	68.8	65.8	71.5	68.7	26.4	22.8	23.7	24.3
7	144.4	142.9	143.5	143.6	75.2	72.8	70.7	72.9
8	133.2	141.6	132	135.6	73.5	78.6	77.1	76.4
9	80.6	79.3	84.3	81.4	30.9	31.2	36.3	32.8
10	130.2	134.5	125	129.9	72.5	68.4	71.0	70.6
11	75.9	79.2	70.5	75.2	33.8	28.6	35.0	32.5
12	102.5	100.4	105.5	102.8	65.2	66.6	63.6	65.1
13	100.1	107.4	101.5	103	53.6	63.9	55.6	57.7
14	96.4	93.5	100.5	96.8	45.5	37.4	43.4	42.1
15	71.8	81.3	75.2	76.1	36.7	39.7	35.2	37.2
16	89.7	88.1	85.3	87.7	39.1	41.5	41.5	40.7

TABLE 6.13: Analysis of variance for microhardness

Source	DF	Adj SS	Adj MS	F-Value	P-Value	R^2
Regression	4	10963.0	2740.76	40.07	0.000	93.6
pH	1	271.6	271.58	3.97	0.072	
Current density	1	3030.7	3030.72	44.31	0.000	
GNP	1	7659.8	7659.79	112.00	0.000	
Agitation	1	0.9	0.92	0.01	0.903	
Error	11	752.3	68.39			
Total	15	11715.4				

TABLE 6.14: Analysis of variance for corrosion protection efficiency

Source	DF	Adj SS	Adj MS	F-Value	P-Value	R^2
Regression	4	5940.04	1485.01	23.03	0.000	89.33
pH	1	14.88	14.88	0.23	0.640	
Current	1	2248.26	2248.26	34.87	0.000	
GNP	1	3524.27	3524.27	54.66	0.000	
RPM	1	152.63	152.63	2.37	0.152	
Error	11	709.29	64.48			
Total	15	6649.33				

variance analysis. The analysis is carried out by using the Taguchi method with significant values of process parameters. The data obtained by this analysis are shown in Table 6.13.

The model was obtained after performing regression analysis which is given in Equation 6.5:

$$\text{Microhardness} = 50.6 + 1.840 \text{ A} + 12.33 \text{ B} + 0.3263 \text{ C} + 0.0023 \text{ D} \tag{6.5}$$

where, microhardness in HV, A is the pH, B is the current (A), C is the amount of GNP concentration (mg/L) and D is agitation (rpm).

The main effect plots of microhardness in terms of different processes parameter are shown in Figure 6.3.

The analysis done for the corrosion protection efficiency is shown in Table 6.14. The corrosion protection efficiency has been investigated by variance analysis. The study is carried out by using the Taguchi method with significant values of process parameters. The data obtained by this analysis are shown in Table 6.14.

The model was obtained after performing regression analysis which is given as Equation 6.6:

$$\eta_{corr} = 13.4 + 0.431 \text{ A} + 10.6 \text{ B} + 0.2214 \text{ C} + 0.0276 \text{ D} \tag{6.6}$$

where Rp represents corrosion protection efficiency in kΩ.cm$_2$, A is the pH, B is the current density (A/dm^2), C is the amount of GNP concentration (mg/L), and D is agitation (rpm).

The analysis done for the corrosion protection efficiency is shown in Table 5. The deposition height has been analyzed by using variance analysis. The study has been carried out using the Taguchi method with significant values of process parameters. The data obtained by this analysis

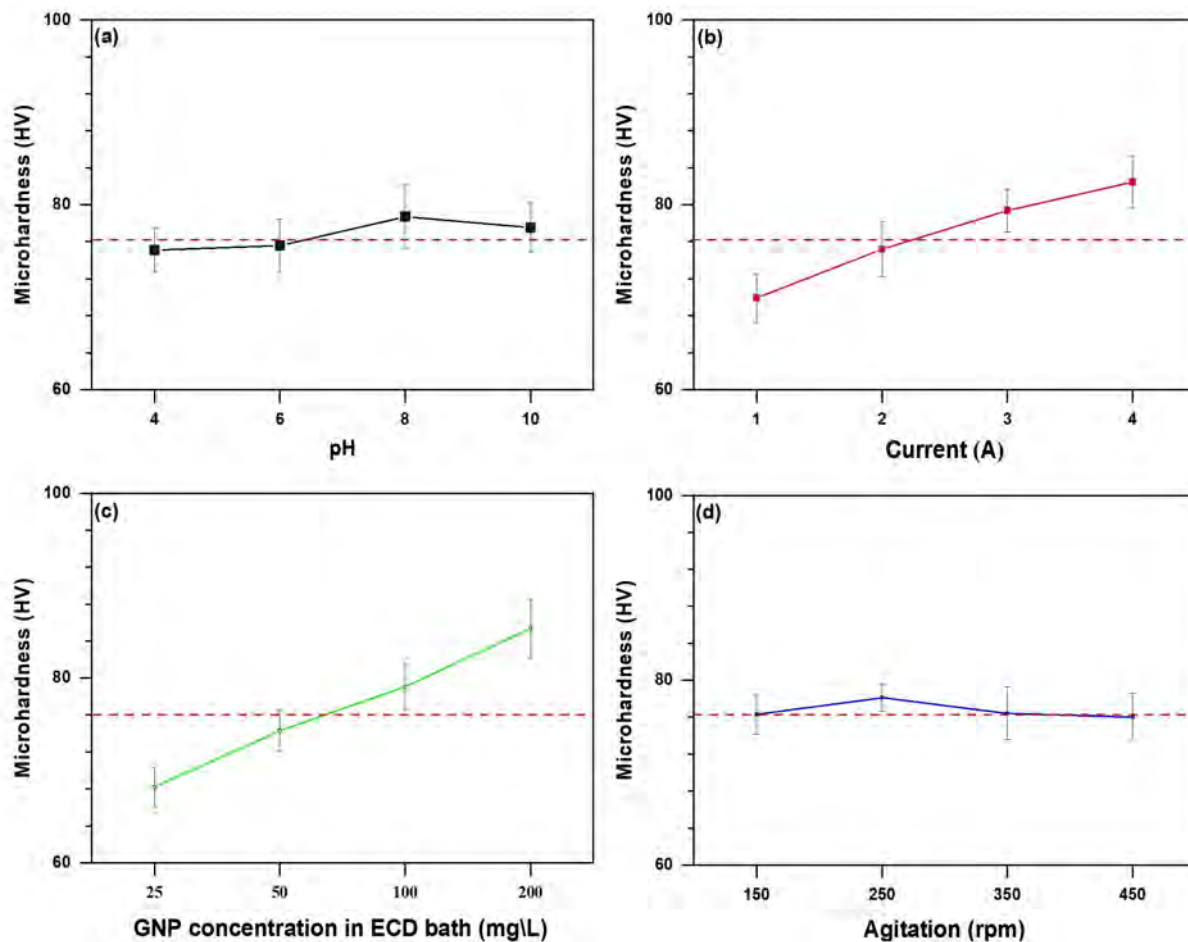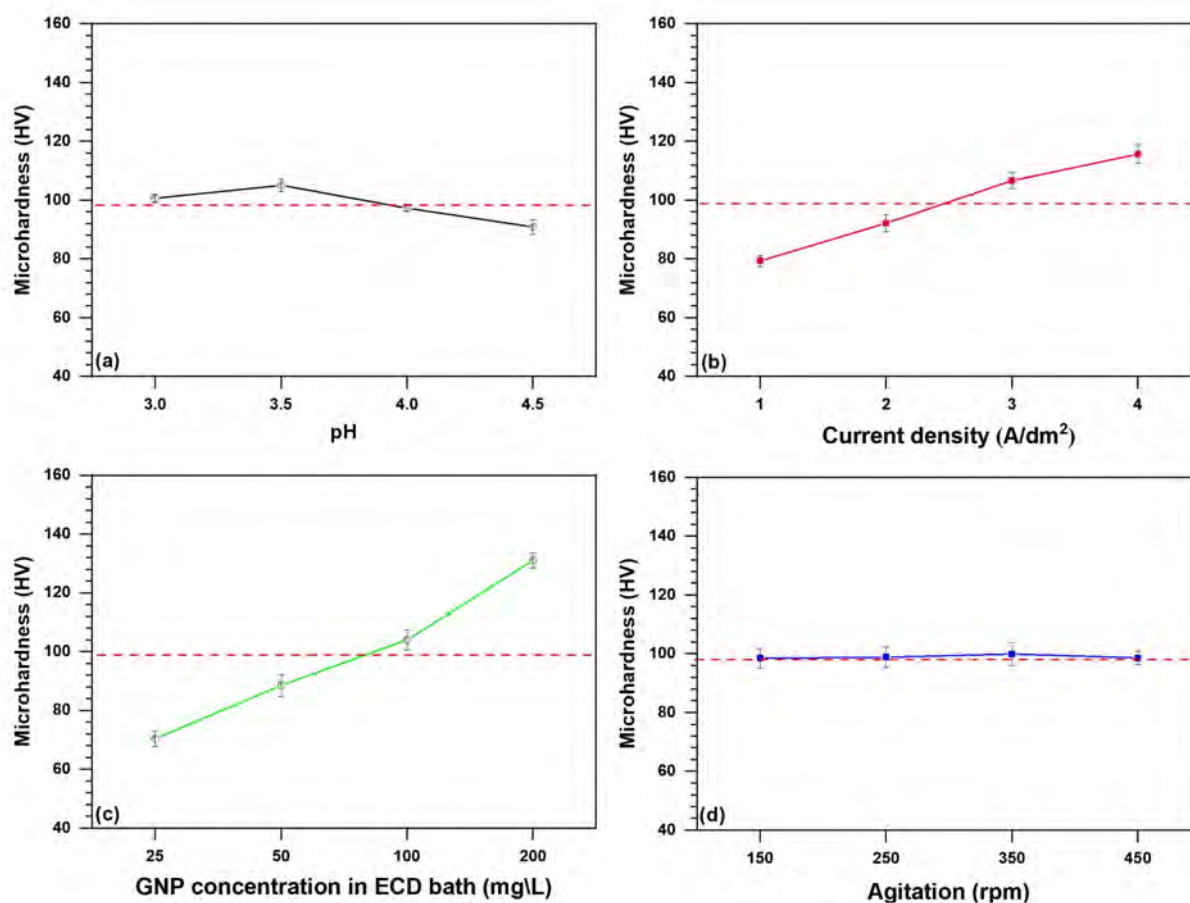FIGURE 6.3: Main effect plot showing effect of process parameters on change in Microhardness.

TABLE 6.15: Experiments for the validation of the regression model developed by variance analysis.

Sr. No.	Process Parameters				Microhardness (HV)		$\eta_{\text{corr}}(\%)$	
	A	B	C	D	Regression predicted	Experimental	Regression predicted	Experimental
1	3	4	50	450	122.7	120.5 ± 2.7	80.5	67.2 ± 1.9
2	4	1	100	150	103.2	98.1 ± 1.4	52.0	54.5 ± 1.0
3	4.5	2	25	150	92.7	94.7 ± 2.4	46.2	44.1 ± 1.5

are shown in Table 5.

The main effect plots of corrosion protection efficiency in terms of different process parameters are shown in Figure 6.4.

For the validation of the developed regression model, a few numbers of experiments have been carried out at random values of process parameters. The data for this set of experiments are shown in Table 6.15.

The optimized values of process parameters for the maximum value of the microhardness and corrosion protection efficiency are shown in Table 6.16.
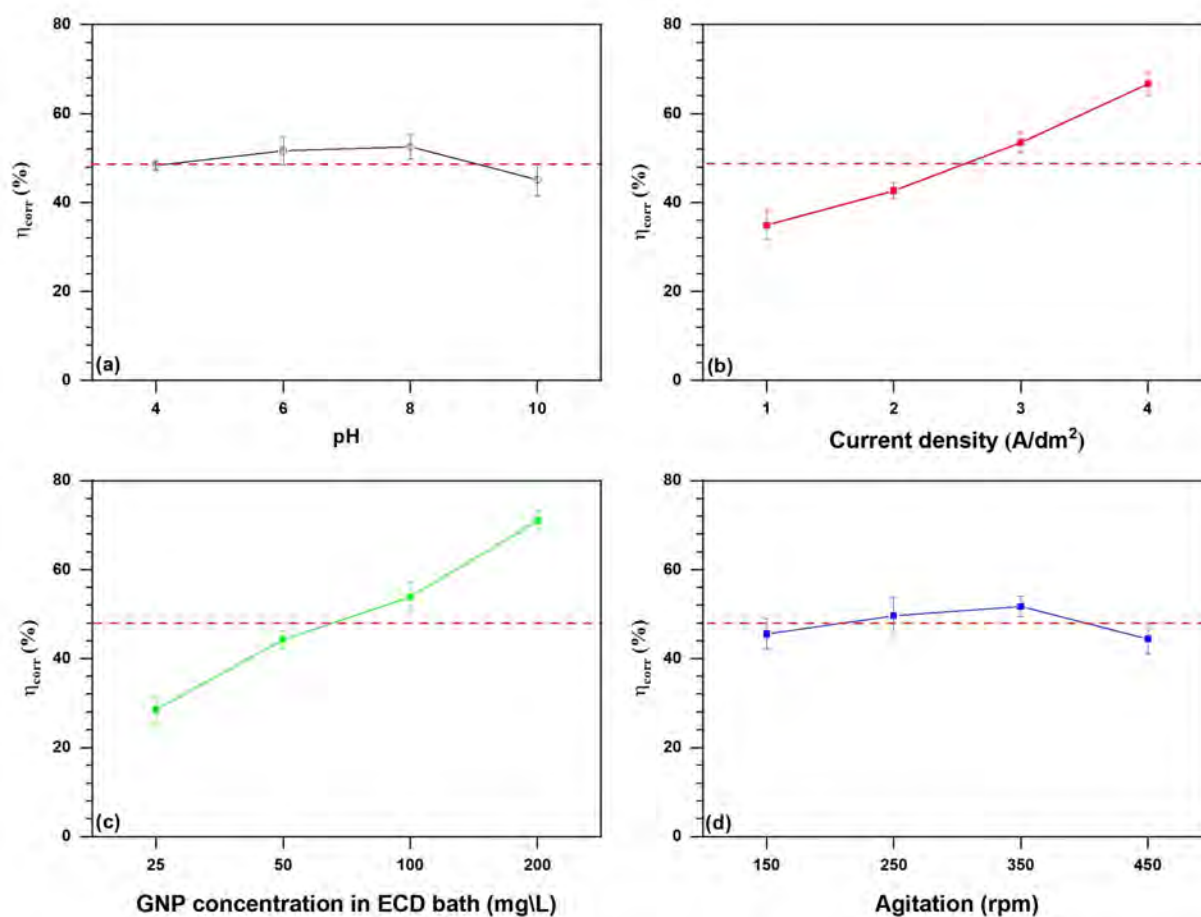
FIGURE 6.4: Main effect plot showing the effect of process parameters on change in corrosion protection efficiency.

TABLE 6.16: The optimized values of process parameters for the maximum value of the microhardness and corrosion protection efficiency of Zn/GNP nanocomposite coatings.

Parameter No.	Description	Value
A	pH	3.5
B	Current density (A/dm^2)	4
C	GNP concentration (mg/L)	200
D	Agitation	350

Zn/GNP nanocomposite coatings are fabricated by a modified ECD method and tested for microhardness and corrosion protection efficiency. The microhardness and corrosion protection efficiency of prepared Zn/GNP nanocomposite coatings were investigated by using a microhardness tester and potentiostat, respectively. All prepared Zn/GNP nanocomposite coatings are tested under identical conditions in a controlled environment. The obtained results reveal that the microhardness and corrosion protection efficiency of the Zn/GNP nanocomposite coatings increases with increasing the GNP concentration in the ECD bath. By Taguchi and regression analysis, it is found that the GNP concentration in the electrolyte is the most influencing parameter of the process for microhardness and corrosion protection efficiency of the Zn/GNP nanocomposite

coatings. The addition of GNP reduced the Zn matrix's crystallite size and required more power for penetration; hence, the microhardness is improved. A higher concentration of high-strength GNP in the electrolyte increases improve the microhardness value in the Zn/GNP nanocomposite [300]. The reinforcement of GNPs in the Zn matrix fills the defects such as several voids, gaps and cracks owing to its nano size, which contributes to the outstanding resistance to the Zn/GNP nanocomposite to undergo corrosion [301].

6.4   Conclusion

- Zn/f-GNP nanocomposite coatings were fabricated by M-ECD method followed by powder metallurgy method and characterized for microhardness and corrosion protection efficeincy. The statistical study of the effect of electro-co-deposition parameters on microhardness and corrosion protection efficiency was carried out using Taguchi statistical method.

- The obtained results revealed that the GNP concentration in the ECD bath and current supplied to ECD bath in the electrolyte significantly influenced the synthesis of GNP-reinforced Zn matrix nanocomposite coatings.

- The other process parameters such as pH of the solution and agitation to ECD bath showed less significance on the microhardness and corrosion protection efficiency of the Zn/f-GNP nanocomposite.

- Also, Zn/GNP nanocomposite coatings were fabricated by ECD method and characterized for microhardness and corrosion protection efficiency.

- The statistical study showed that the GNP concentration in the ECD bath and current density in the electrolyte had the greatest influence on the synthesis of Zn/GNP nanocomposite coatings.

- The other ECD parameters such as the current supplied and pH of the electrolyte exhibited a less significant effect on the microhardness and corrosion resistance.

- The optimized values of pH, current density, GNP concentration and agitation to ECD bath for the maximum value of the microhardness and corrosion protection efficiency of Zn/GNP nanocomposite are 3.5, 4 A/dm^2, 200 mg/L and 250 rpm, respetively.

Chapter 7

Alloy−Zn/GNP Nanocomposites: Synthesis and Properties

7.1 Overview

The alloying of Zn with other metals such as Cu (Copper)[173], Ni (Nickel) [301], Fe (Iron) [302], Mg (Magnesium) [303], and others [304], in a Zn/GNP nanocomposite is a process of incorporating these metals into the Zn matrix to enhance its properties. This can result in improved thermal and electrical conductivity, increased strength and toughness, and improved corrosion resistance, among others, depending on the specific combination of alloy matrix used. The process of alloying with different metals can be achieved through various methods, including ball milling, electro−co−deposition, and chemical vapour deposition. The resulting nanocomposite material has potential applications in various fields such as energy storage, catalysis, and biomedicine.

In this study, Zn−Cu alloys have been considered as potential candidates for bioimplant applications due to their moderate corrosion rate and admirable mechanical properties with nontoxic nature to the human body. However, with the incorporation of advanced reinforcements, such as carbon allotropes, the properties and applicability of Zn−Cu alloy matrix can be further enhanced. Here, GNP-reinforced Zn−Cu/GNP nanocomposites were synthesized through a modified electro co−deposition method with different concentrations of GNP (25, 50 and 100 mg/L) in the ECD bath. The prepared powder samples were compacted and sintered to form pellets. The pellets were tested for mechanical and $in-vitro$ corrosion. The obtained micro−hardness, compressive yield strength (CYS) and ultimate compressive strength (UCS) of Zn−Cu/GNP (100 mg/L) nanocomposite are 151 HV, 340 MPs and 362 MPa with the increment of 84.1%, 118% and 70.7% compared to pure Zn−Cu alloy, respectively. The reduced wear rates and friction coefficients of Zn−Cu/GNP nanocomposites attribute to crystallite size refinement and GNP content. The electrochemical corrosion rate is reduced by 66.6% from 33×10^{-3} mm year^{-1} for pure Zn−Cu alloy to 11×10^{-3} mm year^{-1} for Zn−Cu/GNP (100 mg/L) nanocomposites, owing to GNP barrier protection. The $in-vitro$ cytotoxicity assessment reveals that the prepared Zn−Cu/GNP

nanocomposite is non−toxic for GNP concentration up to 50 mg/L in the ECD bath. The results show that a non−toxic Zn−Cu/GNP nanocomposite with outstanding tribo−mechanical and anti−corrosion properties can be synthesized by the proposed method.

In another study, low-cost and industrial scalable γ-Zn−Ni/GNP nanocomposite coatings were electro-co-deposited from an acid-sulfate-based electrolyte bath. The microstructure, morphology, composition, microhardness, wear performance, corrosion resistance and anti-bacterial properties of the nanocomposite coatings were investigated in detail by comparing them with Zn-Ni alloy coating. The XRD diffraction peaks of prepared coatings confirm the presence of the γ phase of Zn-Ni alloy. Results suggested that the addition of GNP effectively reduced the crystallite size and altered the morphology. As a result, the microhardness, wear performance and corrosion resistance were improved significantly. The γ-Zn−Ni/GNP nanocomposite coating prepared with 100 mg/L of GNP addition in an electrolyte bath displayed the highest microhardness of 243 HV and the lowest coefficient of friction of 0.32. The anti-bacterial activity tests confirmed that the γ-Zn−Ni/GNP (100 mg/L) nanocomposite coating has the highest anti-bacterial activity against both Escherichia coli (E. coli) and Staphylococcus aureus (S. aureus).

7.2 Zn−Cu/GNP nanocomposites for biodegradable application

Nanomaterials and nanocomposites have emerged as suitable alternatives to overcome the limitations of available alloys and nanocomposites and can be applied to various science and engineering fields [8], [305], [306]. Compared to polymeric and ceramic nanocomposites, metallic nanocomposites can deliver superior tribo−mechanical performance for bioimplant applications [307], [308]. According to the literature, Zn−based alloys and nanocomposites have a moderate corrosion rate compared to available Mg, and Fe-based alloys and nanocomposites, and their implants can hold mechanical strength until the completion of their clinical role [288], [309], [310]. In practice, the addition of Cu enhances the tribo−mechanical properties of Zn matrix [311], [312]. Cu is also an essential element of the human body and its deficiency can lead to aberrant cardiac electrophysiology, abnormal glucose and cholesterol metabolism, and chronic immune and neurobehavioral effects [313]. Tang et al. [312] reported that the mechanical properties (mainly the plasticity) of Zn−Cu alloys are superior to the other reported Zn−based alloys such as Zn−X (X = Mg, Sr, Ca) alloys. They also reported that the corrosion rate of Zn−xCu (x = 1–4 wt%) alloys in simulated body fluid (SBF) medium vary from 26×10^{-3} mm year^{-1} to 33×10^{-3} mm year^{-1}, which is much lower compared to the reported Mg alloys. In another study, Niu et al. [311] investigated the in−vitro cytotoxicity behavior of Zn−4%Cu and reported the acceptable range of toxicity for human endothelial cells.

Huang et al. [314] have patented the Zn−xCu (x = 1–4 wt%) alloys prepared by as−cast alloying method followed by hot processing. They reported that the Cu addition enhances the mechanical properties of Zn−Cu alloy and for Zn−4%Cu alloy sample shows the ultimate tensile strength of 271 MPa. Also, they suggested that the corrosion rate of 0.18 mm year^{-1} in a Hank's solution at

37 °C is adequate for bioimplant applications such as bone plates and screws. However, It is also reported that excessive Cu in human body causes neurodegenerative diseases in the human body, including Alzheimer's, Menkes, and Wilson disease [315].

This research uses the electro co−deposition method to synthesise Zn−Cu/GNP nanocomposite powder. The purpose of the modified electro co−deposition method is to avoid the severe mechanical mixing steps of ball milling during powder metallurgy and thus prevent structural damage to GNP layers. Here, the ultrasonicated impermeable GNP layers are electrochemically mixed and co−deposited with Zn^{2+} and Cu^{2+} on the cathode to form Zn−Cu/GNP nanocomposite powder. The obtained Zn−Cu/GNP nanocomposite powder samples from the ECD bath are vacuum dried, uniaxially compacted and sintered. The effects of GNP content on the microstructural, morphological, tribo−mechanical and corrosion properties of Zn−Cu/GNP nanocomposite are investigated systematically. The *in−vitro* cytotoxicity assessment is also conducted to compare the toxicity of prepared nanocomposite samples with the increasing GNP concentrations in the ECD bath.

7.2.1 Experimental details

7.2.1.1 Material

The metal salts and reagents were procured from Merck Specialties Pvt. Ltd. The graphene (thickness 5–15 nm; surface area 500 m^2g^{-1}) were used as reinforcement and supplied by Alfa Aesar. Deionized water of pH 6.9−7 was used for dilution of reagents and other cleansing purposes.

7.2.1.2 Synthesis process

The ECD bath consisted of $ZnSO_4.7H_2O$ (0.2M), $CuSO_4.5H_2O$ (0.01 M), and Ethylenediaminetetraacetic acid (0.15 M) (complexing agent). The GNP (25, 50, and 100 mg/L) was added to the ECD bath under continuous magnetic stirring at 300 rpm for 20 minutes and followed by sonication using direct probe sonication at 20 kHz, 500 W for one hour. Magnetic stirring and direct probe sonication were provided to dissolve the reagents and unbound the agglomerated GNP in the ECD bath. The experimental setup is illustrated in Figure 7.1a and b and working is explained in **chapter 3**. The experimental parameters from Table 7.1 were followed during the synthesis of nanocomposites. The agglomerated clouds of positively charged Zn^{2+} and Cu^{2+} metal ions along with the unbound GNP were co−deposited at exposed cathode tip to form Zn−Cu/GNP nanocomposite. The dried powder nanocomposite samples were stored in an inert atmosphere to avoid oxidation. The dried powder samples were uniaxially compacted at 400 MPa and sintered using an electric furnace at 357 °C temperature ($\sim$ 0.80 Tm, melting temperature of Zn-Cu alloy matrix) for 60 min in an inert atmosphere then followed by furnace cooling, as illustrated in thermal procedure in Figure 7.1c [316]. Pure Zn−Cu alloy samples were prepared without adding GNP in the ECD bath.
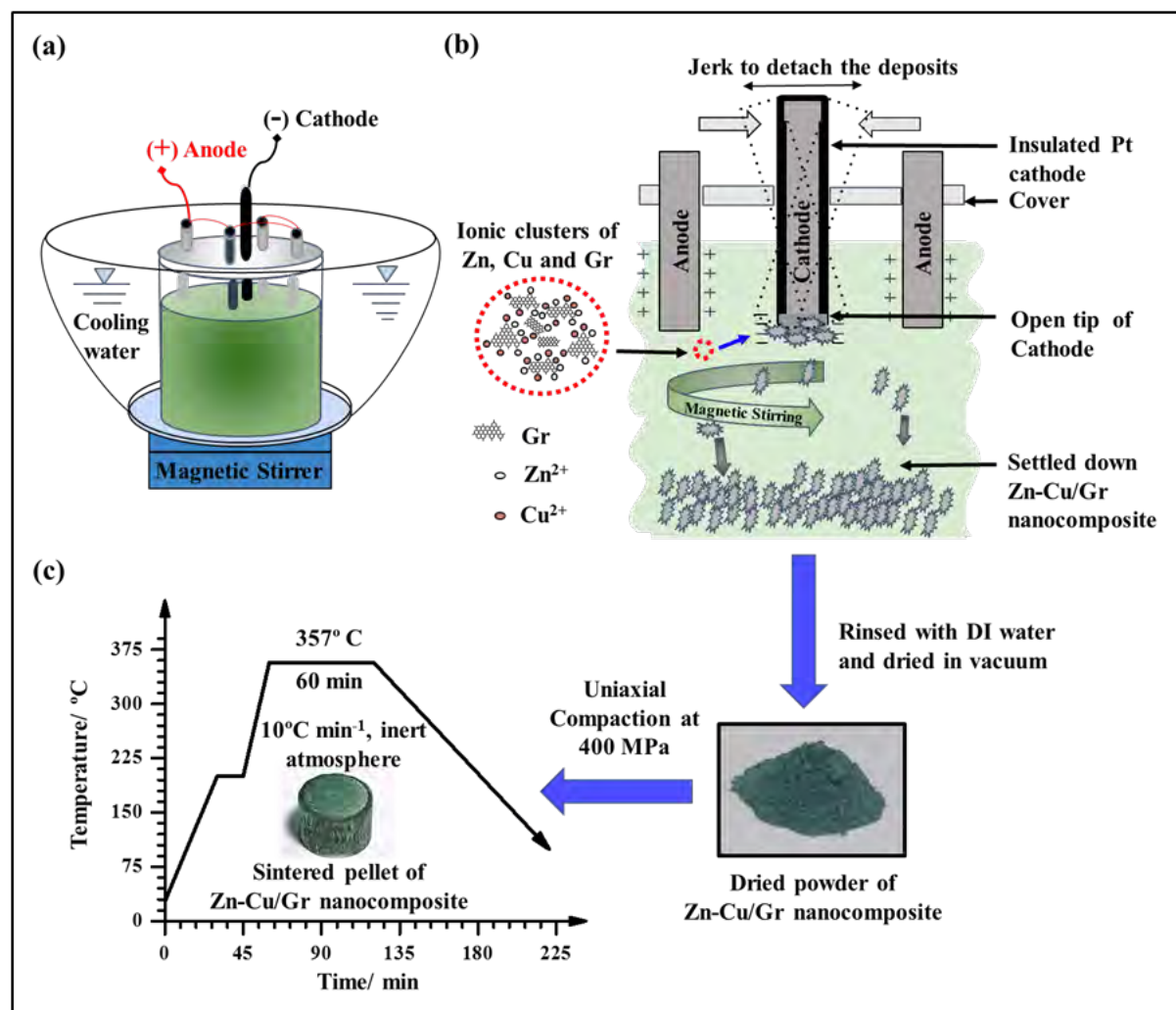
FIGURE 7.1: Synthesis process: (a) experimental setup; (b) co-deposition of Zn-Cu/GNP nanocomposite; Sequence of the thermal procedure applied to sinter Zn-Cu/GNP nanocomposite pellets. GNP is represented as Gr.

TABLE 7.1: ECD bath composition and process parameters

ECD parameters		Bath composition	
pH	10	ZnSO4.7H2O	0.2 M
DC current supply	6 A	CuSO4.5H2O	0.01 M
Agitation	350 - 400 rpm	EDTA	0.15 M
Run time	3 hours.	GNP concentration	25, 50, and 100 mg/L
Temperature	37º C		

7.2.1.3 Microstructural and morphological characterization

X−ray diffractometer (XRD) (Model RIGAKU MiniFlex−II model) (Cu K radiation, $\lambda = 0.15418$ nm) was used to observe the crystallite structure and crystallite size of prepared nanocomposite samples. The diffraction data were collected with a scanning rate of 2 °min^{-1}. The morphology and chemical compositions of prepared nanocomposite samples were determined using field emission scanning electron microscopy (FESEM, JEOL JSM − 6390 LV) with attached energy

dispersive spectrometry (EDS).

7.2.1.4 Tribo−mechanical properties

Microhardness test prepared nanocomposite samples were conducted to investigate the effect of GNP reinforcement on the plasticity of Zn−Cu alloy matrix, which indirectly reveals the ability to resist wear loss. Mitutoyo HM−200 micro Vickers hardness testing machine was used to measure the microhardness using a load of 20 g for 15 s on polished surfaces. The compression test was conducted on uniaxially compacted and sintered nanocomposite samples to compare the effect of GNP content on mechanical strength. The specimens of cylindrical shape (6 mm in diameter by 12 mm in height) were tested as per ASTM standard E9. BISS UNO 100 universal testing machine of 100 kN capacity was used for the compression test with the strain rate of $7 \times 10-4 \text{ s}^{-1}$.

The prepared nanocomposites were investigated for tribological performance using a tribometer (DUCOM). The experimental setup for tribological tests consisted of pin−on−disk arrangement with 6 mm diameter GCr−15 steel grade pin at a constant applied load of 5 N against the rotating disk of the prepared nanocomposite sample. The disk was rotating at a constant speed of 300 rpm with track diameter of 10 mm. The linear travel velocity of the pin was 0.157 m s^{-1} for 600 s under dry conditions (humidity 34%) at a temperature of about 27°C.

7.2.1.5 Corrosion test

The immersion test of prepared Zn−Cu/GNP nanocomposite samples was performed at 37$^{\text{o}}$ C temperature in SBF (simulated body fluid), pH = 7.4 [317]. The immersion media was daily replaced by a newly prepared SBF medium to maintain the pH constant. The samples were rinsed by running DI water and ethanol subsequently to remove the degrades before measuring their residual weight. The corrosion rate, CR$_{Wt}$ (in mm year^{-1}) was calculated after immersion of 14, 21, and 28 days of immersion in SBF solution using the following equation given in **Chapter 3** [318].

An electrochemical process was also used to test the corrosion behavior of prepared Zn−Cu/GNP nanocomposite samples via potentiodynamic polarization curves generated by potentiostat (CHI604E Potentiostat, USA). A three−electrode system was adopted with the standard Ag/AgCl cell as a reference electrode. The experimental tests were performed at 37$^{\text{o}}$ C temperature in SBF, pH = 7.4. The range and scan rate were −0.4 V to +0.1 V and 0.5 mV s^{-1}, respectively. The corrosion current, E$_{corr}$ (in mV), corrosion current, I$_{corr}$ (in A cm−2) and corrosion potential were obtained from potentiodynamic polarization curves, and electrochemical corrosion rate, CR$_{EC}$ (in mm year^{-1}) was calculated using the following equation given in **chapter 3** [319].

TABLE 7.2: EDS data of Zn-Cu/GNP nanocomposite samples

Samples	Atomic percent/ %			Weight percent/ %		
	Zn	Cu	C	Zn	Cu	C
Zn-Cu/GNP (25 mg/L)	84.98	6.09	8.91	91.83	6.4	1.77
Zn-Cu/GNP (50 mg/L)	81.95	5.4	12.58	91.49	5.93	2.58
Zn-Cu/GNP (100 mg/L)	73.99	4.19	21.8	90.15	4.97	4.88

7.2.2 Results and Discussion

7.2.2.1 Microstructural and morphological behavior

The XRD patterns for pure Zn−Cu alloy and Zn−Cu/GNP nanocomposite samples are shown in Figure 7.2a. The dominant crystal orientation of nanocomposite depends on the ECD bath composition and process parameters. The XRD patterns of all prepared samples have shown the intensity peaks for dominant hexagonal−close−packed Zn matrix (JCPDS Card No. 004–0831).12 Also, lower intensity peaks are obtained for face−centered−cubic Cu matrix (JCPDS Card No. 003–1018) [312]. Compared to the XRD pattern of Zn−Cu alloy, the Zn−Cu/GNP nanocomposite powder samples show peak broadening and shifting towards the higher angle due to the micro−stresses caused by GNP content [298]. The crystallite sizes, d (in nm) of the prepared nanocomposites were calculated using the Scherrer equation given in **chapter 3**. Here is the X−ray wavelength with the value of 0.15418 Å, is the Bragg diffraction angle and is the line broadening at half the maximum intensity for Zn (1 0 1) plane. Figure 7.2b shows the obtained average crystallite sizes values for prepared powder samples correspond. After reinforcement of GNP, the average crystalline size was reduced by 18.5% from 44.39 nm for pure Zn−Cu alloy to 36.17 nm for Zn−Cu/GNP (100 mg/L) nanocomposites powder sample. The reduced crystallite size was attributed to the reinforcement of impermeable GNP layers in the alloy matrix, which hindered the process of large crystallite size formation of Zn−Cu/GNP nanocomposite during electrochemical mixing and co−deposition.

The surface morphology of prepared pure Zn−Cu alloy and Zn−Cu/GNP nanocomposite powder samples was studied by FESEM. FESEM image from Figure 7.3a appeared with thin chip shapes of pure Zn−Cu alloy sample. However, the electrochemical mixing and co−deposition of GNP layers and alloy matrix disappeared the chip shapes of Zn−Cu alloy matrix, and the clusters of Zn−Cu/GNP nanocomposite appeared in the FESEM image, from Figure 7.3b–d. EDS data revealed the atomic and weight percentage of individual elements of Zn−Cu/GNP nanocomposite powder samples (from Figure 7.4a–c and Table 7.2). Here, it was observed that the obtained content of carbon gradually varied from 1.77 wt. % to 4.88 wt. % by changing the graphene concentration from 25 mg/L to 100 mg/L of ECD bath, respectively. Also, EDS data confirms the uniform dispersion of GNP layers across Zn−Cu/GNP nanocomposite clusters, as shown in Figure 7.4a–c. The uniform dispersion of GNP layers can serve as a barrier for the dislocation movement and protect the metal alloy matrix from a corrosive environment.
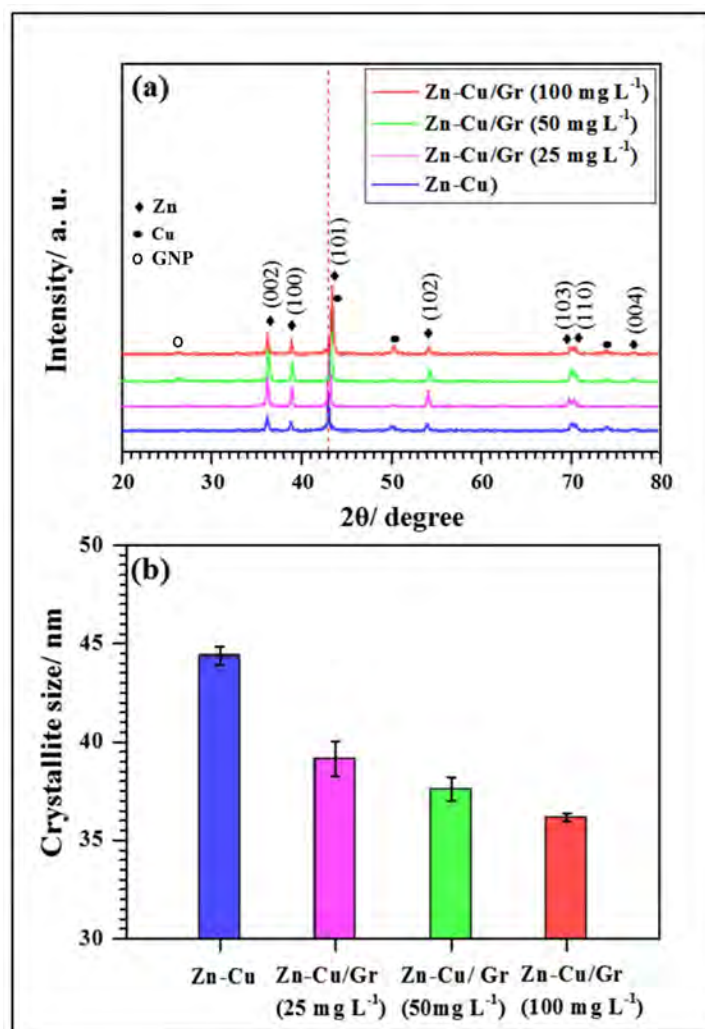
FIGURE 7.2: (a) XRD patterns; (b) crystallite sizes of pure Zn-Cu alloy and Zn-Cu/GNP nanocomposite powder samples. GNP is represented as Gr.

7.2.2.2   Tribo−mechanical properties

The microhardness of compacted and sintered polished nanocomposite samples is shown in Figure 7.5a. Compared to pure Zn−Cu alloy, higher microhardness values were observed in Zn−Cu/GNP nanocomposite for all GNP concentrations. The average microhardness increased by 84.14% from 82 HV for pure Zn−Cu alloy samples to 151 HV for Zn−Cu/GNP (100 mg/L) nanocomposite samples. Here, the GNP content reduces the crystallite size of Zn−Cu/GNP nanocomposite and imparts grain−strengthening effect which helps to reduce the dislocation movement in nanocomposite. The higher shear strength GNP layers across the Zn−Cu/GNP nanocomposite clusters serve as a resistant barrier to the dislocation movement in the nanocomposite, which further improves the average microhardness [268].

General compression tests were conducted for Zn−Cu/GNP nanocomposite samples to investigate the strengthening behavior offered by GNP content. Figure 7.5b shows the engineering stress−strain curves obtained from the compression test of cylindrical specimens of pure Zn−Cu
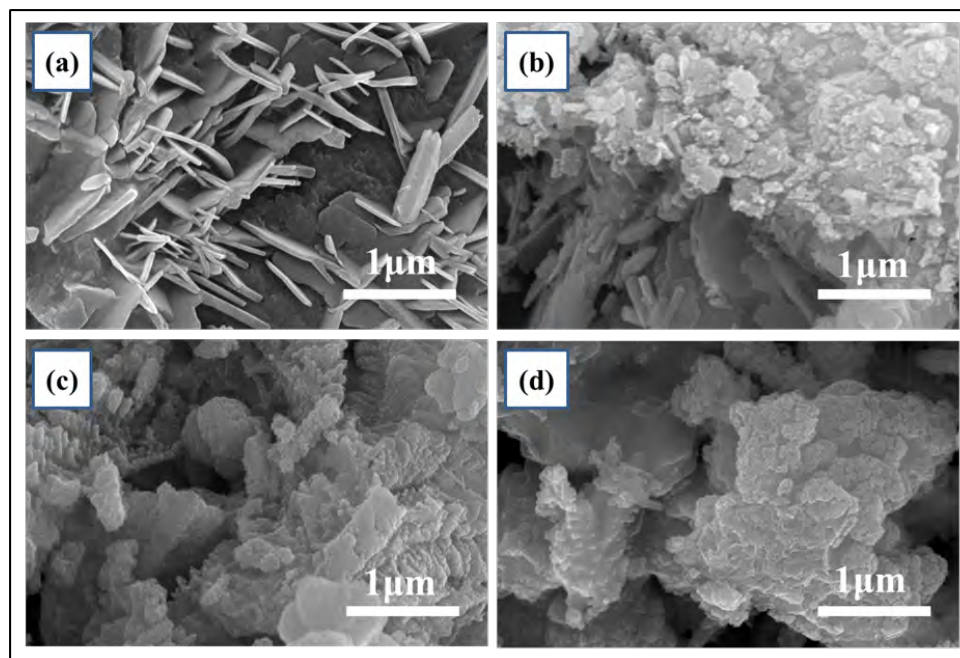
FIGURE 7.3: FESEM images: (a) pure Zn-Cu; (b-c) Zn-Cu/GNP nanocomposite for all prepared
concentrations of Gr: (b) 25 mg/L; (c) 50 mg/L; (d) 100 mg/L.

alloy and Zn−Cu/GNP nanocomposite samples. The compressive yield strength (CYS), ultimate
compressive strength (UCS) and compressive strain (ε_c) of pure Zn−Cu alloy and Zn−Cu/GNP
nanocomposite are tabulated in Table 7.3. The obtained value of CYS and UCS increased by
118.5% and 70.7% from 156 MPa and 212 MPa for pure Zn−Cu alloy to 341Mpa and 362 MPa
for Zn−Cu/GNP (100 mg/L) nanocomposite sample, respectively, which revealed that the GNP
content in Zn−cu nanocomposite increased the compressive strength. Whereas, ε_c reduced by
53.4% from 0.58 for pure Zn−Cu alloy to 0.27 for Zn−Cu/GNP nanocomposite. The improvement
in compressive strength is directly associated with (i) aspect ratio of GNP layers, (ii) interfacial
bonding between GNP layers and Zn−Cu alloy matrix, and (iii) uniform distribution of GNP
layers in Zn−Cu alloy matrix. It is reported that the wrinkled morphology of GNP layers tends
to straighten and flatten during plastic deformation under uniaxial load, which offers initial
ductility in nanocomposite after that, increases the stress concentrations. However, higher GNP
concentrations in the ECD bath promote low aspect ratio GNP layers in Zn−Cu alloy matrix and
thus increase the chance of crack propagation, impart brittleness and cause a brittle fracture in
Zn−Cu/GNP nanocomposite samples. Another reason for brittle facture is the dominance of the
brittle hexagonal−close−packed Zn at room temperature over the ductile face−centered−cubic
Cu across the Zn−Cu/GNP nanocomposite.

The friction coefficient graphs for prepared samples are shown in Figure 7.5c. The graphs were
distinct, stable and comparable after 150 s. The prepared Zn−Cu/GNP nanocomposites samples
were shown smoother graphs with significantly lower average values than that of pure Zn−Cu
alloy i.e. 0.64. The lowest measured average value of friction coefficient was 0.34 for Zn−Cu/GNP
(100 mg/L). The decrease in friction coefficient with increasing the GNP content is attributed
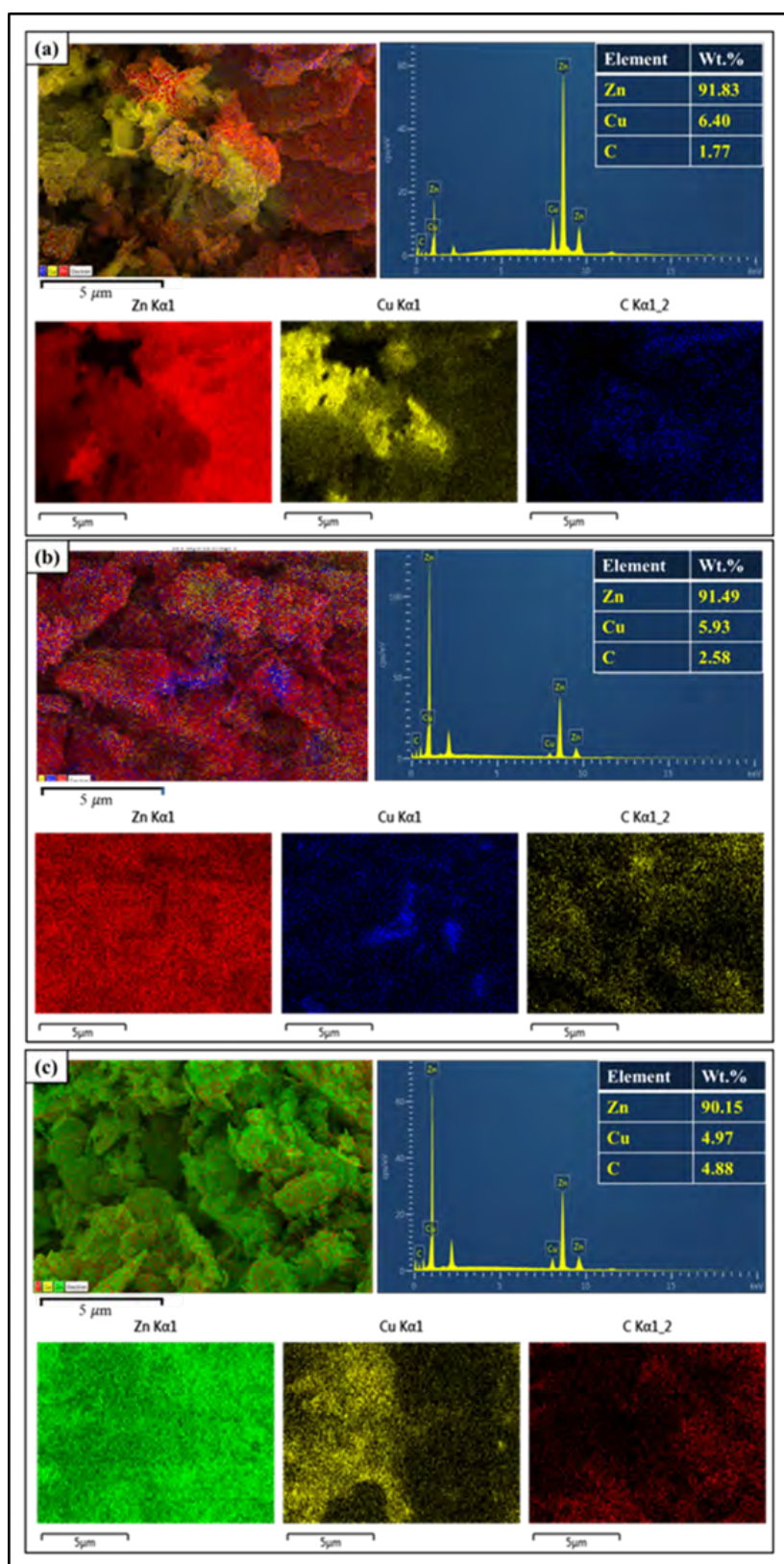
FIGURE 7.4: EDS of Zn-Cu/GNP nanocomposite powder for different concentration of Gr: (a) 25 mg/L; (b) 50 mg/L; (c) 100 mg/L.

Chapter 7. *Alloy−Zn/GNP Nanocomposites: Synthesis and Properties*   138
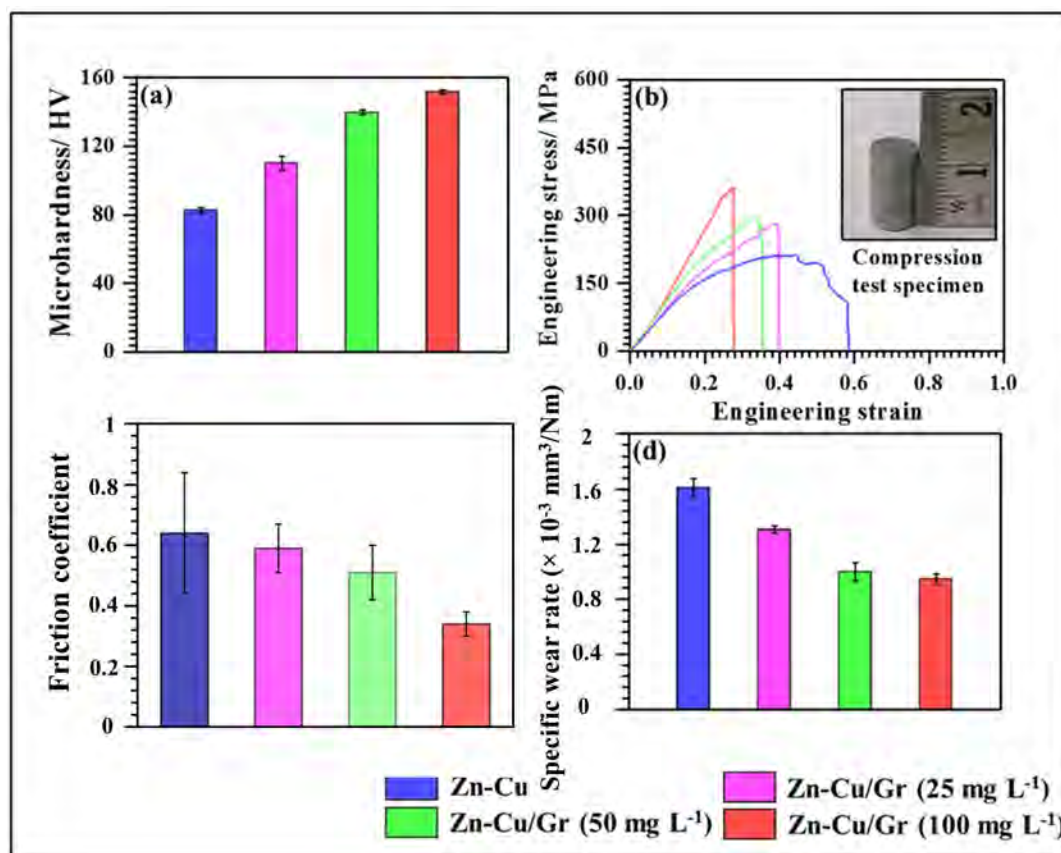
FIGURE 7.5: Tribo-mechanical properties of pure Zn-Cu alloy and Zn-Cu/GNP nanocomposites: (a) microhardness; (b) engineering stress-strain curves; (c) friction coefficient graphs; (d) Specific wear rate. GNP is represented as Gr.

TABLE 7.3: Mechanical properties of pure Zn-Cu alloy and Zn-Cu/GNP nanocomposite samples

Samples	Microhardness/ HV			Compressive strain	Cu	C
	82 ± 1.5	156 ± 2	212 ± 3	0.58 ± 0.02	Cu	C
Zn-Cu/GNP (25 mg/L)	110 ± 3	224 ± 3	283 ± 3	0.39 ± 0.01	6.4	1.77
Zn-Cu/GNP (50 mg/L)	139 ± 1	239 ± 1	298 ± 2	0.35 ± 0.01	5.93	2.58
Zn-Cu/GNP (100 mg/L)	151 ± 2.5	341 ± 1	362 ± 2	0.27 ± 0.01	4.97	4.88

to the increasing microhardness of nanocomposite and the outstanding solid−solid lubrication offered by the graphitic structure of GNP layers [320].

In general, the wear performance of the nanocomposites depends on various experimental parameters such as the applied load, pin hardness and diameter, relative speed between pin and disk, overall sliding distance, and test conditions (such as dry and wet) [321]. The obtained specific wear rate values are shown in Figure 7.5d, which reveals that the wear performance of Zn−Cu/GNP nanocomposite samples enhances with an increased GNP concentration in the ECD bath. The specific wear rate decreased by 41.32% for Zn−Cu/GNP (100 mg/L) than pure Zinc, respectively. Here, the grain−strengthening effect due to reduced crystallite size improves the nanocomposite's microhardness, enhancing the wear performance [320].

TABLE 7.4: Electrochemical corrosion parameters of pure Zn-Cu alloy and Zn-Cu/GNP nanocomposite samples

Sample	E_{corr} (mV)	I_{corr} (μ A/cm^2)	β_a (mV/decad)	β_c (mV/decad)	η_{corr}(%)
Zn-Cu	-219.4	1.605	243.3	246.1	0
Zn-Cu/ GNP (25 mg/L)	-262.8	1.310	200.1	157.1	18.3
Zn-Cu/ GNP (50 mg/L)	-198.2	1.252	245.3	312.9	21.9
Zn-Cu/ GNP (100 mg/L)	-169.9	0.921	88.1	191.3	42.6

7.2.2.3 Corrosion behavior

The electrochemical corrosion properties of the prepared nanocomposite samples found from the potentiodynamic polarization curve shown in Figure 7.6a are listed in Table 7.4. The I_{corr} values of Zn–Cu/GNP nanocomposites get gradually decreased compared with increase in GNP content in nanocomposite (see Table 7.2 and Table 7.4) to pure Zn−Cu alloy.
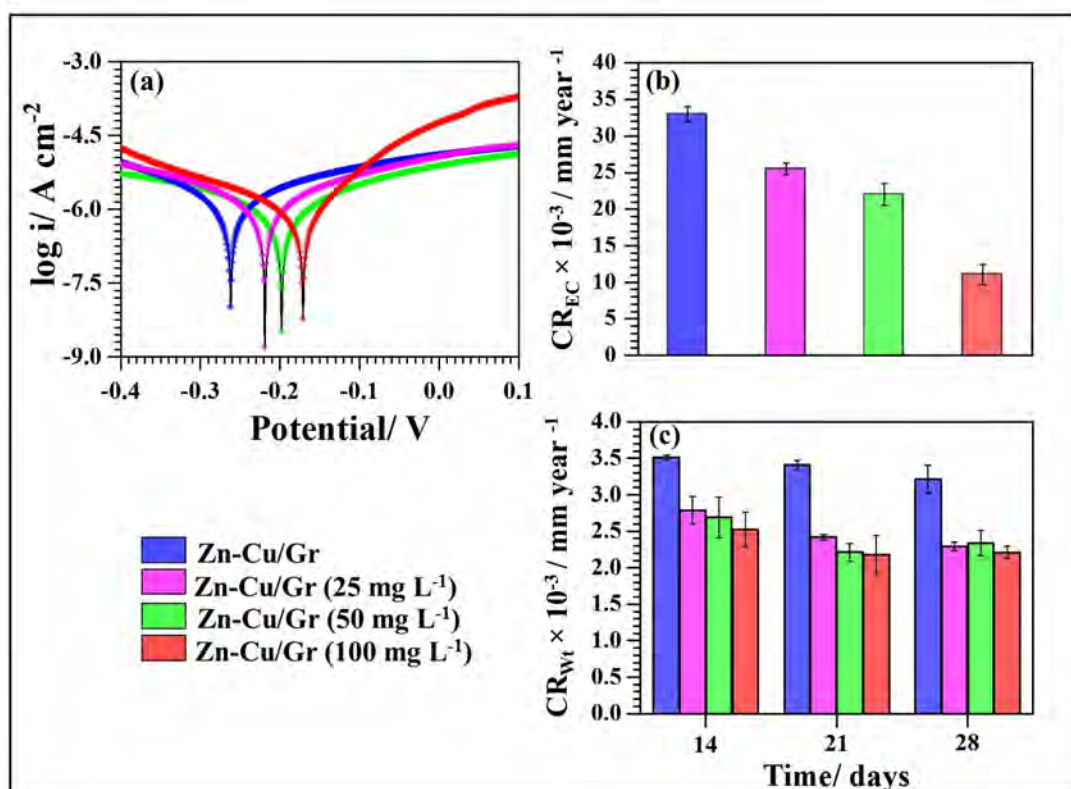
FIGURE 7.6: Corrosion behaviour of pure Zn-Cu alloy and Zn-Cu/GNP nanocomposite samples: (a) potentiodynamic polarization curves; (b) electrochemical corrosion rate; (c) corrosion rate after immersion of 14, 21 and 18 days. GNP is represented as Gr.

From Figure 7.6b, the pure Zn−Cu alloy exhibited highest CR$_{EC}$ value of 33×10^{-3} mm year^{-1}, which decreased by 66.67% for Zn−Cu/GNP nanocomposite with lowest CR$_{EC}$ value of 11×10^{-3} mm year^{-1}. The obtained values of electrochemical corrosion for prepared Zn−Cu/GNP nanocomposites are lower compare to the reported values of Zn−xCu (x = 1–4 wt%) alloys,14 which is about $29 \pm 3 \times 10^{-3}$ mm year^{-1} in SBF solution. The variation of CR$_{Wt}$ with immersion

time is shown in Figure 7.6c. The obtained data reveals that for 14 days of immersion time CR_{Wt} decreased significantly with increasing GNP concentration in the ECD bath. Also, the CR_{Wt} for all nanocomposite samples decreased significantly after 14 days and tended toward stable values, which indicates the formation of protective corrosion products. Here, the corrosion product on the surface and well−distributed impermeable GNP in Zn−Cu alloy matrix act as a
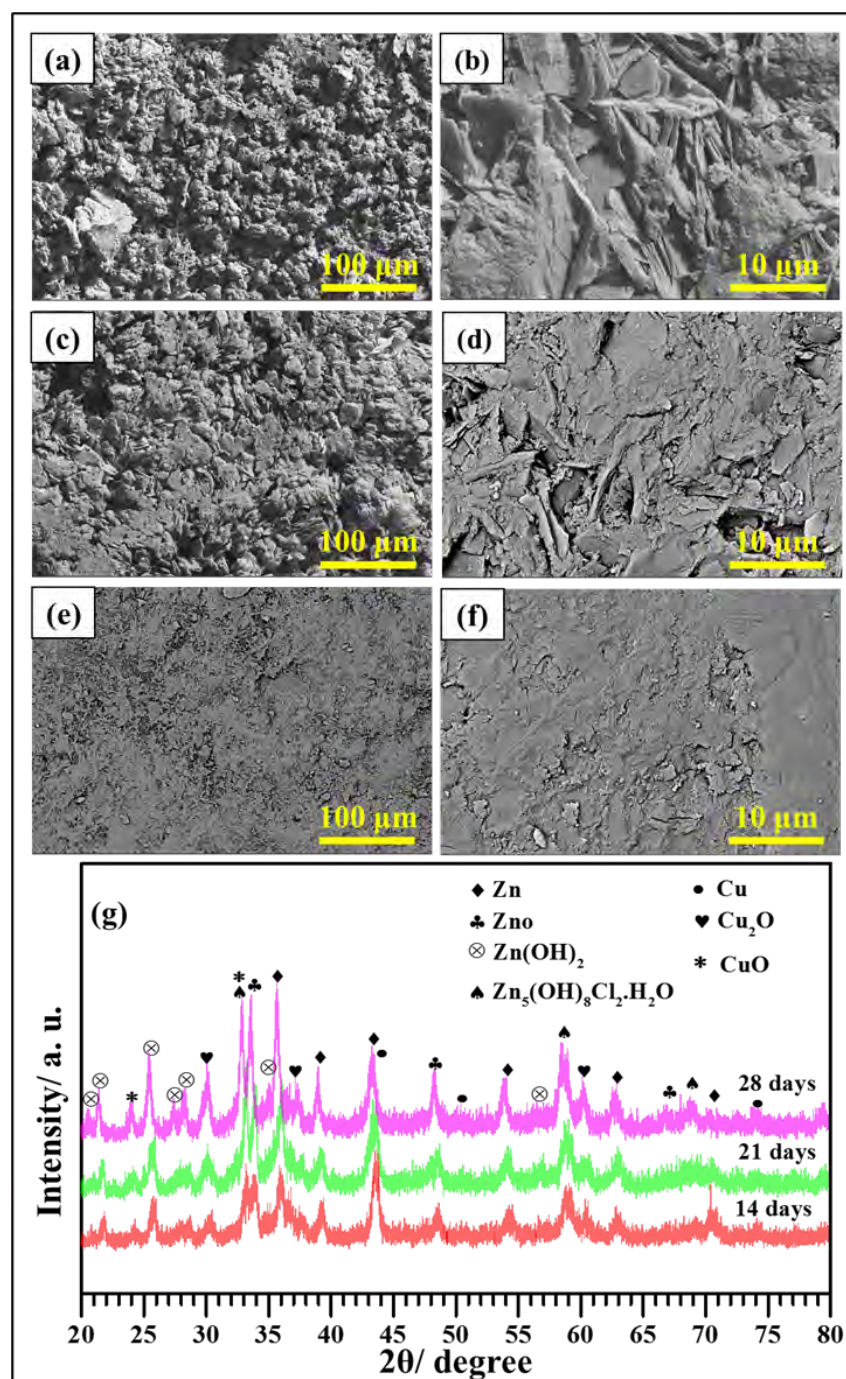
FIGURE 7.7: FESEM images of Zn-Cu/GNP nanocomposite sample after immersion in SBF solution for 28 days; (a-b) 25 mg/L; (c-d) 50 mg/L; (e-f) 100 mg/L and (g) XRD pettern of Zn-Cu/GNP (100 mg/L) nanocomposite sample after immersion in SBF solution for different times.

barrier for the corrosion attack [322]. In addition, the decreased crystallite size (from Figure 7.2b) of Zn−Cu/GNP nanocomposites attributed to reducing the formation of local micro−galvanic cells at pits, voids, and cracks which further reduced the corrosion of prepared nanocomposites.15 The results coincide with the XRD patterns, clearly testifying by the intensity of XRD peaks the corrosion products on the surface of Zn−Cu/GNP (100 mg/L) nanocomposite samples exposed in SBF solution for different immersion times.

Figure 7.7a−f illustrates the corroded surface morphology of Zn−Cu/GNP nanocomposite samples after immersion in SBF solution for 28 days. For Zn−Cu/GNP (25 mg/L) nanocomposite sample, the pores and void are clearly visible on the surface (see Figure 7.7a−b). For 50 mg/L of GNP in the ECD bath, the sample showed reduced sizes and numbers of the pores and voids on the surface morphology which certainly improve the corrosion performance (see Figure 7.7c−d). Further increasing GNP concentration in the ECD bath up to 100 mg/L, the nanocomposite shows very few and small pits and voids (see Figure 7.7e−f), which provides strong barrier protection to the nanocomposite and slower the rate of corrosion. Figure 7.7g describes the XRD pattern of Zn−Cu/GNP (100 mg/L) nanocomposite exposed in SBF solution for the different immersion times. Along with the XRD peaks corresponding to Zn, the peaks of the corrosion product of Zn such as ZnO, $Zn(OH)_2$ and $Zn_5(OH)_8Cl.H_2O$ appear in the profile. The intensity strengthened with extension in immersion time, and the peaks become dominant after of 28 days immersion time. The XRD peaks for copper corrosion products such as Cu_2O and CuO also became stronger with the prolonging of time. The strengthening of XRD peaks confirms the increasing amount of corrosion products with an increase in immersion time [266].

7.2.2.4 *in−vitro* cytotoxic assessment

The toxicity of GNP-reinforced nanocomposites depends on the complex interplay of its physico-chemical properties like shape, size, dose of administration, and exposure times [323]. From the cell viability analysis of 72 hours, it was observed that the IC50 of prepared nanocomposites was around 60 g mL^{-1} to 80 g mL^{-1} concentrations. Cell viability was comparable with that of the control cells, as evident from Figure 7.8. The experiments were performed in triplicates, and obtained results were statistically significant for nanocomposite samples (up to 50 mg/L of GNP concentration in ECD bath) without showing much cytotoxicity over the primary keratinocyte cells. The cell viability with Zn−Cu/GNP (100 mg/L) nanocomposite sample was also analyzed but showed significant cytotoxicity because the higher GNP concentration damages the mito-chondrial activity associated with the plasma membrane and eventually leads to toxicity, and cell death [324].

7.2.3 Summary for prepared Zn−Cu/GNP nanocomposite

The synthesis of Zn−Cu/GNP nanocomposite powder with uniformly distributed GNP layers has been achieved using modified electro co−deposition method. FESEM images of nanocomposites
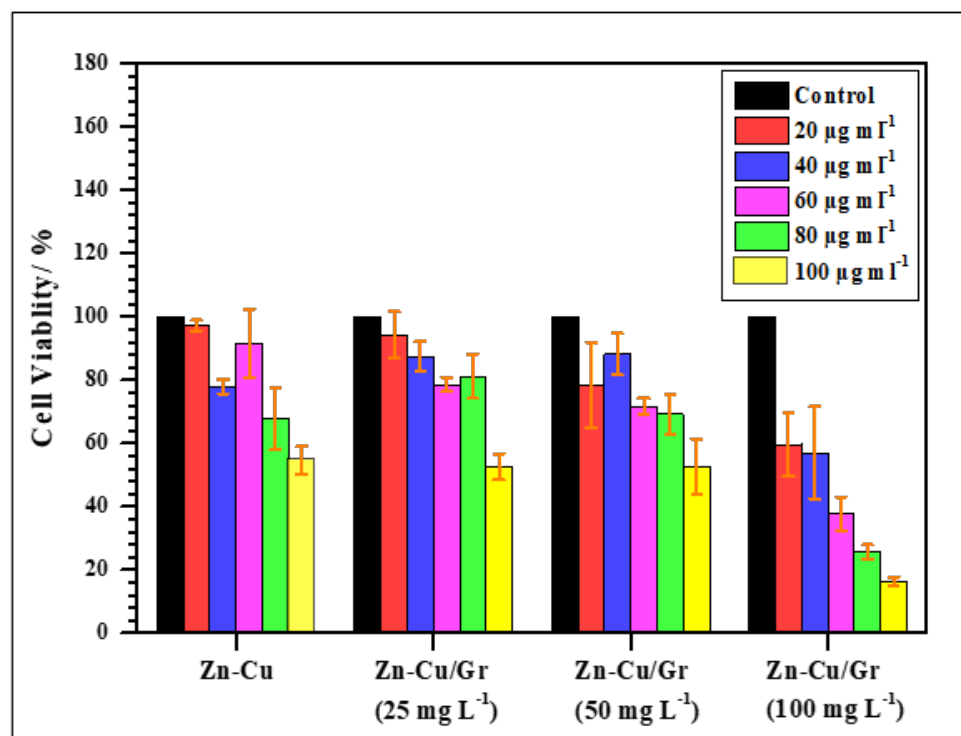
FIGURE 7.8: Cell viability assay of pure Zn-Cu alloy and Zn-Cu/GNP nanocomposite samples. GNP is represented as Gr.

powder samples confirmed that during the synthesis, the impermeable GNP layers along with Zn and Cu were co−deposited to form clusters of Zn−Cu/GNP nanocomposites. The uniform distribution of GNP in prepared nanocomposite was confirmed by EDS of Zn−Cu/GNP nanocomposite powder samples. The microstructural Study by XRD of the prepared nanocomposite confirmed that crystallite size decreased when GNP concentration in the ECD bath increased, which imparts grain strengthening. The grain strengthening effect enhanced tribo−mechanical properties. However, the compressive strain in pure Zn−Cu alloy decreased by 53.4% for reinforcement of 100 mg/L of GNP concentration in the ECD bath. The impermeable GNP layers on the surface of nanocomposite provided barrier protection from corrosive OH^- and Cl^- attack and the electrochemical corrosion rate of prepared nanocomposite samples decreased by 66.67% for Zn−Cu/GNP nanocomposite up to 11×10^{-3} mm year^{-1} with increased GNP content in the nanocomposite. The material has shown non−cytotoxicity up to 50 mg/L of GNP concentration in the ECD bath.

7.3 Antibacterial γ-Zn−Ni/GNP nanocomposite coatings

In recent years, Zn coatings have been studied extensively and widely used for the protection of steel surfaces from corrosion [181], [325]. However, extensive efforts have been devoted to the enhancement of mechanical strength and corrosion resistance of Zn coating to prolong its service life in harsh working conditions. Generally, the functional properties of Zn coating can

be enhanced by alloying with high-strength metals or by the addition of reinforcing elements. Several Zn alloy coatings such as Zn-Ni [326], Zn-Fe [327], Zn-Cu [173], [328] and Zn-Co [329] have been developed and investigated for their mechanical, wear and corrosion properties. Among these, Zn-Ni alloy coatings have been extensively researched owing to high tribo-mechanical, anti-corrosive and anti-bacterial properties [330]–[332].

Various approaches, such as plasma-spraying, thermal-spraying, electroless plating, physical vapor deposition (PVD), chemical vapor deposition (CVD) and electro-co-deposition have been used to fabricate nanocomposite coatings [147]. Here, electro-co-deposition is considered an economical, convenient and scalable method to produce nanocomposite coatings [16], [299]. As per Brenner's classification on Zn–Ni alloy electrodeposition, the deposition follows anomalous co-deposition when zinc, the less noble metal, is preferentially deposited [333]. Wherein, the presence of Ni content remarkably influences the tribo-mechanical and anti-corrosion properties of Zn–Ni alloy. Beltowska-Lehman et al. [334] have reported that the Zn–Ni alloy deposit with 8%–14% Ni content mostly exhibits single γ-phase that can give corrosion protection of 5 to 6 times superior to that of pure Zn deposits. Furthermore, the mechanical strength and anti-corrosion behavior of Zn-Ni alloy coatings can be enhanced by reinforcing the nanofillers such as TiO_2 [335], Al_2O_3 [38], SiO_2 [336], SiC [337] and CNTs [338] have been added to them. However, the anti-bacterial properties of Zn–Ni alloy and nanocomposite coatings were less investigated. Researchers have synthesized the Zn-GNP coatings using electro-co-deposition method [55], [174], [274], [294], but the tribo-mechanical, anti-corrosion and anti-bacterial performance of Gr-based Zn alloy coatings require to be more investigated. In this study, Gr-reinforced γ-Zn−Ni alloy matrix nanocomposite coatings were prepared by using electro-co-deposition method. The effects of different concentrations of GNP in the acid-sulfate bath on the microstructural, morphological, tribo-mechanical, corrosion and anti-bacterial properties of prepared nanocomposite coatings were studied in detail.

7.3.1 Experimental procedure

The electrolyte bath was prepared from AR/GNP grade chemicals and deionized (DI) water. The γ-Zn−Ni alloy coating was deposited from an acid-sulfate bath consisting of $ZnSO_4.7H_2O$ (0.5 M), NiSO4.6H2O (0.5 M), Na_2SO_4 (40 g/ L) and H_3BO_3 (24 g/ L). For depositing γ-Zn−Ni/GNP nanocomposite coatings, GNP (25, 50 and 100 mg/L) was added in the bath under constant magnetic stirring at 400 rpm for 20 min, and subsequently, the electrolyte bath was ultrasonically stirred for 60 min to break the agglomeration of GNP. Further, the electrolyte pH value was adjusted to 4 ± 0.1, and the temperature was 40 ± 1ºC. The deposition was performed under magnetic stirring at 350 rpm for 60 min. Table 7.5 lists the electrolyte bath composition and electrodeposition parameters used in this study. The stainless-steel plate with a dimension of 15 × 20 × 2 mm was employed as a cathode, and the Pt rod was employed as an anode. Prior to deposition, the stainless-steel substrate was polished mechanically using abrasive paper (320, 800

TABLE 7.5: The electrolyte bath composition and electrodeposition parameters.

Electrolyte bath composition	
$ZnSO_4.7H_2O$	0.5 M
$NiSO_4.6H_2O$	0.5 M
Na_2SO_4	40 g/ L
H_3BO_3	24 g/ L
Gr	0, 25, 50 and 100 mg/L
Electrodeposition parameters	
pH	4 ± 0.1
Current density	4 A/ dm^2
Temperature	40 ± 1 °C
Stirring speed	350 rpm
Plating time	60 min

and 2500 grades sequentially) and subsequently cleaned using acetone and DI water to remove oil or any contamination on the surface. The schematic diagram for electro-co-deposition of γ-Zn−Ni/GNP nanocomposite coatings is shown in Figure 7.9.

Scanning electron micrograph analysis of prepared coatings and compositional study were performed by FEI-Apreo-S field emission scanning electron microscopy (FESEM) fitted with built-in energy dispersive spectroscopy (EDS). The X-ray diffraction scanning of prepared coatings was carried out on RIGAKU MiniFlex-II X-ray diffractometer (XRD) with Cu Ka radiation at a scanning rate of 0.5 °C s^{-1}. Microhardness of prepared coatings was measured by Mitutoyo HM 200 Micro Vicker hardness tester at a load of 20 g for 15 s. Wear rate of prepared coatings was calculated by DUCOM tribometer with a pin on disc arrangement. The pin was GCr15 steel with a diameter of 6 mm. The coefficient of friction (COF) was continuously recorded under a load of 5 N for 10 min at ambient temperature without lubrication. The wear track radius and sliding speed were 5 mm and 300 rpm, respectively. The wear weight loss was determined using a digital balance with an accuracy of 0.0001 g. The corrosion performances of prepared coatings were electrochemically evaluated by CHI604E potentiostat with a three-cell arrangement under 3.5 wt.% of NaCl solution at 27 °C temperature. In-vitro anti-bacterial activity of prepared coatings was evaluated against gram-positive bacteria Staphylococcus aureus (MTCC 96) and gram-negative bacteria E. coli (MTCC 1652). The prepared coatings were washed by running water and ethanol followed by dry heating at 120 °C to sterilize before testing the in-vitro anti-bacterial activity. The Zone of Inhibition (ZOI) for prepared coatings was determined by the modified Agar disc diffusion method as defined by the National Committee for Clinical Laboratory Standards (1993). Each Bacterial Strain was grown in Luria Broth Media (Himedia Laboratories, India). 100 L of overnight grown bacterial culture (107 cfu mL_{-1}) was spread using a sterile spreader. The plates were kept on incubation at 37 °C for overnight under aerated conditions, and the zone of inhibition (ZOI) around the prepared coating samples was measured in mm.
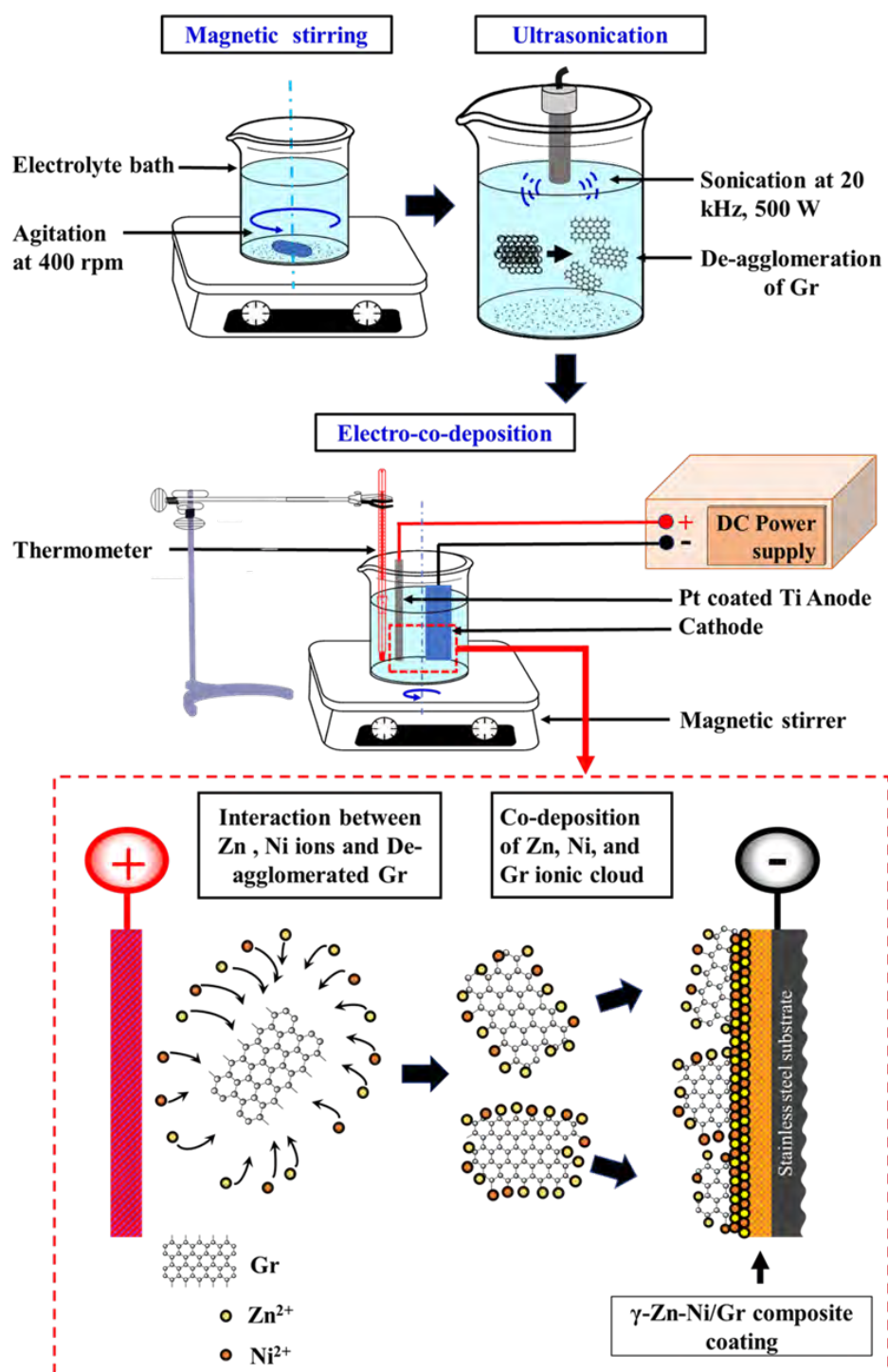
FIGURE 7.9: Schematic diagram of electro-co-deposition of γ-Zn−Ni/GNP nanocomposite coating. GNP is represented as Gr.

7.3.2 Results and discussion

7.3.2.1 XRD analysis

Figure 7.10 demonstrates the XRD diffraction pattern of prepared coatings. The XRD diffraction pattern of all prepared coatings identified as reflections of body-centered cubic (bcc) γ-phase structure (Ni_5Zn_{21}) (according to JCPDS card No. 6-0653) [339], and no other phase of Zn-Ni alloy matrix can be recognized. The single bcc γ-phase structure of Zn-Ni alloy is reported as desirable for better tribo-mechanical and anti-corrosion performance as compared to other intermetallic phase structures of Zn-Ni alloy [340]. It was observed that the reflected peaks of the prepared γ-Zn−Ni/GNP nanocomposite coating was slightly shifted toward a higher angle and broadened on increasing GNP concentration in the electrolyte bath. The shifting of XRD peaks may associate with mainly two reasons: (i) lattice distortion or micro strain developed due to reinforcement of GNP in γ-Zn−Ni alloy nanocomposite coating (ii) change in the composition of γ-Zn−Ni/GNP nanocomposite [169]. Moreover, the peak broadening was associated with the polycrystalline nature of GNP and crystallite size refinement [300]. The crystallite size (D) for all prepared coatings was determined from the (3 3 0) peak using Scherrer equation given in **Chapter 3**.
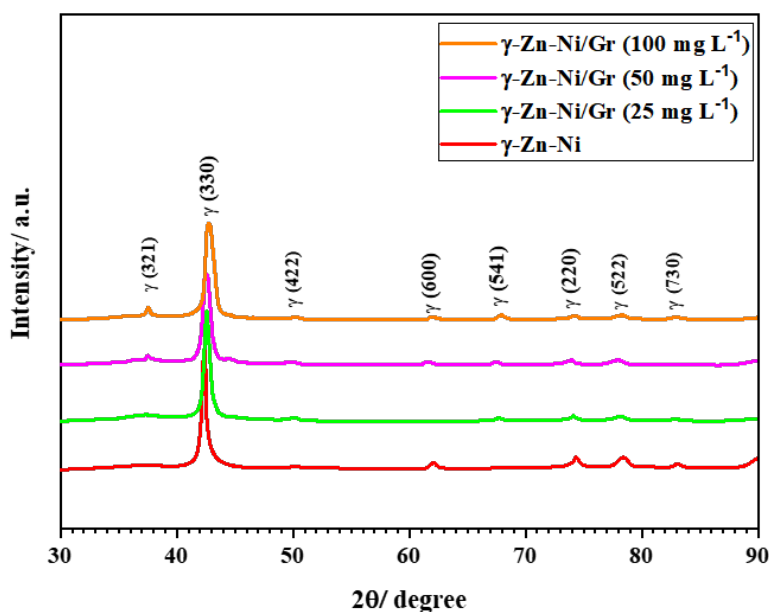
FIGURE 7.10: XRD patterns of γ-Zn−Ni/GNP nanocomposite coatings. GNP is represented as Gr.

The calculated crystallite sizes of all prepared coatings are reported in Table 7.6. The result indicates that after reinforcement of GNP, the D value of γ-Zn−Ni alloy coating decreases from 20.63 nm to 11.58 nm. The γ-Zn−Ni/GNP (100 mg/L) nanocomposite coating exhibits the minimum D value of 11.58 nm. The GNP could provide nucleation sites for Zn and Ni

TABLE 7.6: Crystallite size and composition of prepared coatings.

Coating	Crystallite size (nm)	C (wt.%)
γ-Zn−Ni	20.63 ± 0.5	-
γ-Zn−Ni/GNP (25 mg/L)	16.13 ± 0.4	1.61 ± 0.12
γ-Zn−Ni/GNP (50 mg/L)	12.74 ± 0.8	2.86 ± 0.14
γ-Zn−Ni/GNP (100 mg/L)	11.58 ± 0.6	4.73 ± 0.20

deposition, and hence hinder the crystal growth and consequently decrease the crystallite size of the nanocomposite coating.

7.3.2.2   SEM and EDS analysis

The effects of different concentrations of GNP on the surface morphology of γ-Zn−Ni/GNP nanocomposite coatings are shown in Figure 7.11a-h. The γ-Zn−Ni alloy coating surface is relatively smooth (see Figure 7.11a and b) compared to γ-Zn−Ni/GNP nanocomposite coatings (see Figure 7.11c-h). The surface morphology of the γ-Zn−Ni alloy coatings consists of a nodular structure of grouped pyramidal clusters and hexagonal plates. As seen in Figure 7.11c-h, the γ-Zn−Ni/GNP nanocomposite coatings' surface morphology became coarser with a smaller nodule size by increasing the electrolyte bath GNP concentration from 25 mg/L to 100 mg/L. The incorporation of GNP changed the surface morphology of γ-Zn−Ni/GNP nanocomposite coatings to hexagonal crystals oriented perpendicularly to the substrate surface. The variation in the electrolyte bath GNP concentration significantly decreased the crystallite dimensions due to the rise in nucleation sites for crystal growth during the deposition process, consequently changing the surface morphology.

Figure 7.12 shows EDS mapping and corresponding EDS spectrum of γ-Zn−Ni alloy and γ-Zn−Ni/GNP nanocomposite coatings. The surface elements of γ-Zn−Ni alloy are mainly Zn, Ni and O, as shown in Figure 7.12a. Form Figure 7.12b and d, the main elements on the surface of the γ-Zn−Ni/GNP nanocomposite coatings are Zn, Ni, C and O. As the concentration of GNP in the electrolyte bath increases from 25 mg/L to 100 mg/L, the content of carbon gradually increases from to 1.61 wt.% to 4.73 wt.% (see Table 7.6). This may be attributed to the fact that when the amount of GNP in the electrolyte bath is higher, the GNP have more opportunities to be reinforced into the γ-Zn−Ni alloy matrix36. Furthermore, previous research has revealed that GNP can absorb Ni ions on their defective sites [341]. Thereby, during the deposition process, GNP slightly affected the Ni/Zn ratio. Thus, the increase in GNP concentration from 25 mg/L to 100 mg/L in the electrolyte bath slightly increased the Ni/Zn ratio of γ-Zn−Ni/GNP nanocomposite coating by   1% than that of γ-Zn−Ni alloy coating, which can hardly influence the properties of the resulting nanocomposite coatings studied here.
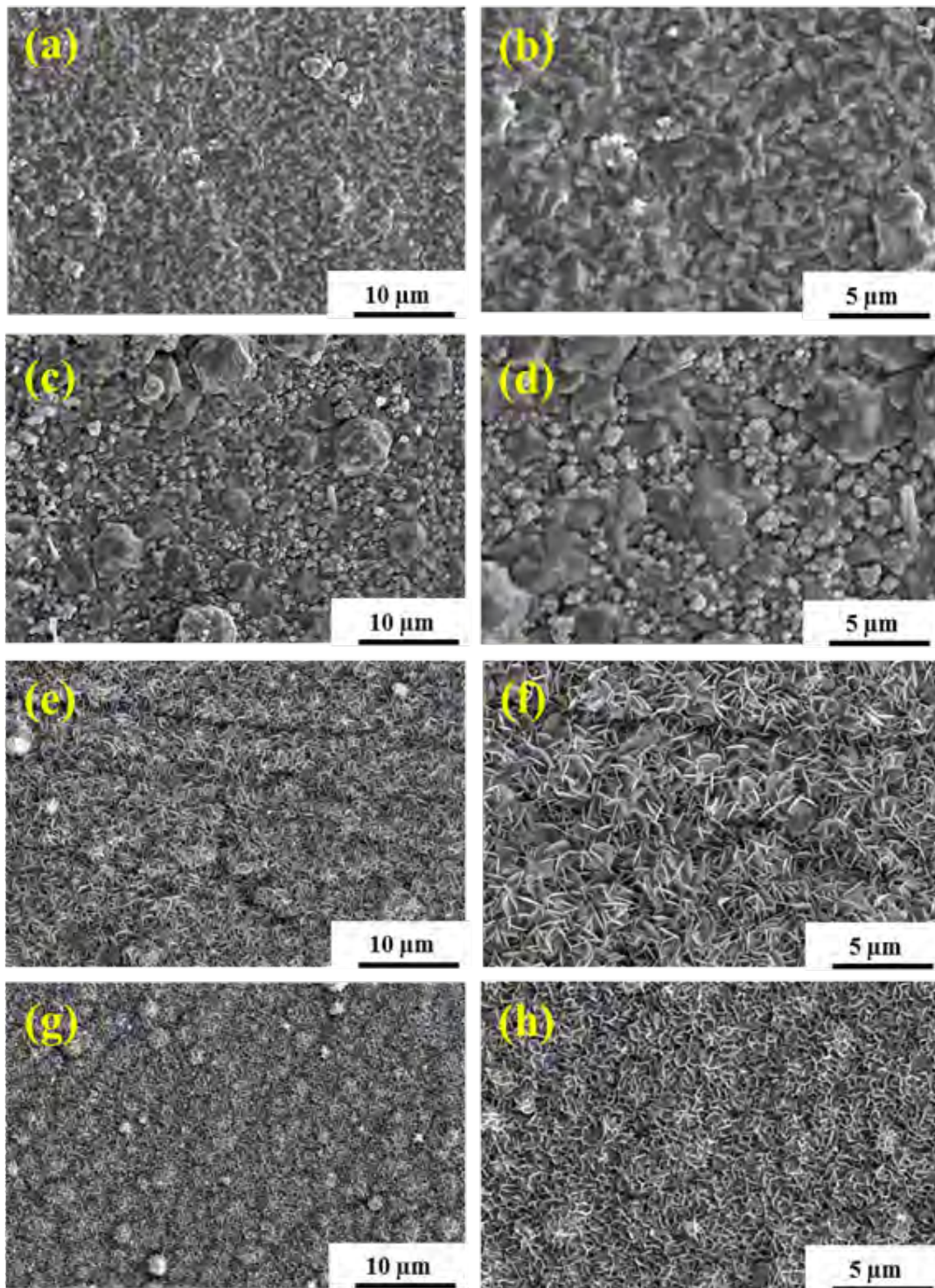
FIGURE 7.11: SEM observation of γ-Zn−Ni/GNP nanocomposite coatings electrodeposited at various concentrations of GNP :(a, b) 0 mg/L, (c, d) 25 mg/L, (e, f) 50 mg/L and (g, h) 100 mg/L, respectively.
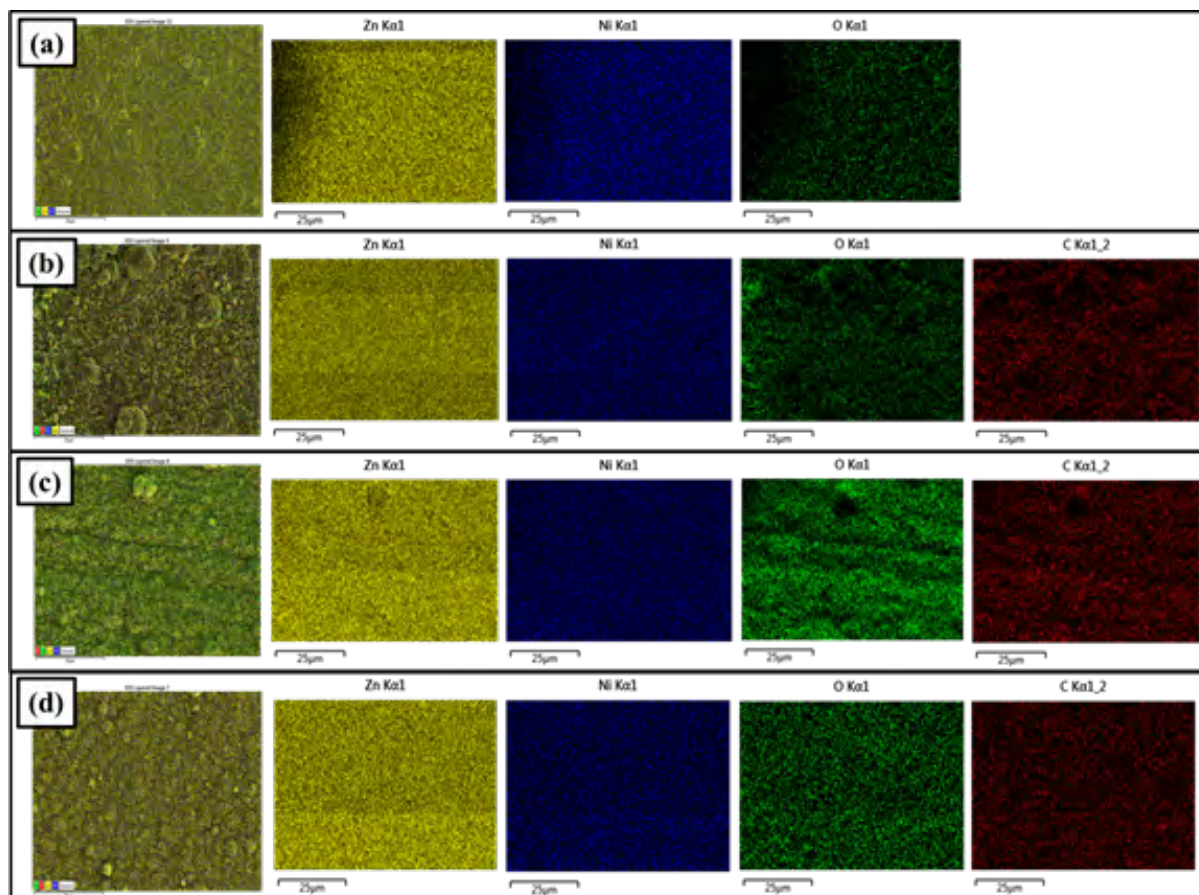
FIGURE 7.12: EDS mapping of γ-Zn−Ni/GNP nanocomposite coatings electrodeposited at various concentrations of GNP :(a) 0 mg/L, (b) 25 mg/L, (c) 50 mg/L and (d) 100 mg/L, respectively.

7.3.2.3   Microhardness testing

The microhardness measurements of both γ-Zn−Ni alloy and γ-Zn−Ni/GNP nanocomposite coatings are illustrated in Figure 7.13. It can be observed that the microhardness values of γ-Zn−Ni/GNP nanocomposite coatings are higher than that of γ-Zn−Ni alloy coating. With the increase in the concentration of GNP in the electrolyte bath, the hardness of the γ-Zn−Ni/GNP nanocomposite coatings increases. Here, γ-Zn−Ni/GNP nanocomposite coatings prepared at 25 mg/L and 50 mg/L of concentration of GNP in the electrolyte bath have microhardness values of 191 HV and 218 HV, respectively. Also, γ-Zn−Ni/GNP (100 mg/L) nanocomposite coating has shown 243 HV of microhardness with a remarkable increase of 69.93 % than that of γ-Zn−Ni alloy coating (143 HV). From the XRD results, the crystallite size of the nanocomposite coating is decreased due to the reinforcement of GNP into the γ-Zn−Ni alloy matrix. According to the Hall-Petch equation, the hardness of coating increases with the decrease in the crystallite size due to grain boundary strengthening. Hence, the enhancement in the microhardness of γ-Zn−Ni/GNP nanocomposite coatings is attributed to the crystallite size refinement, nano-sized GNP content in the γ-Zn−Ni alloy matrix and the outstanding properties of GNP.
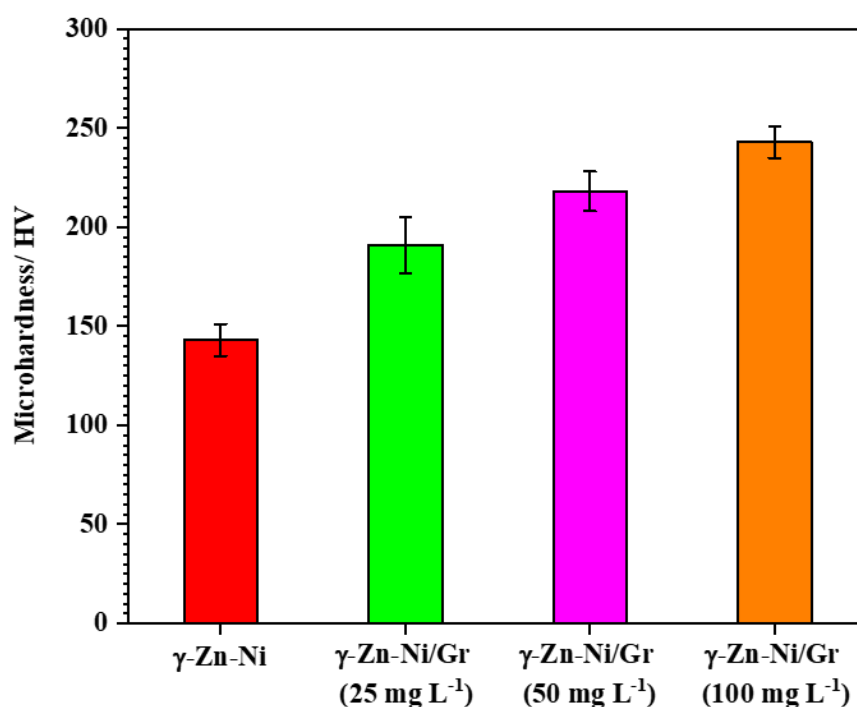
FIGURE 7.13: Microhardness results for γ-Zn−Ni and γ-Zn−Ni/GNP nanocomposite coatings. GNP is represented as Gr.

7.3.2.4 Wear performance

The coefficient of friction (COF) versus time graph of γ-Zn−Ni alloy and γ-Zn−Ni/GNP nanocomposite coatings is shown in Figure 7.14a. As shown in Figure 7.14a, the average COF of γ-Zn−Ni alloy coating is 0.65. With the increase in the concentration of GNP in the electrolyte bath from 25 mg/L to 100 mg/L, the average COF of the γ-Zn−Ni/GNP nanocomposite coatings is gradually decreased from 0.51 to 0.32. The decrease in the average COF of γ-Zn−Ni/GNP nanocomposite coatings is attributed to the increase in the GNP content inside the coating, as observed in the EDS analysis (see Table 7.6). During the sliding test of the γ-Zn−Ni/GNP nanocomposite coating, a thin layer for slip containing GNP forms at the interface by the γ-Zn−Ni alloy matrix and acts as a solid lubricant. The result is a significant decrease in the COF of prepared nanocomposite coatings than that of γ-Zn−Ni alloy coating.

Figure 7.14b presents the specific wear rate of γ-Zn−Ni alloy and γ-Zn−Ni/GNP nanocomposite coatings. It can be seen from Figure 7.14b that the γ-Zn−Ni/GNP nanocomposite coating exhibited lower wear-loss than that of γ-Zn−Ni alloy coating. The wear-loss of prepared nanocomposite coatings decreases with an increase in Gr's concentration in the electrolyte bath. Here, γ-Zn−Ni/GNP (100 mg/L) nanocomposite coating shows a minimum wear loss. This reveals that self-lubricating γ-Zn−Ni/GNP nanocomposite coating shows excellent wear resistance under dry friction condition.
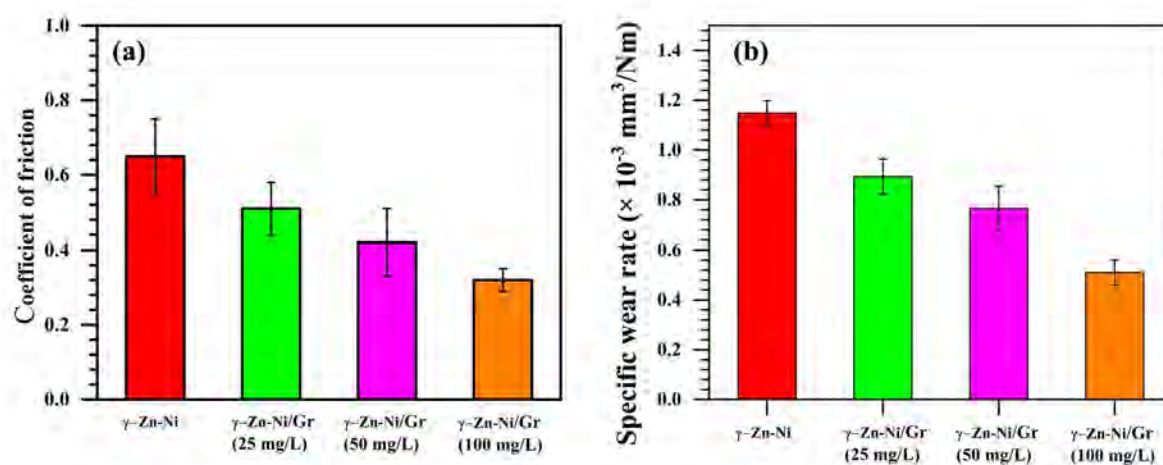
FIGURE 7.14: (a) Coefficient of friction and (b) specific wear rate for γ-Zn−Ni and γ-Zn−Ni/GNP nanocomposite coatings. GNP is represented as Gr.

TABLE 7.7: Corrosion parameters of γ-Zn−Ni alloy and γ-Zn−Ni/GNP nanocomposite coatings.

Coating	I_{corr} (A/ cm^2)	β_a (mV/ decade)	$-\beta_c$ (mV/ decade)	R_p (kΩ cm^2)
γ-Zn−Ni/GNP	0.398 ± 0.05	29.6 ± 2.0	36.3 ± 4.8	17.78 ± 1.6
γ-Zn−Ni/GNP (25 mg/L)	0.282 ± 0.02	34.7 ± 2.8	46.9 ± 2.1	30.70 ± 3.3
γ-Zn−Ni/GNP (50 mg/L)	0.251 ± 0.02	45.6 ± 3.2	75.5 ± 6.3	49.18 ± 2.9
γ-Zn−Ni/GNP (100 mg/L)	0.151 ± 0.01	39.9 ± 5.0	104.7 ± 8.1	83.07 ± 1.1

3.5 Corrosion performance The electrochemical corrosion test of γ-Zn−Ni alloy and γ-Zn−Ni/GNP nanocomposite coatings were performed in a 3.5 wt.% NaCl solution with the scanning corrosion potential ranging from -1.2 V to -0.5 V at a scan rate of 10 mV s^{-1}. The Tafel plots are depicted in Figure 7.15, and the extracted electrochemical parameters such as E$_{corr}$ (corrosion potential), I$_{corr}$ (corrosion current density), R$_p$ (polarization resistance) are tabulated in Table 7.7. When increasing GNP concentration, the E$_{corr}$ value is shifted positively and I$_{corr}$ value is decreased significantly, indicating improvement in the corrosion resistance.

In Table 7.7, the highest R$_p$ value for γ-Zn−Ni/GNP (100 mg/L) nanocomposite coating (83.07 kΩ cm^2) is attributed to the GNP reinforcement into the γ-Zn−Ni alloy matrix, which acts as a barrier to the electrochemical interaction between γ-Zn−Ni alloy matrix and corrosive environment. Also, these smaller crystallite-size γ-Zn−Ni/GNP nanocomposite coatings reduce the chances of forming voids, pits and cracks at the surface, which ultimately reduces the formation of local micro-galvanic cells and hence improve the anti-corrosion performance.

7.3.2.5 Anti-bacterial performance

In this study, the anti-bacterial activities of the prepared coatings against both gram-positive (S. aureus) and gram-negative (E. coli) bacteria were investigated, and results are presented in Table 7.8. The obtained ZOI values range from 18 mm to 26 mm for gram-positive bacteria and
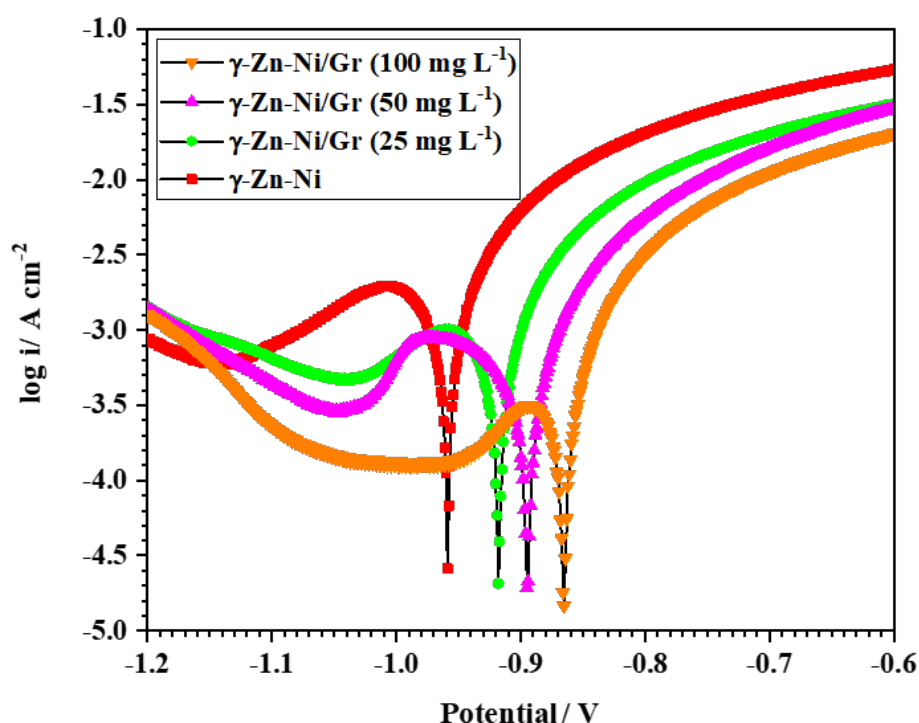
FIGURE 7.15: Tafel polarization curves of coatings in artificial seawater. GNP is represented as Gr.

TABLE 7.8: Anti-bacterial activities of γ-Zn−Ni alloy and γ-Zn−Ni/GNP nanocomposite coatings against selected bacte-rial strains.

Coating	Zone of inhibition (mm)		
	S. aureus	E. coli	
γ-Zn−Ni/GNP	18 ± 1.5	15 ± 1.5	
γ-Zn−Ni/GNP (25 mg/L)	20 ± 1	17 ± 0.5	1.5
γ-Zn−Ni/GNP (50 mg/L)	24 ± 1	20 ± 0.5	
γ-Zn−Ni/GNP (100 mg/L)	26 ± 0.5	23 ± 1.5	

15 mm to 23 mm for gram-negative bacteria. It can be observed from the results that ZOI value for the prepared coatings increases with an increase in GNP concentration in the electroplating bath. The maximum ZOI value was found for γ-Zn−Ni/GNP (100 mg/L) nanocomposite coating i.e. 23 mm for gram-negative bacteria and 26 mm for gram-positive bacteria. It is reported that the micro- or nano-sized flakes of factionalized GNP in the coating are responsible for bacterial interactions that induce the inactivation of bacterial cells by physical and oxidative damages. Hence, the prepared coating samples have shown an increase in anti-bacterial activities with an increase in GNP concentration in the electroplating bath.

7.3.2.6 Summary for prepare γ-Zn−Ni/GNP nanocomposite coatings

In this study, γ-Zn−Ni/GNP nanocomposite coatings were prepared on stainless steel using electro-co-deposition method. The microstructural, mechanical, wear, anti-corrosion and anti-bacterial

properties of γ-Zn−Ni alloy and γ-Zn−Ni/GNP nanocomposite coatings were investigated as a function of GNP concentration in the electrolyte bath. The XRD analysis shows that the only desirable bcc γ-phase structure (Ni_5Zn_{21}) of the γ-Zn−Ni alloy matrix is obtained for all prepared coatings. The microhardness and wear performance of the prepared nanocomposite coatings gradually improved with the increasing GNP concentration in the electrolyte bath. Here, microhardness and COF values for γ-Zn−Ni/GNP (100 mg/L) nanocomposite coating are 243 HV and 0.32, which are 69.93 % higher and 50.76 % lower than that of γ-Zn−Ni alloy coating, respectively. Simultaneously, anti-corrosion and anti-bacterial performance also improved with the increasing concentration of GNP in the electrolyte bath. The impermeable GNP covers on the γ-Zn−Ni matrix of γ-Zn−Ni/GNP nanocomposite improves the barrier protection against the micro-bacterial and corrosion attacks on the coating surface. Based on this study, the prepared nanocomposite coatings can be considered cost-effective and protective for marine structures.

7.4   Conclusion

In conclusion, we proposed a synthesis approach for Zn-alloy-based nanocomposites by electro-co-deposition. The influence of different concentrations of GNPs (0, 25, 50, and 100 mg/L) in the ECD bath on the biodegradation and tribo-mechanical performances of the prepared nanocomposites were investigated for their uniform behaviours. The following conclusions were drawn after analyzing the experimental results of material characterizations, corrosion, tribo-mechanical properties, cytotoxicity and antibacterial test studies:

- The synthesis of Zn−Cu/GNP nanocomposite powder with uniformly distributed GNP content has been achieved using modified electro co−deposition method.

- FESEM images of nanocomposites powder samples confirmed that during the synthesis, the impermeable GNP layers along with Zn and Cu were co−deposited to form clusters of Zn−Cu/GNP nanocomposites.

- The uniform distribution of GNP in prepared nanocomposite was confirmed by EDS of Zn−Cu/GNP nanocomposite powder samples. The decrease in crystallite size is revealed in XRD when GNP concentration is increased.

- The compressive strain in pure Zn−Cu alloy decreased by 53.4% for reinforcement of 100 mg/L of GNP concentration in the ECD bath.

- The impermeable GNP layers on the surface of nanocomposite provided barrier protection from corrosive OH^- and Cl^- attack and the electrochemical corrosion rate of prepared nanocomposite samples decreased by 66.67% for Zn−Cu/GNP nanocomposite up to 11×10^{-3} mm year^{-1} with increased GNP content in the nanocomposite.

- The prepared Zn−Cu/GNP nanocomposite synthesized by the suggested method may be useful in biomedical and biodegradable applications owing to the enhanced tribo−mechanical, anti−corrosion properties and non−cytotoxicity performance up to 50 mg/L of GNP concentration in the ECD bath.

- In this study, γ-Zn−Ni/GNP nanocomposite coatings were prepared on stainless steel using electro-co-deposition method. The XRD analysis shows that the only desirable bcc γ-phase structure (Ni_5Zn_{21}) of the γ-Zn−Ni alloy matrix is obtained for all prepared coatings. The microhardness and wear performance of the prepared nanocomposite coatings gradually improved with the increasing GNP concentration in the electrolyte bath.

- Microhardness for γ-Zn−Ni/GNP (100 mg/L) nanocomposite coating increased by 69.93 % and COF values decreased by 50.76 % than that of γ-Zn−Ni alloy coating. Simultaneously, anti-corrosion and anti-bacterial performance also improved with the increasing concentration of GNP in the electrolyte bath.

  Based on the above conclusions, the proposed Zn−Cu/GNP nanocomposites were non-cytotoxic and γ-Zn−Ni/GNP nanocomposites coating anti-bacterial but also sustainable with respect to degradation and tribo-mechanical performances. Findings of this study may have future implications for Zn−Cu/GNP nanocomposites for low-cost biodegradable orthopedic implants (sutures, screws, pins and plates) and stent (coronary and cardio-vascular) applications. Whereas, the prepared nanocomposite coatings can be considered cost-effective and protective for marine structures.

Chapter 8

Overall Conclusions and Future Scope

8.1 Overall Conclusions

In conclusion, this study has demonstrated the potential of non-cytotoxic Zn/f-GNP nanocomposite and anti-bacterial Zn/GNP nanocomposite coatings as promising materials for different applications. The results indicate that both coatings exhibit excellent tribo-mechanical and corrosion resistance properties due to their composition. The important developments from the present study are summarized in the following paragraphs:

(i) In Chapter 4, We proposed a novel approach for synthesising non-cytotoxic Zn-based nanocomposites by combining a modified electro co-deposition process with the typical powder metallurgy process. Modified-electro co-deposition with continuous bath sonication is a beneficial approach as it allows for excellent control over uniform dispersion and exfoliated form of GNPs, leading to improved performance characteristics. We believe this method has the potential to be used for the fabrication of different metal matrix nanocomposites. We conducted a comprehensive study to assess the effect of varying concentrations of f-GNPs (0, 25, 50, 100 and 200 mg/L) in the ECD bath on biodegradation and tribo-mechanical properties of nanocomposites produced. Results showed that these materials exhibited uniformity and tunability. After a comprehensive review of the experimental studies from material characterizations, in-vitro degradation tests, tribo-mechanical properties studies, cytotoxicity assays and antibacterial evaluations, the results can be summed up in the following points:

- The FT-IR and Raman spectra of the prepared f-GNPs revealed successful covalent bonding between PEG functional groups and GNPs, which was demonstrated by C–O (1090 cm^{-1}) and C–H (2910 cm^{-1}) stretching vibrations.

- A lower I$_{(D/G)}$ ratio for f-GNPs in comparison to that of GNPS suggested that nucleophilic reaction between PEG functional groups and GNPS had caused defects in graphene crystals.

- The hexagonal growth of Zn on f-GNP was achieved, resulting new nucleation sites for co-deposition. FT-IR spectra confirmed the bonding between Zn and f-GNP via Zn–O–C attachments.

- HCP microstructure and 49.28 % reduced crystallite size of the Zn revealed by XRD patterns.

- The electrochemical corrosion ranges from 130.4×10^{-3} mm/year (for pure Zn) to 21×10^{-3} mm/year (for 100 mg/L of f-GNP).

- The compressive yield strength of Zn/f-GNP nanocomposites ranges from 182.3 ± 7.9 MPa (for 25 mg/L of f-GNP) to 284.9 MPa (for 100 mg/L of f-GNP), which was significantly higher than pure Zn and comparable to bone strength.

- The friction coefficient and wear loss of Zn/ f-GNP (100 mg/L) nanocomposites reduced by 58.1% and 47.36%, respectively, on comparing with pure Zn.

- It was found that PEG grafted GNPs had significantly high HaCaT cell viability compared to pristine GNPs. The IC50 up to concentration of 60 g/mL of nanocomposites in cell media, suggesting their non-cytotoxicity level, which further confirmed by DAPI staining for 72 hours of cells attachment.

- The Zn/f-GNP nanocomposite pellets inhabited the growth of *S. aureus* and *E. coli* bacteria in terms of ZOI formation and performed better than the control pure Zn.

The Zn/f-GNP nanocomposites demonstrated remarkable non-cytotoxic and anti-bacterial properties, while simultaneously exhibiting tunable degradation rates and tribo-mechanical performances that make them an attractive option for sustainable use. The results of this study may lead to the use of Zn/f-GNP nanocomposites in the development of low-cost and biodegradable orthopedic implants such as sutures, screws, pins and plates, as well as stents for coronary and cardiovascular applications.

(ii) In Chapter 5, low-cost, industrially scalable, and anti-bacterial Zn/GNP nanocomposite coatings were prepared using ECD method. The different GNP concentrations in the ECD bath were explored to analyze the impacts on tribo-mechanical, surface wetting, anti-corrosion, and anti-bacterial properties of the generated nanocomposite coating. This study reached the following conclusions:

- Formation HCP microstructure of the Zn matrix with reducing crystallite size on increasing the GNP concentration in the ECD bath.

- Disordered morphology and formation of new nucleation sites in nanocomposite coating were observed in FESEM images on increasing the GNP concentration in the ECD bath.

- Distribution of anti-bacterial GNP across the Zn matrix in terms of carbon content was confirmed using EDS mapping. In addition, the presence of oxygen content confirmed the protective ZnO precipitates, which provides corrosion protection.

- Microhardness of 143 HV for Zn/GNP (100 mg/L) nanocomposite coating is 185.57% higher than pure Zn coating.

- The friction coefficient and wear loss of coatings reduced by 31.42% and 53.63%, respectively, on comparing pure Zn coating with Zn/GNP (100 mg/L) nanocomposite coating.

- The Zn/GNP nanocomposite coating performs better than the control pure Zn coating in anti-bacterial behavior against both Gram-positive (*S. aureus*) and Gram-negative (*E. coli*) bacteria when tested for agar well diffusion.

Based on the aforementioned conclusions, the nanocomposite coatings created in this study demonstrated anti-bacterial properties and satisfactory tribo-mechanical and anti-corrosion performance. Thus, Zn/GNP nanocomposite coatings may be a cost-efficient and effective solution for anti-bacterial coating applications that can be manufactured in bulk.

(iii) In chapter 6, the statistical study showed that the GNP concentration in the ECD bath and current supplied for co-deposition had the greatest influence on the synthesis of Zn/GNP nanocomposites. The other electrolysis parameters such as the bath pH and agitation to electrolyte exhibited less significant effect on the microhardness and corrosion protection efficiency.

(iv) In chapter 7, with the continuation in development of sustainable biodegradable-non-cytotoxic material and antibacterial coatings, high-strength alloying elements like Cu and Ni were alloyed with Zn-based nanocomposites to further enhance their characteristic performance. The impact of varying GNP concentrations (0, 25, 50, and 100 mg/L) on the tribo-mechanical and corrosion protection behavior of Zn-Cu nanocomposites Zn-Ni nanocomposite coatings were studied to ensure their uniform performances. After analyzing the experimental results of material characterizations, corrosion, tribo-mechanical properties, cytotoxicity and antibacterial test studies, the following conclusions were drawn:

- FESEM images of Zn-Cu nanocomposites powder samples confirmed that the clusters of Zn−Cu/GNP nanocomposites and the uniform distribution of GNP in prepared nanocomposite was confirmed by EDS of Zn−Cu/GNP nanocomposite powder samples.

- The decrease in crystallite size by 18.5 % is revealed in XRD when GNP concentration is increased from 0 mg/L to 100 mg/L in ECD bath.

- The compressive strain in pure Zn−Cu alloy decreased by 53.4% for reinforcement of 100 mg/L of GNP concentration in the ECD bath.

- The electrochemical corrosion rate of prepared nanocomposite samples decreased by 66.67% for Zn−Cu/GNP nanocomposite up to 11×10^{-3} mm year^{-1} with increased GNP content in the nanocomposite.

- The prepared Zn−Cu/GNP nanocomposite synthesized by the suggested method may be useful in biomedical and biodegradable applications owing to the enhanced tribo−mechanical, anti−corrosion properties and non−cytotoxicity performance up to 50 mg/L of GNP concentration in the ECD bath.

- γ-Zn−Ni/GNP nanocomposite coatings show the desirable bcc γ-phase structure (Ni$_5$Zn$_{21}$) in XRD analysis.

- Microhardness for γ-Zn−Ni/GNP (100 mg/L) nanocomposite coating increased by 69.93 % and COF values decreased by 50.76 % than that of γ-Zn−Ni alloy coating.

- γ-Zn−Ni/GNP (100 mg/L) nanocomposite coatings have also shown anti-bacterial properties against both Gram-negative and Gram-positive bacteria.

The proposed Zn−Cu/GNP nanocomposites were non-cytotoxic and γ-Zn−Ni/GNP nanocomposites coating anti-bacterial but also sustainable with respect to degradation and tribo-mechanical performances.

8.2 Future Scope of the Work

No study ever provides a conclusive and definitive answer; there is always more knowledge to be gained, and research is always ongoing. Further exploration into Zn/GNP nanocomposites can be conducted by broadening the scope of the proposed work in multiple directions. From the perspectives of the present work, further investigation into the following aspects can be conducted in order to achieve more versions of the Zn/GNP nanocomposite. These aspects can include exploring the gaps in current knowledge, identifying potential ethical issues, and examining the potential for future research. Additionally, further research on Zn/GNP-based nanocomposites can be done to determine the most effective methods and best practices for material testing and analysis. With the insights gained from this additional research on biodegradable nanocomposites and antibacterial coatings, it will be possible to create better-informed and more effective approaches related to the study in question. The following aspects can be investigated further:

(i) Despite the fact that *in−vitro* studies have found that Zn/f-GNP nanocomposite is non-cytotoxic, it is still essential to conduct *in−vivo* animal testing before going for human trials. Animal testing provides the opportunity to observe the effects of the nanocomposite material in a living organism, and to identify any potential adverse reactions or side effects. Additionally, animal testing can reveal more about the biocompatibility of the nanocomposite material and provide insights into the potential interactions between the nanocomposite material and living organs. By conducting in-vivo animal testing, researchers

can gain valuable insights that will help inform their decisions when conducting human trials.

(ii) The enhancement of tribo-mechanical and corrosion properties due to the addition of f-GNP for non-cytotoxic applications has been discussed. It would be of both academic and technical interest to study the effect of GNP addition on the electrical and thermal properties of Zn/GNP nanocomposites. Also, mechanical properties like tensile strength and fracture toughness can also be tested. These properties can be beneficial for bio-MEMS applications of Zn/f-GNP nanocomposite.

(iii) Another promising research scope is to investigate the possibilities of using Zn/GNP nanocomposites for energy storage, catalysis, and other applications.

(iv) To date, no studies have been reported on the use of computational techniques to study Zn/GNP nanocomposites. However, computational techniques can be a useful tool for predicting properties of nanocomposites without the need for fabrication. Additionally, computational techniques could be used to analyze the effects of different parameters, such as temperature, pressure, and chemical composition, on the nanocomposites.

Zn-Based Nanocomposite Reinforced with Unfunctionalized GNP

.1 Synthesis process of Zn/GNP nanocomposite powder and pellets

The experimental procedure for the synthesis of Zn/GNP nanocomposite by the electro-co-deposition method followed by uniaxial compaction and sintering is illustrated in Figure 1. The sulphate-based electrolyte bath consisted of $ZnSO_4.7H_2O$ (0.2 M), GNP (100 mg/L), and Na_2SO_4 (0.4 M). The pH of the sulfate-based electrolyte bath was adjusted to pH 3.5 by using 90% diluted sulfuric acid. A DC power supply was provided to four non-consumable Pt-coated titanium anode electrodes which were connected in series, and an electrochemically insulated Pt-coated titanium electrode was used as a cathode. The reagents were diluted in DI water using a magnetic stirrer followed by ultrasonication at 20 kHz frequency (0.5 kW) for uniform distribution of GNP across the electrolyte bath. Continuous agitation at 300 rpm was provided throughout the deposition process to the electrolyte to maintain homogeneity. The electrolyte bath was maintained at room temperature (about 27°C) by water cooling using a running water container. As the process started, the Zn matrix with reinforced GNP was collected on the cathode tip surface, which was dropped down to the bottom of the electrolyte bath by self-weight and uniform jerking to the cathode. Then, obtained nanocomposite powder slurry was filtered and washed in running water to wash out the dissolved impurities and chemicals. After this, the nanocomposite powder was dried and uniaxial compacted at 600 MPa in a die-assisted hydraulic press. Finally, the nanocomposite pellets were sintered in an inert Ar atmosphere at 330°C temperature for 1 hour with a slow temperature ramping rate of 10 °C min^{-1}. Similarly, pure Zn was also prepared by the given process for comparison purposes.

.2 Microstructural, compositional and Morphological analysis of Zn/GNP nanocomposite powder

The XRD diffraction graph of pure Zn and GNP-added Zn nanocomposite powder samples is shown in Figure 2. The obtained diffractive angles (2) for spectrum peaks of Zn are 36.32, 39.03,
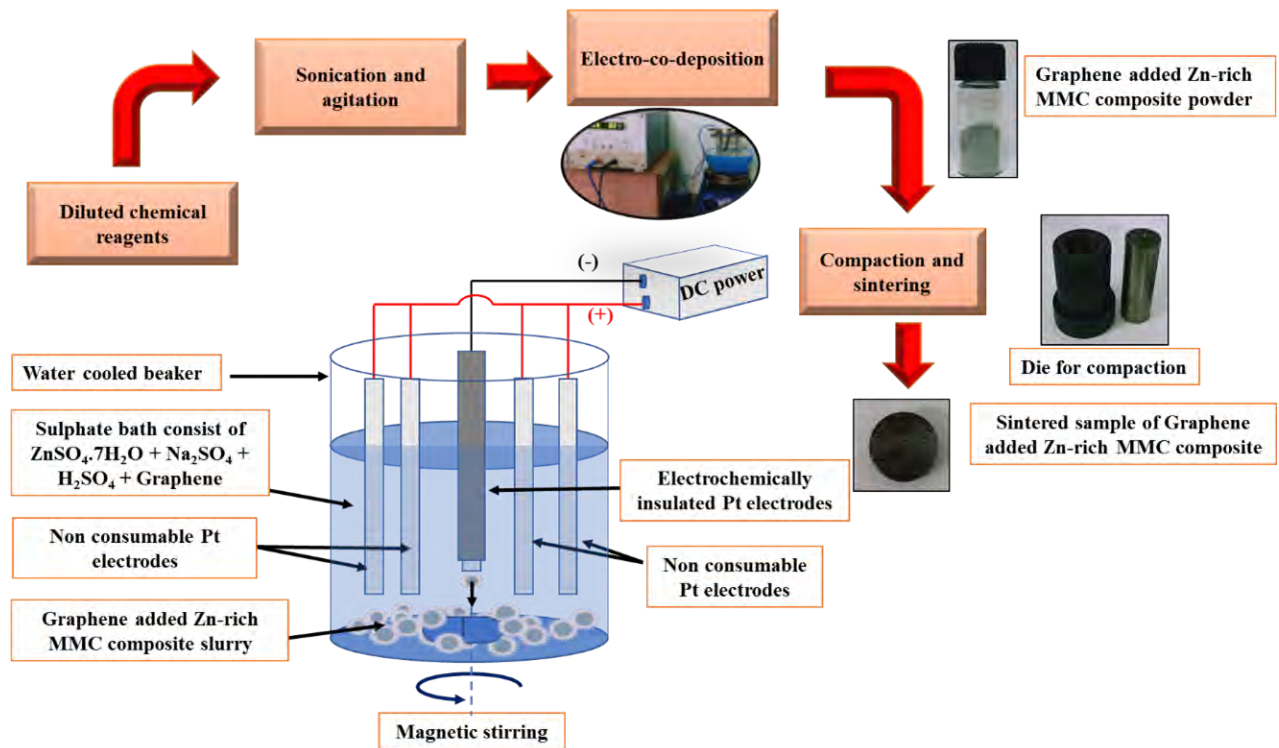
FIGURE 1: Experimental procedure for the synthesis of Zn/GNP nanocomposites powder and pellets

43.26, 54.37, 70.15, 70.70, and 77.13 degrees. The XRD peaks of the pure Zn and GNP-added Zn nanocomposite powder samples show (0 0 2), (1 0 0), (1 0 1), (1 0 2), (1 0 3), (1 1 0), and (0 0 4) diffraction planes, which confirms HCP microstructure of Zn, as per the American mineralogist crystal structure database (AMCSD 0011200) [342]. Comparing the XRD diffraction graph of pure Zn and GNP-added Zn nanocomposite powder sample, a slight shift towards a higher angle was observed for the peak at (1 0 1) plane. Also, the relative intensity of all the peaks present in the XRD spectrum of GNP-added Zn nanocomposite powder sample is reduced than that of pure Zn. This ascertains the nano-reinforcement of the polycrystalline GNP in the Zn matrix is successful. The reduced and shifted peak intensity in the XRD diffraction graph is ascribed to the reduced crystallite size [343]. The crystallite size of pure Zn and GNP-added Zn nanocomposite powder samples are displayed in **??**. By the Scherrer equation, the crystallite size of Zn matrix in the nanocomposite powder sample was 25.5 nm and 32.11 nm, respectively.

FESEM images of the synthesised pure Zn and GNP-added Zn nanocomposite powder samples are shown in Figure 3. From Figure 3a and b, it is evidently seen that the pure Zn powder samples have a large hexagonal shape morphology in a scattered manner, while in GNP-added sample of Zn have shown small and uniformly distributed flaky morphology. The EDS results of the GNP-added Zn nanocomposite powder sample show that the Wt.% of Zn and carbon are about 87.47 and 6.41, respectively, as shown in Figure 4.
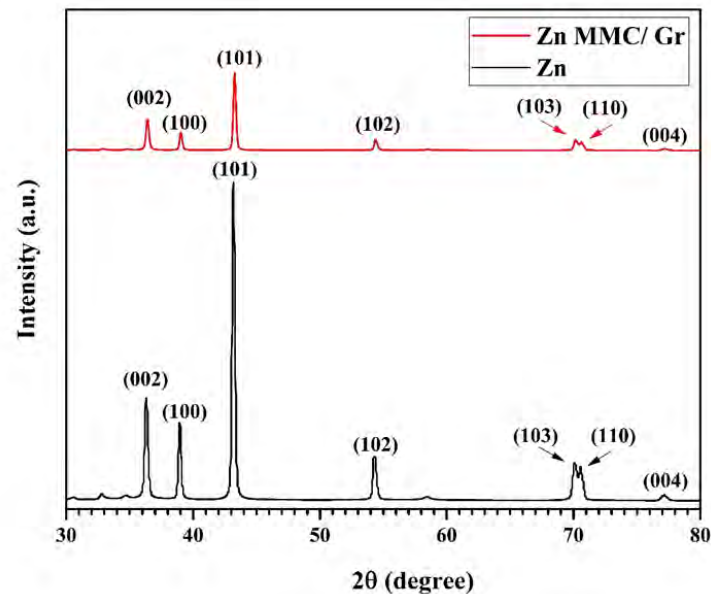
FIGURE 2: XRD diffraction graph for Zn and Zn/GNP nanocomposite powder samples

.3 Tribo-mechanical properties of Zn/GNP nanocomposite

Figure 7.13a shows the micro Vickers hardness graph of pure Zn and GNP-added Zn nanocomposites. The measurement for microhardness is repeated four times for each sample, followed by averaging to evaluate the microhardness. The obtained results show that the microhardness of GNP-added Zn nanocomposite (62 $\pm$ 1 HV) is 36.26 % higher than that of pure Zn (45.5 $\pm$ 1 HV) for the applied indentation load of 50 gm. The GNP layers in the Zn metal matrix with a uniform distribution increase the strength of the Zn metal matrix by owing the superior properties of GNP and refining the crystallite size [219]. According to the grain strengthening mechanism, the increased grain boundary due to grain refinement can reduce the dislocation movement across the Zn matrix, which results in an increase in the hardness of the GNP-added Zn nanocomposite. Also, owing to the shear strength of GNP, the Zn metal matrix can effectively restrict the movement of dislocations among the grains [344].
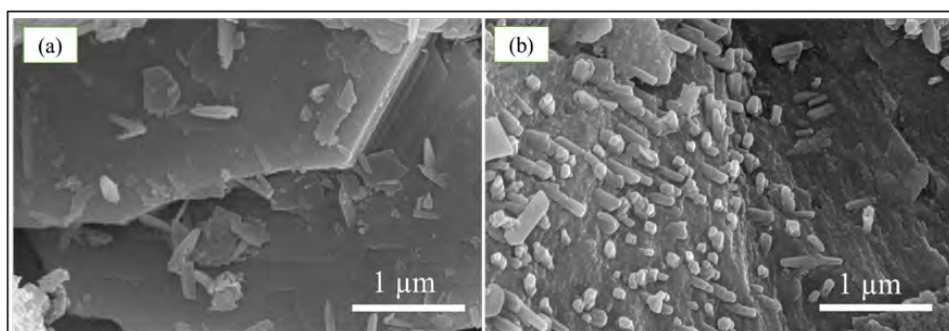
FIGURE 3: FESEM images: (a) Zn and (b) Zn/GNP nanocomposite powder sample.

Element	Wt %
Zn	87.27
C	6.41
O	4.58
S	1.51
K	0.23
Total	100
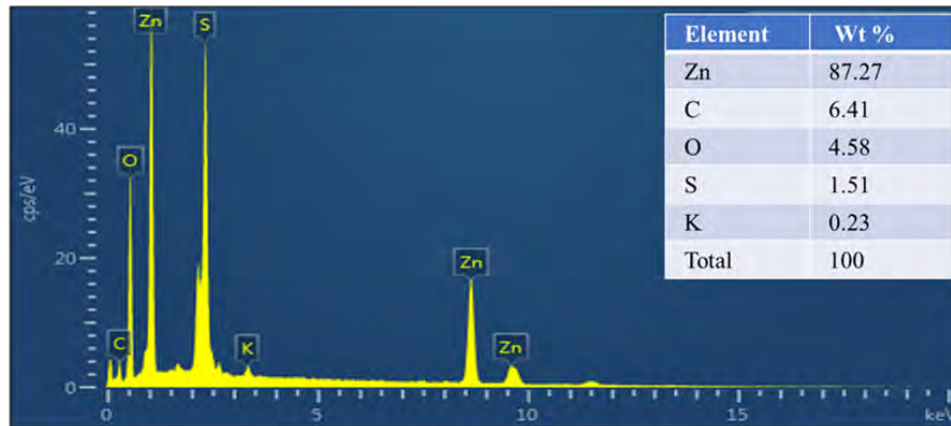
FIGURE 4: EDS results of Zn/GNP nanocomposite powder sample.
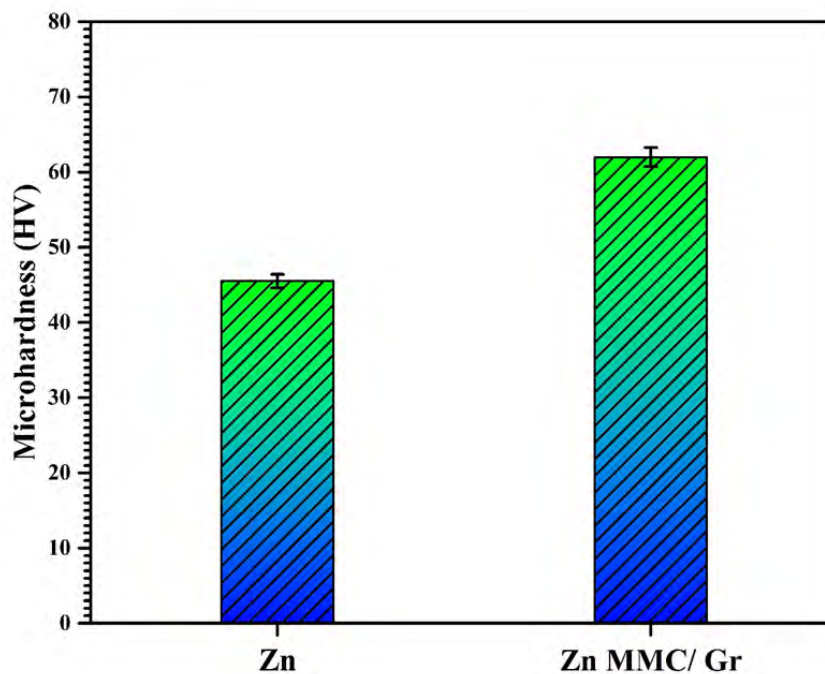
FIGURE 5: Microhardness of Zn/GNP nanocomposite sample

The measured results for the friction coefficient graph of pure Zn and GNP Zn nanocomposite are shown in Figure 6b. After a few initial jerks in the graphs of friction coefficient from 0 s to 180 s, the graphs become smooth, stable, and comparable from 180 s to the last. Here, the graph for the GNP-added sample first settled down for smooth results. It is clear from Figure 6, that the friction coefficient graph of the GNP-added nanocomposite follows significantly lower values of about 0.54 than that of pure Zn (0.72) sample. This 27.7 % decreased value of the friction coefficient of the GNP-added sample is due to the excellent solid-solid lubrication offered by the GNP with its surface properties and single-layered graphitic structure.

The observed wear rate values of GNP-added samples were lower than those of pure Zn samples. It was reduced from 13.4 $\times 10\text{-}4$ mm^3 N^{-1} m^{-1} for pure Zn sample to 5.1 mm^3 N^{-1} m^{-1} for
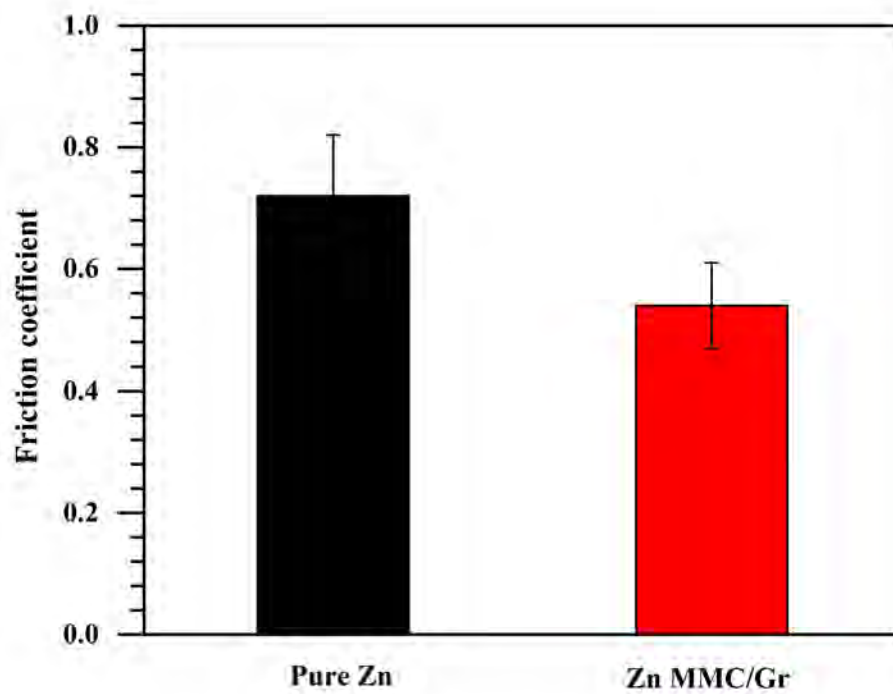
FIGURE 6: Coefficient of friction of Zn/GNP nanocomposite sample

GNP-added nanocomposite. The GNP decreases the wear rate by establishing a lubricant layer between the sliding surfaces, which impedes the mechanical shocks with localized heating and improves the load-carrying capacity. Also, GNP nano reinforcement offers grain refining and strengthening, which helps to decrease the localized plastic deformation in the nanocomposite material, which ultimately improves the wear resistance.

Bibliography

[1] J. R. Jones, "Review of bioactive glass: From hench to hybrids," *Acta biomaterialia*, vol. 9, no. 1, pp. 4457–4486, 2013.

[2] J. Venezuela and M. S. Dargusch, "The influence of alloying and fabrication techniques on the mechanical properties, biodegradability and biocompatibility of zinc: A comprehensive review," *Acta Biomaterialia*, vol. 87, pp. 1–40, 2019, ISSN: 18787568. DOI: 10.1016/j. actbio.2019.01.035. [Online]. Available: https://doi.org/10.1016/j.actbio.2019. 01.035.

[3] S. A. Fadl-allah, "Biocorrosion Control of Electroless Ni-Zn-P Coating Based on Carbon Steel by the Pseudomonas aeruginosa Biofilm," *International Journal of Electrochemical Science*, vol. 11, no. 7, pp. 5490–5506, 2016, ISSN: 14523981. DOI: 10.20964/2016.07.96.

[4] X. Zhai, Y. Ren, N. Wang, *et al.*, "Microbial corrosion resistance and antibacterial property of electrodeposited zn–ni–chitosan coatings," *Molecules*, vol. 24, no. 10, p. 1974, 2019.

[5] H.-S. Han, S. Loffredo, I. Jun, *et al.*, "Current status and outlook on the clinical translation of biodegradable metals," *Materials Today*, vol. 23, pp. 57–71, 2019.

[6] J. J. D. Venezuela, S. Johnston, and M. S. Dargusch, "The Prospects for Biodegradable Zinc in Wound Closure Applications," *Advanced Healthcare Materials*, vol. 8, no. 16, p. 1 900 408, 2019, ISSN: 2192-2640. DOI: 10.1002/adhm.201900408. [Online]. Available: https://onlinelibrary.wiley.com/doi/10.1002/adhm.201900408.

[7] G. Katarivas Levy, J. Goldman, and E. Aghion, "The prospects of zinc as a structural material for biodegradable implants—a review paper," *Metals*, vol. 7, no. 10, 2017, ISSN: 2075-4701. DOI: 10.3390/met7100402. [Online]. Available: https://www.mdpi.com/2075-4701/7/10/402.

[8] M. Prakasam, J. Locs, K. Salma-Ancane, D. Loca, A. Largeteau, and L. Berzina-Cimdina, "Biodegradable Materials and Metallic Implants—A Review," *Journal of Functional Biomaterials*, vol. 8, no. 4, p. 44, 2017, ISSN: 2079-4983. DOI: 10.3390/jfb8040044.

[9] F. Yang, H. Kang, E. Guo, *et al.*, "The role of nickel in mechanical performance and corrosion behaviour of nickel-aluminium bronze in 3.5 wt.% NaCl solution," *Corrosion Science*, vol. 139, no. May, pp. 333–345, 2018, ISSN: 0010938X. DOI: 10.1016/j.corsci. 2018.05.012.

[10] X. Zhao, J. M. Courtney, and H. Qian, *Bioactive materials in medicine: Design and applications*. Elsevier, 2011.

[11] R. N. Jaisinghani, "Antibacterial Properties of Graphene-Based Nanomaterials," *Microbiology Research*, vol. 8, no. 1, pp. 1–32, 2017, ISSN: 2036-7473. DOI: `10.4081/mr.2017.6877`.

[12] V. Harish, D. Tewari, M. Gaur, *et al.*, "Review on nanoparticles and nanostructured materials: Bioimaging, biosensing, drug delivery, tissue engineering, antimicrobial, and agro-food applications," *Nanomaterials*, vol. 12, no. 3, p. 457, 2022.

[13] J. Jeevanandam, A. Barhoum, Y. S. Chan, A. Dufresne, and M. K. Danquah, "Review on nanoparticles and nanostructured materials: History, sources, toxicity and regulations," *Beilstein journal of nanotechnology*, vol. 9, no. 1, pp. 1050–1074, 2018.

[14] K. R. Kreitz, "Catalytic nanoparticle additives in the combustion of ap/htpb composite solid propellant," Ph.D. dissertation, Texas A & M University, 2012.

[15] S. K. Ameta, A. K. Rai, D. Hiran, R. Ameta, and S. C. Ameta, "Use of nanomaterials in food science," in *Biogenic nano-particles and their use in agro-ecosystems*, Springer, 2020, pp. 457–488.

[16] A. D. Pingale, A. Owhal, A. S. Katarkar, S. U. Belgamwar, and J. S. Rathore, "Facile synthesis of graphene by ultrasonic-assisted electrochemical exfoliation of graphite," *Materials Today: Proceedings*, vol. 44, pp. 467–472, 2021, ISSN: 22147853. DOI: `10.1016/j.matpr.2020.10.045`. [Online]. Available: `https://linkinghub.elsevier.com/retrieve/pii/S2214785320376100`.

[17] A. Owhal, A. D. Pingale, S. U. Belgamwar, and J. S. Rathore, "A brief manifestation of antibacterial nanofiller reinforced coatings against the microbial growth based novel engineering problems," *Materials Today: Proceedings*, vol. 47, pp. 3320–3330, 2021, ISSN: 22147853. DOI: `10.1016/j.matpr.2021.07.151`. [Online]. Available: `https://linkinghub.elsevier.com/retrieve/pii/S2214785321050100`.

[18] A. Owhal, A. Pingale, and S. Belgamwar, "Developing sustainable Zn-MWCNTs composite coatings using electrochemical co-deposition method: Tribological and surface wetting behavior," *Advances in Materials and Processing Technologies*, pp. 1–14, 2022, ISSN: 2374-068X. DOI: `10.1080/2374068X.2022.2035968`. [Online]. Available: `https://www.tandfonline.com/doi/full/10.1080/2374068X.2022.2035968`.

[19] M. Rosso, "Ceramic and metal matrix composites: Routes and properties," *Journal of Materials Processing Technology*, vol. 175, no. 1-3, pp. 364–375, 2006, ISSN: 09240136. DOI: `10.1016/j.jmatprotec.2005.04.038`. [Online]. Available: `https://linkinghub.elsevier.com/retrieve/pii/S092401360500419X`.

[20] L. Hao, X. Li, and L. Zhi, "Carbonaceous Electrode Materials for Supercapacitors," *Advanced Materials*, vol. 25, no. 28, pp. 3899–3904, 2013, ISSN: 09359648. DOI: `10.1002/adma.201301204`. [Online]. Available: `https://onlinelibrary.wiley.com/doi/10.1002/adma.201301204`.

[21] C. R. Thurber, Y. H. Ahmad, M. C. Calhoun, *et al.*, "Metal Matrix Composite Coatings of Cupronickel Embedded with Nanoplatelets for Improved Corrosion Resistant Properties," *International Journal of Corrosion*, vol. 2018, pp. 1–11, 2018, ISSN: 1687-9325. DOI: `10.1155/2018/5250713`. [Online]. Available: `https://www.hindawi.com/journals/ijc/2018/5250713/`.

[22] P. K. Rohatgi, N. Gupta, and A Daoud, "Synthesis and processing of cast metal-matrix composites and their applications," *ASM handbook*, vol. 15, pp. 1149–1164, 2008.

[23] A. Dorri Moghadam, E. Omrani, P. L. Menezes, and P. K. Rohatgi, "Mechanical and tribological properties of self-lubricating metal matrix nanocomposites reinforced by carbon nanotubes (CNTs) and graphene – A review," *Composites Part B: Engineering*, vol. 77, pp. 402–420, 2015, ISSN: 13598368. DOI: `10.1016/j.compositesb.2015.03.014`. [Online]. Available: `https://linkinghub.elsevier.com/retrieve/pii/S135983681500133X`.

[24] K. Chu and C. Jia, "Enhanced strength in bulk graphene-copper composites," *Physica Status Solidi (A) Applications and Materials Science*, vol. 211, no. 1, pp. 184–190, 2014, ISSN: 18626300. DOI: `10.1002/pssa.201330051`.

[25] A. Nikiforov, X. Deng, Q. Xiong, *et al.*, "Non-thermal plasma technology for the development of antimicrobial surfaces: A review," *Journal of Physics D: Applied Physics*, vol. 49, no. 20, 2016, ISSN: 13616463. DOI: `10.1088/0022-3727/49/20/204002`.

[26] W. Zhang, X. Xia, C. Qi, C. Xie, and S. Cai, "A porous Cu/LDPE composite for copper-containing intrauterine contraceptive devices," *Acta Biomaterialia*, vol. 8, no. 2, pp. 897–903, 2012, ISSN: 17427061. DOI: `10.1016/j.actbio.2011.09.024`.

[27] M. Rashad, F. Pan, M. Asif, and A. Tang, "Powder metallurgy of Mg-1%Al-1%Sn alloy reinforced with low content of graphene nanoplatelets (GNPs)," *Journal of Industrial and Engineering Chemistry*, vol. 20, no. 6, pp. 4250–4255, 2014, ISSN: 22345957. DOI: `10.1016/j.jiec.2014.01.028`.

[28] H. Feng, R. Cheng, X. Zhao, X. Duan, and J. Li, "A low-temperature method to produce highly reduced graphene oxide," *Nature communications*, vol. 4, no. 1, pp. 1–8, 2013.

[29] C Kostagiannakopoulou, X Tsilimigkra, G Sotiriadis, and V Kostopoulos, "Synergy effect of carbon nano-fillers on the fracture toughness of structural composites," *Composites Part B: Engineering*, vol. 129, pp. 18–25, 2017.

[30] R. Casati and M. Vedani, "Metal Matrix Composites Reinforced by Nano-Particles—A Review," *Metals*, vol. 4, no. 1, pp. 65–83, 2014, ISSN: 2075-4701. DOI: `10.3390/met4010065`.

[31] M. Malaki, W. Xu, A. K. Kasar, *et al.*, *Advanced metal matrix nanocomposites.* 2019, vol. 9, ISBN: 8415683111. DOI: `10.3390/met9030330`.

[32] M. Bastwros, G.-Y. Y. Kim, C. Zhu, *et al.*, "Effect of ball milling on graphene reinforced Al6061 composite fabricated by semi-solid sintering," *Composites Part B: Engineering*, vol. 60, pp. 111–118, 2014, ISSN: 13598368. DOI: `10.1016/j.compositesb.2013.12.043`. [Online]. Available: `https://linkinghub.elsevier.com/retrieve/pii/S1359836813007737`.

[33] H. F. Li, X. H. Xie, Y. F. Zheng, *et al.*, "Development of biodegradable Zn-1X binary alloys with nutrient alloying elements Mg, Ca and Sr," *Scientific Reports*, vol. 5, pp. 1–14, 2015, ISSN: 20452322. DOI: `10.1038/srep10719`.

[34] S. F. Bartolucci, J. Paras, M. A. Rafiee, *et al.*, "Graphene-aluminum nanocomposites," *Materials Science and Engineering A*, vol. 528, no. 27, pp. 7933–7937, 2011, ISSN: 09215093. DOI: `10.1016/j.msea.2011.07.043`.

[35] K. Delgado, R. Quijada, R. Palma, and H. Palza, "Polypropylene with embedded copper metal or copper oxide nanoparticles as a novel plastic antimicrobial agent," *Letters in Applied Microbiology*, vol. 53, no. 1, pp. 50–54, 2011, ISSN: 02668254. DOI: `10.1111/j.1472-765X.2011.03069.x`. [Online]. Available: `http://doi.wiley.com/10.1111/j.1472-765X.2011.03069.x`.

[36] J. Zhao, K. Yu, L. Chen, S. Li, Y. Hu, and L. Lei, "Mechanical properties and biodegradable behavior of Mg–6%Zn–Ca 3 (PO 4) 2 metal matrix composites in Ringer's solution," *International Journal of Materials Research*, vol. 103, no. 6, pp. 723–728, 2012, ISSN: 1862-5282. DOI: `10.3139/146.110686`. [Online]. Available: `http://www.hanser-elibrary.com/doi/abs/10.3139/146.110686`.

[37] M. Ramya, M. M. Pillai, R. Selvakumar, B. Raj, and K. R. Ravi, "Hydroxyapatite particle (HAp) reinforced biodegradable Mg-Zn-Ca metallic glass composite for bio-implant applications," *Biomedical Physics and Engineering Express*, vol. 4, no. 2, 2018, ISSN: 20571976. DOI: `10.1088/2057-1976/aa85be`.

[38] S. Ghaziof and W. Gao, "Zn–Ni–Al2O3 nano-composite coatings prepared by sol-enhanced electroplating," *Applied Surface Science*, vol. 351, pp. 869–879, 2015, ISSN: 01694332. DOI: `10.1016/j.apsusc.2015.06.010`. [Online]. Available: `http://dx.doi.org/10.1016/j.apsusc.2015.06.010https://linkinghub.elsevier.com/retrieve/pii/S0169433215013434`.

[39] J. Hu, Z. Zhong, F. Zhang, W. Xing, W. Jin, and N. Xu, "High-efficiency, Synergistic ZnO-Coated SiC Photocatalytic Filter with Antibacterial Properties," *Industrial & Engineering Chemistry Research*, vol. 55, no. 23, pp. 6661–6670, 2016, ISSN: 0888-5885. DOI: `10.1021/acs.iecr.6b00988`. [Online]. Available: `http://library1.nida.ac.th/termpaper6/sd/2554/19755.pdfhttps://pubs.acs.org/doi/10.1021/acs.iecr.6b00988`.

[40] A. Owhal, A. Pingale, and S. Belgamwar, "Developing sustainable Zn-MWCNTs composite coatings using electrochemical co-deposition method: Tribological and surface wetting behavior," *Advances in Materials and Processing Technologies*, pp. 1–14, 2022, ISSN: 2374-068X. DOI: `10.1080/2374068X.2022.2035968`. [Online]. Available: `https://www.tandfonline.com/doi/full/10.1080/2374068X.2022.2035968`.

[41] P. Wang, J. Shen, T. Chen, Q. Li, L. Wang, *et al.*, "Fabrication of graphene nanoplatelets reinforced mg matrix composites via powder thixoforging," *Journal of Magnesium and Alloys*, 2021.

[42] C. Song, D. Wu, F. Zhang, P. Liu, Q. Lu, and X. Feng, "Gemini surfactant assisted synthesis of two-dimensional metal nanoparticles/graphene composites," *Chemical Communications*, vol. 48, no. 15, pp. 2119–2121, 2012.

[43] K. Munir, C. Wen, and Y. Li, "Graphene nanoplatelets-reinforced magnesium metal matrix nanocomposites with superior mechanical and corrosion performance for biomedical applications," *Journal of Magnesium and Alloys*, vol. 8, no. 1, pp. 269–290, 2020.

[44] S. Pandit, K. Gaska, R. Kádár, and I. Mijakovic, "Graphene-Based Antimicrobial Biomedical Surfaces," *ChemPhysChem*, 2020, ISSN: 14397641. DOI: `10.1002/cphc.202000769`.

[45] A. N. Banerjee, "Graphene and its derivatives as biomedical materials: Future prospects and challenges," *Interface Focus*, vol. 8, no. 3, 2018, ISSN: 20428901. DOI: `10.1098/rsfs.2017.0056`.

[46] P. C. S. Boyapati, K. Srinivas, and S. Akhil, "Green synthesized graphene-hydroxyapatite nanocomposites for bioimplant applications," *Materials Letters*, vol. 327, p. 133 059, 2022.

[47] J. Tian, S. Wu, X. Yin, and W. Wu, "Novel preparation of hydrophilic graphene/graphene oxide nanosheets for supercapacitor electrode," *Applied Surface Science*, vol. 496, p. 143 696, 2019, ISSN: 01694332. DOI: `10.1016/j.apsusc.2019.143696`.

[48] Y. Xu and J. Liu, "Graphene as transparent electrodes: Fabrication and new emerging applications," *Small*, vol. 12, no. 11, pp. 1400–1419, 2016.

[49] H. Huang, S. Su, N. Wu, *et al.*, "Graphene-based sensors for human health monitoring," *Frontiers in chemistry*, p. 399, 2019.

[50] G. Jnawali, H. Lee, J.-W. Lee, *et al.*, "Graphene-complex-oxide nanoscale device concepts," *ACS nano*, vol. 12, no. 6, pp. 6128–6136, 2018.

[51] S Kumar, G. Duesberg, R Pratap, and S Raghavan, "Graphene field emission devices," *Applied Physics Letters*, vol. 105, no. 10, p. 103 107, 2014.

[52] J. S. Lewis, T. Perrier, Z. Barani, F. Kargar, and A. A. Balandin, "Thermal interface materials with graphene fillers: Review of the state of the art and outlook for future applications," *Nanotechnology*, vol. 32, no. 14, p. 142 003, 2021.

[53] S. Lo, S Dionne, and F. Goodwin, "Overview on the development of zinc-based metal matrix composites," *World Zinc'93*, pp. 607–612, 1993.

[54] S. S. Owoeye, D. O. Folorunso, B. Oji, and S. G. Borisade, "Zinc-aluminum (za-27)-based metal matrix composites: A review article of synthesis, reinforcement, microstructural, mechanical, and corrosion characteristics," *The International Journal of Advanced Manufacturing Technology*, vol. 100, no. 1, pp. 373–380, 2019.

[55] A. Owhal, A. D. Pingale, S. U. Belgamwar, and J. S. Rathore, "Preparation of novel Zn/Gr MMC using a modified electro-co-deposition method: Microstructural and tribomechanical properties," *Materials Today: Proceedings*, vol. 44, no. xxxx, pp. 222–228, 2021, ISSN: 22147853. DOI: `10.1016/j.matpr.2020.09.459`. [Online]. Available: `https://doi.org/10.1016/j.matpr.2020.09.459https://linkinghub.elsevier.com/retrieve/pii/S2214785320371753`.

[56] V. Georgakilas, J. A. Perman, J. Tucek, and R. Zboril, "Broad family of carbon nanoallotropes: Classification, chemistry, and applications of fullerenes, carbon dots, nanotubes, graphene, nanodiamonds, and combined superstructures," *Chemical reviews*, vol. 115, no. 11, pp. 4744–4822, 2015.

[57] S. Teng, Y. Gao, F. Cao, *et al.*, "Zinc-reduced graphene oxide for enhanced corrosion protection of zinc-rich epoxy coatings," *Progress in Organic Coatings*, vol. 123, pp. 185–189, 2018.

[58] N. H. Othman, M. C. Ismail, M. Mustapha, N. Sallih, K. E. Kee, and R. A. Jaal, "Graphene-based polymer nanocomposites as barrier coatings for corrosion protection," *Progress in Organic Coatings*, vol. 135, pp. 82–99, 2019.

[59] K. Ollik and M. Lieder, "Review of the application of graphene-based coatings as anticorrosion layers," *Coatings*, vol. 10, no. 9, p. 883, 2020.

[60] M. Shahin, K. Munir, C. Wen, and Y. Li, "Magnesium-based composites reinforced with graphene nanoplatelets as biodegradable implant materials," *Journal of Alloys and Compounds*, vol. 828, p. 154 461, 2020.

[61] R. Hänsch and R. R. Mendel, "Physiological functions of mineral micronutrients (cu, zn, mn, fe, ni, mo, b, cl)," *Current opinion in plant biology*, vol. 12, no. 3, pp. 259–266, 2009.

[62] X. Tong, H. Wang, L. Zhu, *et al.*, "A biodegradable in situ zn–mg2ge composite for bone-implant applications," *Acta Biomaterialia*, vol. 146, pp. 478–494, 2022.

[63] I. Onche, O. Osagie, and S INuhu, "Removal of orthopaedic implants: Indications, outcome and economic implications," *Journal of the West African College of Surgeons*, vol. 1, no. 1, p. 101, 2011.

[64] M. Ilyas, M. Ilyas, F. Sher, *et al.*, "Advantages and challenges of biodegradable electronic devices," in *Conducting Polymers*, CRC Press, 2022, pp. 287–304.

[65] W. J. Smith, F. E. Goodwin, Z. Alloys, S. Rebars, A. Alloys, and M. Material, "Zinc Coating,"

[66] A McIlhagger, E Archer, and R McIlhagger, "Manufacturing processes for composite materials and components for aerospace applications," in *Polymer composites in the aerospace industry*, Elsevier, 2020, pp. 59–81.

[67] P. D. Pastuszak and A. Muc, "Application of composite materials in modern constructions," in *Key Engineering Materials*, Trans Tech Publ, vol. 542, 2013, pp. 119–129.

[68] "Antifouling Coatings Market 84.1666666666667 Global Analysis, Industry Size, Share, Trends, Application Analysis and Growth Opportunities Forecast to 2027 : Reports and Data," *SBWire*, 2020. [Online]. Available: `http://www.sbwire.com/press-releases/ antifouling - coatings - market - 2020 - global - analysis - industry - size - share - trends - application - analysis - and - growth - opportunities - forecast - to - 2027 - reports-and-data-1321393.htm`.

[69] *Antimicrobial Coatings Market*, 2019. [Online]. Available: `https://www.gminsights.com/ industry-analysis/antimicrobial-coatings-market-report`.

[70] "Antimicrobial coatings market expected to increase due to COVID-19 pandemic," *Focus on Powder Coatings*, vol. 2020, no. 9, p. 7, 2020, ISSN: 13645439. DOI: `10.1016/j.fopow. 2020.08.031`. [Online]. Available: `https://linkinghub.elsevier.com/retrieve/pii/ S136454392030277X`.

[71] *New Self-healing Anti-corrosion Coating for Zinc-Plated & Galvanized Steel*, 2014. [Online]. Available: `https://www.neicorporation.com/self-healing-anti-corrosion- coating-for-zinc-plated-galvanized-steel/`.

[72] J. W. Costerton, "Bacterial Biofilms: A Common Cause of Persistent Infections," *Science*, vol. 284, no. 5418, pp. 1318–1322, 1999, ISSN: 00368075. DOI: `10.1126/science.284. 5418.1318`. [Online]. Available: `https://link.springer.com/article/10.1023/A$\% $3A1020720504942https://www.sciencemag.org/lookup/doi/10.1126/science.284. 5418.1318`.

[73] W. Ahmed, Z. Zhai, and C. Gao, "Adaptive antibacterial biomaterial surfaces and their applications," *Materials Today Bio*, vol. 2, no. March, 2019, ISSN: 25900064. DOI: `10.1016/ j.mtbio.2019.100017`.

[74] Z. Khatoon, C. D. McTiernan, E. J. Suuronen, T. F. Mah, and E. I. Alarcon, "Bacterial biofilm formation on implantable devices and approaches to its treatment and prevention," *Heliyon*, vol. 4, no. 12, 2018, ISSN: 24058440. DOI: `10.1016/j.heliyon.2018.e01067`.

[75] R. O. Darouiche, "Antimicrobial approaches for preventing infections associated with surgical implants," *Clinical Infectious Diseases*, vol. 36, no. 10, pp. 1284–1289, 2003, ISSN: 10584838. DOI: `10.1086/374842`.

[76] M. Ribeiro, F. J. Monteiro, and M. P. Ferraz, "Infection of orthopedic implants with emphasis on bacterial adhesion process and techniques used in studying bacterial-material interactions," *Biomatter*, vol. 2, no. 4, pp. 176–194, 2012, ISSN: 2159-2535. DOI: 10.4161/biom.22905. [Online]. Available: http://www.tandfonline.com/doi/abs/10.4161/biom.22905.

[77] B. Allegranzi, S. B. Nejad, G. G. Castillejos, C. Kilpatrick, E. Kelley, and E. Mathai, "Report on the Burden of Endemic Health Care-Associated Infection Worldwide," World Health Organization, Geneva, Tech. Rep., 2011. [Online]. Available: https://apps.who.int/iris/handle/10665/80135.

[78] N. Ciacotich, R. U. Din, J. J. Sloth, P. Møller, and L. Gram, "An electroplated copper–silver alloy as antibacterial coating on stainless steel," *Surface and Coatings Technology*, vol. 345, no. 2017, pp. 96–104, 2018, ISSN: 02578972. DOI: 10.1016/j.surfcoat.2018.04.007. [Online]. Available: https://linkinghub.elsevier.com/retrieve/pii/S0257897218303621.

[79] M. Muller, C. MacDougall, M Lim, *et al.*, "Antimicrobial surfaces to prevent healthcare-associated infections: a systematic review," *Journal of Hospital Infection*, vol. 92, no. 1, pp. 7–13, 2016, ISSN: 01956701. DOI: 10.1016/j.jhin.2015.09.008. [Online]. Available: https://linkinghub.elsevier.com/retrieve/pii/S0195670115003667.

[80] P Zarb, B Coignard, J Griskeviciene, *et al.*, "The European Centre for Disease Prevention and Control (ECDC) pilot point prevalence survey of healthcare-associated infections and antimicrobial use," *Eurosurveillance*, vol. 17, no. 46, pp. 1–16, 2012, ISSN: 1560-7917. DOI: 10.2807/ese.17.46.20316-en. [Online]. Available: http://www.eurosurveillance.org/content/10.2807/ese.17.46.20316-en.

[81] M. Ramasamy and J. Lee, "Recent Nanotechnology Approaches for Prevention and Treatment of Biofilm-Associated Infections on Medical Devices," *BioMed Research International*, vol. 2016, pp. 1–17, 2016, ISSN: 2314-6133. DOI: 10.1155/2016/1851242. [Online]. Available: https://www.hindawi.com/journals/bmri/2016/1851242/.

[82] J. M. Boyce, "Environmental contamination makes an important contribution to hospital infection," *Journal of Hospital Infection*, vol. 65, no. SUPPL. 2, pp. 50–54, 2007, ISSN: 01956701. DOI: 10.1016/S0195-6701(07)60015-2. [Online]. Available: https://linkinghub.elsevier.com/retrieve/pii/S0195670107600152.

[83] S. Achinas, N. Charalampogiannis, and G. J. W. Euverink, "A brief recap of microbial adhesion and biofilms," *Applied Sciences (Switzerland)*, vol. 9, no. 14, pp. 1–15, 2019, ISSN: 20763417. DOI: 10.3390/app9142801.

[84] M. Schmidt, C. Salgado, K. Freeman, *et al.*, "Antimicrobial surfaces to prevent healthcare-associated infections: a systematic review – a different view," *Journal of Hospital Infection*, vol. 99, no. 3, pp. 309–311, 2018, ISSN: 01956701. DOI: `10.1016/j.jhin.2018.02.007`. [Online]. Available: `https://linkinghub.elsevier.com/retrieve/pii/S0195670118300999`.

[85] O. P. Abioye, C. A. Loto, and O. S. I. Fayomi, "Evaluation of Anti-biofouling Progresses in Marine Application," *Journal of Bio- and Tribo-Corrosion*, vol. 5, no. 1, p. 22, 2019, ISSN: 2198-4220. DOI: `10.1007/s40735-018-0213-5`. [Online]. Available: `http://link.springer.com/10.1007/s40735-018-0213-5`.

[86] M. A. Champ, "Economic and environmental impacts on ports and harbors from the convention to ban harmful marine anti-fouling systems," *Marine Pollution Bulletin*, vol. 46, no. 8, pp. 935–940, 2003, ISSN: 0025326X. DOI: `10.1016/S0025-326X(03)00106-1`. [Online]. Available: `https://linkinghub.elsevier.com/retrieve/pii/S0025326X03001061`.

[87] H. A. Videla and W. G. Characklis, "Biofouling and microbially influenced corrosion," *International Biodeterioration & Biodegradation*, vol. 29, no. 3-4, pp. 195–212, 1992, ISSN: 09648305. DOI: `10.1016/0964-8305(92)90044-O`. [Online]. Available: `https://www.scientific.net/AMR.794.539https://linkinghub.elsevier.com/retrieve/pii/0964830592900440`.

[88] P. Hu, Q. Xie, C. Ma, and G. Zhang, "Silicone-Based Fouling-Release Coatings for Marine Antifouling," *Langmuir*, vol. 36, no. 9, pp. 2170–2183, 2020, ISSN: 15205827. DOI: `10.1021/acs.langmuir.9b03926`. [Online]. Available: `https://pubs.acs.org/doi/abs/10.1021/acs.langmuir.9b03926`.

[89] N. O. San, H. Nazır, and G. Dönmez, "Microbially influenced corrosion and inhibition of nickel–zinc and nickel–copper coatings by Pseudomonas aeruginosa," *Corrosion Science*, vol. 79, pp. 177–183, 2014, ISSN: 0010938X. DOI: `10.1016/j.corsci.2013.11.004`.

[90] A. Cavallaro, S. Taheri, and K. Vasilev, "Responsive and "smart" antibacterial surfaces: Common approaches and new developments (Review)," *Biointerphases*, vol. 9, no. 2, p. 029 005, 2014, ISSN: 1934-8630. DOI: `10.1116/1.4866697`. [Online]. Available: `http://library1.nida.ac.th/termpaper6/sd/2554/19755.pdfhttp://avs.scitation.org/doi/10.1116/1.4866697`.

[91] S. Kittler, C. Greulich, J. Diendorf, M. Ko ller, and M. Epple, "Toxicity of Silver Nanoparticles Increases during Storage Because of Slow Dissolution under Release of Silver Ions," *Chemistry of Materials*, vol. 22, no. 16, pp. 4548–4554, 2010, ISSN: 0897-4756. DOI: `10.1021/cm100023p`. [Online]. Available: `http://library1.nida.ac.th/termpaper6/sd/2554/19755.pdfhttps://pubs.acs.org/doi/10.1021/cm100023p`.

[92] V. K. Truong, R. Lapovok, Y. S. Estrin, *et al.*, "The influence of nano-scale surface roughness on bacterial adhesion to ultrafine-grained titanium," *Biomaterials*, vol. 31, no. 13, pp. 3674–3683, 2010, ISSN: 01429612. DOI: `10.1016/j.biomaterials.2010.01.071`. [Online]. Available: `https://linkinghub.elsevier.com/retrieve/pii/S0142961210001031`.

[93] C. G. van Hoogmoed, H. C. van der Mei, and H. J. Busscher, "The influence of calcium on the initial adhesion of S. thermophilus to stainless steel under flow studied by metallurgical microscopy," *Biofouling*, vol. 11, no. 2, pp. 167–176, 1997, ISSN: 0892-7014. DOI: `10.1080/08927019709378327`. [Online]. Available: `http://www.tandfonline.com/doi/abs/10.1080/08927019709378327`.

[94] M. Katsikogianni, I. Spiliopoulou, D. P. Dowling, and Y. F. Missirlis, "Adhesion of slime producing Staphylococcus epidermidis strains to PVC and diamond-like carbon/silver/fluorinated coatings," *Journal of Materials Science: Materials in Medicine*, vol. 17, no. 8, pp. 679–689, 2006, ISSN: 0957-4530. DOI: `10.1007/s10856-006-9678-8`. [Online]. Available: `http://link.springer.com/10.1007/s10856-006-9678-8`.

[95] C. Sousa, P. Teixeira, and R. Oliveira, "Influence of Surface Properties on the Adhesion of Staphylococcus epidermidis to Acrylic and Silicone," *International Journal of Biomaterials*, vol. 2009, pp. 1–9, 2009, ISSN: 1687-8787. DOI: `10.1155/2009/718017`. [Online]. Available: `http://www.hindawi.com/journals/ijbm/2009/718017/`.

[96] N. Høiby, T. Bjarnsholt, M. Givskov, S. Molin, and O. Ciofu, "Antibiotic resistance of bacterial biofilms," *International Journal of Antimicrobial Agents*, vol. 35, no. 4, pp. 322–332, 2010, ISSN: 09248579. DOI: `10.1016/j.ijantimicag.2009.12.011`. [Online]. Available: `https://linkinghub.elsevier.com/retrieve/pii/S0924857910000099`.

[97] D Pavithra and M. Doble, "Biofilm formation, bacterial adhesion and host response on polymeric implants—issues and prevention," *Biomedical Materials*, vol. 3, no. 3, p. 034 003, 2008, ISSN: 1748-6041. DOI: `10.1088/1748-6041/3/3/034003`. [Online]. Available: `http://library1.nida.ac.th/termpaper6/sd/2554/19755.pdfhttps://iopscience.iop.org/article/10.1088/1748-6041/3/3/034003`.

[98] T. R. Khan, A. Erbe, M. Auinger, F. Marlow, and M. Rohwerder, "Electrodeposition of zinc–silica composite coatings: challenges in incorporating functionalized silica particles into a zinc matrix," *Science and Technology of Advanced Materials*, vol. 12, no. 5, p. 055 005, 2011, ISSN: 1468-6996. DOI: `10.1088/1468-6996/12/5/055005`. [Online]. Available: `http://www.tandfonline.com/doi/full/10.1088/1468-6996/12/5/055005`.

[99] M. Azizi, W. Schneider, and W. Plieth, "Electrolytic co-deposition of silicate and mica particles with zinc," *Journal of Solid State Electrochemistry*, vol. 9, no. 6, pp. 429–437, 2005, ISSN: 1432-8488. DOI: `10.1007/s10008-004-0572-3`. [Online]. Available: `http://link.springer.com/10.1007/s10008-004-0572-3`.

[100] T. J. Tuaweri and G. D. Wilcox, "Behaviour of Zn-SiO2 electrodeposition in the presence of N,N-dimethyldodecylamine," *Surface and Coatings Technology*, vol. 200, no. 20-21, pp. 5921–5930, 2006, ISSN: 02578972. DOI: 10.1016/j.surfcoat.2005.09.023.

[101] E Hamzah, S. N. Saud, and E Akbari, "Structure, corrosion behavior, and antibacterial properties of nano-silica/graphene oxide coating on biodegradable magnesium alloy for biomedical applications," *Vaccum*, 2016. DOI: 10.1016/j.vacuum.2016.05.021.This.

[102] X. G. Zhang, *Corrosion and Electrochemistry of Zinc*. Boston, MA: Springer US, 1996, ISBN: 978-1-4757-9879-1. DOI: 10.1007/978-1-4757-9877-7. [Online]. Available: http://library1.nida.ac.th/termpaper6/sd/2554/19755.pdfhttp://link.springer.com/10.1007/978-1-4757-9877-7.

[103] S. Pandit, Z. Cao, V. R. S. S. Mokkapati, *et al.*, "Vertically Aligned Graphene Coating is Bactericidal and Prevents the Formation of Bacterial Biofilms," *Advanced Materials Interfaces*, vol. 5, no. 7, p. 1 701 331, 2018, ISSN: 21967350. DOI: 10.1002/admi.201701331. [Online]. Available: http://doi.wiley.com/10.1002/admi.201701331.

[104] Z. Noreen, N. Khalid, R. Abbasi, S. Javed, I. Ahmad, and H. Bokhari, "Visible light sensitive Ag/TiO2/graphene composite as a potential coating material for control of Campylobacter jejuni," *Materials Science and Engineering: C*, vol. 98, no. December 2018, pp. 125–133, 2019, ISSN: 09284931. DOI: 10.1016/j.msec.2018.12.087. [Online]. Available: https://linkinghub.elsevier.com/retrieve/pii/S0928493118307082.

[105] S. Wang, X. Zou, X. Xie, *et al.*, "Electrochemical Fabrication of Micro / Nanoporous Copper by Electrosynthesis-Dealloying of Cu – Zn Alloy in Deep Eutectic Solvent," 2018.

[106] A. Naskar, S. Bera, R. Bhattacharya, *et al.*, "Synthesis, characterization and antibacterial activity of Ag incorporated ZnO–graphene nanocomposites," *RSC Advances*, vol. 6, no. 91, pp. 88 751–88 761, 2016, ISSN: 2046-2069. DOI: 10.1039/C6RA14808E. [Online]. Available: http://xlink.rsc.org/?DOI=C6RA14808E.

[107] O. Akhavan, M. Abdolahad, Y. Abdi, and S. Mohajerzadeh, "Silver nanoparticles within vertically aligned multi-wall carbon nanotubes with open tips for antibacterial purposes," *Journal of Materials Chemistry*, vol. 21, no. 2, pp. 387–393, 2011, ISSN: 09599428. DOI: 10.1039/c0jm02395g.

[108] S. K. Singhal, M. Lal, Lata, S. R. Kabi, and R. B. Mathur, "Synthesis of Cu/CNTs nanocomposites for antimicrobial activity," *Advances in Natural Sciences: Nanoscience and Nanotechnology*, vol. 3, no. 4, p. 045 011, 2012, ISSN: 2043-6262. DOI: 10.1088/2043-6262/3/4/045011. [Online]. Available: https://iopscience.iop.org/article/10.1088/2043-6262/3/4/045011.

[109] A. M. Díez-Pascual and A. L. Díez-Vicente, "PEGylated boron nitride nanotube-reinforced poly(propylene fumarate) nanocomposite biomaterials," *RSC Advances*, vol. 6, no. 83, pp. 79 507–79 519, 2016, ISSN: 2046-2069. DOI: `10.1039/C6RA09884C`. [Online]. Available: `http://xlink.rsc.org/?DOI=C6RA09884C`.

[110] K. Hongmin, Y. Zhaoyi, and Z. Ning, "Preparation of Ni-SiC Composite Coating by Electrochemical Deposition," *Rare Metal Materials and Engineering*, vol. 44, no. 12, pp. 2960–2964, 2015, ISSN: 18755372. DOI: `10.1016/S1875-5372(16)60030-9`. [Online]. Available: `https://linkinghub.elsevier.com/retrieve/pii/S1875537216600309`.

[111] M. Hussein, N. Ankah, A. M. Kumar, *et al.*, "Mechanical, biocorrosion, and antibacterial properties of nanocrystalline TiN coating for orthopedic applications," *Ceramics International*, vol. 46, no. 11, pp. 18 573–18 583, 2020, ISSN: 02728842. DOI: `10.1016/j.ceramint. 2020.04.164`. [Online]. Available: `https://linkinghub.elsevier.com/retrieve/pii/ S0272884220311081`.

[112] R. K. Matharu, L. Ciric, G. Ren, and M. Edirisinghe, "Comparative Study of the Antimicrobial Effects of Tungsten Nanoparticles and Tungsten Nanocomposite Fibres on Hospital Acquired Bacterial and Viral Pathogens," *Nanomaterials*, vol. 10, no. 6, p. 1017, 2020, ISSN: 2079-4991. DOI: `10.3390/nano10061017`. [Online]. Available: `http://library1.nida.ac. th/termpaper6/sd/2554/19755.pdfhttps://www.mdpi.com/2079-4991/10/6/1017`.

[113] M. A. Muflikhun, M. C. Frommelt, M. Farman, A. Y. Chua, and G. N. C. Santos, "Structures, mechanical properties and antibacterial activity of Ag/TiO 2 nanocomposite materials synthesized via HVPG technique for coating application," *Heliyon*, vol. 5, no. 4, 2019, ISSN: 24058440. DOI: `10.1016/j.heliyon.2019.e01475`.

[114] Y. Reyes-Vidal, R. Suarez-Rojas, C. Ruiz, *et al.*, "Electrodeposition, characterization, and antibacterial activity of zinc/silver particle composite coatings," *Applied Surface Science*, vol. 342, no. 1, pp. 34–41, 2015, ISSN: 01694332. DOI: `10.1016/j.apsusc.2015.03.037`. [Online]. Available: `http://library1.nida.ac.th/termpaper6/sd/2554/19755. pdfhttps://linkinghub.elsevier.com/retrieve/pii/S0169433215006042`.

[115] C. Chambers, S. Stewart, B. Su, H. Jenkinson, J. Sandy, and A. Ireland, "Silver doped titanium dioxide nanoparticles as antimicrobial additives to dental polymers," *Dental Materials*, vol. 33, no. 3, e115–e123, 2017, ISSN: 01095641. DOI: `10.1016/j.dental. 2016.11.008`. [Online]. Available: `https://linkinghub.elsevier.com/retrieve/pii/ S0109564116306522`.

[116] R. J. Pinto, S. Daina, P. Sadocco, C. P. Neto, and T. Trindade, "Antibacterial activity of nanocomposites of copper and cellulose," *BioMed Research International*, vol. 2013, 2013, ISSN: 23146141. DOI: `10.1155/2013/280512`.

[117]   C. Ning, X. Wang, L. Li, *et al.*, "Concentration Ranges of Antibacterial Cations for Showing the Highest Antibacterial Efficacy but the Least Cytotoxicity against Mammalian Cells: Implications for a New Antibacterial Mechanism," *Chemical Research in Toxicology*, vol. 28, no. 9, pp. 1815–1822, 2015, ISSN: 15205010. DOI: `10.1021/acs.chemrestox.5b00258`.

[118]   H. Dasarathy, C. Riley, H. D. Coble, W. R. Lacefield, and G. Maybee, "Hydroxyapatite/metal composite coatings formed by electrocodeposition," *Journal of Biomedical Materials Research*, vol. 31, no. 1, pp. 81–89, 1996, ISSN: 0021-9304. DOI: `10.1002/ (SICI)1097-4636(199605)31:1<81::AID-JBM10>3.0.CO;2-P`. [Online]. Available: `https://onlinelibrary.wiley.com/doi/10.1002/(SICI)1097-4636(199605)31: 1$\%$3C81::AID-JBM10$\%$3E3.0.CO;2-P`.

[119]   M. Ueno, H. Miyamoto, M. Tsukamoto, *et al.*, "Silver-Containing Hydroxyapatite Coating Reduces Biofilm Formation by Methicillin-Resistant Staphylococcus aureus In Vitro and In Vivo," *BioMed Research International*, vol. 2016, pp. 1–7, 2016, ISSN: 2314-6133. DOI: `10.1155/2016/8070597`. [Online]. Available: `https://www.hindawi.com/journals/ bmri/2016/8070597/`.

[120]   A. Borkowski, T. Cłapa, M. Szala, A. Gąsiński, and M. Selwet, "Synthesis of SiC/Ag/Cellulose Nanocomposite and Its Antibacterial Activity by Reactive Oxygen Species Generation," *Nanomaterials*, vol. 6, no. 9, p. 171, 2016, ISSN: 2079-4991. DOI: `10.3390/nano6090171`. [Online]. Available: `http://www.mdpi.com/2079-4991/6/9/171`.

[121]   M. S. Stan, I. C. Nica, M. Popa, *et al.*, "Reduced graphene oxide/TiO2 nanocomposites coating of cotton fabrics with antibacterial and self-cleaning properties," *Journal of Industrial Textiles*, vol. 49, no. 3, pp. 277–293, 2019, ISSN: 15308057. DOI: `10.1177/ 1528083718779447`.

[122]   X. Xia, I. Zhitomirsky, and J. R. McDermid, "Electrodeposition of zinc and composite zinc–yttria stabilized zirconia coatings," *Journal of Materials Processing Technology*, vol. 209, no. 5, pp. 2632–2640, 2009, ISSN: 09240136. DOI: `10.1016/j.jmatprotec.2008. 06.031`.

[123]   K Kamburova, N Boshkova, N Tabakova, N Boshkov, and T. Radeva, "Application of polymeric modified polyaniline-silica particles for improved corrosion resistance of hybrid zinc coatings," *Colloids and Surfaces A: Physicochemical and Engineering Aspects*, vol. 592, p. 124 546, 2020, ISSN: 09277757. DOI: `10.1016/j.colsurfa.2020.124546`.

[124]   B. Fedi, M. P. Gigandet, J. Y. Hihn, and S. Mierzejewski, "Structure determination of electrodeposited zinc-nickel alloys: thermal stability and quantification using XRD and potentiodynamic dissolution," *Electrochimica Acta*, vol. 215, pp. 652–666, 2016, ISSN: 00134686. DOI: `10.1016/j.electacta.2016.08.141`. [Online]. Available: `http: //dx.doi.org/10.1016/j.electacta.2016.08.141`.

[125] M. K. Punith Kumar, M. Y. Rekha, and C. Srivastava, "Electrogalvanization using new generation coatings with carbonaceous additives: progress and challenges," *Corrosion Reviews*, vol. 39, no. 1, pp. 15–26, 2021, ISSN: 2191-0316. DOI: 10.1515/corrrev-2020-0035. [Online]. Available: https://www.degruyter.com/document/doi/10.1515/corrrev-2020-0035/html.

[126] D. Aussavy, S. Costil, O. El Kedim, G. Montavon, and A. F. Bonnot, "Metal Matrix Composite Coatings Manufactured by Thermal Spraying: Influence of the Powder Preparation on the Coating Properties," *Journal of Thermal Spray Technology*, vol. 23, no. 1-2, pp. 190–196, 2014, ISSN: 1059-9630. DOI: 10.1007/s11666-013-9999-3. [Online]. Available: http://link.springer.com/10.1007/s11666-013-9999-3.

[127] O. Sharifahmadian, H. R. Salimijazi, M. H. Fathi, J. Mostaghimi, and L. Pershin, "Study of the Antibacterial Behavior of Wire Arc Sprayed Copper Coatings," *Journal of Thermal Spray Technology*, vol. 22, no. 2-3, pp. 371–379, 2013, ISSN: 1059-9630. DOI: 10.1007/s11666-012-9842-2. [Online]. Available: http://library1.nida.ac.th/termpaper6/sd/2554/19755.pdfhttp://link.springer.com/10.1007/s11666-012-9842-2.

[128] M. Yandouzi, H. Bu, M. Brochu, and B. Jodoin, "Nanostructured Al-Based Metal Matrix Composite Coating Production by Pulsed Gas Dynamic Spraying Process," *Journal of Thermal Spray Technology*, vol. 21, no. 3-4, pp. 609–619, 2012, ISSN: 1059-9630. DOI: 10.1007/s11666-011-9727-9. [Online]. Available: http://library1.nida.ac.th/termpaper6/sd/2554/19755.pdfhttp://link.springer.com/10.1007/s11666-011-9727-9.

[129] M. R. Hasniyati, H. Zuhailawati, and S. Ramakrishnan, "A Statistical Prediction of Multiple Responses Using Overlaid Contour Plot on Hydroxyapatite Coated Magnesium via Cold Spray Deposition," *Procedia Chemistry*, vol. 19, pp. 181–188, 2016, ISSN: 18766196. DOI: 10.1016/j.proche.2016.03.091. [Online]. Available: https://linkinghub.elsevier.com/retrieve/pii/S1876619616001376.

[130] J. Yuan, Y. Zhu, X. Zheng, H. Ji, and T. Yang, "Fabrication and evaluation of atmospheric plasma spraying WC Co Cu MoS2 composite coatings," *Journal of Alloys and Compounds*, vol. 509, no. 5, 2011, ISSN: 09258388.

[131] R. Deuis, J. Yellup, and C. Subramanian, "Metal-matrix composite coatings by PTA surfacing," *Composites Science and Technology*, vol. 58, no. 2, pp. 299–309, 1998, ISSN: 02663538. DOI: 10.1016/S0266-3538(97)00131-0. [Online]. Available: https://linkinghub.elsevier.com/retrieve/pii/S0266353897001310.

[132] Y Yang, "Biaxial residual stress states of plasma-sprayed hydroxyapatite coatings on titanium alloy substrate," *Biomaterials*, vol. 21, no. 13, pp. 1327–1337, 2000, ISSN: 01429612. DOI: 10.1016/S0142-9612(99)00272-0. [Online]. Available: https://linkinghub.elsevier.com/retrieve/pii/S0142961299002720.

[133] D. R. Marantz, *HIGH-VELOCITY FLAME SPRAY APPARATUS AND METHOD OF FORMING MATERIALS*, 1991. [Online]. Available: `https://patents.google.com/patent/US5019686A/en?oq=US+5019686+`.

[134] T. Hanson, C. Hackett, and G. Settles, "Independent Control of HVOF Particle Velocity and Temperature," *Journal of Thermal Spray Technology*, vol. 11, no. 1, pp. 75–85, 2002, ISSN: 00000000. DOI: `10.1361/105996302770349005`. [Online]. Available: `http://link.springer.com/10.1361/105996302770349005`.

[135] K Khor, "Characterization of the bone-like apatite precipitated on high velocity oxy-fuel (HVOF) sprayed calcium phosphate deposits," *Biomaterials*, vol. 24, no. 5, pp. 769–775, 2003, ISSN: 01429612. DOI: `10.1016/S0142-9612(02)00413-1`. [Online]. Available: `https://linkinghub.elsevier.com/retrieve/pii/S0142961202004131`.

[136] D. R. Marantz, R David, and A Keith, *HIGH VELOCITY ELECTRIC-ARC SPRAY APPARATUS AND METHOD OF FORMING MATER ALS*, 1995. [Online]. Available: `https://patents.google.com/patent/US5442153A`.

[137] P. Fauchais and A. Vardelle, "Solution and Suspension Plasma Spraying of Nanostructure Coatings," in *Advanced Plasma Spray Applications*, InTech, 2012. DOI: `10.5772/34449`. [Online]. Available: `http://www.intechopen.com/books/advanced-plasma-spray-applications/solution-and-suspension-plasma-spraying-of-nanostructure-coatings`.

[138] P. L. Fauchais, J. V. Heberlein, and M. I. Boulos, *Thermal Spray Fundamentals*. Boston, MA: Springer US, 2014, ISBN: 978-0-387-28319-7. DOI: `10.1007/978-0-387-68991-3`. [Online]. Available: `http://link.springer.com/10.1007/978-0-387-68991-3`.

[139] R. M. Poorman, H. B. Sargent, and L. Headlee, *Method and apparatus utilizing detonation waves for spraying and other purposes*, 1955. [Online]. Available: `https://patents.google.com/patent/US2714563A/en`.

[140] M. Geetha, S. Sathish, K. Chava, and S. V. Joshi, "Detonation gun sprayed Al 2 O 3 –13TiO 2 coatings for biomedical applications," *Surface Engineering*, vol. 30, no. 4, pp. 229–236, 2014, ISSN: 0267-0844. DOI: `10.1179/1743294414Y.0000000245`. [Online]. Available: `http://www.tandfonline.com/doi/full/10.1179/1743294414Y.0000000245`.

[141] D. M. Yenni, W. C. Mcgill, and J. W. Lyle, *ELECTRICARC SPRAYNG*, 1961. [Online]. Available: `https://dl.acm.org/doi/10.1145/178951.178972`.

[142] X. Yuan, G. Liu, H. Jin, and K. Chen, "In situ synthesis of TiC reinforced metal matrix composite (MMC) coating by self propagating high temperature synthesis (SHS)," *Journal of Alloys and Compounds*, vol. 509, no. 30, pp. L301–L303, 2011, ISSN: 09258388. DOI: `10.1016/j.jallcom.2011.04.150`. [Online]. Available: `https://linkinghub.elsevier.com/retrieve/pii/S0925838811010358`.

[143] Y. Wu, X. Liu, G. Ma, C. Li, and J. Zhang, "High energy milling method to prepare Al/WC composite coatings in Al–Si alloys," *Journal of Alloys and Compounds*, vol. 497, no. 1-2, pp. 139–141, 2010, ISSN: 09258388. DOI: `10.1016/j.jallcom.2010.03.086`. [Online]. Available: `https://linkinghub.elsevier.com/retrieve/pii/S0925838810005670`.

[144] H. Liu, T. Gu, M. Asif, G. Zhang, and H. Liu, "The corrosion behavior and mechanism of carbon steel induced by extracellular polymeric substances of iron-oxidizing bacteria," *Corrosion Science*, vol. 114, no. 1, pp. 102–111, 2017, ISSN: 0010938X. DOI: `10.1016/j.corsci.2016.10.025`. [Online]. Available: `https://linkinghub.elsevier.com/retrieve/pii/S0010938X16310186`.

[145] F. S. Ertaş, R. Kaş, A. Mikó, and Ö. Birer, "Anticorrosion efficiency of ultrasonically deposited silica coatings on titanium," *Applied Surface Science*, vol. 276, pp. 810–816, 2013, ISSN: 01694332. DOI: `10.1016/j.apsusc.2013.03.176`. [Online]. Available: `http://library1.nida.ac.th/termpaper6/sd/2554/19755.pdfhttps://linkinghub.elsevier.com/retrieve/pii/S0169433213006764`.

[146] X. Liu, Z. Yue, T. Romeo, *et al.*, "Biofunctionalized anti-corrosive silane coatings for magnesium alloys," *Acta Biomaterialia*, vol. 9, no. 10, pp. 8671–8677, 2013, ISSN: 17427061. DOI: `10.1016/j.actbio.2012.12.025`. [Online]. Available: `http://library1.nida.ac.th/termpaper6/sd/2554/19755.pdfhttps://linkinghub.elsevier.com/retrieve/pii/S1742706112006174`.

[147] A. D. Pingale, S. U. Belgamwar, and J. S. Rathore, "Effect of Graphene Nanoplatelets Addition on the Mechanical, Tribological and Corrosion Properties of Cu–Ni/Gr Nanocomposite Coatings by Electro-co-deposition Method," *Transactions of the Indian Institute of Metals*, vol. 73, no. 1, pp. 99–107, 2020, ISSN: 0972-2815. DOI: `10.1007/s12666-019-01807-9`. [Online]. Available: `https://doi.org/10.1007/s12666-019-01807-9http://link.springer.com/10.1007/s12666-019-01807-9`.

[148] S. U. Belgamwar, A. D. Pingale, and N. N. Sharma, "Investigation on electrical properties of Cu matrix composite reinforced by multi-walled carbon nanotubes," *Materials Today: Proceedings*, vol. 18, pp. 3201–3208, 2019, ISSN: 22147853. DOI: `10.1016/j.matpr.2019.07.196`. [Online]. Available: `https://doi.org/10.1016/j.matpr.2019.07.196`.

[149] A. S. Katarkar, B. Majumder, A. D. Pingale, S. U. Belgamwar, and S. Bhaumik, "A review on the effects of porous coating surfaces on boiling heat transfer," *Materials Today: Proceedings*, no. xxxx, 2020, ISSN: 22147853. DOI: `10.1016/j.matpr.2020.09.744`.

[150] A. D. Pingale, A. Owhal, S. U. Belgamwar, and J. S. Rathore, "Effect of Current on the Characteristics of CuNi-G Nanocomposite Coatings Developed by DC, PC and PRC Electrodeposition," *JOM*, 2021, ISSN: 1047-4838. DOI: `10.1007/s11837-021-04815-7`. [Online]. Available: `https://link.springer.com/10.1007/s11837-021-04815-7`.

[151] A. Zielinski and M. Bartmanski, *Electrodeposited biocoatings, their properties and fabrication technologies: A review.* 2020, vol. 10, ISBN: 4850132936. DOI: 10.3390/COATINGS10080782.

[152] S. U. Belgamwar and N. N. Sharma, "Synergistic electro-co-deposition and molecular mixing for reinforcement of multi-walled carbon nanotube in copper," *Materials Science and Engineering B: Solid-State Materials for Advanced Technology*, vol. 178, no. 20, pp. 1452–1457, 2013, ISSN: 09215107. DOI: 10.1016/j.mseb.2013.09.006. [Online]. Available: http://dx.doi.org/10.1016/j.mseb.2013.09.006.

[153] A. V. Radhamani, H. C. Lau, and S. Ramakrishna, "Nanocomposite coatings on steel for enhancing the corrosion resistance: A review," *Journal of Composite Materials*, vol. 54, no. 5, pp. 681–701, 2020, ISSN: 1530793X. DOI: 10.1177/0021998319857807.

[154] B. Mahltig, T. Grethe, and H. Haase, "Handbook of Sol-Gel Science and Technology," *Handbook of Sol-Gel Science and Technology*, 2017. DOI: 10.1007/978-3-319-19454-7.

[155] S. Amiri and A. Rahimi, "Hybrid nanocomposite coating by sol–gel method: a review," *Iranian Polymer Journal (English Edition)*, vol. 25, no. 6, pp. 559–577, 2016, ISSN: 17355265. DOI: 10.1007/s13726-016-0440-x.

[156] N. Lam, U. Vo, T. T. V. Nguyen, T. Nguyen, and P. A. Nguyen, "Antibacterial Shoe Insole-Coated CuO-ZnO Nanocomposite Synthesized by the Sol-Gel Technique," vol. 2020, 2020.

[157] P. Piszczek and A. Radtke, "Silver Nanoparticles Fabricated Using Chemical Vapor Deposition and Atomic Layer Deposition Techniques: Properties, Applications and Perspectives: Review," in *Noble and Precious Metals - Properties, Nanoscale Effects and Applications*, InTech, 2018. DOI: 10.5772/intechopen.71571. [Online]. Available: http://www.intechopen.com/books/noble-and-precious-metals-properties-nanoscale-effects-and-applications/silver-nanoparticles-fabricated-using-chemical-vapor-deposition-and-atomic-layer-deposition-techniqu.

[158] J. Kratochvíl, A. Kuzminova, and O. Kylián, "State-of-the-art, and perspectives of, silver/plasma polymer antibacterial nanocomposites," *Antibiotics*, vol. 7, no. 3, 2018, ISSN: 20796382. DOI: 10.3390/antibiotics7030078.

[159] J. A. Gan and C. C. Berndt, "Nanocomposite coatings: Thermal spray procebing, microstructure and performance," *International Materials Reviews*, vol. 60, no. 4, pp. 195–244, 2015, ISSN: 17432804. DOI: 10.1179/1743280414Y.0000000048.

[160] G. Gupta and A. Satapathy, "Characterisation and wear performance of plasma sprayed borosilicate glass micro-sphere coatings on metallic substrates," *International Journal of Surface Science and Engineering*, vol. 9, no. 1, p. 81, 2015, ISSN: 1749-785X. DOI: 10.1504/IJSURFSE.2015.067041. [Online]. Available: http://www.inderscience.com/link.php?id=67041.

[161] P. R. Pati and A. Satapathy, "A Study on Coatability of Linz-Donawitz (LD) Slag by Plasma Spraying Route," in *ASME 2013 Gas Turbine India Conference*, American Society of Mechanical Engineers, 2013, ISBN: 978-0-7918-5616-1. DOI: 10.1115/GTINDIA2013-3534. [Online]. Available: https://asmedigitalcollection.asme.org/GTINDIA/proceedings/GTINDIA2013/35161/Bangalore,Karnataka,India/274456.

[162] M. De Kwaadsteniet, M. Botes, and T. E. Cloete, "Application of nanotechnology in antimicrobial coatings in the water industry," *Nano*, vol. 6, no. 5, pp. 395–407, 2011, ISSN: 17932920. DOI: 10.1142/S1793292011002779.

[163] S. Nastyshyn, J. Raczkowska, Y. Stetsyshyn, *et al.*, "Non-cytotoxic, temperature-responsive and antibacterial POEGMA based nanocomposite coatings with silver nanoparticles," *RSC Advances*, vol. 10, no. 17, pp. 10 155–10 166, 2020, ISSN: 20462069. DOI: 10.1039/c9ra10874b.

[164] V. Mišković-Stanković, A. Janković, S. Eraković, and K. Yop Rhee, "Graphene Based Biomedical Composite Coatings Produced by Electrophoretic Deposition on Titanium," *Eurasian Chemico-Technological Journal*, vol. 17, no. 1, p. 3, 2014, ISSN: 1562-3920. DOI: 10.18321/ectj189. [Online]. Available: http://ect-journal.kz/index.php/ectj/article/view/155.

[165] D. Tonelli, E. Scavetta, and I. Gualandi, "Electrochemical Deposition of Nanomaterials for Electrochemical Sensing," *Sensors*, vol. 19, no. 5, p. 1186, 2019, ISSN: 1424-8220. DOI: 10.3390/s19051186. [Online]. Available: https://www.mdpi.com/1424-8220/19/5/1186.

[166] M. Diba and A. R. Boccaccini, "Electrophoretic deposition of graphene-based materials and their energy-related applications," *Graphene Science Handbook: Fabrication Methods*, pp. 173–186, 2016. DOI: 10.1201/b19606-14.

[167] A. Janković, S. Eraković, M. Vukašinović-Sekulić, V. Mišković-Stanković, S. J. Park, and K. Y. Rhee, "Graphene-based antibacterial composite coatings electrodeposited on titanium for biomedical applications," *Progress in Organic Coatings*, vol. 83, pp. 1–10, 2015, ISSN: 03009440. DOI: 10.1016/j.porgcoat.2015.01.019. [Online]. Available: https://linkinghub.elsevier.com/retrieve/pii/S0300944015000284.

[168] A. R. Shelke, J. Balwada, S. Sharma, A. D. Pingale, S. U. Belgamwar, and J. S. Rathore, "Development and characterization of Cu-Gr composite coatings by electro-co-deposition technique," *Materials Today: Proceedings*, vol. 28, pp. 2090–2095, 2020, ISSN: 22147853. DOI: 10.1016/j.matpr.2020.03.244.

[169] A. D. Pingale, S. U. Belgamwar, and J. S. Rathore, "The influence of graphene nanoplatelets (GNPs) addition on the microstructure and mechanical properties of Cu-GNPs composites fabricated by electro-co-deposition and powder metallurgy," *Materials Today: Proceedings*, no. xxxx, 2020, ISSN: 22147853. DOI: 10.1016/j.matpr.2020.02.728. [Online]. Available: https://doi.org/10.1016/j.matpr.2020.02.728.

[170] A. Ashok, H. S. Maharana, and A Basu, "Effect of electro-co-deposition parameters on surface mechanical properties of Cu – TiO 2 composite coating," vol. 38, no. 2, pp. 335–342, 2015.

[171] C. Guo, Y. Zuo, X. Zhao, J. Zhao, and J. Xiong, "The effects of electrodeposition current density on properties of Ni–CNTs composite coatings," *Surface and Coatings Technology*, vol. 202, no. 14, pp. 3246–3250, 2008, ISSN: 02578972. DOI: `10.1016/j.surfcoat.2007.11.032`. [Online]. Available: `https://linkinghub.elsevier.com/retrieve/pii/S0257897207012200`.

[172] A. Pingale, "by Ajay Pingale," 2020.

[173] A. Owhal, M. Choudhary, S. U. Belgamwar, S. Mukherjee, and J. S. Rathore, "Co-deposited Zn-Cu/Gr nanocomposite: Corrosion behaviour and in-vitro cytotoxicity assessment," *Transactions of the IMF*, vol. 99, no. 4, pp. 215–223, 2021, ISSN: 0020-2967. DOI: `10.1080/00202967.2021.1899493`. [Online]. Available: `https://www.tandfonline.com/doi/full/10.1080/00202967.2021.1899493`.

[174] M. Hilder, O. Winther-Jensen, B. Winther-Jensen, and D. R. MacFarlane, "Graphene/zinc nano-composites by electrochemical co-deposition," *Physical Chemistry Chemical Physics*, vol. 14, no. 40, pp. 14 034–14 040, 2012, ISSN: 14639076. DOI: `10.1039/c2cp42385e`.

[175] M. M. Momeni, S. Hashemizadeh, M. Mirhosseini, A. Kazempour, and S. A. Hosseinizadeh, "Preparation, characterisation, hardness and antibacterial properties of Zn–Ni–TiO2 nanocomposites coatings," *Surface Engineering*, vol. 32, no. 7, pp. 490–494, 2016, ISSN: 17432944. DOI: `10.1179/1743294415Y.0000000049`.

[176] H. Rojbani, M. Nyan, K. Ohya, and S. Kasugai, "Evaluation of the osteoconductivity of α-tricalcium phosphate, β-tricalcium phosphate, and hydroxyapatite combined with or without simvastatin in rat calvarial defect," *Journal of Biomedical Materials Research Part A*, vol. 98, no. 4, pp. 488–498, 2011.

[177] P. A. Tran, L. Sarin, R. H. Hurt, and T. J. Webster, "Opportunities for nanotechnology-enabled bioactive bone implants," *Journal of Materials Chemistry*, vol. 19, no. 18, pp. 2653–2659, 2009.

[178] A. Popa, G. Stan, M Enculescu, C Tanase, D. Tulyaganov, and J. Ferreira, "Superior biofunctionality of dental implant fixtures uniformly coated with durable bioglass films by magnetron sputtering," *Journal of the mechanical behavior of biomedical materials*, vol. 51, pp. 313–327, 2015.

[179] H. Plenk Jr, "The role of materials biocompatibility for functional electrical stimulation applications," *Artificial organs*, vol. 35, no. 3, pp. 237–241, 2011.

[180] F. Bergmann, S. Stadlmayr, F. Millesi, M. Zeitlinger, A. Naghilou, and C. Radtke, "Biomaterials advances,"

[181] H. Tian, Z. Tang, X. Zhuang, X. Chen, and X. Jing, "Biodegradable synthetic polymers: Preparation, functionalization and biomedical application," *Progress in Polymer Science*, vol. 37, no. 2, pp. 237–280, 2012.

[182] S. K. Prajapati, A. Jain, A. Jain, and S. Jain, "Biodegradable polymers and constructs: A novel approach in drug delivery," *European polymer journal*, vol. 120, p. 109 191, 2019.

[183] C. Godavitarne, A. Robertson, J. Peters, and B. Rogers, "Biodegradable materials," *Orthopaedics and trauma*, vol. 31, no. 5, pp. 316–320, 2017.

[184] Y. Xie, Y. Chen, M. Sun, and Q. Ping, "A mini review of biodegradable calcium phosphate nanoparticles for gene delivery," *Current pharmaceutical biotechnology*, vol. 14, no. 10, pp. 918–925, 2013.

[185] M. Peron, F. Berto, and J. Torgersen, *Magnesium and Its Alloys as Implant Materials: Corrosion, Mechanical and Biological Performances*. CRC Press, 2020.

[186] P. Zartner, R. Cesnjevar, H. Singer, and M. Weyand, "First successful implantation of a biodegradable metal stent into the left pulmonary artery of a preterm baby," *Catheterization and Cardiovascular Interventions*, vol. 66, no. 4, pp. 590–594, 2005.

[187] K. S. Ødegaard, J. Torgersen, and C. W. Elverum, "Structural and Biomedical Properties of Common Additively Manufactured Biomaterials: A Concise Review," *Metals*, vol. 10, no. 12, p. 1677, 2020, ISSN: 2075-4701. DOI: `10.3390/met10121677`. [Online]. Available: `https://www.mdpi.com/2075-4701/10/12/1677`.

[188] "Biomaterials Market Size, Share and Trends Analysis Report By Product (Natural, Metallic, Polymer), By Application (Cardiovascular, Orthopedics, Plastic Surgery), By Region, And Segment Forecasts, 2020 - 2030," *SBWire*, 2020. [Online]. Available: `https://www.grandviewresearch.com/industry-analysis/biomaterials-industry`.

[189] S. Steinemann, "Metal implants and surface reactions," *Injury*, vol. 27, S/C16–S/C22, 1996, ISSN: 00201383. DOI: `10.1016/0020-1383(96)89027-9`. [Online]. Available: `https://linkinghub.elsevier.com/retrieve/pii/0020138396890279`.

[190] J Cordero, L Munuera, and M. Folgueira, "Influence of metal implants on infection. An experimental study in rabbits," *The Journal of Bone and Joint Surgery. British volume*, vol. 76-B, no. 5, pp. 717–720, 1994, ISSN: 0301-620X. DOI: `10.1302/0301-620X.76B5.8083257`. [Online]. Available: `https://online.boneandjoint.org.uk/doi/10.1302/0301-620X.76B5.8083257`.

[191] A. Goharian and M. R. Abdullah, "Bioinert Metals (Stainless Steel, Titanium, Cobalt Chromium)," in *Trauma Plating Systems*, Elsevier, 2017, pp. 115–142. DOI: `10.1016/B978-0-12-804634-0.00007-0`. [Online]. Available: `https://linkinghub.elsevier.com/retrieve/pii/B9780128046340000070`.

[192] H. Kabir, K. Munir, C. Wen, and Y. Li, "Recent research and progress of biodegradable zinc alloys and composites for biomedical applications: Biomechanical and biocorrosion perspectives," *Bioactive Materials*, vol. 6, no. 3, pp. 836–879, 2021, ISSN: 2452199X. DOI: `10.1016/j.bioactmat.2020.09.013`. [Online]. Available: `https://linkinghub.elsevier.com/retrieve/pii/S2452199X20302334`.

[193] V. Verma and A. Khvan, "A Short Review on Al MMC with Reinforcement Addition Effect on Their Mechanical and Wear Behaviour," *Advances in Composite Materials Development*, 2019. DOI: `10.5772/intechopen.83584`.

[194] Y. K. Gautam, N. Somani, M. Kumar, and S. K. Sharma, "A review on fabrication and characterization of copper metal matrix composite (CMMC)," *AIP Conference Proceedings*, vol. 2018, no. Cmmc, 2018, ISSN: 15517616. DOI: `10.1063/1.5058254`.

[195] A. Padnuru Sripathy and M. Gupta, "Insight into layered metal matrix composites," in *Encyclopedia of Materials: Composites*, D. Brabazon, Ed., Oxford: Elsevier, 2021, pp. 121–139, ISBN: 978-0-12-819731-8. DOI: `https://doi.org/10.1016/B978-0-12-819724-0.00021-5`. [Online]. Available: `https://www.sciencedirect.com/science/article/pii/B9780128197240000215`.

[196] A. Evans, C. San Marchi, and A. Mortensen, *Metal Matrix Composites in Industry*. Boston, MA: Springer US, 2003, ISBN: 978-1-4020-7521-6. DOI: `10.1007/978-1-4615-0405-4`. [Online]. Available: `http://link.springer.com/10.1007/978-1-4615-0405-4`.

[197] H. M. Cheng, Z. H. Lin, B. L. Zhou, Z. G. Zhen, K. Kobayashi, and Y. Uchiyama, "Preparation of carbon fibre reinforced aluminium via ultrasonic liquid infiltration technique," *Materials Science and Technology*, vol. 9, no. 7, pp. 609–614, 1993, ISSN: 0267-0836. DOI: `10.1179/mst.1993.9.7.609`. [Online]. Available: `http://www.tandfonline.com/doi/full/10.1179/mst.1993.9.7.609`.

[198] M. A. Howes, "Ceramic-reinforced mmc fabricated by squeeze casting," *JOM*, vol. 38, no. 3, pp. 28–29, 1986.

[199] P. Mathur, D. Apelian, and E Lawley, "Fundamentals of Spray Deposition Via Osprey Processing," *Powder Metallurgy*, vol. 34, no. 2, pp. 109–111, 1991, ISSN: 0032-5899. DOI: `10.1179/pom.1991.34.2.109`. [Online]. Available: `http://www.tandfonline.com/doi/full/10.1179/pom.1991.34.2.109`.

[200] R. W. Evans, A. G. Leatham, and R. G. Brooks, "The Osprey Preform Process," *Powder Metallurgy*, vol. 28, no. 1, pp. 13–20, 1985, ISSN: 0032-5899. DOI: `10.1179/pom.1985.28.1.13`. [Online]. Available: `http://www.tandfonline.com/doi/full/10.1179/pom.1985.28.1.13`.

[201] C. C. Piras, S. Fernández-Prieto, and W. M. De Borggraeve, "Ball milling: a green technology for the preparation and functionalisation of nanocellulose derivatives," *Nanoscale Advances*, vol. 1, no. 3, pp. 937–947, 2019, ISSN: 2516-0230. DOI: `10.1039/C8NA00238J`. [Online]. Available: `http://xlink.rsc.org/?DOI=C8NA00238J`.

[202] S. U. Belgamwar and N. N. Sharma, "Copper-philic carbon nanotubes," *AIP Conference Proceedings*, vol. 1724, no. 2016, 2016, ISSN: 15517616. DOI: `10.1063/1.4945185`.

[203] S. V. Dorozhkin, "Surface modification of magnesium and its biodegradable alloys by calcium orthophosphate coatings to improve corrosion resistance and biocompatibility," *Surface Modification of Magnesium and Its Alloys for Biomedical Applications*, vol. 2, pp. 151–191, 2015. DOI: `10.1016/B978-1-78242-078-1.00007-4`.

[204] Z. Ma, M. Gao, D. Na, Y. Li, L. Tan, and K. Yang, "Study on a biodegradable antibacterial Fe-Mn-C-Cu alloy as urinary implant material," *Materials Science and Engineering C*, vol. 103, no. January, 2019, ISSN: 18730191. DOI: `10.1016/j.msec.2019.05.003`.

[205] Y. Xin, T. Hu, and P. Chu, "In vitro studies of biomedical magnesium alloys in a simulated physiological environment: A review," *Acta Biomaterialia*, vol. 7, no. 4, pp. 1452–1459, 2011, ISSN: 17427061. DOI: `10.1016/j.actbio.2010.12.004`. [Online]. Available: `https://linkinghub.elsevier.com/retrieve/pii/S1742706110005556`.

[206] D. Hernández-Escobar, S. Champagne, H. Yilmazer, B. Dikici, C. J. Boehlert, and H. Hermawan, "Current status and perspectives of zinc-based absorbable alloys for biomedical applications," *Acta Biomaterialia*, vol. 97, pp. 1–22, 2019, ISSN: 18787568. DOI: `10.1016/j.actbio.2019.07.034`.

[207] P. Wen, L. Jauer, M. Voshage, Y. Chen, R. Poprawe, and J. H. Schleifenbaum, "Densification behavior of pure Zn metal parts produced by selective laser melting for manufacturing biodegradable implants," *Journal of Materials Processing Technology*, vol. 258, no. January, pp. 128–137, 2018, ISSN: 09240136. DOI: `10.1016/j.jmatprotec.2018.03.007`. [Online]. Available: `https://doi.org/10.1016/j.jmatprotec.2018.03.007https://linkinghub.elsevier.com/retrieve/pii/S0924013618301067`.

[208] C. Wei, K. Cho, and D. Srivastava, "Tensile strength of carbon nanotubes under realistic temperature and strain rate," *Physical Review B*, vol. 67, no. 11, p. 115407, 2003, ISSN: 0163-1829. DOI: `10.1103/PhysRevB.67.115407`. [Online]. Available: `https://link.aps.org/doi/10.1103/PhysRevB.67.115407`.

[209] P. K. Bowen, J. Drelich, and J. Goldman, "Zinc exhibits ideal physiological corrosion behavior for bioabsorbable stents," *Advanced Materials*, vol. 25, no. 18, pp. 2577–2582, 2013, ISSN: 09359648. DOI: `10.1002/adma.201300226`.

[210] P. K. Bowen, R. J. Guillory, E. R. Shearier, *et al.*, "Metallic zinc exhibits optimal biocompatibility for bioabsorbable endovascular stents.," *Materials science & engineering. C, Materials for biological applications*, vol. 56, pp. 467–72, 2015, ISSN: 1873-0191. DOI: `10.1016/j.msec.2015.07.022`. [Online]. Available: `http://dx.doi.org/10.1016/j.msec.2015.07.022https://linkinghub.elsevier.com/retrieve/pii/S0928493115302125http://www.ncbi.nlm.nih.gov/pubmed/26249616http://www.pubmedcentral.nih.gov/articlerender.fcgi?artid=PMC4529538`.

[211] Y. Su, I. Cockerill, Y. Wang, *et al.*, "Zinc-Based Biomaterials for Regeneration and Therapy," *Trends in Biotechnology*, vol. 37, no. 4, pp. 428–441, 2019, ISSN: 01677799. DOI: `10.1016/j.tibtech.2018.10.009`. [Online]. Available: `https://linkinghub.elsevier.com/retrieve/pii/S0167779918303056`.

[212] X. Yang, Q. Hu, W. Li, *et al.*, "Compression-compression fatigue performance of aluminium matrix composite foams reinforced by carbon nanotubes," *Fatigue & Fracture of Engineering Materials & Structures*, vol. 43, no. 4, pp. 744–756, 2020, ISSN: 8756-758X. DOI: `10.1111/ffe.13159`. [Online]. Available: `https://onlinelibrary.wiley.com/doi/10.1111/ffe.13159`.

[213] H. Kazimierczak, N. Eliaz, K. Szymkiewicz, Ł. Rogal, and E. Gileadi, "Direct Current Electrodeposition of Zn-SiC Nanocomposite Coatings from Citrate Bath," vol. 165, no. 11, pp. 526–535, 2018. DOI: `10.1149/2.0421811jes`.

[214] S. Mosavat, M. Shariat, and M. Bahrololoom, "Study of corrosion performance of electrodeposited nanocrystalline Zn–Ni alloy coatings," *Corrosion Science*, vol. 59, pp. 81–87, 2012, ISSN: 0010938X. DOI: `10.1016/j.corsci.2012.02.012`. [Online]. Available: `https://linkinghub.elsevier.com/retrieve/pii/S0010938X12000911`.

[215] M. R. de Almeida, E. P. Barbano, M. F. de Carvalho, I. A. Carlos, J. L. Siqueira, and L. L. Barbosa, "Electrodeposition of copper-zinc from an alkaline bath based on EDTA," *Surface and Coatings Technology*, vol. 206, no. 1, pp. 95–102, 2011, ISSN: 02578972. DOI: `10.1016/j.surfcoat.2011.06.050`.

[216] A. L. Patterson, "The Scherrer Formula for X-Ray Particle Size Determination," *Physical Review*, vol. 56, no. 10, pp. 978–982, 1939, ISSN: 0031-899X. DOI: `10.1103/PhysRev.56.978`.

[217] J. Wang, Z. Li, G. Fan, H. Pan, Z. Chen, and D. Zhang, "Reinforcement with graphene nanosheets in aluminum matrix composites," *Scripta Materialia*, vol. 66, no. 8, pp. 594–597, 2012, ISSN: 13596462. DOI: `10.1016/j.scriptamat.2012.01.012`. [Online]. Available: `https://linkinghub.elsevier.com/retrieve/pii/S1359646212000280`.

[218] D. Kuang, L. Xu, L. Liu, W. Hu, and Y. Wu, "Graphene–nickel composites," *Applied Surface Science*, vol. 273, pp. 484–490, 2013. DOI: 10.1016/j.apsusc.2013.02.066. [Online]. Available: https://linkinghub.elsevier.com/retrieve/pii/S016943321300384Xhttp://dx.doi.org/10.1016/j.apsusc.2013.02.066.

[219] N. V. Ponraj, A. Azhagurajan, S. C. Vettivel, X. Sahaya Shajan, P. Y. Nabhiraj, and M. Sivapragash, "Graphene nanosheet as reinforcement agent in copper matrix composite by using powder metallurgy method," *Surfaces and Interfaces*, vol. 6, pp. 190–196, 2017, ISSN: 24680230. DOI: 10.1016/j.surfin.2017.01.010.

[220] Y. Gao, C. Liu, S. Fu, J. Jin, X. Shu, and Y. Gao, "Electroless nickel plating on ZM6 (Mg–2.6Nd–0.6Zn–0.8Zr) magnesium alloy substrate," *Surface and Coatings Technology*, vol. 204, no. 21-22, pp. 3629–3635, 2010, ISSN: 02578972. DOI: 10.1016/j.surfcoat.2010.04.040. [Online]. Available: http://dx.doi.org/10.1016/j.surfcoat.2010.04.040https://linkinghub.elsevier.com/retrieve/pii/S0257897210003075.

[221] H. Conrad and T. D. Golden, "Electrodeposited Zinc-Nickel Nanocomposite Coatings," *Nanocomposites - Recent Evolutions*, 2019. DOI: 10.5772/intechopen.80219.

[222] Z. Li, Q. Guo, Z. Li, *et al.*, "Enhanced Mechanical Properties of Graphene (Reduced Graphene Oxide)/Aluminum Composites with a Bioinspired Nanolaminated Structure," *Nano Letters*, vol. 15, no. 12, pp. 8077–8083, 2015, ISSN: 15306992. DOI: 10.1021/acs.nanolett.5b03492.

[223] L. Wang, R. Aversa, Z. Houa, *et al.*, "Bioresorption Control and Biological Response of Magnesium Alloy AZ31 Coated with Poly-β-Hydroxybutyrate," *Applied Sciences*, vol. 11, no. 12, p. 5627, 2021, ISSN: 2076-3417. DOI: 10.3390/app11125627. [Online]. Available: https://www.mdpi.com/2076-3417/11/12/5627.

[224] A. Owhal, M. Choudhary, A. D. Pingale, S. U. Belgamwar, S. Mukherjee, and J. S. Rathore, "Non-cytotoxic zinc/f-graphene nanocomposite for tunable degradation and superior tribo-mechanical properties: Synthesized via modified electro co-deposition route," *Materials Today Communications*, p. 105 112, 2022, ISSN: 2352-4928.

[225] E. Mostaed, M. Sikora-Jasinska, A. Mostaed, *et al.*, "Novel Zn-based alloys for biodegradable stent applications: Design, development and in vitro degradation," *Journal of the Mechanical Behavior of Biomedical Materials*, vol. 60, pp. 581–602, 2016, ISSN: 18780180. DOI: 10.1016/j.jmbbm.2016.03.018. [Online]. Available: http://dx.doi.org/10.1016/j.jmbbm.2016.03.018.

[226] H. Yang, C. Wang, C. Liu, *et al.*, "Evolution of the degradation mechanism of pure zinc stent in the one-year study of rabbit abdominal aorta model," *Biomaterials*, vol. 145, pp. 92–105, 2017, ISSN: 01429612. DOI: 10.1016/j.biomaterials.2017.08.022. [Online]. Available: https://linkinghub.elsevier.com/retrieve/pii/S014296121730532X.

[227] J. Wang, F. Witte, T. Xi, *et al.*, "Recommendation for modifying current cytotoxicity testing standards for biodegradable magnesium-based materials," *Acta Biomaterialia*, vol. 21, pp. 237–249, 2015, ISSN: 17427061. DOI: `10.1016/j.actbio.2015.04.011`. [Online]. Available: `https://linkinghub.elsevier.com/retrieve/pii/S1742706115001828`.

[228] Y. Liu, H. Li, J. Xu, *et al.*, "Biodegradable metal-derived magnesium and sodium enhances bone regeneration by angiogenesis aided osteogenesis and regulated biological apatite formation," *Chemical Engineering Journal*, vol. 410, no. July 2020, p. 127 616, 2021, ISSN: 13858947. DOI: `10.1016/j.cej.2020.127616`. [Online]. Available: `https://linkinghub.elsevier.com/retrieve/pii/S1385894720337384`.

[229] E. Demirel, E. Karaca, and Y. Yuksel Durmaz, "Effective PEGylation method to improve biocompatibility of graphene derivatives," *European Polymer Journal*, vol. 124, p. 109 504, 2020, ISSN: 00143057. DOI: `10.1016/j.eurpolymj.2020.109504`. [Online]. Available: `https://linkinghub.elsevier.com/retrieve/pii/S0014305719323675`.

[230] Y. Zheng, X. Gu, and F. Witte, "Biodegradable metals," *Materials Science and Engineering: R: Reports*, vol. 77, pp. 1–34, 2014, ISSN: 0927796X. DOI: `10.1016/j.mser.2014.01.001`. [Online]. Available: `https://linkinghub.elsevier.com/retrieve/pii/S0927796X14000023`.

[231] J. J. D. Venezuela, S. Johnston, and M. S. Dargusch, "The Prospects for Biodegradable Zinc in Wound Closure Applications," *Advanced Healthcare Materials*, vol. 1900408, no. 16, pp. 1–15, 2019, ISSN: 21922659. DOI: `10.1002/adhm.201900408`.

[232] X. Wei, P. Liu, S. Ma, *et al.*, "Improvement on corrosion resistance and biocompability of ZK60 magnesium alloy by carboxyl ion implantation," *Corrosion Science*, vol. 173, p. 108 729, 2020, ISSN: 0010938X. DOI: `10.1016/j.corsci.2020.108729`. [Online]. Available: `https://linkinghub.elsevier.com/retrieve/pii/S0010938X19322747`.

[233] H. Yang, B. Jia, Z. Zhang, *et al.*, "Alloying design of biodegradable zinc as promising bone implants for load-bearing applications," *Nature Communications*, vol. 11, no. 1, p. 401, 2020, ISSN: 2041-1723. DOI: `10.1038/s41467-019-14153-7`. [Online]. Available: `http://dx.doi.org/10.1038/s41467-019-14153-7http://www.nature.com/articles/s41467-019-14153-7`.

[234] A. Fattah-alhosseini and R. Chaharmahali, "Enhancing corrosion and wear performance of PEO coatings on Mg alloys using graphene and graphene oxide additions: A review," *FlatChem*, vol. 27, p. 100 241, 2021, ISSN: 24522627. DOI: `10.1016/j.flatc.2021.100241`. [Online]. Available: `https://linkinghub.elsevier.com/retrieve/pii/S2452262721000209`.

[235] M Handayani, M Ganta, N Darsono, *et al.*, "Multi-walled Carbon Nanotubes Reinforced-Based Magnesium Metal Matrix Composites Prepared by Powder Metallurgy," *IOP Conference Series: Materials Science and Engineering*, vol. 578, no. 1, p. 012 041, 2019, ISSN: 1757-8981. DOI: 10.1088/1757-899X/578/1/012041. [Online]. Available: https://iopscience.iop.org/article/10.1088/1757-899X/578/1/012041.

[236] E. Zanni, E. Bruni, C. R. Chandraiahgari, *et al.*, "Evaluation of the antibacterial power and biocompatibility of zinc oxide nanorods decorated graphene nanoplatelets: new perspectives for antibiodeteriorative approaches," *Journal of Nanobiotechnology*, vol. 15, no. 1, p. 57, 2017, ISSN: 1477-3155. DOI: 10.1186/s12951-017-0291-4. [Online]. Available: http://jnanobiotechnology.biomedcentral.com/articles/10.1186/s12951-017-0291-4.

[237] D. Lahiri, R. Dua, C. Zhang, *et al.*, "Graphene Nanoplatelet-Induced Strengthening of UltraHigh Molecular Weight Polyethylene and Biocompatibility In vitro," *ACS Applied Materials & Interfaces*, vol. 4, no. 4, pp. 2234–2241, 2012, ISSN: 1944-8244. DOI: 10.1021/am300244s. [Online]. Available: https://pubs.acs.org/doi/10.1021/am300244s.

[238] C. J. Bullock and C. Bussy, "Biocompatibility Considerations in the Design of Graphene Biomedical Materials," *Advanced Materials Interfaces*, p. 1 900 229, 2019, ISSN: 2196-7350. DOI: 10.1002/admi.201900229. [Online]. Available: https://onlinelibrary.wiley.com/doi/10.1002/admi.201900229.

[239] M. Shahin, C. Wen, K. Munir, and Y. Li, "Mechanical and corrosion properties of graphene nanoplatelet–reinforced Mg–Zr and Mg–Zr–Zn matrix nanocomposites for biomedical applications," *Journal of Magnesium and Alloys*, 2021, ISSN: 22139567. DOI: 10.1016/j.jma.2021.05.011. [Online]. Available: https://linkinghub.elsevier.com/retrieve/pii/S2213956721001304.

[240] L. Chen, Y. Zhao, H. Hou, *et al.*, "Development of AZ91D magnesium alloy-graphene nanoplatelets composites using thixomolding process," *Journal of Alloys and Compounds*, vol. 778, pp. 359–374, 2019, ISSN: 09258388. DOI: 10.1016/j.jallcom.2018.11.148. [Online]. Available: https://linkinghub.elsevier.com/retrieve/pii/S0925838818342713.

[241] M. Rashad, F. Pan, A. Tang, *et al.*, "Improved strength and ductility of magnesium with addition of aluminum and graphene nanoplatelets (Al+GNPs) using semi powder metallurgy method," *Journal of Industrial and Engineering Chemistry*, vol. 23, pp. 243–250, 2015, ISSN: 1226086X. DOI: 10.1016/j.jiec.2014.08.024. [Online]. Available: https://linkinghub.elsevier.com/retrieve/pii/S1226086X14004158.

[242] Q. Dai, S. Peng, Z. Zhang, Y. Liu, M. Fan, and F. Zhao, "Microstructure and Mechanical Properties of Zinc Matrix Biodegradable Composites Reinforced by Graphene," *Frontiers in Bioengineering and Biotechnology*, vol. 9, no. March, pp. 1–14, 2021, ISSN: 2296-4185.

DOI: 10.3389/fbioe.2021.635338. [Online]. Available: `https://www.frontiersin.org/articles/10.3389/fbioe.2021.635338/full`.

[243] S. Dorozhkin, "Surface modification of magnesium and its biodegradable alloys by calcium orthophosphate coatings to improve corrosion resistance and biocompatibility," in *Surface Modification of Magnesium and its Alloys for Biomedical Applications*, Elsevier, 2015, pp. 151–191. DOI: `10.1016/B978-1-78242-078-1.00007-4`. [Online]. Available: `https://linkinghub.elsevier.com/retrieve/pii/B9781782420781000074`.

[244] L. Ou, B. Song, H. Liang, *et al.*, "Toxicity of graphene-family nanoparticles: a general review of the origins and mechanisms," *Particle and Fibre Toxicology*, vol. 13, no. 1, p. 57, 2016, ISSN: 1743-8977. DOI: `10.1186/s12989-016-0168-y`. [Online]. Available: `http://particleandfibretoxicology.biomedcentral.com/articles/10.1186/s12989-016-0168-y`.

[245] S. Mullick Chowdhury, S. Dasgupta, A. E. McElroy, and B. Sitharaman, "Structural disruption increases toxicity of graphene nanoribbons," *Journal of Applied Toxicology*, vol. 34, no. 11, pp. 1235–1246, 2014, ISSN: 0260437X. DOI: `10.1002/jat.3066`. [Online]. Available: `https://onlinelibrary.wiley.com/doi/10.1002/jat.3066`.

[246] S. Das, S. Singh, V. Singh, *et al.*, "Oxygenated Functional Group Density on Graphene Oxide: Its Effect on Cell Toxicity," *Particle & Particle Systems Characterization*, vol. 30, no. 2, pp. 148–157, 2013, ISSN: 09340866. DOI: `10.1002/ppsc.201200066`. [Online]. Available: `https://onlinelibrary.wiley.com/doi/10.1002/ppsc.201200066`.

[247] S. Mallakpour, A. Abdolmaleki, and S. Borandeh, "Covalently functionalized graphene sheets with biocompatible natural amino acids," *Applied Surface Science*, vol. 307, pp. 533–542, 2014, ISSN: 01694332. DOI: `10.1016/j.apsusc.2014.04.070`. [Online]. Available: `https://linkinghub.elsevier.com/retrieve/pii/S0169433214008344`.

[248] Z. Du, C. Wang, R. Zhang, X. Wang, and X. Li, "Applications of Graphene and Its Derivatives in Bone Repair: Advantages for Promoting Bone Formation and Providing Real-Time Detection, Challenges and Future Prospects," *International Journal of Nanomedicine*, vol. Volume 15, pp. 7523–7551, 2020, ISSN: 1178-2013. DOI: `10.2147/IJN.S271917`. [Online]. Available: `https://www.dovepress.com/applications-of-graphene-and-its-derivatives-in-bone-repair-advantages-peer-reviewed-article-IJN`.

[249] X. Pei, Z. Zhu, Z. Gan, *et al.*, "PEGylated nano-graphene oxide as a nanocarrier for delivering mixed anticancer drugs to improve anticancer activity," *Scientific Reports*, vol. 10, no. 1, p. 2717, 2020, ISSN: 2045-2322. DOI: `10.1038/s41598-020-59624-w`. [Online]. Available: `http://www.nature.com/articles/s41598-020-59624-w`.

[250] G. Hooftman, S. Herman, and E. Schacht, "Review: Poly(Ethylene Glycol)s with Reactive Endgroups. II. Practical Consideration for the Preparation of Protein-PEG Conjugates," *Journal of Bioactive and Compatible Polymers*, vol. 11, no. 2, pp. 135–159, 1996, ISSN: 0883-9115. DOI: 10.1177/088391159601100205. [Online]. Available: http://journals.sagepub.com/doi/10.1177/088391159601100205.

[251] N. Kundu, D. Mukherjee, T. K. Maiti, and N. Sarkar, "Protein-Guided Formation of Silver Nanoclusters and Their Assembly with Graphene Oxide as an Improved Bioimaging Agent with Reduced Toxicity," *The Journal of Physical Chemistry Letters*, vol. 8, no. 10, pp. 2291–2297, 2017, ISSN: 1948-7185. DOI: 10.1021/acs.jpclett.7b00600. [Online]. Available: https://pubs.acs.org/doi/10.1021/acs.jpclett.7b00600.

[252] Y. Toumia, B. Cerroni, P. Trochet, *et al.*, "Performances of a Pristine Graphene-Microbubble Hybrid Construct as Dual Imaging Contrast Agent and Assessment of Its Biodistribution by Photoacoustic Imaging," *Particle & Particle Systems Characterization*, vol. 35, no. 7, p. 1 800 066, 2018, ISSN: 09340866. DOI: 10.1002/ppsc.201800066. [Online]. Available: https://onlinelibrary.wiley.com/doi/10.1002/ppsc.201800066.

[253] K. Munir, J. Lin, C. Wen, P. F. Wright, and Y. Li, "Mechanical, corrosion, and biocompatibility properties of Mg-Zr-Sr-Sc alloys for biodegradable implant applications," *Acta Biomaterialia*, vol. 102, pp. 493–507, 2020, ISSN: 18787568. DOI: 10.1016/j.actbio.2019.12.001. [Online]. Available: https://doi.org/10.1016/j.actbio.2019.12.001.

[254] A. V. Singhal, D. Malwal, S. Thiyagarajan, and I. Lahiri, "Antimicrobial and antibiofilm activity of GNP-Tannic Acid-Ag nanocomposite and their epoxy-based coatings," *Progress in Organic Coatings*, vol. 159, no. March, 2021, ISSN: 03009440. DOI: 10.1016/j.porgcoat.2021.106421.

[255] X. Zhao and P. Liu, "Biocompatible graphene oxide as a folate receptor-targeting drug delivery system for the controlled release of anti-cancer drugs," *RSC Adv.*, vol. 4, no. 46, pp. 24 232–24 239, 2014, ISSN: 2046-2069. DOI: 10.1039/C4RA02466D. [Online]. Available: http://xlink.rsc.org/?DOI=C4RA02466D.

[256] Y. Luo, X. Cai, H. Li, Y. Lin, and D. Du, "Hyaluronic Acid-Modified Multifunctional Q-Graphene for Targeted Killing of Drug-Resistant Lung Cancer Cells," *ACS Applied Materials & Interfaces*, vol. 8, no. 6, pp. 4048–4055, 2016, ISSN: 1944-8244. DOI: 10.1021/acsami.5b11471. [Online]. Available: https://pubs.acs.org/doi/10.1021/acsami.5b11471.

[257] G. M. Neelgund and A. Oki, "Graphene-Coupled ZnO: A Robust NIR-Induced Catalyst for Rapid Photo-Oxidation of Cyanide," *ACS Omega*, vol. 2, no. 12, pp. 9095–9102, 2017, ISSN: 2470-1343. DOI: 10.1021/acsomega.7b01398. [Online]. Available: https://pubs.acs.org/doi/10.1021/acsomega.7b01398.

[258] P. Dong, Y. Wang, L. Guo, *et al.*, "A facile one-step solvothermal synthesis of graphene/rod-shaped TiO2 nanocomposite and its improved photocatalytic activity," *Nanoscale*, vol. 4, no. 15, p. 4641, 2012, ISSN: 2040-3364. DOI: `10.1039/c2nr31231j`. [Online]. Available: `http://xlink.rsc.org/?DOI=c2nr31231j`.

[259] Y. Esmaeili, E. Bidram, A. Zarrabi, A. Amini, and C. Cheng, "Graphene oxide and its derivatives as promising In-vitro bio-imaging platforms," *Scientific Reports*, vol. 10, no. 1, p. 18 052, 2020, ISSN: 2045-2322. DOI: `10.1038/s41598-020-75090-w`. [Online]. Available: `https://www.nature.com/articles/s41598-020-75090-w`.

[260] M. Ahamed, M. A. M. Khan, M. J. Akhtar, H. A. Alhadlaq, and A. Alshamsan, "Role of Zn doping in oxidative stress mediated cytotoxicity of TiO2 nanoparticles in human breast cancer MCF-7 cells," *Scientific Reports*, vol. 6, no. 1, p. 30 196, 2016, ISSN: 2045-2322. DOI: `10.1038/srep30196`. [Online]. Available: `http://www.nature.com/articles/srep30196`.

[261] A. C. Ferrari, "Raman spectroscopy of graphene and graphite: Disorder, electron–phonon coupling, doping and nonadiabatic effects," *Solid State Communications*, vol. 143, no. 1-2, pp. 47–57, 2007, ISSN: 00381098. DOI: `10.1016/j.ssc.2007.03.052`. [Online]. Available: `https://linkinghub.elsevier.com/retrieve/pii/S0038109807002967`.

[262] T. Xu, L. Zhang, H. Cheng, and Y. Zhu, "Significantly enhanced photocatalytic performance of ZnO via graphene hybridization and the mechanism study," *Applied Catalysis B: Environmental*, vol. 101, no. 3-4, pp. 382–387, 2011, ISSN: 09263373. DOI: `10.1016/j.apcatb.2010.10.007`. [Online]. Available: `https://linkinghub.elsevier.com/retrieve/pii/S0926337310004546`.

[263] A. Owhal, A. D. Pingale, S. Khan, S. U. Belgamwar, P. N. Jha, and J. S. Rathore, "Facile and Scalable Co-deposition of Anti-bacterial Zn-GNS Nanocomposite Coatings for Hospital Facilities: Tribo-Mechanical and Anti-corrosion Properties," *JOM*, 2021, ISSN: 1047-4838. DOI: `10.1007/s11837-021-04968-5`. [Online]. Available: `https://link.springer.com/10.1007/s11837-021-04968-5`.

[264] J. Song, H. Jiang, J. Wu, Y. Huang, and K.-C. Hwang, "Stone–Wales transformation in boron nitride nanotubes," *Scripta Materialia*, vol. 57, no. 7, pp. 571–574, 2007, ISSN: 13596462. DOI: `10.1016/j.scriptamat.2007.06.027`. [Online]. Available: `https://linkinghub.elsevier.com/retrieve/pii/S1359646207004538`.

[265] M. Y. Rekha, C. Srivastava, R. M Y, and C. Srivastava, "Microstructure and corrosion properties of zinc-graphene oxide composite coatings," *Corrosion Science*, vol. 152, no. March, pp. 234–248, 2019, ISSN: 0010938X. DOI: `10.1016/j.corsci.2019.03.015`. [Online]. Available: `https://doi.org/10.1016/j.corsci.2019.03.015`.

[266] Y. Meng, L. Liu, D. Zhang, *et al.*, "Initial formation of corrosion products on pure zinc in saline solution," *Bioactive Materials*, vol. 4, no. 1, pp. 87–96, 2019, ISSN: 2452199X. DOI: `10.1016/j.bioactmat.2018.08.003`. [Online]. Available: `https://linkinghub.elsevier.com/retrieve/pii/S2452199X18300240`.

[267] H.-S. Lee, J. K. Singh, M. A. Ismail, *et al.*, "Corrosion mechanism and kinetics of Al-Zn coating deposited by arc thermal spraying process in saline solution at prolong exposure periods," *Scientific Reports*, vol. 9, no. 1, p. 3399, 2019, ISSN: 2045-2322. DOI: `10.1038/s41598-019-39943-3`. [Online]. Available: `http://www.nature.com/articles/s41598-019-39943-3`.

[268] A. Sanaty-Zadeh and P. K. Rohatgi, "Comparison between current models for the strength of particulate-reinforced metal matrix nanocomposites with emphasis on consideration of Hall-Petch effect," *Materials Science and Engineering A*, vol. 531, pp. 112–118, 2012. DOI: `https://doi.org/10.1016/j.msea.2011.10.043`. [Online]. Available: `https://doi.org/10.1016/j.msea.2011.10.043`.

[269] P. K. Bowen, E. R. Shearier, S. Zhao, *et al.*, "Biodegradable Metals for Cardiovascular Stents: from Clinical Concerns to Recent Zn-Alloys," *Advanced Healthcare Materials*, vol. 5, no. 10, pp. 1121–1140, 2016, ISSN: 21922640. DOI: `10.1002/adhm.201501019`. [Online]. Available: `https://onlinelibrary.wiley.com/doi/10.1002/adhm.201501019`.

[270] N. Krasteva, D. Staneva, B. Vasileva, G. Miloshev, and M. Georgieva, "Bioactivity of PEGylated Graphene Oxide Nanoparticles Combined with Near-Infrared Laser Irradiation Studied in Colorectal Carcinoma Cells," *Nanomaterials*, vol. 11, no. 11, p. 3061, 2021, ISSN: 2079-4991. DOI: `10.3390/nano11113061`. [Online]. Available: `https://www.mdpi.com/2079-4991/11/11/3061`.

[271] L. Du, S. Wu, Y. Li, X. Zhao, X. Ju, and Y. Wang, "Cytotoxicity of PEGylated graphene oxide on lymphoma cells," *Bio-Medical Materials and Engineering*, vol. 24, no. 6, pp. 2135–2141, 2014, ISSN: 09592989. DOI: `10.3233/BME-141024`. [Online]. Available: `https://www.medra.org/servlet/aliasResolver?alias=iospress\&doi=10.3233/BME-141024`.

[272] M. B. Kannan, C. Moore, S. Saptarshi, S. Somasundaram, M. Rahuma, and A. L. Lopata, "Biocompatibility and biodegradation studies of a commercial zinc alloy for temporary mini-implant applications," *Scientific Reports*, vol. 7, no. 1, pp. 1–11, 2017, ISSN: 20452322. DOI: `10.1038/s41598-017-15873-w`. [Online]. Available: `http://dx.doi.org/10.1038/s41598-017-15873-w`.

[273] D. Zhu, I. Cockerill, Y. Su, *et al.*, "Mechanical Strength, Biodegradation, and in Vitro and in Vivo Biocompatibility of Zn Biomaterials," *ACS Applied Materials & Interfaces*, vol. 11, no. 7, pp. 6809–6819, 2019, ISSN: 1944-8244. DOI: `10.1021/acsami.8b20634`. [Online]. Available: `https://pubs.acs.org/doi/10.1021/acsami.8b20634`.

[274] Yang, Zhang, Wang, *et al.*, "Effect of Graphene Oxide Concentration in Electrolyte on Corrosion Behavior of Electrodeposited Zn–Electrochemical Reduction Graphene Composite Coatings," *Coatings*, vol. 9, no. 11, p. 758, 2019, ISSN: 2079-6412. DOI: `10.3390/coatings9110758`. [Online]. Available: `https://www.mdpi.com/2079-6412/9/11/758`.

[275] Z. Yang, H. Gu, G. Sha, *et al.*, "TC4/Ag Metal Matrix Nanocomposites Modified by Friction Stir Processing: Surface Characterization, Antibacterial Property, and Cytotoxicity in Vitro," *ACS Applied Materials and Interfaces*, vol. 10, no. 48, pp. 41 155–41 166, 2018, ISSN: 19448252. DOI: `10.1021/acsami.8b16343`.

[276] M. Razzaghi, M. Kasiri-Asgarani, H. R. Bakhsheshi-Rad, and H. Ghayour, "In Vitro Degradation, Antibacterial Activity and Cytotoxicity of Mg-3Zn-xAg Nanocomposites Synthesized by Mechanical Alloying for Implant Applications," *Journal of Materials Engineering and Performance*, vol. 28, no. 3, pp. 1441–1455, 2019, ISSN: 1059-9495. DOI: `10.1007/s11665-019-03923-5`. [Online]. Available: `http://link.springer.com/10.1007/s11665-019-03923-5`.

[277] E. R. Shearier, P. K. Bowen, W. He, *et al.*, "In Vitro Cytotoxicity, Adhesion, and Proliferation of Human Vascular Cells Exposed to Zinc," *ACS Biomaterials Science & Engineering*, vol. 2, no. 4, pp. 634–642, 2016, ISSN: 2373-9878. DOI: `10.1021/acsbiomaterials.6b00035`. [Online]. Available: `https://pubs.acs.org/doi/10.1021/acsbiomaterials.6b00035`.

[278] H. Mohammed, A. Kumar, E. Bekyarova, *et al.*, "Antimicrobial Mechanisms and Effectiveness of Graphene and Graphene-Functionalized Biomaterials. A Scope Review," *Frontiers in Bioengineering and Biotechnology*, vol. 8, no. May, 2020, ISSN: 2296-4185. DOI: `10.3389/fbioe.2020.00465`. [Online]. Available: `https://www.frontiersin.org/article/10.3389/fbioe.2020.00465/full`.

[279] I. Borges, P. C. Henriques, R. N. Gomes, *et al.*, "Exposure of Smaller and Oxidized Graphene on Polyurethane Surface Improves its Antimicrobial Performance," *Nanomaterials*, vol. 10, no. 8, p. 1470, 2020, ISSN: 2079-4991. DOI: `10.3390/nano10081470`. [Online]. Available: `https://www.mdpi.com/2079-4991/10/8/1470`.

[280] P. Kumar, P. Huo, R. Zhang, and B. Liu, "Antibacterial Properties of Graphene-Based Nanomaterials," *Nanomaterials*, vol. 9, no. 5, p. 737, 2019, ISSN: 2079-4991. DOI: `10.3390/nano9050737`. [Online]. Available: `https://euroasia-science.ru/veterinarnye-nauki/antibakterialnye-svojstva-chaya-31-33/https://www.mdpi.com/2079-4991/9/5/737`.

[281] W.-C. Hou, P.-L. Lee, Y.-C. Chou, and Y.-S. Wang, "Antibacterial property of graphene oxide: the role of phototransformation," *Environmental Science: Nano*, vol. 4, no. 3, pp. 647–657, 2017, ISSN: 2051-8153. DOI: `10.1039/C6EN00427J`. [Online]. Available: `http://xlink.rsc.org/?DOI=C6EN00427J`.

[282] G. Duan, Y. Zhang, B. Luan, *et al.*, "Graphene-Induced Pore Formation on Cell Membranes," *Scientific Reports*, vol. 7, no. 1, p. 42 767, 2017, ISSN: 2045-2322. DOI: `10.1038/srep42767`. [Online]. Available: `http://dx.doi.org/10.1038/srep42767http://www.nature.com/articles/srep42767`.

[283] S. S. A. An, S. S. Nanda, and D. K. Yi, "Oxidative stress and antibacterial properties of a graphene oxide-cystamine nanohybrid," *International Journal of Nanomedicine*, p. 549, 2015, ISSN: 1178-2013. DOI: `10.2147/IJN.S75768`. [Online]. Available: `http://dx.doi.org/10.2147/IJN.S75768http://www.dovepress.com/oxidative-stress-and-antibacterial-properties-ofnbspanbspgraphene-oxid-peer-reviewed-article-IJN`.

[284] F. Murphy, A. Tchetchik, and I. Furxhi, "Reduction of Health Care-Associated Infections (HAIs) with Antimicrobial Inorganic Nanoparticles Incorporated in Medical Textiles: An Economic Assessment," *Nanomaterials*, vol. 10, no. 5, p. 999, 2020, ISSN: 2079-4991. DOI: `10.3390/nano10050999`. [Online]. Available: `https://www.mdpi.com/2079-4991/10/5/999`.

[285] N. Noor, S. Mutalik, M. W. Younas, *et al.*, "Durable Antimicrobial Behaviour from Silver-Graphene Coated Medical Textile Composites," *Polymers*, vol. 11, no. 12, p. 2000, 2019, ISSN: 2073-4360. DOI: `10.3390/polym11122000`. [Online]. Available: `https://www.mdpi.com/2073-4360/11/12/2000`.

[286] Y. Tong1, S. Bohm, and M. Song, "Graphene based materials and their composites as coatings," *Austin Journal of Nanomedicine & Nanotechnology*, vol. 1, no. 1003, pp. 1–16, 2013, ISSN: 2381-8956 |.

[287] L.-Y. Lin, D.-E. Kim, W.-K. Kim, and S.-C. Jun, "Friction and wear characteristics of multi-layer graphene films investigated by atomic force microscopy," *Surface and Coatings Technology*, vol. 205, no. 20, pp. 4864–4869, 2011, ISSN: 02578972. DOI: `10.1016/j.surfcoat.2011.04.092`. [Online]. Available: `https://linkinghub.elsevier.com/retrieve/pii/S0257897211004488`.

[288] N. T. Kirkland, N. Birbilis, and M. P. Staiger, "Assessing the corrosion of biodegradable magnesium implants: A critical review of current methodologies and their limitations," *Acta Biomaterialia*, vol. 8, no. 3, pp. 925–936, 2012, ISSN: 17427061. DOI: `10.1016/j.actbio.2011.11.014`. [Online]. Available: `http://dx.doi.org/10.1016/j.actbio.2011.11.014`.

[289] S. Sreevatsa, A. Banerjee, and G. Haim, "Graphene as a Permeable Ionic Barrier," *ECS Transactions*, vol. 19, no. 5, pp. 259–264, 2019, ISSN: 1938-6737. DOI: `10.1149/1.3119550`. [Online]. Available: `https://iopscience.iop.org/article/10.1149/1.3119550`.

[290] M. J. Nine, M. A. Cole, D. N. H. Tran, and D. Losic, "Graphene: a multipurpose material for protective coatings," *Journal of Materials Chemistry A*, vol. 3, no. 24, pp. 12 580–12 602, 2015, ISSN: 2050-7488. DOI: `10.1039/C5TA01010A`. [Online]. Available: `www.rsc.org/materialsAhttp://xlink.rsc.org/?DOI=C5TA01010A`.

[291] A. Yli-Pentti, "Electroplating and Electroless Plating," in *Comprehensive Materials Processing*, Elsevier, 2014, pp. 277–306. DOI: `10.1016/B978-0-08-096532-1.00413-1`. [Online]. Available: `https://linkinghub.elsevier.com/retrieve/pii/B9780080965321004131`.

[292] P. A. Popoola, N. Malatji, and O. S. Fayomi, "Fabrication and Properties of Zinc Composite Coatings for Mitigation of Corrosion in Coastal and Marine Zone," in *Applied Studies of Coastal and Marine Environments*, InTech, 2016. DOI: `10.5772/62205`. [Online]. Available: `http://www.intechopen.com/books/applied-studies-of-coastal-and-marine-environments/fabrication-and-properties-of-zinc-composite-coatings-for-mitigation-of-corrosion-in-coastal-and-mar`.

[293] P. A. Popoola, N. Malatji, and O. S. Fayomi, "Fabrication and Properties of Zinc Composite Coatings for Mitigation of Corrosion in Coastal and Marine Zone," in *Applied Studies of Coastal and Marine Environments*, InTech, 2016. DOI: `10.5772/62205`. [Online]. Available: `http://www.intechopen.com/books/applied-studies-of-coastal-and-marine-environments/fabrication-and-properties-of-zinc-composite-coatings-for-mitigation-of-corrosion-in-coastal-and-mar`.

[294] M. K. Punith Kumar, M. P. Singh, and C. Srivastava, "Electrochemical behavior of Zn–graphene composite coatings," *RSC Advances*, vol. 5, no. 32, pp. 25 603–25 608, 2015, ISSN: 2046-2069. DOI: `10.1039/C5RA02898A`. [Online]. Available: `http://dx.doi.org/10.1039/C5RA02898Ahttp://xlink.rsc.org/?DOI=C5RA02898A10.1039/c5ra02898a`.

[295] H. Yang, X. Qu, W. Lin, *et al.*, "Enhanced Osseointegration of Zn-Mg Composites by Tuning the Release of Zn Ions with Sacrificial Mg-Rich Anode Design," *ACS Biomaterials Science & Engineering*, vol. 5, no. 2, pp. 453–467, 2019, ISSN: 2373-9878. DOI: `10.1021/acsbiomaterials.8b01137`. [Online]. Available: `https://pubs.acs.org/doi/10.1021/acsbiomaterials.8b01137`.

[296] Q.-h. Hu, X.-t. Wang, C. Hao, and Z.-f. Wang, "Synthesis of ni/graphene sheets by an electroless ni-plating method," *New Carbon Materials*, vol. 27, no. 1, pp. 35–41, 2012.

[297] P. Hidalgo-Manrique, X. Lei, R. Xu, M. Zhou, I. A. Kinloch, and R. J. Young, "Copper/graphene composites: a review," *Journal of Materials Science*, vol. 54, no. 19, pp. 12 236–12 289, 2019, ISSN: 15734803. DOI: `10.1007/s10853-019-03703-5`. [Online]. Available: `https://doi.org/10.1007/s10853-019-03703-5`.

[298]   A. D. Pingale, A. Owhal, A. S. Katarkar, S. U. Belgamwar, and J. S. Rathore, "Recent researches on Cu-Ni alloy matrix composites through electrodeposition and powder metallurgy methods: A review," *Materials Today: Proceedings*, vol. 47, pp. 3301–3308, 2021, ISSN: 22147853. DOI: `10.1016/j.matpr.2021.07.145`. [Online]. Available: `https://linkinghub.elsevier.com/retrieve/pii/S2214785321050045`.

[299]   U. Sarac and M. C. Baykul, "Morphological and microstructural properties of two-phase Ni–Cu films electrodeposited at different electrolyte temperatures," *Journal of Alloys and Compounds*, vol. 552, pp. 195–201, 2013, ISSN: 09258388. DOI: `10.1016/j.jallcom.2012.10.071`. [Online]. Available: `https://linkinghub.elsevier.com/retrieve/pii/S0925838812018233`.

[300]   A. Owhal, A. D. Pingale, S. Khan, S. U. Belgamwar, P. N. Jha, and J. S. Rathore, "Facile and Scalable Co-deposition of Anti-bacterial Zn-GNS Nanocomposite Coatings for Hospital Facilities: Tribo-Mechanical and Anti-corrosion Properties," *JOM*, 2021, ISSN: 1047-4838. DOI: `10.1007/s11837-021-04968-5`. [Online]. Available: `https://link.springer.com/10.1007/s11837-021-04968-5`.

[301]   A. Owhal, A. D. Pingale, S. Khan, S. U. Belgamwar, P. N. Jha, and J. S. Rathore, "Electro-codeposited γ-Zn-Ni/Gr composite coatings: Effect of graphene concentrations in the electrolyte bath on tribo-mechanical, anti-corrosion and anti-bacterial properties," *Transactions of the IMF*, pp. 1–8, 2021, ISSN: 0020-2967. DOI: `10.1080/00202967.2021.1979815`. [Online]. Available: `https://www.tandfonline.com/doi/full/10.1080/00202967.2021.1979815`.

[302]   A. Kafri, S. Ovadia, J. Goldman, J. Drelich, and E. Aghion, "The suitability of Zn-1.3%fe alloy as a biodegradable implant material," *Metals*, vol. 8, no. 3, pp. 1–15, 2018, ISSN: 20754701. DOI: `10.3390/met8030153`.

[303]   H. Yang, X. Qu, W. Lin, *et al.*, "Enhanced Osseointegration of Zn-Mg Composites by Tuning the Release of Zn Ions with Sacrificial Mg-Rich Anode Design," *ACS Biomaterials Science & Engineering*, vol. 5, no. 2, pp. 453–467, 2019, ISSN: 2373-9878. DOI: `10.1021/acsbiomaterials.8b01137`. [Online]. Available: `https://pubs.acs.org/doi/10.1021/acsbiomaterials.8b01137`.

[304]   L. Yao, J. Ao, M.-j. Jeng, *et al.*, "CZTSe solar cells prepared by electrodeposition of Cu / Sn / Zn stack layer followed by selenization at low Se pressure," pp. 1–11, 2014.

[305]   Y. Yun, Z. Dong, N. Lee, *et al.*, "Revolutionizing biodegradable metals," *Materials Today*, vol. 12, no. 10, pp. 22–32, 2009, ISSN: 13697021. DOI: `10.1016/S1369-7021(09)70273-1`. [Online]. Available: `http://dx.doi.org/10.1016/S1369-7021(09)70273-1`.

[306] C. Redlich, P. Quadbeck, M. Thieme, and B. Kieback, "Molybdenum – A biodegradable implant material for structural applications?" *Acta Biomaterialia*, vol. 104, no. xxxx, pp. 241–251, 2020, ISSN: 17427061. DOI: `10.1016/j.actbio.2019.12.031`. [Online]. Available: `https://linkinghub.elsevier.com/retrieve/pii/S1742706119308694`.

[307] H. Hermawan, "Updates on the research and development of absorbable metals for biomedical applications," *Progress in Biomaterials*, vol. 7, no. 2, pp. 93–110, 2018, ISSN: 2194-0509. DOI: `10.1007/s40204-018-0091-4`. [Online]. Available: `https://doi.org/10.1007/s40204-018-0091-4`.

[308] C. Shuai, S. Li, S. Peng, P. Feng, Y. Lai, and C. Gao, "Biodegradable metallic bone implants," *Materials Chemistry Frontiers*, vol. 3, no. 4, pp. 544–562, 2019, ISSN: 20521537. DOI: `10.1039/c8qm00507a`.

[309] M. Rahim, S. Ullah, and P. Mueller, "Advances and Challenges of Biodegradable Implant Materials with a Focus on Magnesium-Alloys and Bacterial Infections," *Metals*, vol. 8, no. 7, p. 532, 2018, ISSN: 2075-4701. DOI: `10.3390/met8070532`. [Online]. Available: `http://www.mdpi.com/2075-4701/8/7/532`.

[310] H. Tapiero and K. D. Tew, "Trace elements in human physiology and pathology: Zinc and metallothioneins," *Biomedicine and Pharmacotherapy*, vol. 57, no. 9, pp. 399–411, 2003, ISSN: 07533322. DOI: `10.1016/S0753-3322(03)00081-7`.

[311] J. Niu, Z. Tang, H. Huang, *et al.*, "Research on a Zn-Cu alloy as a biodegradable material for potential vascular stents application," *Materials Science & Engineering C*, vol. 69, pp. 407–413, 2016, ISSN: 0928-4931. DOI: `10.1016/j.msec.2016.06.082`. [Online]. Available: `http://dx.doi.org/10.1016/j.msec.2016.06.082`.

[312] Z. Tang, *Potential biodegradable Zn-Cu binary alloys developed for cardiovascular implant applications $_{E}lsevierEnhancedReader.pdf$*. 2017, pp. 182–199.

[313] J. Y. Uriu-Adams and C. L. Keen, "Copper, oxidative stress, and human health," *Molecular Aspects of Medicine*, vol. 26, no. 4-5, pp. 268–298, 2005, ISSN: 00982997. DOI: `10.1016/j.mam.2005.07.015`. [Online]. Available: `http://www.sciencedirect.com/science/article/pii/S0098299705000488https://linkinghub.elsevier.com/retrieve/pii/S0098299705000488`.

[314] H. Huang and G. Yuan, *Medical bodegradable Zn-Cu alloy and its preparation methodas well as applications*, 2017. [Online]. Available: `https://patentimages.storage.googleapis.com/14/e8/1c/70e9dd3591c601/US20170218483A1.pdf`.

[315] Y. Chen, J. Zou, S. J. Campbell, and G. Le Caer, "Boron nitride nanotubes: Pronounced resistance to oxidation," *Applied Physics Letters*, vol. 84, no. 13, pp. 2430–2432, 2004, ISSN: 0003-6951. DOI: `10.1063/1.1667278`. [Online]. Available: `http://aip.scitation.org/doi/10.1063/1.1667278`.

[316] J. G. Miranda-Hernández, H. Herrera-Hernández, C. O. González-Morán, J. N. Rivera Olvera, I. Estrada-Guel, and F. Botello Villa, "Synthesis and Characterization of Zn-Ni x Advanced Alloys Prepared by Mechanical Milling and Sintering at Solid-State Process," *Advances in Materials Science and Engineering*, vol. 2017, pp. 1–12, 2017, ISSN: 1687-8434. DOI: `10.1155/2017/7967848`. [Online]. Available: `https://www.hindawi.com/journals/amse/2017/7967848/`.

[317] ASTM International G31-71, "ASTM DESIGNATION: G31-71(Reapproved 2004) Standard Practice for Laboratory Immersion Corrosion Testing of METALS," *Annual Book of ASTM Standards*, vol. i, no. Reapproved, 2004.

[318] M. Dehestani, E. Adolfsson, and L. A. Stanciu, "Mechanical properties and corrosion behavior of powder metallurgy iron-hydroxyapatite composites for biodegradable implant applications," *Materials and Design*, vol. 109, pp. 556–569, 2016, ISSN: 18734197. DOI: `10.1016/j.matdes.2016.07.092`. [Online]. Available: `http://dx.doi.org/10.1016/j.matdes.2016.07.092`.

[319] S. N. H. Mohamad Rodzi, H. Zuhailawati, and B. K. Dhindaw, "Mechanical and degradation behaviour of biodegradable magnesium–zinc/hydroxyapatite composite with different powder mixing techniques," *Journal of Magnesium and Alloys*, vol. 7, no. 4, pp. 566–576, 2019, ISSN: 22139567. DOI: `10.1016/j.jma.2019.11.003`. [Online]. Available: `https://doi.org/10.1016/j.jma.2019.11.003`.

[320] A. D. Pingale, S. U. Belgamwar, and J. S. Rathore, "Synthesis and characterization of Cu–Ni/Gr nanocomposite coatings by electro-co-deposition method: effect of current density," *Bulletin of Materials Science*, vol. 43, no. 1, p. 66, 2020, ISSN: 0250-4707. DOI: `10.1007/s12034-019-2031-x`. [Online]. Available: `https://doi.org/10.1007/s12034-019-2031-xhttp://link.springer.com/10.1007/s12034-019-2031-x`.

[321] A. Akinci, S. Sen, and U. Sen, "Friction and wear behavior of zirconium oxide reinforced PMMA composites," *Composites Part B: Engineering*, vol. 56, pp. 42–47, 2014, ISSN: 13598368. DOI: `10.1016/j.compositesb.2013.08.015`. [Online]. Available: `http://dx.doi.org/10.1016/j.compositesb.2013.08.015https://linkinghub.elsevier.com/retrieve/pii/S135983681300423X`.

[322] T. C. Huang, Y. A. Su, T. C. Yeh, *et al.*, "Advanced anticorrosive coatings prepared from electroactive epoxy-SiO 2 hybrid nanocomposite materials," *Electrochimica Acta*, vol. 56, no. 17, pp. 6142–6149, 2011, ISSN: 00134686. DOI: `10.1016/j.electacta.2011.04.053`.

[323] G. Lalwani, M. D'Agati, A. M. Khan, and B. Sitharaman, "Toxicology of graphene-based nanomaterials," *Advanced Drug Delivery Reviews*, vol. 105, no. February 2018, pp. 109–144, 2016, ISSN: 18728294. DOI: `10.1016/j.addr.2016.04.028`. [Online]. Available: `http://dx.doi.org/10.1016/j.addr.2016.04.028`.

[324] M. Pelin, L. Fusco, V. León, *et al.*, "Differential cytotoxic effects of graphene and graphene oxide on skin keratinocytes," *Scientific Reports*, vol. 7, pp. 1–12, 2017, ISSN: 20452322. DOI: 10.1038/srep40572. [Online]. Available: http://dx.doi.org/10.1038/srep40572.

[325] N. Boshkova, K. Kamburova, N. Koprinarov, M. Konstantinova, N. Boshkov, and T. Radeva, "Obtaining and Corrosion Performance of Composite Zinc Coatings with Incorporated Carbon Spheres," *Coatings*, vol. 10, no. 7, p. 665, 2020, ISSN: 2079-6412. DOI: 10.3390/coatings10070665. [Online]. Available: http://library1.nida.ac.th/termpaper6/sd/2554/19755.pdfhttps://www.mdpi.com/2079-6412/10/7/665.

[326] S. Anwar, Y. Zhang, and F. Khan, "Electrochemical behaviour and analysis of Zn-Ni alloy anti-corrosive coatings deposited from citrate baths," *IOP Conference Series: Materials Science and Engineering*, vol. 458, no. 1, p. 012005, 2018, ISSN: 1757-899X. DOI: 10.1088/1757-899X/458/1/012005. [Online]. Available: https://iopscience.iop.org/article/10.1088/1757-899X/458/1/012005.

[327] C. Panagopoulos, E. Georgiou, P. Agathocleous, and K. Giannakopoulos, "Mechanical behaviour of Zn–Fe alloy coated mild steel," *Materials & Design*, vol. 30, no. 10, pp. 4267–4272, 2009, ISSN: 02613069. DOI: 10.1016/j.matdes.2009.04.026. [Online]. Available: https://linkinghub.elsevier.com/retrieve/pii/S0261306909001757.

[328] C Oulmas, S Mameri, D Boughrara, *et al.*, "Comparative study of Cu–Zn coatings electrodeposited from sulphate and chloride baths," *Heliyon*, vol. 5, no. 7, e02058, 2019, ISSN: 24058440. DOI: 10.1016/j.heliyon.2019.e02058. [Online]. Available: https://linkinghub.elsevier.com/retrieve/pii/S2405844019357184.

[329] J Mahieu, K De Wit, B. C. De Cooman, and A De Boeck, "The properties of electrodeposited Zn-Co coatings," *Journal of Materials Engineering and Performance*, vol. 8, no. 5, pp. 561–570, 1999, ISSN: 1544-1024. DOI: 10.1007/s11665-999-0010-x.

[330] M. J. Rahman, S. R. Sen, M Moniruzzaman, and K. M. Shorowordi, "MORPHOLOGY AND PROPERTIES OF ELECTRODEPOSITED ZN-NI ALLOY COATINGS ON MILD STEEL," *Journal of Mechanical Engineering*, vol. 40, no. 1, pp. 9–14, 1970, ISSN: 0379-4318. DOI: 10.3329/jme.v40i1.3468. [Online]. Available: https://www.banglajol.info/index.php/JME/article/view/3468.

[331] S. Fashu, C. Gu, X. Wang, and J. Tu, "Influence of electrodeposition conditions on the microstructure and corrosion resistance of Zn–Ni alloy coatings from a deep eutectic solvent," *Surface and Coatings Technology*, vol. 242, pp. 34–41, 2014, ISSN: 02578972. DOI: 10.1016/j.surfcoat.2014.01.014. [Online]. Available: https://linkinghub.elsevier.com/retrieve/pii/S0257897214000309.

[332] H. Park and J. Szpunar, "The role of texture and morphology in optimizing the corrosion resistance of zinc-based electrogalvanized coatings," *Corrosion Science*, vol. 40, no. 4-5, pp. 525–545, 1998, ISSN: 0010938X. DOI: `10.1016/S0010-938X(97)00148-0`. [Online]. Available: `https://linkinghub.elsevier.com/retrieve/pii/S0010938X97001480`.

[333] A. Brenner, "Electrodeposition of Alloys," *Academic Press*, vol. Bd. 68, Nr, p. 1964, 1964.

[334] E. Beltowska-Lehman, P. Ozga, Z. Swiatek, and C. Lupi, "Influence of structural factor on corrosion rate of functional Zn–Ni coatings," *Crystal Engineering*, vol. 5, no. 3-4, pp. 335–345, 2002, ISSN: 14630184. DOI: `10.1016/S1463-0184(02)00045-X`. [Online]. Available: `https://linkinghub.elsevier.com/retrieve/pii/S146301840200045X`.

[335] A. Gomes, I. Almeida, T. Frade, and A. C. Tavares, "Stability of Zn–Ni–TiO2 and Zn–TiO2 nanocomposite coatings in near-neutral sulphate solutions," *Journal of Nanoparticle Research*, vol. 14, no. 2, p. 692, 2012, ISSN: 1388-0764. DOI: `10.1007/s11051-011-0692-5`. [Online]. Available: `http://link.springer.com/10.1007/s11051-011-0692-5`.

[336] Y. Ullal and A. Chitharanjan Hegde, "Corrosion protection of electrodeposited multilayer nanocomposite Zn-Ni-SiO2 coatings," *Surface Engineering and Applied Electrochemistry*, vol. 49, no. 2, pp. 161–167, 2013, ISSN: 1068-3755. DOI: `10.3103/S1068375513020142`. [Online]. Available: `http://link.springer.com/10.3103/S1068375513020142`.

[337] C. Müller, M. Sarret, and M. Benballa, "ZnNi/SiC composites obtained from an alkaline bath," *Surface and Coatings Technology*, vol. 162, no. 1, pp. 49–53, 2003, ISSN: 02578972. DOI: `10.1016/S0257-8972(02)00360-2`. [Online]. Available: `https://linkinghub.elsevier.com/retrieve/pii/S0257897202003602`.

[338] V. N. Tseluikin and A. A. Koreshkova, "Electrodeposition of zinc–nickel–carbon nanotubes composite coatings in a reversing mode," *Protection of Metals and Physical Chemistry of Surfaces*, vol. 52, no. 6, pp. 1040–1042, 2016, ISSN: 2070-2051. DOI: `10.1134/S2070205116060204`. [Online]. Available: `http://link.springer.com/10.1134/S2070205116060204`.

[339] L. Magagnin, L. Nobili, and P. L. Cavallotti, "Metastable zinc–nickel alloys deposited from an alkaline electrolyte," *Journal of Alloys and Compounds*, vol. 615, no. S1, S444–S447, 2014, ISSN: 09258388. DOI: `10.1016/j.jallcom.2014.01.240`. [Online]. Available: `https://linkinghub.elsevier.com/retrieve/pii/S0925838814003326`.

[340] N. Belhamra, A. R. Boulebtina, and O. Belahssen1, "EFFECT OF TiO2 NANOPARTICLES ON THE MECHANICAL AND ANTICORROSIVE PROPERTIES OF Zn-Ni COMPOSITE COATINGS," *Acta Metallurgica Slovaca*, vol. 25, no. 2, pp. 107–113, 2019. DOI: `10.12776/ams.v25i2.1268`.

[341] L. Xiang, Q. Shen, Y. Zhang, W. Bai, and C. Nie, "One-step electrodeposited Ni-graphene composite coating with excellent tribological properties," *Surface and Coatings Technology*, vol. 373, pp. 38–46, 2019, ISSN: 02578972. DOI: 10.1016/j.surfcoat.2019.05.074. [Online]. Available: https://linkinghub.elsevier.com/retrieve/pii/S0257897219305638.

[342] R. T. Downs, K. L. Bartelmehs, G. V. Gibbs, and M. B. Boisen, "Interactive software for calculating and displaying X-ray or neutron powder diffractometer patterns of crystalline materials," *American Mineralogist*, vol. 78, no. 9-10, pp. 1104–1107, 1993, ISSN: 0003004X.

[343] M. Chen, X. Qin, and G. Zeng, "Biodegradation of Carbon Nanotubes, Graphene, and Their Derivatives," *Trends in Biotechnology*, vol. 35, no. 9, pp. 836–846, 2017, ISSN: 18793096. DOI: 10.1016/j.tibtech.2016.12.001.

[344] S. Dixit, A. Mahata, D. R. Mahapatra, S. V. Kailas, and K. Chattopadhyay, "Multi-layer graphene reinforced aluminum – Manufacturing of high strength composite by friction stir alloying," *Composites Part B: Engineering*, vol. 136, no. October 2017, pp. 63–71, 2018, ISSN: 13598368. DOI: 10.1016/j.compositesb.2017.10.028. [Online]. Available: https://doi.org/10.1016/j.compositesb.2017.10.028.

List of Publications

- **International Journal Publications**

    1. **A. Owhal**, M. Choudhary, A. D. Pingale, S. U. Belgamwar, S. Mukherjee, and J. S. Rathore, "Non-cytotoxic zinc/f-graphene nanocomposite for tunable degradation and superior tribo-mechanical properties: Synthesized via modified electro co-deposition route," Materials Today Communications, vol. 34, p. 105 112, 2023.

    2. **A. Owhal**, A. D. Pingale, S. Khan, S. U. Belgamwar, P. N. Jha, and J. S. Rathore, "Facile and scalable co-deposition of anti-bacterial Zn-GNS nanocomposite coatings for hospital facilities: Tribo-mechanical and anti-corrosion properties," JOM, vol. 73, pp. 4270–4278, 2021.

    3. **A. Owhal**, M. Choudhary, S. Belgamwar, S. Mukherjee, and J. Rathore, "Co-deposited Zn-Cu/Gr nanocomposite: Corrosion behaviour and in-vitro cytotoxicity assessment," Trans. of the IMF, Taylor & Francis, vol. 99, no. 4, pp. 215–223, 2021.

    4. **A. Owhal**, A. D. Pingale, S. Khan, S. U. Belgamwar, P. N. Jha, and J. S. Rathore, "Electro-codeposited $\gamma-$zn-Ni/Gr composite coatings: Effect of graphene concentrations in the electrolyte bath on tribo-mechanical, anti-corrosion and anti-bacterial properties," Trans. of the IMF, Taylor & Francis, vol. 99, no. 6, pp. 324–331, 2021.

- **International Conference Publications**

    1. **A. Owhal**, A. D. Pingale, S. U. Belgamwar, and J. S. Rathore, "A brief manifestation of anti-bacterial nanofiller reinforced coatings against the microbial growth based novel engineering problems," Mater. Today Proc., vol. 47, Elsevier, 2021, pp. 3320–3330.

    2. **A. Owhal**, A. D. Pingale, S. U. Belgamwar, and J. S. Rathore, "Preparation of novel Zn/Gr mmc using a modified electro-co-deposition method: Microstructural and tribo-mechanical properties," Mater. Today Proc., vol. 44, 2021, pp. 222-228.

- **Book Chapter Publications**

    1. **A. Owhal** A. D. Pingale, S. U. Belgamwar, and J. S. Rathore, "The prospects for low-cost and facile fabrication of zinc/graphene composite coatings and structural materials," in Recent Advances in Materials, Manufacturing and Machine Learning Processes, CRC Press, 2022.

Brief Biography of the Candidate

Ayush Owhal joined Birla Institute of Technology and Science, Pilani, Pilani Campus, Rajasthan, India in Jan 2019 with broad expertise in material & mechanical characterization, structural design and CAD-Modelling. He completed a B.E. degree in Mechanical engineering from Rajiv Gandhi Technical University, Bhopal, India in 2015, and an M.E. in Computer Intergrated Manufacturing from Shri G. S. Institute of Technology and Science, Indore, India in 2018. His research activities focused on nanocomposite fabrication, material characterization, development of composite fabrication methods, Bio-MEMS & NEMS devices, molecular dynamics and finite element simulation of various composites.

Brief Biography of the Supervisor

Prof. Sachin U. Belgamwar received his B.E. degree in Mechanical Engineering from Anuradha Engineering College, Chikhli, Amaravati University, India in 1999, and the M.E. and Ph.D. degree in Mechanical Engineering from Birla Institute of Technology and Science, Pilani (BITS Pilani) India, in 2001 and 2014 respectively. His Ph.D. research was on "Investigations on Multiwalled Carbon Nanotube Reinforced Copper". After working for six years in different engineering colleges, he joined the Mechanical Engineering Department, Birla Institute of Technology and Science, BITS-Pilani, Pilani Campus, in January 2007 as a Lecturer. Currently he is working as Associate Professor in Mechanical Engineering Department and he also holds the position of Associate Dean, Academic-Undergraduate Studies (AUGS) Division. at BITS Pilani, Pilani Campus, India. His area of research is on

- Electrochemical synthesis of carbon nanotube (CNT) reinforced metal matrix composites (MMCs).
- Quantification of CNT distribution in composite and microstructure property correlations.
- Thermo-physical properties and characterization of the nanocomposite.
- MEMS

He has 15+ years teaching expertise on MEMS, Thermodynamics, Power Plant Engineering, Transport Phenomena, Mechanics of Solids, Fluid Mechanics, Computer Aided Design and Kinematics and dynamics of Machines. He has supervised several Ph.D., master and undergraduate students for thesis and project work.

Prof. Belgamwar has served as Principal Investigator, and Co-Principal Investigator in many projects based on CNT reinforced Metal Matrix Composites, Electrical characterizations of nanocomposites, Dynamic modelling and Experimental Analysis of Double Row Deep Groove Ball Bearing with Multiple Localized Defects funded by BITS-Pilani Seed Grant, Research Initiation Grant and Aerodynamics R&D Board respectively, Currently, he is Principal Investigator of an on-going project based on "Powder assistive hybrid e-trike (PAH e-trike) for disabled person in rural and urban region of India". He has more than 30 national and International publications and one granted patent on "method of producing uniform mixture of copper and carbon nanotube in bulk for copper metal composites".

Brief Biography of the Co-Supervisor

Prof. Jitendra Singh Rathore completed his B.E. (Mechanical) from M. B. M. Engineering College, Jodhpur, M. Tech. (Machine Design) from Indian Institute of Technology, Roorkee, and Ph.D. from Birla Institute of Technology and Science (BITS), Pilani. After working for four years in Indian Ordnance Factories Organization, he joined the Mechanical Engineering Department, BITS, Pilani, India, in December 2006. Currently, He is a faculty in Mechanical Engineering Department, BITS, Pilani for over 16 years and serving as an Associate Professor. His research interests include nanorobotics, low Reynolds number hydrodynamics, skin tribology and biomaterials.